BAYESIAN MODEL SELECTION FOR THE SOLUTION OF SPATIAL INVERSE PROBLEMS WITH GEOPHYSICAL, GEOTECHNICAL AND THERMODYNAMICAL APPLICATIONS

A Dissertation

by

SABA SEYEDPOUR ESMAILZADEH

Submitted to the Office of Graduate and Professional Studies of
Texas A&M University
in partial fulfillment of the requirements for the degree of

DOCTOR OF PHILOSOPHY

Chair of Committee,	Zenon Medina-Cetina
Committee Members,	Charles Aubeny
	James M. Kaihatu
	Mark E. Everett
	Craig Shipp
Head of Department,	Robin Autenrieth

August 2014

Major Subject: Civil Engineering

ABSTRACT

Bayesian inference is based on three evidence components: experimental observations, model predictions and expert's beliefs. Integrating experimental evidence into the calibration or selection of a model, either empirically of physically based, is of great significance in almost every area of science and engineering because it maps the response of the process of interest into a set of parameters, which aim at explaining the process' governing characteristics. This work introduces the use of the Bayesian paradigm to construct full probabilistic description of parameters of spatial processes. The influence of uncertainty is first discussed on the calibration of an empirical relationship between remolded undrained shear strength S_{u-r} and liquidity index I_L, as a potential predictor of the soil strength. Two site-specific datasets are considered in the analysis. The key emphasis of the study is to construct a unified regression model reflecting the characteristics of the both contributing data sets, while the site dependency of the data is properly accounted for. We question the regular Bayesian updating process, since a test of statistics proves that the two data sets belong to different populations. Application of "Disjunction" probability operator is proposed as an alternative to arrive at a more conclusive $S_{u-r} - I_L$ model. Next, the study is extended to a functional inverse problem where the object of inference constructs a spatial random field. We introduce a methodology to infer the spatial variation of the elastic characteristics of a heterogeneous earth model via Bayesian approach, given the probed medium's response to interrogating waves measured at the surface. A reduced dimension, self regularized treatment of the inverse problem using partition modeling is introduced, where the velocity field is discretized by a variable number of disjoint regions defined by Voronoi tessellations. The number of partitions, their geometry and weights dynamically vary during the inversion, in order to recover the subsurface image. The idea of treating the number of tessellation (number of parameters) as a parameter itself is closely associated with probabilistic model selection. A reversible jump Markov chain Monte Carlo

(RJMCMC) scheme is applied to sample the posterior distribution of varying dimension. Lastly, direct treatment of a Bayesian model selection through the definition of the Bayes factor (BF) is developed for linear models, where it is employed to define the most likely order of the virial Equation of State (EOS). Virial equation of state is a constitutive model describing the thermodynamic behavior of low-density fluids in terms of the molar density, pressure and temperature. Bayesian model selection has successfully determined the best EOS that describes four sets of isotherms, where approximate (BIC) method either failed to select a model or fevered an overly-flexible model, which specifically perform poorly in terms of prediction.

DEDICATION

To my Family

ACKNOWLEDGEMENTS

I could not have completed this study without the support and encouragement of many people. Most especially, I would like to thank my adviser Dr. Zenon Medina-Cetina for his valuable guidance, scholarly inputs and consistent encouragement I received throughout the course of this research. I acknowledge his patience, understanding and continuous financial support. Thanks also goes to my committee members Dr. Charles Aubeny, Dr. James Kaihatu, Dr. Mark Everett and Dr. Craig Shipp for their help and advice which undoubtedly improved my work. I also would like to thank Prof. Loukas Kallivokas (University of Texas at Austin) and Prof. Jun Won Kang (Hongik University), for their support on the use of their 1D-2D wave propagation model. I am grateful to Prof. Kenneth Hall (Chemical Engineering Department) and his group, for providing the Argon data and their support on the collection of references on EOS and corresponding deterministic calibration methods. I would like to thank TEES (Texas A&M Engineering Experiment Station), Simula School of Research and Innovation (Computational Geoscience) and Statoil for sponsoring the development of this work.

I dedicate this work to my beloved husband, Navid, whose unwavering love have encouraged me to improve myself in every way. I thank my parents, my sister Sarah, and my brother Amin, for their faith in me, their unconditional love, and support. I hope I have made them proud.

TABLE OF CONTENTS

Page

ABSTRACT ii

DEDICATION iv

ACKNOWLEDGEMENTS v

TABLE OF CONTENTS vi

LIST OF FIGURES ix

LIST OF TABLES xvii

1. INTRODUCTION 1

    1.1 Problem Statement 1
    1.2 Thesis Outline 3

2. JOINT STATES OF INFORMATION FROM DIFFERENT PROBABILISTIC CALIBRATIONS OF UNDRAINED SHEAR STRENGTH OF SUBMARINE CLAYS 8

    2.1 Overview 8
    2.2 Introduction 8
    2.3 The Data Sets 10
    2.4 Method of Analysis 11
        2.4.1 A Model for the Remolded Undrained Shear Strength Data 12
        2.4.2 Bayesian Regression 16
        2.4.3 The AND and OR Probability Operators 18
    2.5 Case Study 21
        2.5.1 Homoscedastic Variance Model 22
        2.5.2 Heteroscedastic Variance Model 24
        2.5.3 Integrating the Information Content of the Two Model Calibrations 25
    2.6 Conclusion 40

3. VARYING DIMENSIONAL BAYESIAN ACOUSTIC WAVEFORM INVERSION FOR 1D SEMI-INFINITE HETEROGENEOUS MEDIA 41

    3.1 Overview 41
    3.2 Introduction 42
    3.3 Forward Model 45

3.4 Bayesian Approach to Inverse Problems . . . 46
3.5 Bayesian Partition Models . . . 49
3.6 Bayesian Model Selection . . . 51
3.7 Reversible Jump MCMC . . . 53
3.7.1 Reversible Jump MCMC Algorithm . . . 54
3.7.2 Prior Elicitation . . . 55
3.7.3 Reversible Jump MCMC Implementation as Birth-Death Process . . . 58
3.8 Application to a Synthetic Case . . . 63
3.9 Results . . . 66
3.10 Concluding Remarks . . . 74

4. VARIABLE DIMENSIONAL BAYESIAN FULL WAVEFORM INVERSION FOR 2D SEMI-INFINITE HETEROGENEOUS MEDIA . . . 76

4.1 Overview . . . 76
4.2 Introduction . . . 77
4.3 The Forward Model . . . 84
4.4 Methodology . . . 89
4.4.1 Hierarchical Bayesian Inverse Modeling . . . 90
4.4.2 Velocity Field Parameterization Using Voronoi Tessellations . . . 92
4.4.3 The Choice of Priors . . . 93
4.4.4 Bayesian Computation . . . 99
4.5 Numerical Results . . . 107
4.6 Concluding Remarks . . . 135

5. JOINT STATES OF INFORMATION FROM DIFFERENT PROBABILISTIC GEO-PROFILE RECONSTRUCTION METHODS . . . 142

5.1 Overview . . . 142
5.2 Introduction . . . 142
5.3 Rationale . . . 144
5.4 Fundamentals of the Bayesian Approach to Inverse Problems . . . 154
5.5 Vertical Electrical Sounding (VES) . . . 156
5.6 Vertical Seismic Sounding (VSS) . . . 158
5.7 Basic Probability Operators . . . 161
5.8 Application to a 1D Tomography Study . . . 164
5.8.1 Integration of Evidence Among Different Physics: VES-VSS . . . 164
5.8.2 Integration of Evidence Among the Same Physics . . . 173
5.9 Concluding Remarks . . . 180

6. BAYESIAN MODEL SELECTION FOR VIRIAL EQUATIONS OF STATE . . . 181

6.1 Overview . . . 181
6.2 Introduction . . . 181
6.3 Virial Equation of State . . . 184
6.4 Bayesian Model Selection . . . 187

6.5 Bayesian Linear Regression . . . 188
6.5.1 Selection of Priors . . . 189
6.5.2 Bayesian Point Estimation . . . 192
6.5.3 Bayesian Linear Model Comparison . . . 193
6.5.4 Posterior Statistics . . . 194
6.6 Bayesian Inference for Virial Equation of State . . . 198
6.6.1 Data Description . . . 198
6.6.2 Bayesian Model Choice for the Virial EOS . . . 198
6.6.3 Probabilistic Calibration of a Virial Equation of State . . . 201
6.7 Concluding Remarks . . . 212

7. CONCLUSION . . . 214

7.1 Observations . . . 214
7.2 Future Work . . . 217

REFERENCES . . . 219

APPENDIX A. POSTERIOR INTEGRATION USING THE MCMC-METROPOLIS HASTINGS ALGORITHM . . . 235

APPENDIX B. PARALLEL TEMPERING MARKOV CHAIN MONTE CARLO . 237

APPENDIX C. ALTERNATIVE APPROACHES TO INFER PARAMETERS OF A DISTRIBUTION FROM TWO SETS OF DATA . . . 240

APPENDIX D. BAYESIAN OCCAM'S RAZOR . . . 241

APPENDIX E. BAYESIAN MODEL SELECTION AND UNIDENTIFIABLE BAYES FACTORS . . . 242

APPENDIX F. THE JACOBIAN OF THE DIMENSION MATCHING TRANSFORMATION . . . 244

LIST OF FIGURES

FIGURE Page

2.1 (a) Global data set (b) Local data set 11

2.2 (a) Global data set (b) Local data set, including the optimal fits of the exponential model. 13

2.3 Absolute residual plots for (a) Global data set (b) Local data set showing an exponential trend. Optimal fits of the residual model is superimposed. . 14

2.4 Quantile-Quantile (Q-Q) plots of the both data sets ($\triangle$: Local data set $\circ$: Global data set). Also shown are straight lines corresponding to the normal distributions. 15

2.5 Representation of the frequency response of the 'Conjunction' and 'Disjunction' of two synthetic probability functions (a) and (b). Results of (c) conjunction and (d) disjunction operations over these two probability densities. 20

2.6 Posterior probability projections of the regression parameters, Homoscedastic model, Global data set 22

2.7 Posterior probability projections of the regression parameters, Homoscedastic model, Local data set 23

2.8 Posterior probability projections of the regression parameters, Heteroscedastic model, Global data set 25

2.9 Posterior probability projections of the regression parameters, Heteroscedastic model, Local data set 26

2.10 Cumulative probability density functions (cdf) for the global and the local datasets. The Kolmogorov-Smirnov statistical test proves provided that the two data sets belong to the same population, the probability of observing two samples with the illustrated level of cdf misfit is 1.79×10^{-20}. Therefore, the null hypothesis is rejected. 29

2.11 Posterior probability projections of the regression parameters, Homoscedastic model, AND operator 33

2.12 Posterior probability projections of the regression parameters, Heteroscedastic model, AND operator 34

2.13 Posterior probability projections of the regression parameters, Homoscedastic model, OR operator 35

2.14 Posterior probability projections of the regression parameters, Heteroscedastic model, OR operator 36

2.15 Posterior mean estimates of the S_{u-r} together with 95% credible intervals around the mean, homoscedastic variance model, (a) Global data set (b) Local data set (c) merged state of information from the use of AND operator (d) merged state of information from the use of OR operator 37

2.16 Posterior mean estimates of the S_{u-r} together with 95% credible intervals around the mean, heteroscedastic variance model, (a) Global data set (b) Local data set (c) merged state of information from the use of AND operator (d) merged state of information from the use of OR operator 38

2.17 Posterior prediction statistics: (a),(c) Posterior mean estimates of S_{u-r} together with the optimal fits of the exponential model for the global data, local data, AND, and OR operators. (b),(d) Degree of variation around the posterior mean estimate. 39

3.1 Schematic presentation of the 1D problem. (a) Original semi-infinite soil media (b) PML truncated domain 46

3.2 Partition model presentation of the 1D velocity random field 51

3.3 Benchmark soil velocity profile 64

3.4 (a) Time history of the applied stress $p(t)$ (b) Frequency spectrum of the applied stress $p(t)$ 65

3.5 (a) Measured displacement response at the surface (b) Synthetic data: Measured displacement response at $z = 0$ perturbed with 20% Gaussian noise . 65

3.6 Number of basis functions (layer interfaces) variation in first 300 RJ-MCMC iterations 67

3.7 Number of layers (k) in the partition model 67

3.8 Marginal posterior density of the layer thicknesses given $k = 5$ and the corresponding target values (dashed line) 69

3.9 Marginal posterior density of the layer velocities given $k = 5$ and the corresponding target values (dashed line) 70

3.10 Marginal posterior density for model hyper-parameters 71

3.11 Prior and posterior model predictions 73

3.12 Posterior mean estimate together with 95% credible intervals for the mean posterior and the mean prior 73

3.13 Posterior displacement prediction together with 95% credible intervals around the mean 74

4.1 Benchmark soil velocity profile 86

4.2 Schematic of a 2D computational domain surrounded by a PML absorbing boundary 87

4.3 An example of Voronoi tessellation formed about 18 pseudo random points on the plane populated from a bivariate normal density. The boundary of two neighboring tessellations is the perpendicular bisector of the line connecting their nuclei. 94

4.4 Definition of the neighborhood set for a given tessellation: In a Markov Random field the distribution of the spatial process at a given location depends only on the attributes of the process at the neighboring cells 95

4.5 (a) Source time signal $p(t)$ (b) Frequency spectrum of the time signal $p(t)$ with $f_{\max} = 15$ Hz 108

4.6 Target shear wave velocity profile A (c_s = 110 m/s, c_s = 115 m/s and $c_s = 130$ m/s from top to bottom) 109

4.7 (a) Displacement responses $u(\mathbf{x}, t)$ measured over the surface. Data is obtained by applying a uniformly-distributed Gaussian pulse with $f_{\max}$ = 15 Hz over the entire surface of profile A. (b) Synthetic data: Measured displacement response at the ground level perturbed with 10% Gaussian noise 110

4.8 (a) RJ-MCMC sampling sequence of the number of cells in the Voronoi diagram k; (b) and (c) Convergence diagnosis: plots the cumulative mean and standard deviation (over iterations) for element-wise velocities corresponding to target profile A. 113

4.9 Reversible jump MCMC output for target profile A: (a) Average solution (posterior mean velocity field estimate) (b) Best solution which maximizes the posterior density (c) Posterior mass function $p(k|\mathbf{d}_{\text{obs}})$ of the number of cells in the Voronoi diagram (d) Estimated error map showing the pointwise variability of the post burn-in velocity draws. 114

4.10 Cross-section profiles showing the true models (solid res dots), posterior mean estimates (black hollow dots) and 95% credible intervals for the posterior mean (black dotted line) corresponding to profile A. 115

4.11 Configuration of the six benchmark elements for target shear wave velocity profile A. 115

4.12 Marginal posterior density of the shear wave velocities and the corresponding target values (dashed line) at six selected elements a, b, c, d, e, and f (profile A). 116

4.13 Posterior cumulative density function (cdf) of the shear wave velocities at six selected elements a, b, c, d, e, and f (profile A). 117

4.14 (a)-(d) Marginal posterior density for model hyper-parameters. (e) Scatter plot of τ and ϕ MCMC samples, displaying the correlation structure between the two hyper-parameters (profile A). 121

4.15 Target shear wave velocity profile B ($c_s = 110$ m/s and $c_s = 135$ m/s from top to bottom) 122

4.16 (a) Displacement responses $u(\mathbf{x}, t)$ measured over the surface. Data is obtained by applying a uniformly-distributed Gaussian pulse with $f_{\max} =$ 15 Hz over the entire surface of profile B. (b) Synthetic data: Measured displacement response at the ground level perturbed with 20% Gaussian noise 122

4.17 Convergence diagnosis: plots the cumulative mean and standard deviation (over iterations) for element-wise velocities corresponding to target profile B. 123

4.18 Reversible jump MCMC output for target profile B: (a) Average solution (posterior mean velocity field estimate) (b) Best solution which maximizes the posterior density (c) Posterior mass function $p(k|\mathbf{d}_{\text{obs}})$ of the number of cells in the Voronoi diagram (d) Estimated error map showing the pointwise variability of the post burn-in velocity draws. 124

4.19 Cross-section profiles showing the true models (solid res dots), posterior mean estimates (black hollow dots) and 95% credible intervals for the posterior mean (black dotted line) corresponding to profile B. 125

4.20 Configuration of the six benchmark elements for target shear wave velocity profile B. 125

4.21 Marginal posterior density of the shear wave velocities and the corresponding target values (dashed line) at six selected elements a, b, c, d, e, and f (profile B). 126

4.22 Posterior cumulative density function (cdf) of the shear wave velocities at six selected elements a, b, c, d, e, and f (profile B). 127

4.23 Marginal posterior density for model hyper-parameters (profile B). 128

4.24 Target shear wave velocity profile C (the background velocity is $c_s = 115$ m/s and velocity of the ellipsoidal anomaly is $c_s = 150$ m/s) 128

4.25 (a) Displacement responses $u(\mathbf{x}, t)$ measured over the surface. Data is obtained by applying a uniformly-distributed Gaussian pulse with $f_{\max} =$ 15 Hz over the entire surface of profile C. (b) Synthetic data: Measured displacement response at the ground level perturbed with 20% Gaussian noise 129

4.26 Reversible jump MCMC output for target profile C: (a) Average solution (posterior mean velocity field estimate) (b) Best solution which maximizes the posterior density (c) Posterior mass function $p(k|\mathbf{d}_{\text{obs}})$ of the number of cells in the Voronoi diagram (d) Estimated error map showing the pointwise variability of the post burn-in velocity draws. 130

4.27 Cross-section profiles showing the true models (solid res dots), posterior mean estimates (black hollow dots) and 95% credible intervals for the posterior mean (black dotted line) corresponding to profile C. 131

4.28 Configuration of the six benchmark elements for target shear wave velocity profile C. 131

4.29 Marginal posterior density of the shear wave velocities and the corresponding target values (dashed line) at six selected elements a, b, c, d, e, and f (profile C). 132

4.30 Posterior cumulative density function (cdf) of the shear wave velocities at six selected elements a, b, c, d, e, and f (profile C). 133

4.31 Marginal posterior density for model hyper-parameters (profile C). 134

4.32 Target shear wave velocity profile D (the background velocities are $c_s =$ 115 m/s and $c_s = 135$ m/s from top to bottom and velocity of the ellipsoidal anomaly is $c_s = 150$ m/s). 136

4.33 (a) Displacement responses $u(\mathbf{x}, t)$ measured over the surface. Data is obtained by applying a uniformly-distributed Gaussian pulse with $f_{\max} =$ 15 Hz over the entire surface of profile D. (b) Synthetic data: Measured displacement response at the ground level perturbed with 20% Gaussian noise 136

4.34 Reversible jump MCMC output for target profile D: (a) Average solution (posterior mean velocity field estimate) (b) Best solution which maximizes the posterior density (c) Posterior mass function $p(k|\mathbf{d}_{\text{obs}})$ of the number of cells in the Voronoi diagram (d) Estimated error map showing the pointwise variability of the post burn-in velocity draws. 137

4.35 Cross-section profiles showing the true models (solid res dots), posterior mean estimates (black hollow dots) and 95% credible intervals for the posterior mean (black dotted line) corresponding to profile D. 138

4.36 Configuration of the nine benchmark elements for target shear wave velocity profile D. 138

4.37 Marginal posterior density of the shear wave velocities and the corresponding target values (dashed line) at nine selected elements a, b, c, d, e, f, g, h and i (profile D). 139

4.38 posterior cumulative density function (cdf) of the shear wave velocities at nine selected elements a, b, c, d, e, f, g, h and i (profile D). 140

4.39 Marginal posterior density for model hyper-parameters (profile D). 141

5.1 Parametrization of the material field (i.e. forming model vector $\mathbf{m}(\mathbf{x})$): (a) Layered model (b) Gridded model (c) Parametric model 146

5.2 Schematic representation of a probabilistic geophysical inversion. Right to left (the forward problem): $\mathbf{d}_{\text{obs}} = g\left(P\left(\mathbf{z},t\right),\mathbf{m}\left(\mathbf{x}\right)\right)$ denotes the forward modeling: the process of obtaining the seismic response of earth to a given excitation $P\left(\mathbf{z},t\right)$ given the spatial variation of the subsurface material properties $\mathbf{m}\left(\mathbf{x}\right)$ is fully known. Left to right (the inverse problem): $g^{-1}\left(\mathbf{d}_{\text{obs}}\right)$. The inverse deduction of the spatial distribution of the subsurface material properties, given the data $\mathbf{d}_{\text{obs}}$ is observed over the surface. The solution to an inverse problem is not unique. i.e., at each point $\mathbf{x}^i$ in space $\mathcal{D}$, the value of the material property $\mathbf{m}\left(\mathbf{x}^i\right)$ is not certain. This uncertainty is fully quantified by a probability density function. 148

5.3 Schematic representation of the classification process; defining the identifier function. 150

5.4 Schematic representation of the probabilistic classification process:
(I): Random realizations from $\mathbf{m}\left(\mathbf{x}\right)$,
(II): Corresponding binomial mappings (defining the identifier function for each realization of the material random field) $h_q\left(\mathbf{x}\right)$,
(III): Joint probability distribution $f\left(h_q\left(\mathbf{x}\right)\right)$ which gives the probability of occurrence of geomorphological event h_q at point $\mathbf{x}$ 152

5.5 Workflow of computing the probability of finding geomorphological event q at point $\mathbf{x}$: $f\left(h_q\left(\mathbf{x}\right)\right)$ 153

5.6 Problem configuration (benchmark).
Left: Acoustic imaging with a Gaussian pulse type load excitation over the surface.
Right: Vertical electrical sounding with Schlumberger electrode configuration. 157

5.7 Schematic presentation of the 1D problem. (a) Original semi-infinite soil media (b) PML truncated domain. 160

5.8 Conjunction and disjunction in a 1D probability space; (a),(b): Input probabilities, (c): Conjunction, (d): Disjunction. 163

5.9 Excitation time signal and its Fourier spectrum. 165

5.10 Synthetic data. a) Measured displacement response at the surface (solid line) perturbed with 20% Gaussian noise. b) Theoretical apparent resistivity curve generated for the benchmark two layer Earth model (solid line) perturbed with 15% Gaussian random noise. 166

5.11 Marginal posterior densities regarding the vertical electrical sounding, together with the target values (dashed line). 169

5.12 Marginal posterior densities regarding the seismic inversion, together with the target values (dashed line). 170

5.13 Marginal posterior densities regarding the joint seismic-electrical resistivity inversion, together with the target values (dashed line). 175

5.14 Correlation structure between compressional wave velocity and electrical resistivity. Posterior probability projections of the p-wave velocity vs resistivity for a) top layer and b) bottom layer. 176

5.15 Seismic-electrical resistivity inversion of depth of the layer interface for a 2-layer Earth model, superimposed with multi-physics reconstructed soil profile via a) Conjunction operator and b) Disjunction operator. 176

5.16 Excitation time signals and their Fourier spectrum. 177

5.17 Synthetic data generated by perturbing the model response with 20% Gaussian noise (SNR=5) together with the measured displacement response at the ground level (solid curve). 177

5.18 Inverted compressional wave velocities (a and b) and inverted depth of the boundary (c) of a 2-layer earth model corresponding to sources with $f_{max} =$ 20 Hz and $f_{max} = 70$ Hz, together with the target values (dashed line). The measurements are made every 0.02 sec (101 data points). 178

5.19 Inverted compressional wave velocities (a and b) and inverted depth of the boundary (c) of a 2-layer earth model corresponding to sources with $f_{max} =$ 20 Hz and $f_{max} = 70$ Hz, together with the target values (dashed line). The measurements are made every 0.01 sec (202 data points). 179

6.1 Data series of isothermal experimental observations 199

6.2 Results of the model selection study in terms of the normalized BIC as a function of the order of the virial EOS. 202

6.3 Posterior probability projections of the virial coefficients at $T = 153K$ . . . 206

6.4 Posterior probability projections of the virial coefficients at $T = 220K$ . . . 207

6.5 Posterior probability projections of the virial coefficients at $T = 280K$ . . . 208

6.6 Posterior probability projections of the virial coefficients at $T = 295K$ . . . 209

6.7 Posterior probability projection of regression parameters and variance of the error component at $T = 153K$ 209

6.8 Posterior prediction statistics for cubic, quartic, and quintic virial EOS, $T = 153K$ 211

6.9 Posterior prediction statistics for quadratic, cubic, and quartic virial EOS, $T = 295K$ 211

D.1 Schematic presentation of Bayesian Occam's razor 241

LIST OF TABLES

TABLE Page

2.1 First order statistics: Expected values of the regression parameters and the hyper-parameters 32

2.2 Second order statistics: Covariance matrix of the regression parameters and hyper-parameters 33

5.1 Statistics of the posterior parameters of the independent resistivity and seismic inversions. 171

5.2 Statistics of the posterior parameters of the coupled resistivity and seismic inversion. 172

5.3 Statistics of the seismic inversion where the media is probed with two sources of different frequencies 174

6.1 Bayes Factor interpretation: grades of evidence corresponding to values of the BF against $\mathscr{M}_j$ 188

6.2 Bayes Factors relative to a lower degree model 202

6.3 Bayes Factors relative to a quadratic base model 203

6.4 Results of the model selection study in terms of the BIC as a function of the order of the virial EOS. 203

6.5 Bayes estimate of regression coefficients 205

6.6 Covariance matrices of regression coefficients 210

6.7 Bayes estimates of variances of random error component σ^2 210

1. INTRODUCTION

1.1 Problem Statement

In a physical process an inverse problem consists in estimating the key parameters describing the relevant characteristics that governs it, through a set of directly measurable responses of the system or experimental observations. In general, these measurements or experimental observations are random, sparse and limited compared to the dimension or complexity of the model space. This leads to the ill-posed nature of inverse problems. That is, no solution might exist in the strict sense, multiple solutions might exist and/or the solution might not depend continuously on the experimental observations (Engl *et al.*, 1996). Further complexity might be posed when dealing with functional inverse problems, where the parameter set (unknowns) constitute a function of spatial coordinates and/or time (a spatial or temporal field) or stochastic coordinates. Hence, the observations are used to retrieve essentially infinite number of unknowns (pointwise values of the unknown field), where, in general, no information is available on spatial variability of the property of interest. The reconstructed solution is highly uncertain, acknowledging that infinite solutions are equally compatible with a single data set.

To attain meaningful results to the inverse problem, enforcement of additional assumptions or information on the model space is required. Classical deterministic approaches based on exact matching or least-squares optimizations, minimizes a functional form of objective function, defined by the deviation between the experimental observations and model predications (misfit function) (Yan *et al.*, 2009). The well-posedness of the problem (solution uniqueness) is enforced by ad-hoc constraints on the unknown space, so-called regularization terms in the objective function. The deterministic inference output is a point estimate of unknowns, without rigorously considering stochastic nature of the all available sources of evidence (i.e. experimental observations, theoretical model, and expert's beliefs). Meanwhile, the validity of the constructed solution is highly dependent on how accurately

the underlying physics is simulated (does the model captures all the physics that contribute to the data?). Therefore, the deterministic estimation of the parameters could be considered of limited use, considering all the sources of uncertainty. The straightforward recognition of the noted uncertainties has led to introduction of stochastic inverse theory. Recently, several methods for the inverse analysis under uncertainties have been developed, such as sensitivity analysis (Sun & Yeh, 1992), the extended maximum likelihood method (Fadale *et al.*, 1995), the spectral stochastic methods (Ghanem & Spanos, 2003; Marzouk *et al.*, 2007), and the Bayesian inference approach (Kaipio & Somersalo, 2005). The latter constructs the basis of this dissertation.

Among the stochastic methods in use, the Bayesian inference has a number of distinctive attributes. The probabilistic model calibration via the Bayesian paradigm is implemented to address the later concerns as this allows a systematic exploration of all combinations of the model parameters within a transparent definition of the impact of the participating uncertainty sources. During such exhaustive parameter exploration, a probability metric can assess the likelihood of selecting sets of parameters that approximate the experimental observations (so called the likelihood function). In addition, a probability metric reflects the degree of a-priori knowledge about the model parameters (the prior probability). As a result the output of the Bayesian inference is not a point estimate, but a probability distribution summarizing all the available evidence (carried by the likelihood function and the prior density). That is, the solution non-uniqueness is quantitatively treated by considering all parameter values lying in the support of the prior and the likelihood, where relative plausibility of each individual parameter value is quantified by the posterior.

Bayesian model calibration yields the following benefits: a transition from deterministic to probabilistic model parameters (where the degree of confidence on the predictive accuracy of the model is quantitative), assessment of the type and degree of correlation between the model parameters (e.g. linear or non-linear), measurement of the impact of the varying experimental observations (e.g. the effect of the number of observations on the prediction of confidence levels), founding a systematic framework to combine/joint the

states of information derived from the calibration of the different participating sources of evidence in the probability space, assessment of the model performance (i.e., having a number of competing models to describe the observations, defining the theory that represents data "best" in some sense). Moreover, the possibility of modeling the spatial correlation of the data and non-Gaussian error structures are reserved. Standard prior distributions which bears smoothness constraints (Gaussian process or Markov random field priors) can provide more flexible regularization in the sense that the nontrivial task of defining appropriate regularization parameter is resolved through hierarchical Bayesian models (Yan *et al.*, 2009). Owing to the advances in computational power and significant growth in efficiency of the Markov Chain Monte Carlo (MCMC) methods, the Bayesian inference has attracted a great deal of interest in diverse applications of science and engineering. This dissertation specifically looks into Bayesian inversion and model selection in 1) probabilistic analysis of a submarine clay-rich sediment data to calibrate an empirical relationship between the remolded undrained shear strength and the liquidity index 2) Full elastic waveform inversion in one- and two-dimensional heterogeneous half space, and 3) Bayesian model selection of a thermodynamic constitutive model (Virial equation of state).

1.2 Thesis Outline

This dissertation is organized as follows: In Chapter 2, we discuss probabilistic calibration of the empirical relationship between the remolded undrained shear strength S_{u-r} and the liquidity index, I_L, as a potential predictor of soil strength. Of special interest is to assess the site dependency of the fitted empirical model. We address the applicability of the Bayesian updating where the inference from the first data set is updated, as new data is introduced into the statistical inference, while the data sets belongs to different populations. Remolded undrained shear strength is used in the assessment of debris stability in retrogressive landslides (Kvalstada *et al.*, 2005). It is also widely employed to calculate force and deformation of seafloor structures (Demars, 1978; Lee *et al.*, 1991; Bang *et al.*, 2000). Furthermore, drag forces exerted on the submarine structures is found to be proportional to the S_{u-r} assigned to the sliding masses. These justify an inclusive uncertainty based

study of the correlation between I_L and S_{u-r}. Moreover, since index physical properties can easily be measured in the laboratory, it is of great interest to approximate a mechanical parameter, such as S_{u-r} from a state parameter (e.g. I_L). Previous studies on clayey soils statistically prove that a natural relationship between I_L and S_{u-r} can be described by an exponential model in the 'physical space' (Liszkowski *et al.*, 2004). Two different data sets are analyzed: The "global" data set of clayey submarine sediment samples, collected from twelve different locations around the globe, and the local data set sampled from the sediments of the Storegga Slide offshore Norway reflecting the regional soil characteristics. The key interest of the study is to establish a framework to merge the two states of information (represented by probability density functions) extracted from the global and the local data sets to reconstruct a more conclusive model space, particularly capable of accounting for the site dependency effect.

Chapters 3 and 4 set out a Bayesian framework for elastic full wavefrom inversion, for recovering the stratigraphy in one- and two-dimensional heterogeneous soil medium, respectively. We are seeking to infer the elastic characteristics of a heterogenous semi-infinite soil model by leveraging the medium's response to interrogating waves. A stress load is applied on the soil's surface to probe the stratigraphy, and the displacement response of the medium is directly recorded in the time-domain at the sensors also situated on the surface. The recorded response is fed to the inverse solver to reconstruct the spatially variable wave velocity field.

This describes a nonlinear inverse problem in which the object of inference constructs a spatial random field. Two major modelling and computational challenges are involved in this construction. First, the number of unknowns (i.e., pointwise values of the field) is essentially infinite. Hence, the unknown field is approximated by its spatial discretization. This discretization is often according to the resolution of the forward solver leading to an often very high dimensional parameter space. Large dimensionality of the input space with a nonlinear forward mapping lead to multimodal, strongly correlated and skewed posteriors, which in turn gives rise to major complications in the posterior sampling. Moreover, as the

number of unknowns increases (at times, higher than the number of data) overfitting the data might occur which brings about spurious large fluctuations in the inverted material property values. This results could be completely erroneous and yet very well fit the data. Such solutions also perform poorly in terms of prediction (Koutsourelakis, 2009). Secondly, Simulation based inference schemes (Monte Carlo methods) usually requires a high number of forward model calls in order to arrive at stationary state of the chain and approximate the estimators. Repeated evaluation of the forward model, particularly when faced with large-scale inverse problems, even though possible in theory, could be computationally intractable, rendering the inference impractical for real applications.

One approach to cope with the addressed challenges is reducing the dimensionality of the parameter space. We opted for a relatively new choice of parametrization, based on Bayesian partition modeling (BPM) (Denison *et al.*, 2002a,b), which is especially suitable when dealing with earth models with sharp material interfaces. Partition modeling involves in discretizing the spatial/temporal random field into a number of disjoint regions, where the number of regions and their geometry dynamically vary during the inversion to adapt to the structure and properties of the target model. Therefore, the number, geometry (shape, size and position), and the weight of the partitions (describing the intensity of the parametric field of interest) are inversion parameters, directly determined by the data. Hence, representation of the velocity field is not tied to the resolution of the forward model, and the latter influences the inference only through the estimation of the likelihood.

The idea of treating the number of partitions (number of parameters) as a parameter itself is closely associated with probabilistic model selection, where a collection of models with varying number of parameters are presented for inversion, and the task is to select the model that most likely describe the experimental observations. The greatest advantage of treating an inverse problem as a Bayesian model selection is the notion of Bayesian parsimony, also known as "Occam's razor" stating that the simplest model consistent with the data should be favored over more complex models, and optimum complexity of the model must be inferred from the data. As a result, the smallest model (less parameters) that

adequately describes the data is chosen. Reducing dimensionality of the parameter space means that regularizing the solution through global damping procedures (in deterministic optimization problems) or specific prior distributions which bears smoothness constraints (in a Bayesian inversion framework), is precluded. A generalization of the simulation-based Markov Chain Monte Carlo methods, so called reversible jump Green (1995), is used to sample the posterior distribution of varying dimensionality.

A key advantage of Bayesian analysis of geophysical data, is that the information is projected into the probability space, casted in form of a posterior density function, where the basic probability operators could be operated to merge/combine the geophysiacal evidence from varying sources of survey. This idea is developed in chapter 5. We introduce a methodology to populate probability maps of geomorphological features that can be applied to characteristics observed in different geophysical investigations over the same region, where Tarantola's "collaboration" probability operators, so called Conjunction and Disjunction, operate across these maps to improve (or enrich) the resulting mechanistic stratigraphy representing the geological 'Earth model'. The development relies on the fact that an Earth model consistent with multiple geophysical datasets is more likely to represent the true subsurface than a model consistent with only a single survey data (Lelièvre *et al.*, 2012). Specifically, if data sets are collected from different geophysical methods (which sense different physical properties) they usually contain complementary information about the site's stratigraphy. The concept is illustrated in a 1D setup, where soil stratigraphy is recovered by both vertical electrical sounding and acoustic imaging (using the scheme presented in chapter 3) of the subsurface, and compressional wave velocity, electrical conductivity, and the location of the transition between soil units (geomorphological information) are recovered.

As previously noted, the transdimensional formulation of elastic full waveform inversion, outlined in chapters 3 and 4, is based on Bayesian model selection. That is, having a number of competing models (theories) to describe a set of data, it is desired to find the model that describes the data best while over-fitting the data is avoided. The Bayesian

model choice is conducted through a quantity called Bayes factor (BF), which offers a sound criteria to directly compare relative plausibility of a number of competing models. However, definition of the BF requires calculation of often high dimensional integrations, which makes the direct use of the BF practically infeasible in general conditions. An example is our non-linear inverse wave problem where in order to determine the most likely number of partitions, a Monte carlo search (RJMCMC algorithm) is applied to perform the posterior integration. Approximate methods such as BIC (Bayesian information criteria) are alternative approaches to conduct Bayesian model selection. For normal linear models, however, the exact analytic evaluation the BF is possible, given a specific (conjugate) family of priors is specified to the model parameters. The full development of Bayesian model selection for linear models is provided in chapter 6, where it is employed to define the most likely order of the virial Equation of State. Virial equation of state in a constitutive model describing the thermodynamic behavior of low-density fluids in terms of the molar density, pressure and thermodynamic temperature (ρ, P, T). Virial EOS presents the molar compressibility factor Z for a fluid as an infinite power series in the molar density, for which the number of terms contributing to the fluid behavior (truncation term) must be inferred from the data. Current practice on the deterministic model calibration techniques applied to EOS and its corresponding standard statistical inferences overlooks model uncertainty. Hence, typical EOS parameterizations make use of subjective or optimization-based selections of a truncation term in the virial expansion model. Emphasis is given solely to a qualitative curve fitting to the data, without questioning the potential influence of the various sources uncertainties involved in the process. The Bayesian calibration and model selection sets out a coherent framework to calibrate isothermal experimental curves of pure Argon (Ar) measurements. Proper characterization of gas models of equation of state is of critical importance in industrial application, and lack of an uncertainty quantification may translate into significant economical loses due to the large trading volumes involved.

2. JOINT STATES OF INFORMATION FROM DIFFERENT PROBABILISTIC CALIBRATIONS OF UNDRAINED SHEAR STRENGTH OF SUBMARINE CLAYS

2.1 Overview

The remolded undrained shear strength (S_{u-r}) of submarine clays is a key parameter in the analysis of retrogressive-type of clay landslides. This is correlated with the liquidity index I_L, for which the quantification of inherent uncertainties becomes of significant value for a more rational assessment of the stability of this type of structures. The influence of the uncertainty on the predictions of an empirical relationship between remolded undrained shear strength and liquidity index is discussed in this work, by utilizing the concept of joint states of information proposed by Tarantola (Tarantola, 1987), as a generalization of the Bayesian paradigm for the solution of inverse problems. By using Tarantola's approach, this study aims at accounting for the site dependency effect when comparing a global and a local data set, which is a characteristic that is not captured by traditional probabilistic methods.

2.2 Introduction

Proper assessment of the risk involved in various offshore activities, including the natural resources field development, calls for an appropriate evaluation of the submarine geohazards specifically slope failure and mass wasting processes. This, inturn, relies on the clear understanding of the geotechnical behavior and mechanical properties of the seabed clay-rich deposits.

Normally, limited soil investigation data is available, especially in deep water environments. This may result in an uncertain estimation of the physical and mechanical design properties of submarine sediments, and their interrelation. A body of regression type analysis has been conducted to formalize the relationship between key physical and mechanical parameters of clay-rich sediments, e.g. (Wroth & Wood, 1978; Carrier & Beckman, 1984;

Locat & Demers, 1988; Hirata *et al.*, 1990; Terzaghi *et al.*, 1996). However, the significant uncertainty arising from lack of data (which is naturally contaminated with noise) and the model error (i.e. whether the adopted regression model is the true process from which the data is generated) renders point estimates of little use. Moreover, it is essential to quantify the confidence in the estimates generated. Most importantly, the predictive ability of the fitted model must be quantified. The majority of the published work do not quantify the predictive accuracy of the correlation, the necessary piece of information for an engineer to construct safety factors in slope stability analysis and foundation design.

This paper introduces a probabilistic analysis to calibrate the empirical relationship between the remolded undrained shear strength S_{u-r} and the liquidity index, I_L, as a potential predictor of soil strength. Of special interest is to quantify the credibility of the established correlation given the data. The lack of proper uncertainty quantification, the limited nature of soil exploration data, as well as the rigorous site dependency of the fitted models tends to restrict the applicability of the deterministic regression relationships to a narrow range of practices.

S_{u-r} is used in the assessment of debris stability in retrogressive landslides (Kvalstada *et al.*, 2005). It is widely used to calculate force and deformation of seafloor structures (Demars, 1978; Lee *et al.*, 1991; Bang *et al.*, 2000). Also, drag forces exerted on the submarine structures is found to be proportional to the S_{u-r} assigned to the sliding masses. These justify an inclusive uncertainty based study of the correlation between I_L and S_{u-r}. Moreover, since index physical properties can easily be measured in the laboratory, it is of great interest to move from a state parameter (e.g. I_L) to a mechanical parameter, such as S_{u-r}, accounting for the inherent uncertainty. Previous studies on clayey soils statistically prove that a natural relationship between I_L and S_{u-r} can be described by an exponential model in the 'physical space' (Liszkowski *et al.*, 2004).

Two different data sets have been analyzed in this paper: The "global" data set of clayey submarine sediment samples collected from twelve different locations around the globe, and the "local" data set sampled from the sediments of the Storegga Slide, offshore

Norway, reflecting the regional soil characteristics. The key interest of this paper is to establish a framework to merge the two states of information (represented by probability density functions) extracted from the global and the local data sets to reconstruct a more conclusive model space, particularly capable of accounting for the site dependency effect, where applicability of two probability operators is investigated to transfer the state of knowledge from one site characterization to another.

The paper is organized as follows: In section 2.3 the data sets are introduced. In section 2.4 we detail the method of analysis. A proper regression model first adopted to adequately describe the data (section 2.4.1). We formalize the Bayesian regression, specify the prior distribution and the likelihood function, and briefly cover the Bayesian computation (section 2.4.2). Section 2.4.3 is devoted to introducing the two basic operators in the probability space employed as a tool to join states of information from different probabilistic calibrations of the undrained shear strength. The analysis results are presented in section 2.5. Some conclusions are drawn in section 2.6.

2.3 The Data Sets

Two different data sets have been studied in this paper and earlier works of Yang et al. and Esmailzadeh et al. (Yang *et al.*, 2010; Esmailzadeh *et al.*, 2011). The first data set, namely, the global data set retrieved from a previously constructed data base at NGI (NGI, 2002) also used for the assessment of the correlation among the soil physical and mechanical parameters of the clay-rich deposits. The global data set has been collected from twelve sites from the Norwegian sea, the North sea (the North sea petroleum fields Troll East and Sleipner B, located at the south of the Storegga slide), the Atlantic Ocean, the west coast of Ireland, offshore Nigeria, offshore Angola, and the Gulf of Mexico.

The second data set, being pointed here as the local data set, is a regional data collected from the Storegga Slide area out of the Norwegian coastline. The Storegga Slide occurred 8200 years ago (Haflidason *et al.*, 2005). The Slide, considered the largest exposed submarine slide in the world, has affected the region of approximately $95,000$ km^2 and involves displacement of about 3000 km^3 of debris (Kvalstada *et al.*, 2005). Since the Ormen Lange

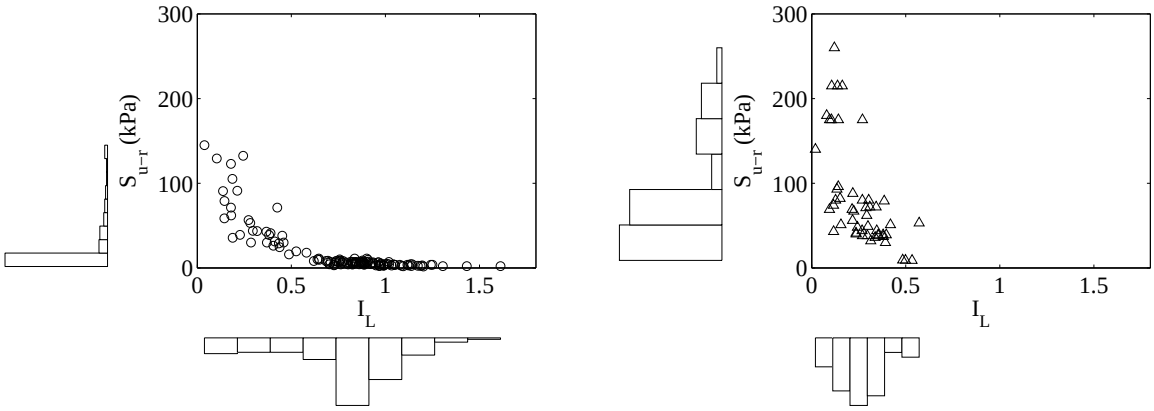

(a) (b)

Figure 2.1: (a) Global data set (b) Local data set

natural gas field as well as several other offshore projects is located in the slide region, the incident has been thoroughly investigated to secure safe field development (Solheim *et al.*, 2005; Mienert, 2004). Geotechnical testing have been conducted over the borehole samples ranging from 20 to 450 m in depth. Despite the relative sparsity of the collected samples, the drilled sections covers the major lithological units within the slide-prone part of the region. Both the global and local databases contain S_{u-r} measured by means of fall-cone test. The both data sets together with the S_{u-r} and I_L marginal histograms are presented in figure 5.10.

2.4 Method of Analysis

The aim of this study is not only to assess a correlation trend between S_{u-r} and I_L, but also to investigate the influence of the inadequate/uncertain nature of the data and possibly the regression model (i.e., type of the regression model describes the correlation the best given the available evidence) for prediction purposes. To perform an uncertainty based analysis of the remolded undrained shear strength data, the response parameter S_{u-r} and the model parameters (the regression parameters and the calibration error) are assumed to be random variables.

The probabilistic model calibration via the Bayesian paradigm is implemented to address the later concerns, as this allows a systematic exploration of all combinations of the model parameters within a transparent definition of the impact of the participating uncertainty sources. During such exhaustive parameter exploration, a probability metric can assess the likelihood of selecting sets of parameters that approximate the experimental observations (so called the likelihood function). In addition, a probability metric reflects the degree of a-priori knowledge about the model parameters (the prior probability). The combination of these two states of knowledge about the model of interest yields the following benefits: a transition from deterministic to probabilistic model parameters (where the degree of confidence on the predictive accuracy of the regression model is quantitative), assessment of the type and degree of correlation between the model parameters (e.g. linear or non-linear), measurement of the impact of the varying experimental observations (e.g. the effect of the number of observations on the prediction confidence levels), founding a systematic framework to combine/joint the states of information derived from the calibration of the different participating sources of evidence in the probability space (via the probability operators as will be discussed in this article), assessment of the model performance (having a number of competing (regression) models that describe the observations equally well, it is desired to find the theory that describes data "best" in some sense). Moreover, the possibility of modeling the spatial correlation of the geotechnical data and accounting for its site dependent nature is reserved. Non-Gaussian error structures can also be easily incorporated into the analysis. The two latter conditions are not the concern of this paper.

First, we treat each of the two data sets independently. Figure 2.1 shows the two data sets superimposed by the best-fit regression of exponential type for each case estimated using nonlinear least squares scheme.

2.4.1 A Model for the Remolded Undrained Shear Strength Data

The model describing the correlation between the remolded undrained shear strength and the liquidity index is given by

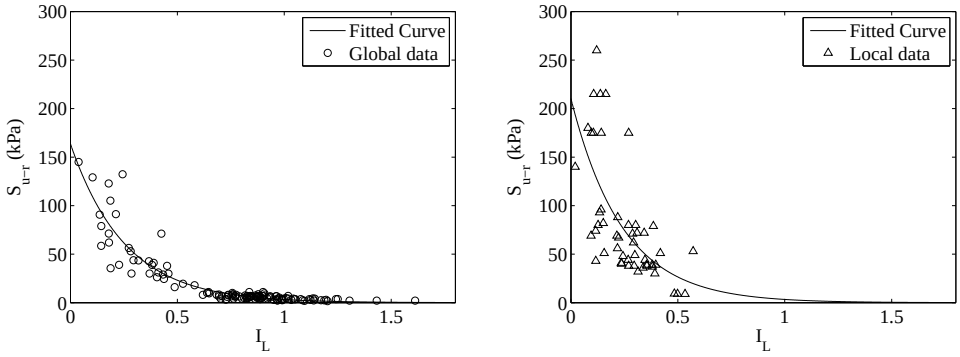

Figure 2.2: (a) Global data set (b) Local data set, including the optimal fits of the exponential model.

$$S_{(u-r)_j} = \mu(I_{L_j}; \boldsymbol{\beta}) + \epsilon_j; \quad j = 1, \ldots, n \tag{2.1}$$

in which $\mathbf{S}_{(u-r)} = (S_{(u-r)_1}, \ldots, S_{(u-r)_n})$ is the vector of undrained shear strength data (the response variable), and $\boldsymbol{\mu}$ is a deterministic exponential regression model as suggested by figure 2.1 and defined in equation 2.2. n is the number of data points in each data set and $\boldsymbol{\epsilon}$ is the vector of random error term (the discrepancy term between the fitted model and the actual observations). The error components are assumed to be independent and identically distributed random variables populated from a normal density with zero mean and variance of σ^2. σ^2 is the measure of scatter about the trend curve. Hence $\boldsymbol{\epsilon} \sim \mathcal{N}(\mathbf{0}, \sigma^2 \mathbf{I}_n)$, which implies that the observations are also populated from a normal density.

The normality assumption of the random error components can be checked by a simple quantile-quantile (Q-Q) plot (Martinez & Martinez, 2001). The Q-Q test is a graphical mean of assessing whether a sample is populated from a specific distribution. The quantiles of the residual term $\boldsymbol{\epsilon}$ are plotted versus standard normal quantiles and departures from linearity of the resulting plot determine how the dataset differs from the Gaussianity assumption. The Q-Q plot is shown in figure 2.4. The inspection of the plot indicates a

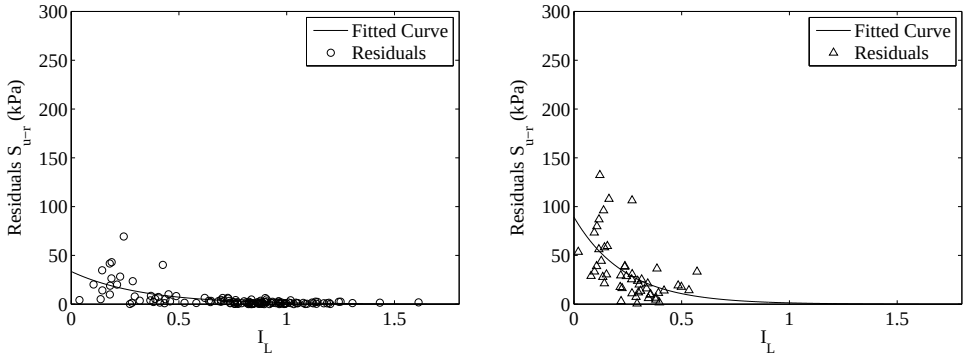

Figure 2.3: Absolute residual plots for (a) Global data set (b) Local data set showing an exponential trend. Optimal fits of the residual model is superimposed.

reasonable match to the normality assumption, although a clear deviation is observed at the two extreme values of I_L.

The mean regression model is an exponential type as presented in figure 2.2

$$\mu(I_L;\boldsymbol{\beta}) = \beta_0 \exp\left(-\beta_1 I_L\right); \quad \boldsymbol{\beta} = (\beta_0, \beta_1)^T \tag{2.2}$$

in which $\boldsymbol{\beta}$ is the vector of regression parameters. Nonlinear least squares estimate of the regression parameters (β_0, β_1) are equal to $(163.66, 3.92)$ and $(210.31, 4.14)$ for the global and the local datasets, respectively.

In addition to the regression parameters, in Bayesian parameterization it is possible to account for the unknown nature of the variability of the data and the goodness of fit by representing σ^2 as a random variable (referred to as a hyper-parameter). By examining the residuals of the optimal fit for the both data sets in figure 2.3, it is observed that for the proposed exponential regression model the variance of the error component σ^2 is not constant within the range of variation of I_L. The higher data-model deviation corresponds to the greater values of the predictor variable I_L. This observation suggests assuming an explicit variance model to capture this variance heterogeneity.

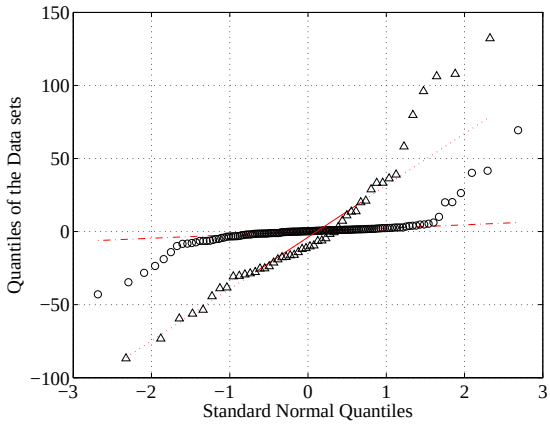

Figure 2.4: Quantile-Quantile (Q-Q) plots of the both data sets (△: Local data set ○: Global data set). Also shown are straight lines corresponding to the normal distributions.

Two different variance structures are considered in this study:

First Homoscedastic variance model, where the error variance σ^2 is assumed to be identical for all values of I_L. In other words, the scatter about the trend line is assumed to be constant along the range of variation of I_L. This is the underlying assumption in traditional deterministic regression techniques.

Second Heteroscedastic variance model, where the variance of the error complement is varying over the I_L domain (which is seemingly the case for the both data sets)

A general representation of a heteroscedastic regression model is given by

$$\begin{aligned} \sigma^2 = \mathrm{Var}(S_{(u-r)_j}) &= \sigma_0^2 g^2\left(I_{L_j};\boldsymbol{\beta},\eta\right) \\ &= \sigma_0^2\left[\exp\left(-I_{L_j}\eta\right)\right]^2 \end{aligned} \tag{2.3}$$

The data variance model, in general, can be a function of the regression parameters. Here, an exponential variance model is suggested by figure 2.3 for the both data sets. A homoscedastic model is a special case of a heteroscedastic model where $g\left(I_{L_j};\boldsymbol{\beta},\theta\right) = 1$, which leads to $\mathrm{Var}(S_{(u-r)_j}) = \sigma_0^2$. η is also assumed to be a random parameter being

inferred from the data.

2.4.2 Bayesian Regression

In the preceding section, a regression model was formulated to describe $S_{u-r} - I_L$ data. In this section, the basic elements of the Bayesian regression will be covered.

To proceed with the implementation of the Bayesian regression, a prior distribution must be assigned to each model unknown, which quantifies the initial uncertainty about the parameters. Technically, the prior distribution formalizes the a-priori unknown variability of the model parameters in form of a density function. The prior density $p(\mathbf{m})$ assigned to the parameters of each model is given by

$$p(\mathbf{m}) = \begin{cases} \frac{1}{\sigma_0^2} \mathrm{I}_{(0,+\infty)}(\boldsymbol{\beta}), & \text{Homoscedastic} \\ \frac{1}{\sigma_0^2} \mathrm{I}_{(0,+\infty)}(\boldsymbol{\beta}) \mathrm{I}_{(0,+\infty)}(\eta), & \text{Heteroscedastic} \end{cases} \tag{2.4}$$

where $\mathbf{m} = \{\boldsymbol{\beta}, \sigma_0^2\}$ for the regression model with homoscedastic variance structure, and $\mathbf{m} = \{\boldsymbol{\beta}, \sigma_0^2, \eta\}$ for the heteroscedastic condition. $\mathrm{I}_A(x)$ is an indicator function which assumes 1 if $x \in A$ and zero otherwise. The above equation signifies that the prior on β_0 and β_1 is uniform for positive values of the covariate, the prior on $\log(\sigma_0)$ is uniform in $(0, \infty)$, and the prior on η for the heteroscedastic model is uniform over $(0, \infty)$. This representation assumes that all the model parameters are independent a priori. This is not a limiting assumption, since in case the parameters are correlated, the correlation structure will be formed as the data is introduced to the analysis.

The contribution from the observations is represented by the so called likelihood function. The likelihood function $p(\mathbf{S}_{u-r}|\mathbf{m})$, describing the data-error statistics, is the probability that the observed realizations $\mathbf{S}_{u-r}$ are produced by model $\mu(I_L; \boldsymbol{\beta})$. Under the assumption that the random error components are such that $\boldsymbol{\epsilon} \overset{iid}{\sim} \mathcal{N}\left(\mathbf{0}, \sigma^2 \mathbf{I}_n\right)$ (e.g. uncertainty associated with the data is multi-variate normal, and data points are independent of each other) the likelihood is defined by

$$p\left(\mathbf{S}_{u-r}|\mathbf{m}\right) = \frac{1}{\left[(2\pi)^n|\mathbf{C}_d|\right]^{1/2}} \exp\left[-\frac{1}{2}\left(\mu(I_L;\boldsymbol{\beta}) - \mathbf{S}_{u-r}\right)^T \mathbf{C}_d^{-1}\left(\mu(I_L;\boldsymbol{\beta}) - \mathbf{S}_{u-r}\right)\right] \quad (2.5)$$

where n is the number of observations, and $\mathbf{I}_n$ is an $n \times n$ identity matrix, and $\mathbf{C}_d = \sigma^2\mathbf{I}_n$ is the covariance of the error term, with σ^2 being defined in equation 2.3. The normality assumption was assessed in figure 2.4.

By the virtue of the Bayes theorem, the most general solution to a regression problem is casted in the form of a probability density function, namely the posterior density, which is the full description of the model parameters given the data is observed. Hence, unlike the deterministic regression, where the result is a single vector of model parameters: the optimal, in a probabilistic regression, the solution is composed of all the plausible values of model parameters each weighted by its corresponding probability of occurrence (Gauer *et al.*, 2009). According to the Bayes theorem, the posterior density $p\left(\mathbf{m}|\mathbf{S}_{u-r}\right)$ is given by

$$p\left(\mathbf{m}|\mathbf{S}_{u-r}\right) = \frac{p\left(\mathbf{S}_{u-r}|\mathbf{m}\right)p\left(\mathbf{m}\right)}{\int_{\mathfrak{M}} p\left(\mathbf{S}_{u-r}|\mathbf{m}\right)p\left(\mathbf{m}\right)\ \mathrm{d}\mathbf{m}} \quad (2.6)$$

The integral in the denominator is defined over the parameter space $\mathfrak{M}$. The quantity in the denominator is a proportionality constant such that the posterior is integrated to one.

The estimation of posterior moments, posterior quantiles, and marginals, requires that the integral of equation 2.6 is computed. Bayesian inference relies on the ability to compute probabilities and other quantities which summarizes the statistics of interest associated with the posterior distribution. If $p\left(\mathbf{S}_{u-r}|\mathbf{m}\right)p\left(\mathbf{m}\right)$ cannot be integrated analytically some form of numerical integration is required.

Monte Carlo integration using Markov chains (MCMC methods) has been excessively employed to integrate over the posterior distribution of the model parameters given the observations (Gilks *et al.*, 1996; Robert & Casella, 2004). Monte Carlo methods draw samples from the target distribution, through which the posterior statistics are approximated. The Markov chain converges to the target density as the number of samples grows. Mainly, the

samples are drawn by running a Markov chain constructed by Metropolis Hastings (MH) criteria. The simple MCMC-MH algorithm is illustrated by considering the pseudo-code listed in A.

2.4.3 The AND and OR Probability Operators

The fundamentals of the Bayesian regression was outlined in the preceding section. The method will be applied to the two datasets, separately, to infer the parameters of the empirical exponential relationship of equation 2.1. The next step will be to constitute a framework to joint the information retrieved from each dataset into a single probability density. Before launching into the concept of the joint states of information from the multiple Bayesian calibrations, we introduce the two basic operators in the probability space as presented by Tarantola (Tarantola, 1987).

Structure of all the probability distributions space is constructed on two basic operations AND and OR, symbolically denoted by $\wedge$ and $\vee$, respectively. For any subset $\mathcal{A}$, and for any two probability distributions P_1 and P_2 these operators are defined to satisfy the set of axioms below:

$$\begin{aligned} (P_1 \vee P_2)(\mathcal{A}) \neq 0 &\Rightarrow P_1(\mathcal{A}) \neq 0 \text{ or } P_2(\mathcal{A}) \neq 0 \\ (P_1 \wedge P_2)(\mathcal{A}) \neq 0 &\Rightarrow P_1(\mathcal{A}) \neq 0 \text{ and } P_2(\mathcal{A}) \neq 0 \end{aligned} \tag{2.7}$$

$P_1 \wedge P_2$ and $P_1 \vee P_2$ are called 'conjunction' and 'disjunction' of the two probabilities, respectively. The first axiom states that for the disjunction to be different from zero, either P_1 OR P_2 (or both) needs to be different from zero. The second axiom indicates that the conjunction of the two probabilities is zero if the probability of the either of the events (or both) is zero.

The generalized definitions of the two axioms above for the corresponding probability density functions $p_1, p_2, \ldots, p_N$ are:

$$(p_1 \vee p_2 \vee \ldots \vee p_N)(\mathbf{x}) = \frac{1}{N}(p_1(\mathbf{x}) + p_2(\mathbf{x}) + \ldots + p_N(\mathbf{x})) \tag{2.8a}$$

$$\frac{(p_1 \wedge p_2 \wedge \ldots \wedge p_N)(\mathbf{x})}{\zeta(\mathbf{x})} = \frac{1}{k}\frac{p_1(\mathbf{x})}{\zeta(\mathbf{x})}\frac{p_2(\mathbf{x})}{\zeta(\mathbf{x})}\cdots\frac{p_N(\mathbf{x})}{\zeta(\mathbf{x})} \tag{2.8b}$$

where k is a normalization constant. Also a neutral element Z exists for the AND operator which is interpreted as a probability distribution that carries no information. $\zeta(\mathbf{x})$ in equation 2.8 is the probability density function representing Z, where:

$$P \wedge Z = P \tag{2.9}$$

These concepts constitute what is called the inference space. To illustrate these axioms, figures 2.5a and 2.5b show two probability densities with differing measure of dispersion and opposite signs. These two input densities are combined via the two introduced probability operators. Figures 2.5c and 2.5d present the corresponding probability maps of the conjunction and disjunction states of information created using equation 2.8. The conjunction of information conveys the same notion as the Bayesian updating with a notable reduction of uncertainty, whereas the disjunction captures the original features of the sources or probabilities, which provides a sense for carrying information content where dependency is required like in the case of using previous knowledge generated from one site investigation to another.

We emphasize that the AND operator, as pointed out above, resembles the Bayesian theorem. This could be understood by comparing equations 2.8b and 2.6, where the prior beliefs regarding a process of interests (the prior density-p_1) is updated as the new data (the likelihood-p_2) is introduced into the statistical inference. The updated density (the posterior density) is the conjunction of the two input densities ($p_1 \wedge p_2$).

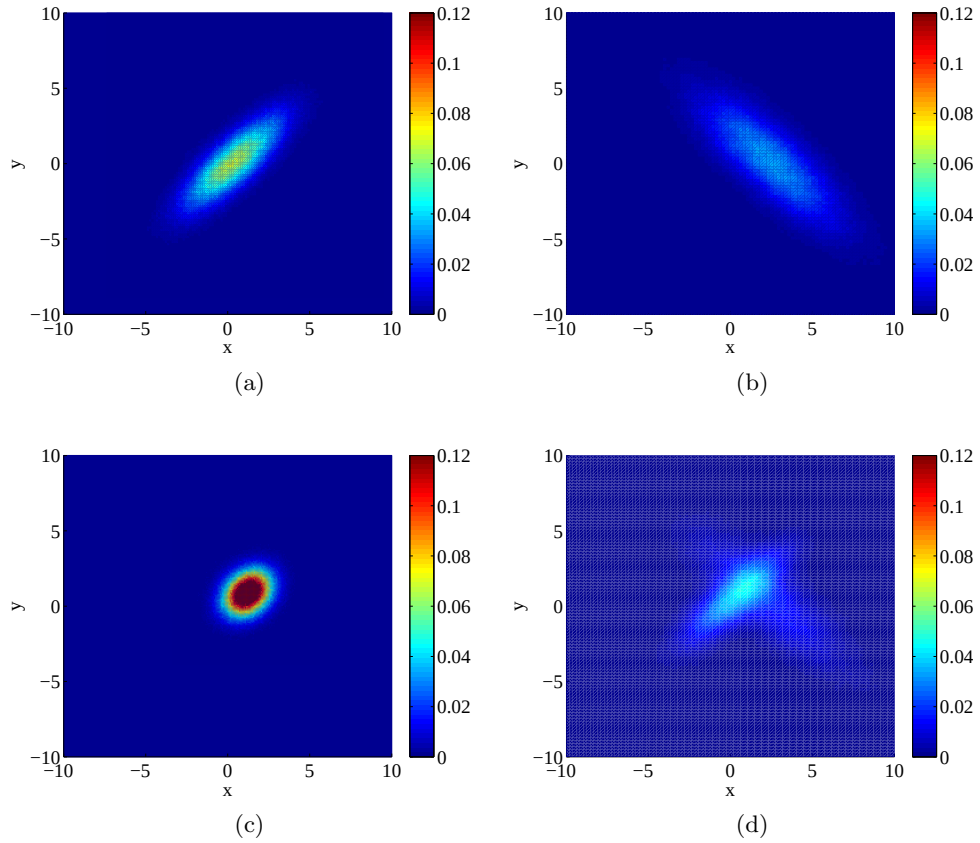

Figure 2.5: Representation of the frequency response of the 'Conjunction' and 'Disjunction' of two synthetic probability functions (a) and (b). Results of (c) conjunction and (d) disjunction operations over these two probability densities.

2.5 Case Study

The probabilistic calibration described in the preceding sections will be introduced to the global and the local datasets for the calibration of an empirical model (shown in equation 2.1) between S_{u-r} and I_L.

We execute the primary analyses in four different categories, composed of the cross-combination of the two data sets and the two regression models (homoscedastic–heteroscedastic). In each case the posterior is constructed using equation 2.6 where the elements of the posterior are provided by equations 2.4 and 2.5. A Markov chain Monte Carlo method is used to approximate the posterior joint distribution of the model unknowns. The MCMC does not require the constant of proportionality in equation 2.6 to be known. Therefore, the posterior kernel is constructed up to the proportionality by simply multiplying the prior and the likelihood $p\left(\mathbf{m}|\mathbf{S}_{u-r}\right) \propto p\left(\mathbf{S}_{u-r}|\mathbf{m}\right) p\left(\mathbf{m}\right)$.

The posterior integration is carried out numerically using a Markov chain Monte Carlo scheme, so called parallel tempering MCMC (Geyer & Thompson, 1995; Earl & Deem, 2005; Radford, 1996). Parallel tempering is a MCMC algorithm with improved dynamic behavior, to expedite posterior chain mixing and convergence. A regular Metropolis-Hastings MCMC may run into trouble fully sampling the posterior parameter space if the target density is multimodal with widely separated peaks. The situation may even be exacerbated if some of the modes are significantly narrower than the others. In such cases, the Markov chain is highly likely to either be trapped in the sharper local minima or not be broad enough to explore the whole allowed parameter range and detect the unknowns modes of the target. This problem is similar to the one arises in finding a global minimum in nonlinear optimization problems. The interested reader is referred to Appendix B for a more detailed discussion on the sampling methodology.

The solution of the numerical integration of the posterior was obtained after 2×10^6 parallel tempering MCMC simulations where convergence was guaranteed. The initial 2×10^5 samples are discarded as burn-in iterations, only after which the MCMC algorithm is judged to sample from the posterior density. To obtain similar results (e.g., for the

case of figure 2.8) using regular Metropolis-Hastings MCMC (Appendix A) nearly 50×10^6 samples had to be collected from the multi modal posterior for the MCMC chain to reach convergence. The resulting parameter space is illustrated in figures 2.6 to 2.14 for both the local and global data sets. These figures show the capability of the probabilistic approach to retrieve a full probability description of the model parameters. From this figure it can be observed the presence of a significant amount of variability on the local data set compared with the global data. Bellow, each case will be discussed separately.

2.5.1 Homoscedastic Variance Model

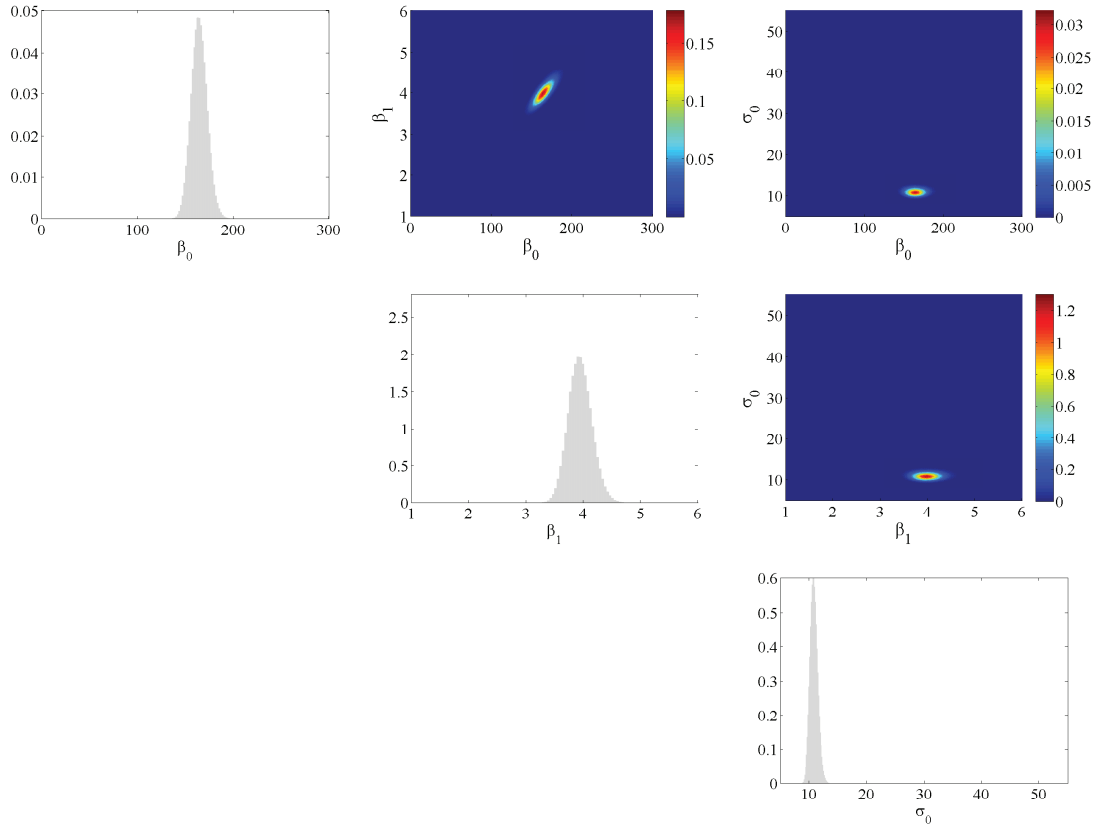

Figure 2.6: Posterior probability projections of the regression parameters, Homoscedastic model, Global data set

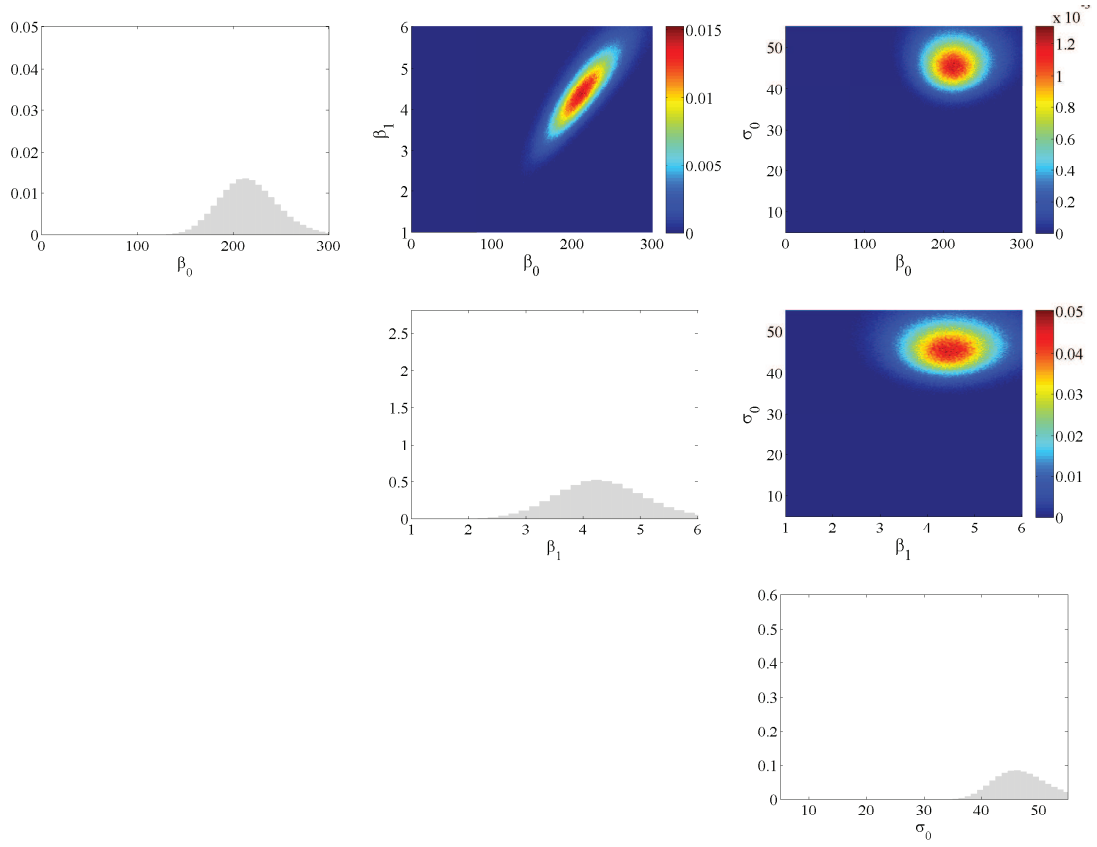

Figure 2.7: Posterior probability projections of the regression parameters, Homoscedastic model, Local data set

The parameters of the empirical $S_{u-r} - I_L$ relationship is determined from the global and the local data sets separately, considering the first variance scenario. Figures 2.6 and 2.7 present the parametrization result containing the regression coefficients (β_0, β_1) and the variance parameter σ_0^2 and their associated uncertainties. A major advantage of the probabilistic model calibration is that it makes it feasible to retrieve the correlation structure defining the degree of association between the regression parameters. This cannot be achieved by typical deterministic calibrations. The histograms along the diagonal in these figures illustrate the posterior marginal distribution of the model parameters and the hyper-parameter. The off-diagonal joint probability maps are cross-plots for all combinations of the regression parameters two at a time. The marginal posterior histograms

(diagonal plots) are scaled to compare the level of uncertainty conveyed by each data set. A significantly higher variability is observed around the mean parameter estimates for the local data set. The joint posterior densities depicted in figures 2.6 and 2.7 also indicate that the regression parameters β_0 and β_1 are linearly correlated. The regression parameters dose not show any correlation with the hyper-parameter σ_0 in both cases.

Although the homogenous variance assumption does not appear to be realistic according to figure 2.3, still examining this scenario is instructive since the assumption is the basis for all the deterministic parameter estimations.

2.5.2 Heteroscedastic Variance Model

Next, we consider the case where the variance heterogeneity is expressed with an exponential fit as a function of the covariate I_L (equation 2.3). Inversion parameters in this case are the regression parameters (β_0, β_1), scale parameter σ_0, and the structural variance parameter η. Figures 2.8 and 2.9 illustrate information about the parameter uncertainty, as well as parameter correlation structure for the global and the local data sets, respectively. The information in these figures are extracted from 2×10^6 random realizations drawn from the posterior density. Calibration of the global data results in a bimodal posterior for all the model parameters (figure 2.8). This effect can be attributed to the two separate data clusters observed in the data (figure 2.2a), crudely detected as data points with $I_L > 0.6$ and $I_L < 0.6$, respectively. Inclusion of the additional variance parameter η provides an extra flexibility to the model that the weaker mode can be evolved. This secondary peak proves to better describe the data cluster corresponding to the higher values of I_L and lower S_{u-r}. The main peak is close to the one obtained in the homoscedastic model calibration.

These results shows how a set of plausible solutions (as suggested by the additional mode appeared in marginal posterior densities of β_0 and β_1; see the diagonal plots of figure 2.8) is possibly ignored by using a customary yet inappropriate homoscedastic variance model, which is the case in a deterministic scheme such as nonlinear least squares.

$\beta_0 - \sigma_0$, $\beta_1 - \sigma_0$, $\beta_0 - \eta$, $\beta_1 - \eta$ cross plots in figure 2.8 display strong correlation between the regression parameters and the hyper parameters σ_0 and η.

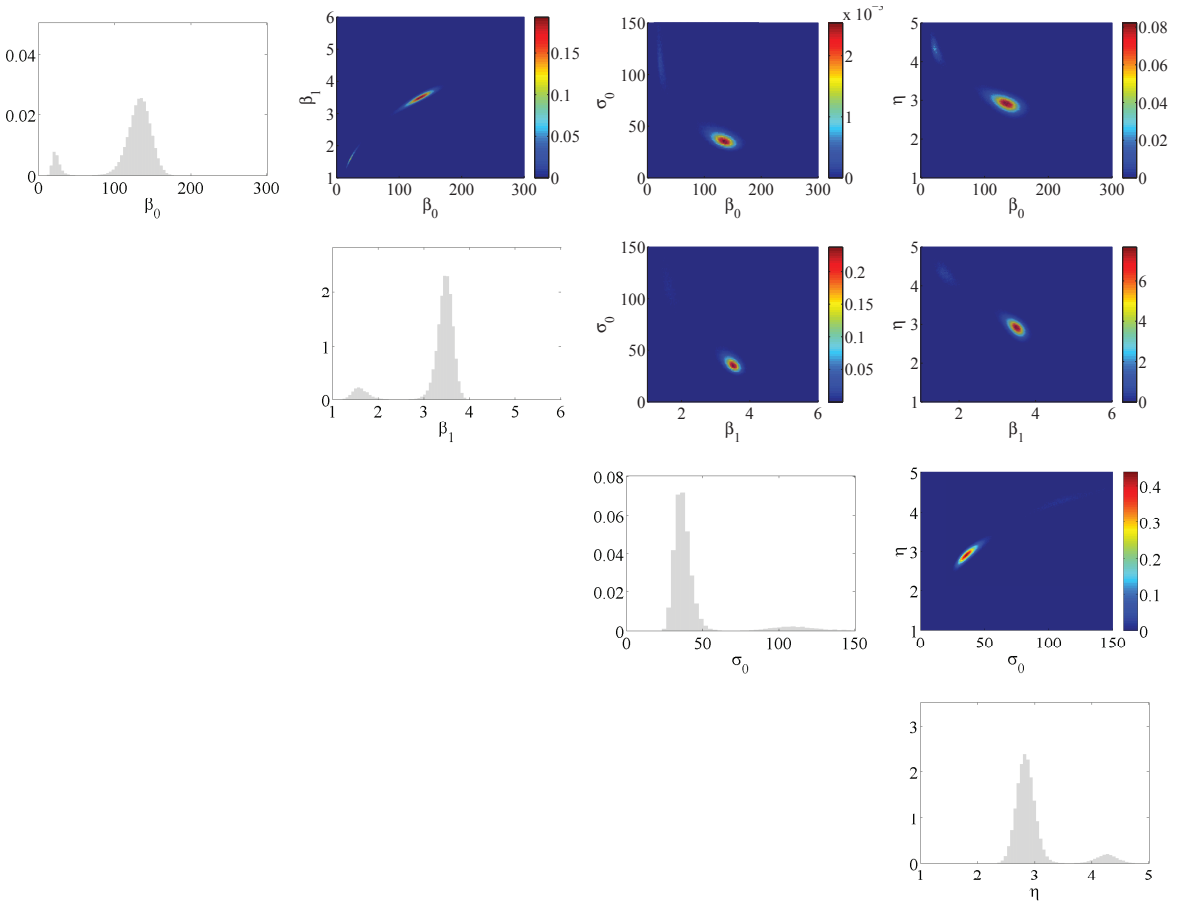

Figure 2.8: Posterior probability projections of the regression parameters, Heteroscedastic model, Global data set

2.5.3 Integrating the Information Content of the Two Model Calibrations

Having two sets of data, each showing a different $S_{u-r} - I_L$ behaviour, we are aiming at constructing a unified regression model reflecting the characteristics of both contributing data sets. The most natural way of joining the information content of the global and the local data sets is to merge them prior to any regression is conducted. This way the Bayesian regression could be performed on the combined global-local data.

Alternatively, one may consider running the Bayesian regression for one data set (say the global) first by assigning a non-informative type of prior (equation 2.4) to the model

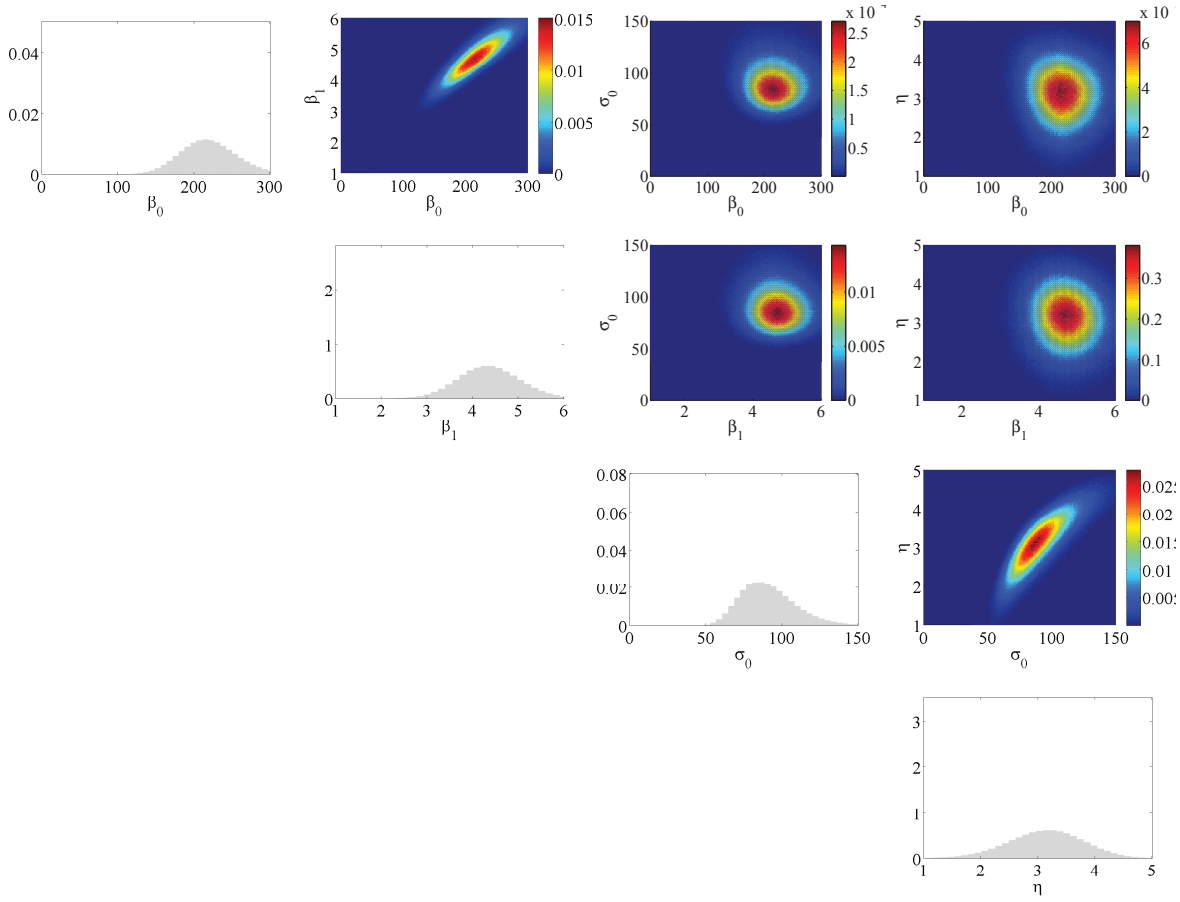

Figure 2.9: Posterior probability projections of the regression parameters, Heteroscedastic model, Local data set

parameters. The posterior density obtained from the first stage will serve as the prior to the next stage, where the local data set is introduced to the analysis (forming the likelihood function). The procedure is called the Bayesian updating.

The key interest of this paper is to merge the two states of information extracted from the global and the local data sets to reconstruct a more conclusive model space, particularly capable of accounting for the site dependency effect. The discussion of this very same problem, treated by traditional statistical methods and the Bayesian paradigm, can be found in Yang *et al.* (Yang *et al.*, 2010). Herein, the merged parametric space is reproduced using the probabilistic operators introduced in equation 2.8.

As previously noted in section 2.4.3, uniting states of knowledge derived from the two data sets using the AND operator is the same practice as using the posterior from the first experiment (i.e., global data) as the prior, and updating the model information in light of the second experiment (which forms the likelihood function). This practice, in turn, is identical to the second alternative listed above: treating both data sets as a big set of data which is used to construct the likelihood. This equivalency, however, holds only if the two data sets are independent, meaning that observing one data set dose not affect the likelihood of observing the other. The global and the local data sets are independent according to this definition. A simple proof is provided in Appendix C.

Figures 2.11 to 2.14 depict the resulting parametric "joint" model space constructed from 2×10^6 randomly derived samples from the target distribution. The target density is constructed using equations 2.8 with p_1 and p_2 referring to the posterior densities obtained from the global and local data sets, respectively.

Under the homoscedasticity assumption, results from the use of the AND operator is presented in figure 2.11. Comparing joint posterior densities in figures 2.6 and 2.11 (e.g., $\beta_0 - \beta_1$), reveals an increased parameter variability as a result of applying the AND operator. This findings is in contradiction with the philosophy of Bayesian paradigm; reducing the uncertainty as a result of updating process (equivalently, reducing the model uncertainty as the sample size grows).

Reduction of model parameter variability as a result of sample size increase, is an intuitive concept. However, the proof can be found in general Bayesian statistics text books (see for example Gelman *et al.* (2003)). The necessary condition for this rule to maintain, however, is that the observations (in both data sets) must be independent outcomes sampled from a common distribution. In a more precise statistical language, the data points must be iid (identically independently distributed). We hypothesize that the contradictory observation of figure 2.11 is due to the fact that the global and the local data belong to different populations. This hypothesis is examined in the proceeding section.

2.5.3.1 The Two Dimensional Kolmogorov-Smirnov Test for Two Independent Samples

The question is whether the global and the local data sets belong to the same population (drawn from same distribution function)? In proper statistical words, is it possible to a certain level of significance disprove the null hypothesis that the two independent data sets represent the same population?

The classical Kolmogorov-Smirnov (K-S) test is an efficient non-parametric statistic for comparing two independent samples base on deviations in cumulative density functions (cdf). The test involves in the comparison of the largest absolute difference between the two cumulative distribution functions as a measure of disagreement between two independent samples. The test protocol is designed such that in case of significant difference at any point along the two cdfs, it can be deduced that there is a high likelihood that the samples are derived from different populations (Sheskin, 2004).

K-S test is highly efficient as it is sensitive to any kind of distributional differences (i.e., differences with respect to central tendency, dispersion, and skewness). Moreover, K-S belongs to a class of tests namely distribution free, in which the expected distribution of the test statistic is not necessarily assumed to belong to a particular distribution (Peacock, 1983).

Within the frame work of the statistical hypothesis testing (Montgomery & Runger, 2010), the definition of the null and the alternative hypothesis are as follows:

$$\begin{cases} H_0 & : F_G(I_L, S_{r-u}) = F_G(I_L, S_{r-u}) \ \ \forall I_L, S_{r-u} \\ H_1 & : F_G(I_L, S_{r-u}) \neq F_G(I_L, S_{r-u}) \ \ \forall I_L, S_{r-u} \end{cases}$$

H_0, and H_1 are the null and the alternative hypothesis, and $F_G(I_L, S_{r-u})$ and $F_L(I_L, S_{r-u})$ represent the population distributions from which the global and the local data sets are derived, respectively. The null hypothesis states that the distribution of data in the population that the global data set is derived from is consistent with the distribution of data in the population that the local data set is sampled from. H_0 and H_1 are complementary

hypotheses.

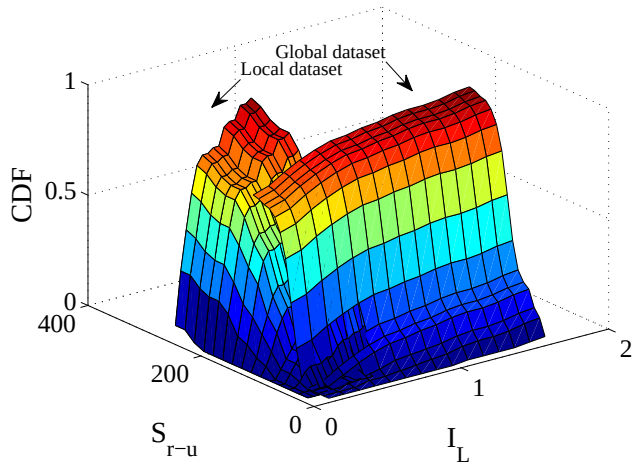

Figure 2.10: Cumulative probability density functions (cdf) for the global and the local datasets. The Kolmogorov-Smirnov statistical test proves provided that the two data sets belong to the same population, the probability of observing two samples with the illustrated level of cdf misfit is 1.79×10^{-20}. Therefore, the null hypothesis is rejected.

Provided that the null hypothesis is true (data sets are drawn from the same distribution), the p-value is the probability of obtaining a random sample from the population that at no point the greatest vertical distance between the cdf for the global data set and the cdf for the local data set is larger than what would be expected by chance.

The integral probability distribution of the K-S test statistics (D), independent of the sample size, asymptotically (as the sample size tends to infinity) forms the following infinite power series (Feldman & Valdez-Flores, 2010):

$$Q_{K-S}(d) = P(D > d) = 2\sum_{j=1}^{\infty} (-1)^{j-1} \exp\left(-2j^2 d^2\right) \tag{2.10}$$

This function is a monotonic function with the limiting values $Q_{K-S}(0) = 1$ and $Q_{K-S}(\infty) = 0$. The significance level of the observed value of d (the largest absolute difference between

the global and the local cdfs), as a falsification of the null hypothesis, is given approximately by

$$P\left(D > d\right) = Q_{K-S}\left(\left[\sqrt{N_e} + 0.12 + \frac{0.11}{\sqrt{N_e}}\right]d\right) \tag{2.11}$$

in which $N_e = \frac{n_G n_L}{n_G + n_L}$ is the effective sample size, and N_G and N_L are the size of the global and the local data sets, respectively. The above approximation for the significance level $P\left(D > d\right)$ becomes accurate as $N_e \to \infty$, however the approximation is reasonably fair for $N_e \geq 4$.

The P-value from equation 2.11 is found to be 1.79×10^{-20}, which indicates that in case the two data sets belong to the same population, the probability of observing the two samples with the current level of misfit (see figure 2.10) is 1.79×10^{-20}. Therefore, the two observed cumulative probability distributions (figure 2.10) is an extremely rare event if the null hypothesis $F_G(I_L, S_{r-u}) = F_G(I_L, S_{r-u})$ is actually true. The null hypothesis is rejected with any significance level greater than 1.79×10^{-20}.

Continuing with the application of the conjunction operator, figure 2.12 shows the merged posterior plots for the case of heteroscedastic variance. Only the mode which is in common between the two input densities (figures 2.8 and 2.9) is reflected in the conjunction plot, which results in the reduced variability of the posterior parameter estimates.

Similar plots for the disjunction of input probabilities are introduced in figures 2.13 and 2.14. These figures show that the OR operator is able to incorporate all the information from the two sets of data to construct all the possible combination of model parameters, accounting for their corresponding uncertainty. This capability is accommodated by a considerable increase of uncertainty which is clearly observable from the diagonal histograms in the both figures. This gives a notion of 'sharing' at a cost of redistributing the uncertainty.

The first and second order summary statistics of the posterior parameter densities are provided in tables 2.1 and 2.2, respectively. For the case of the global data-heteroscedastic model the statistics are provided for each posterior mode separately. The hats denote

posterior estimate (expected value) of the parameters.

Once the probability maps are generated for each case, likely realizations of the empirical model can be obtained by randomly sampling different parameters combinations following the probability distributions obtained in figures 2.6-2.9 and 2.11-2.14 . These model responses are utilized to generate the posterior predictive estimates such as the posterior mean estimate, the corresponding confidence levels (figures 2.15, 2.16, 2.17a and 2.17c), and the variability of the posterior predictions (figures 2.17b and 2.17d). To generate these plots 5×10^3 random realizations of the regression parameters are fed into the regression model 2.2.

Figures 2.15 and 2.16 display posterior mean model $\hat{\mu}\left(I_L; \boldsymbol{\beta}\right)$ (black solid curves), together with 95% credible intervals for the posterior predictions (shaded area), under the homoscedasticity and the heteroscedasticity assumptions, respectively. The increased variability around the mean posterior model in figure 2.15c is in agreement with with the similar observation of figure 2.11, and attributed to the fact that the two datasets are not identically distributed as discussed in section 2.5.3.1. The increased variability of the model prediction as a result of the OR operator is clearly observed in the both figures 2.15d and 2.16d.

The observations of figures 2.15 and 2.16 are summarized in figure 2.17. Figure 2.17 presents a comparative analysis between the mean posterior prediction of the regression model (figures 2.17a and 2.17c) and the measure of uncertainty around the posterior mean estimate (figures 2.17b and 2.17d) for the 'conjunction' and the 'disjunction' operations (the two source models from the global and the local data sets are also included as a reference).

By studying the homoscedastic condition (figures 2.17a and 2.17b), it is observed that, the posterior mean prediction in this case perfectly matches the nonlinear least-square (NLLS) fit for the both data sets (the mean curve completely overlaps the NLLS fit for the global data), as both the NLLS and the presented homoscedastic Bayesian regression are based on the same assumptions. The trend mean from the conjunction and disjunction

falls between the mean global and the mean local model (conjunction mean leans closer to the mean of the local model). Comparison of the variability of the model performances as presented in figure 2.17b confirms that the maximum uncertainty corresponds to the disjunction model (small I_L). The conjunction uncertainty is higher than the both global and the local models for the homoscedastic condition.

The heteroscedastic calibration (figures 2.17c and 2.17d) is of major interest in this study as it describes the behaviour of the data more realistically. In this case the global trend mean considerably differs from the NLLS fit. This finding is rational considering that the posterior densities of β_0 and β_1 are bi-modal. The added flexibility provided by the homoscedasticity assumption does not noticeably affect the local model in terms of the posterior predictions (local mean model and the NLLS fit matches). Again, trends of both the conjunction and the disjunction models fall between those of the two participating data sets, indicating a rational behavior on the translation of the knowledge from the global and the local data sets into a unified predictive model. However, the considerably lower prediction uncertainty of the conjunction model compared to the disjunction model suggests that the AND operator (equivalently the Bayesian updating) is the most proper way to 'update' the sate of knowledge from one site characterization to another.

Table 2.1: First order statistics: Expected values of the regression parameters and the hyper-parameters

		Global	Local	Conjunction
Homoscedastic	$\hat{\beta_0}$	164.499	216.018	199.791
	$\hat{\beta_1}$	3.942	4.320	4.219
	$\hat{\sigma_0}$	10.834	47.086	25.887
Heteroscedastic	$\hat{\beta_0}$	(23.328, 131.970)	219.930	164.803
	$\hat{\beta_1}$	(1.604, 3.463)	4.369	3.668
	$\hat{\sigma_0}$	(113.592, 37.010)	91.548	68.513
	$\hat{\eta}$	(4.261, 2.839)	3.135	3.288

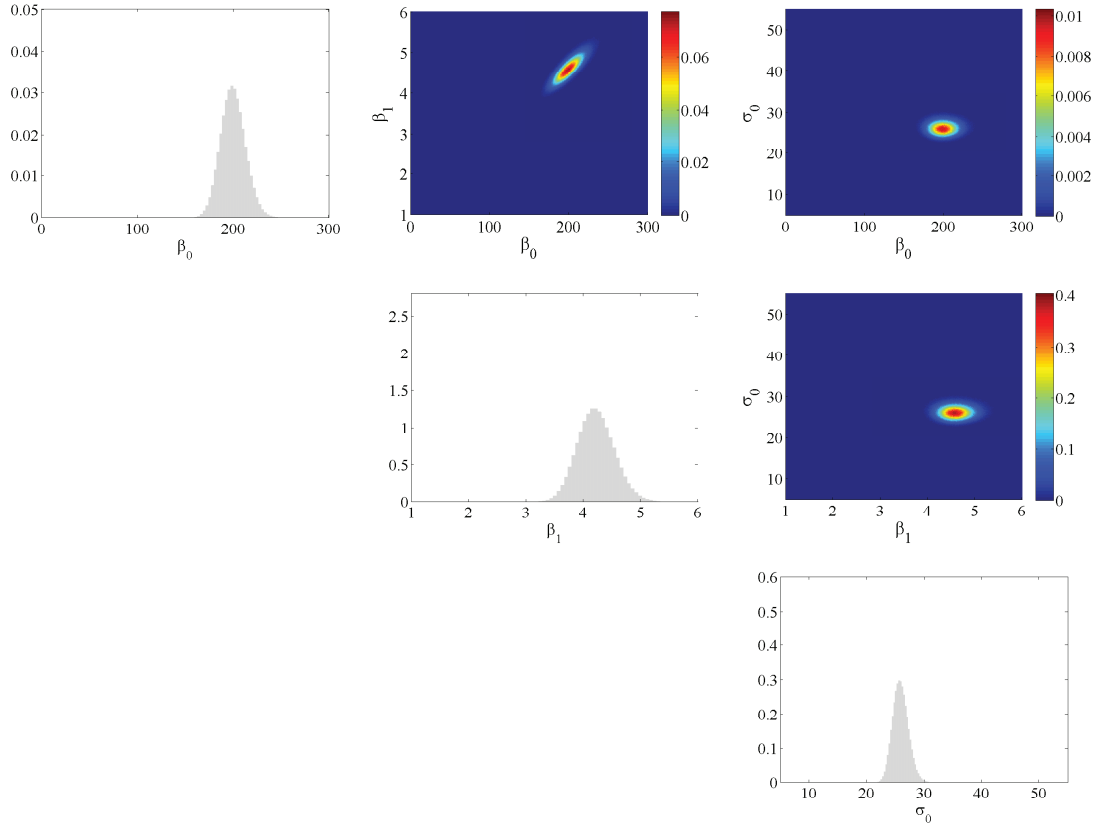

Figure 2.11: Posterior probability projections of the regression parameters, Homoscedastic model, AND operator

Table 2.2: Second order statistics: Covariance matrix of the regression parameters and hyper-parameters

		Global	Local	Conjunction
Homoscedastic	$\mathrm{COV}(\beta_0, \beta_1)$	$\begin{bmatrix} 69.310 & 1.383 \\ 1.388 & 0.0412 \end{bmatrix}$	$\begin{bmatrix} 935.234 & 20.700 \\ 20.700 & 0.634 \end{bmatrix}$	$\begin{bmatrix} 162.592 & 3.395 \\ 3.395 & 0.102 \end{bmatrix}$
	$\mathrm{Var}(\sigma_0)$	0.438	24.183	1.811
Heteroscedastic	$\mathrm{COV}(\beta_0, \beta_1)$	$\begin{bmatrix} 26.548 & 0.863 \\ 0.863 & 0.029 \end{bmatrix}, \begin{bmatrix} 230.415 & 2.460 \\ 2.460 & 0.029 \end{bmatrix}$	$\begin{bmatrix} 1392.321 & 2.264 \\ 2.264 & 0.475 \end{bmatrix}$	$\begin{bmatrix} 200.315 & 1.779 \\ 1.779 & 0.021 \end{bmatrix}$
	$\mathrm{COV}(\sigma_0, \eta)$	$\begin{bmatrix} 241.757 & 2.367 \\ 2.367 & 0.029 \end{bmatrix}, \begin{bmatrix} 28.922 & 0.770 \\ 0.770 & 0.026 \end{bmatrix}$	$\begin{bmatrix} 350.509 & 10.357 \\ 10.357 & 0.438 \end{bmatrix}$	$\begin{bmatrix} 37.305 & 0.549 \\ 0.549 & 0.0137 \end{bmatrix}$

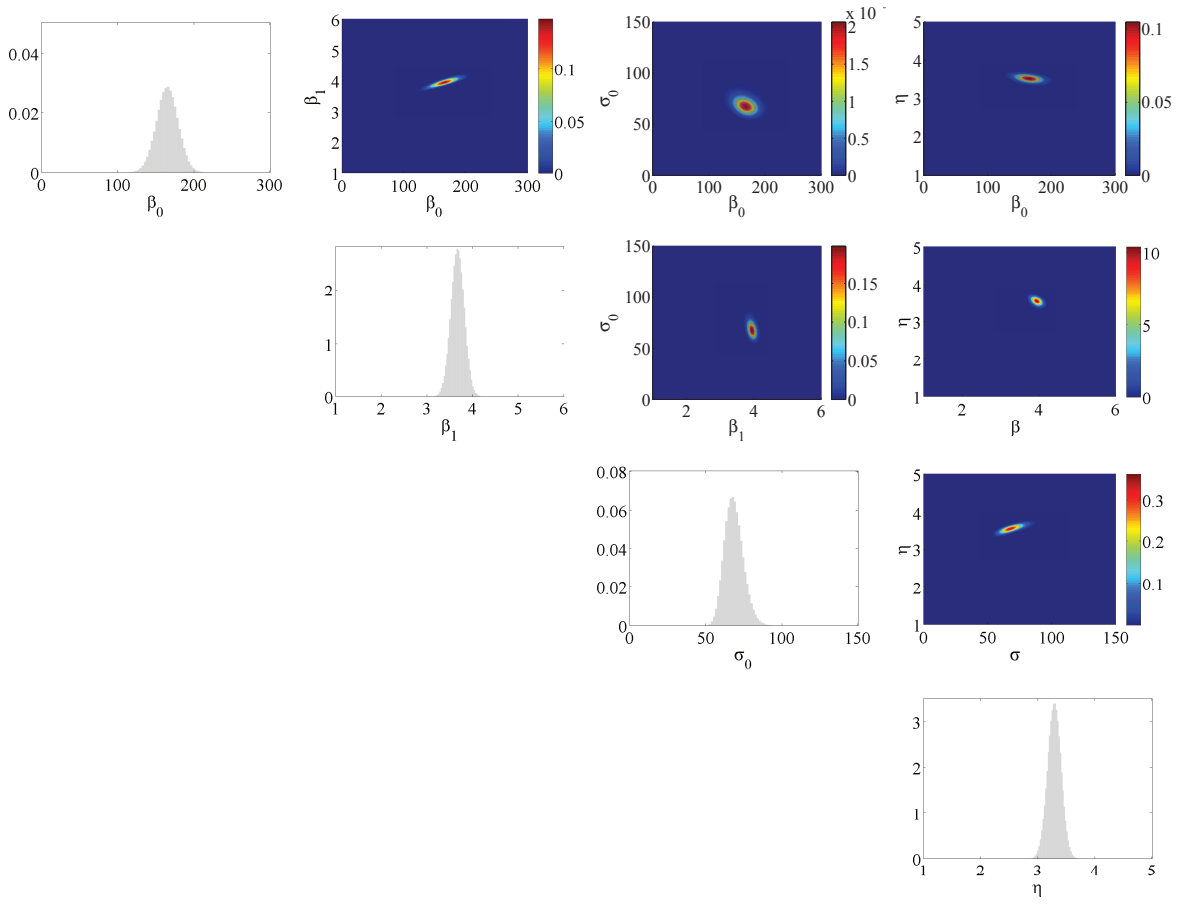

Figure 2.12: Posterior probability projections of the regression parameters, Heteroscedastic model, AND operator

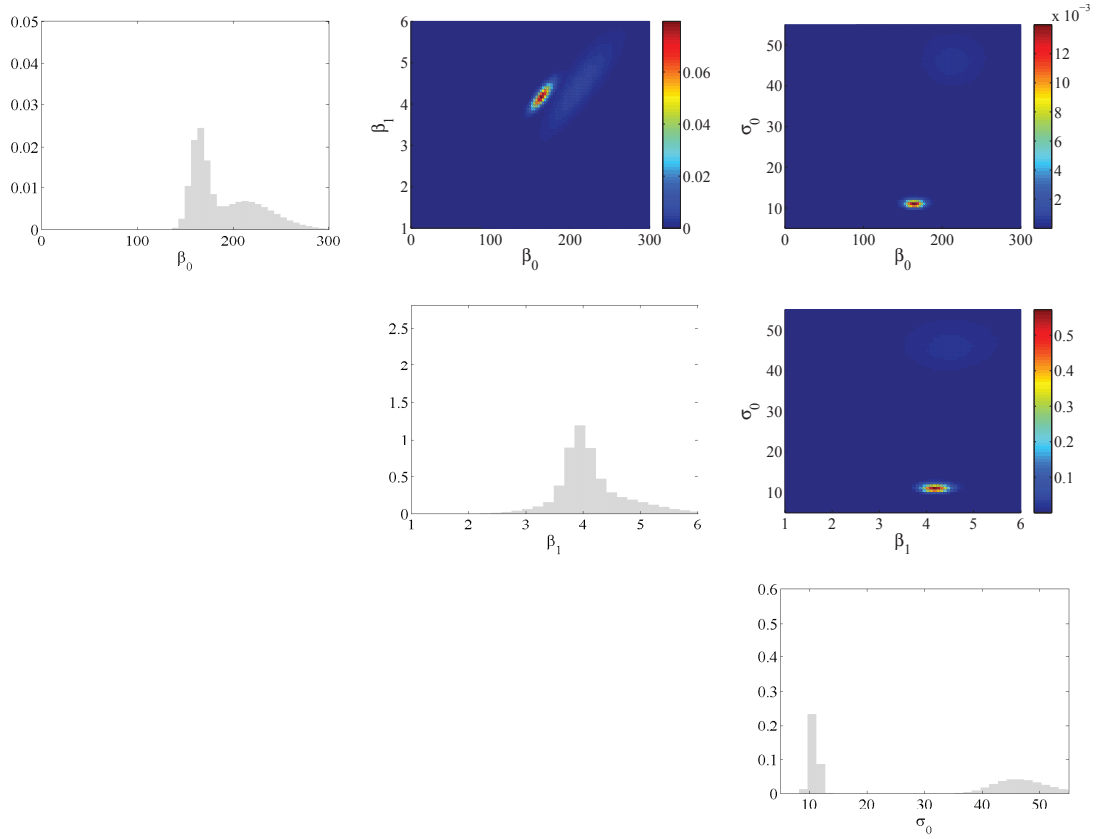

Figure 2.13: Posterior probability projections of the regression parameters, Homoscedastic model, OR operator

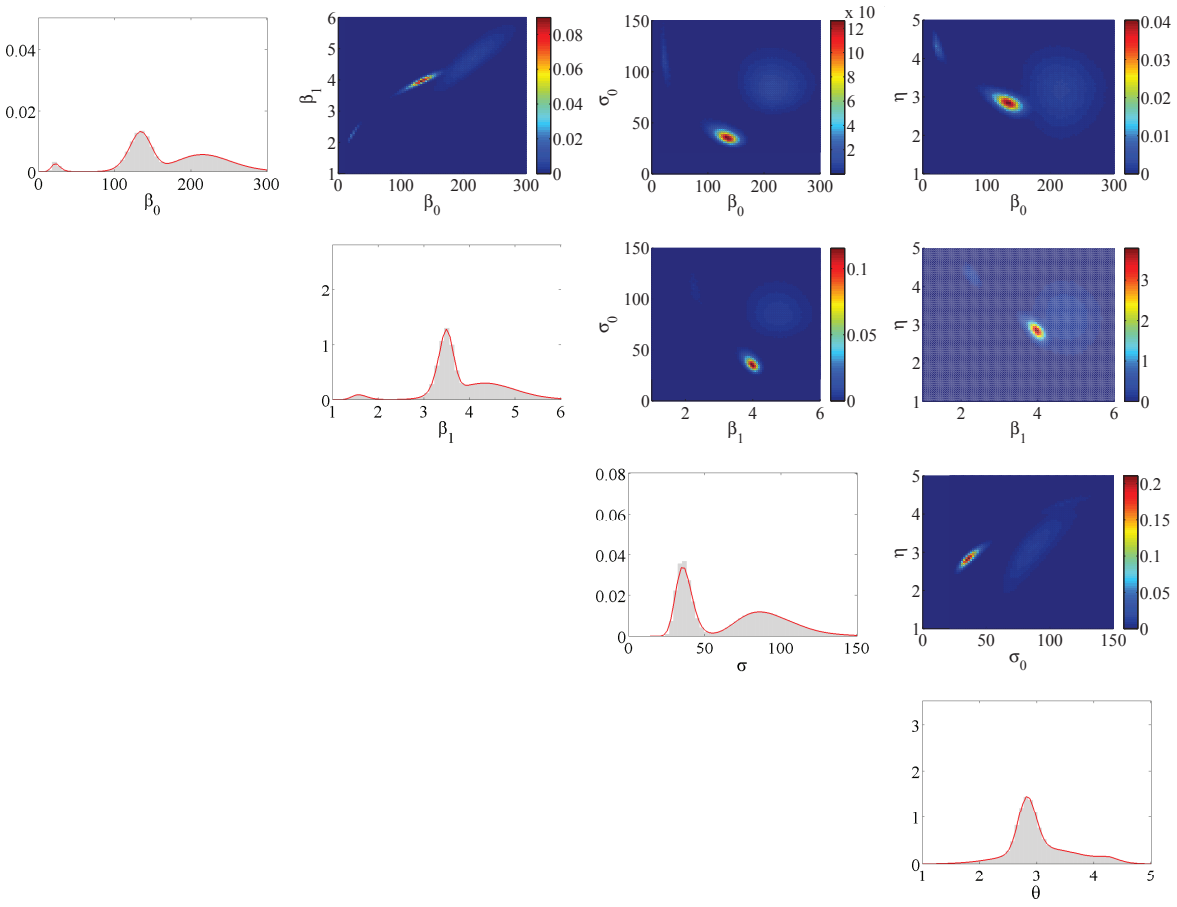

Figure 2.14: Posterior probability projections of the regression parameters, Heteroscedastic model, OR operator

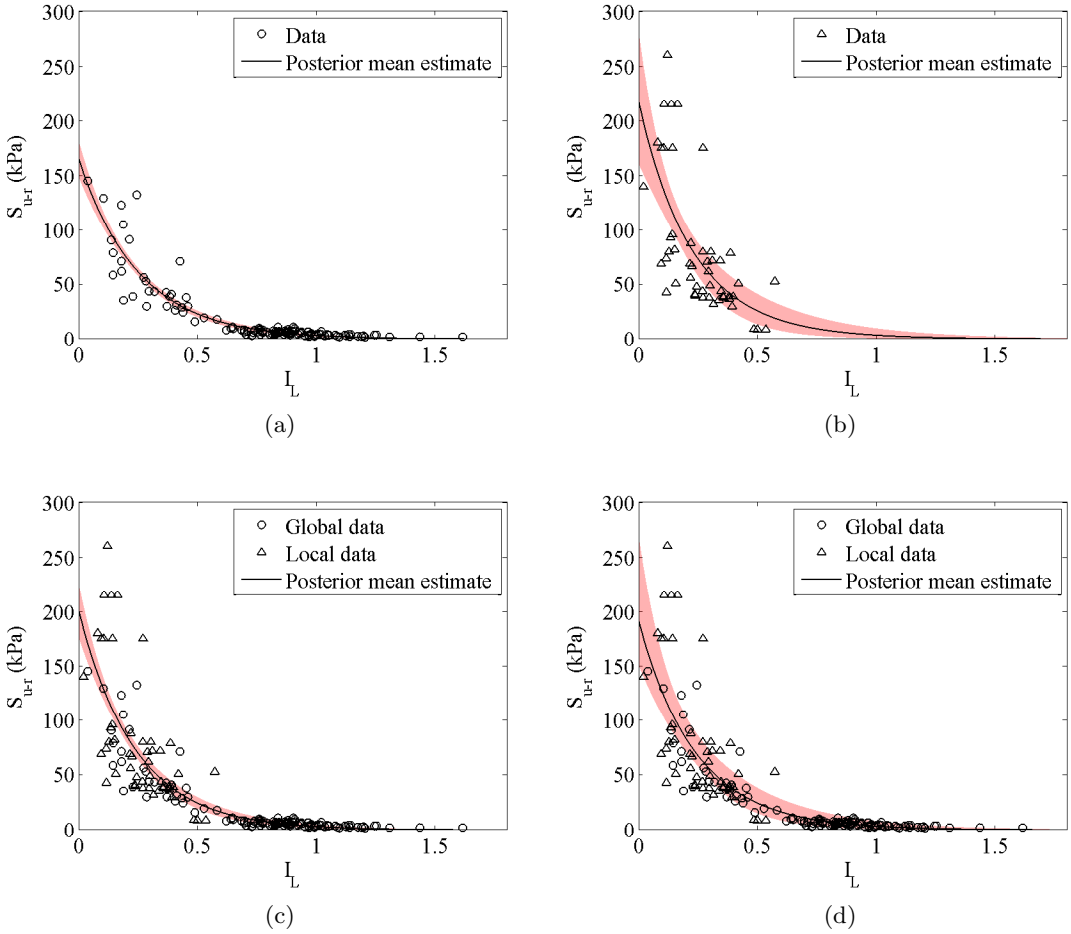

Figure 2.15: Posterior mean estimates of the S_{u-r} together with 95% credible intervals around the mean, homoscedastic variance model, (a) Global data set (b) Local data set (c) merged state of information from the use of AND operator (d) merged state of information from the use of OR operator

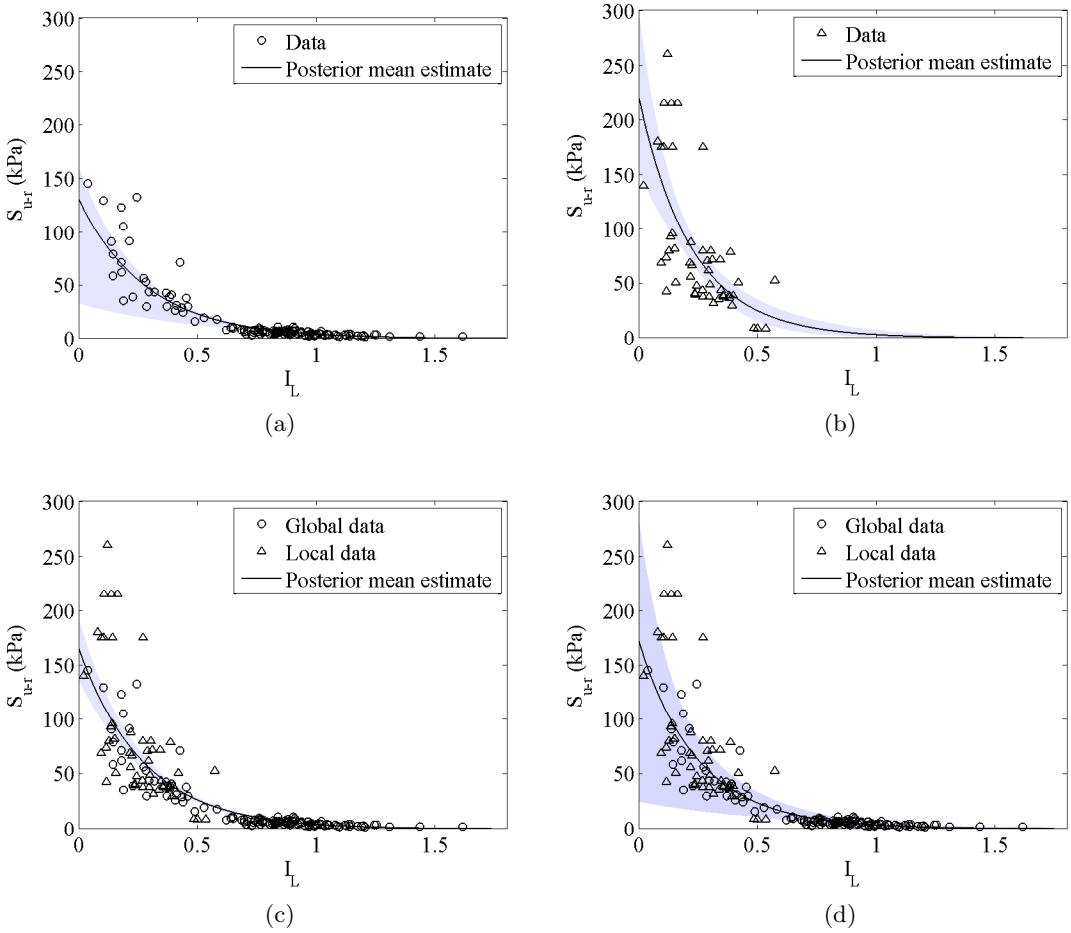

Figure 2.16: Posterior mean estimates of the S_{u-r} together with 95% credible intervals around the mean, heteroscedastic variance model, (a) Global data set (b) Local data set (c) merged state of information from the use of AND operator (d) merged state of information from the use of OR operator

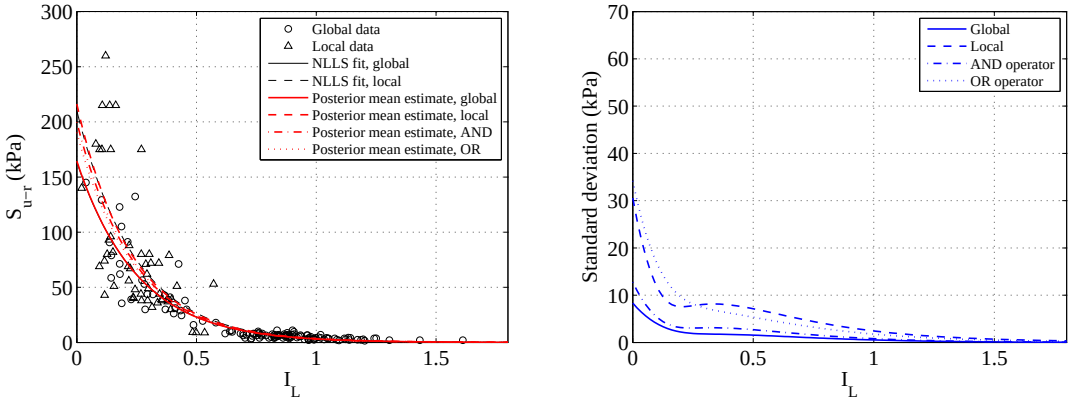

(a) Homoscedastic model

(b) Homoscedastic model

(c) Heteroscedastic model

(d) Heteroscedastic model

Figure 2.17: Posterior prediction statistics: (a),(c) Posterior mean estimates of S_{u-r} together with the optimal fits of the exponential model for the global data, local data, AND, and OR operators. (b),(d) Degree of variation around the posterior mean estimate.

2.6 Conclusion

An uncertainty based parametrization has been conducted to study the correlation between the remolded undrained shear strength and the liquidity index for a global and a local data set. Once the probability maps of the global and local independent calibrations were obtained using the Bayesian regression methodology, the conjunction (AND) and disjunction (OR) operator were introduced as a way to illustrate two different types of integrating information. Making use of conjunction operator results in the most certain model with the mean of the model response leaning towards the more certain data set given by the global response, whereas the disjunction model response showed a better agreement with the transferring of knowledge form the global to the local data set. The uncertainty assessment for both operators, show a consistent identification of the conjunction operator with the Bayesian approach, whereas the model uncertainty when using the disjunction operator indicates a higher variation on the model response, as a consequence of accepting the merging of two different sources of information.

3. VARYING DIMENSIONAL BAYESIAN ACOUSTIC WAVEFORM INVERSION FOR 1D SEMI-INFINITE HETEROGENEOUS MEDIA

3.1 Overview

This paper introduces a methodology to infer the spatial variation of the acoustic characteristics of a 1D vertical elastic heterogeneous earth model via a probabilistic calibration approach, given a prescribed sequence of loading and the corresponding time history response registered at the ground level. From a Bayesian point of view, the probabilistic calibration represents a solution to an inverse problem, formulated as a density function or posterior of a random field of model parameters, which by definition overcomes the inversion's inherent non-uniqueness difficulty. Once the probabilistic inversion is completed, statistical moments of the posterior summarize all the information about the spacial variation of the unknown material field. Here, the subsurface earth model is defined in the form of a partition model, where the number of layers, the location of the layers' interfaces, and their corresponding mechanical characteristics are presented as random variables. Partition model parameterization of an inverse medium problem is closely related to Bayesian model selection, where the likely dimensionality of the inverse problem (number of unknowns) is inferred conditioned on the experimental observations. A unique characteristic of the Bayesian probabilistic calibration, is that it inherently favors the selection of simple models, resulting in an optimal probabilistic solution to the inverse problem, as opposed to existing non-Bayesian methods which rely on adding subjective regularization terms to penalize the complexity of the inverted earth model. Therefore, the main challenge of the proposed approach is the sampling of the posterior, due to its varying-dimensional nature. To tackle this problem, the Reversible Jump Markov Chain Monte Carlo (RJMCMC) algorithm is used to sample the target posterior of varying dimension, dependent on the number of layers. The governing forward physics consist of a 1D transient scalar acoustic wave propagation, where in order to model the semi-infinite extent of the physical domain,

a perfectly matched layer (PML) is introduced at the truncation boundary to emulate the infiniteness of the earth structure. A synthetic case study is provided to indicate the applicability of the implemented technique. Key applications of the proposed approach include integrated studies for site characterization, since the recovery of geophysical mechanical parameters allows enhanced geomechanical characterization.

3.2 Introduction

A subsurface earth model is composed of complex geophysical formations, which embodies a wide range of physical and mechanical heterogeneities. The aim of probabilistic inverse modeling is to reconstruct the random field structure of these subsurface properties, while accounting for various sources of uncertainty stemming from measurement errors, aleatory formations, and limited theoretical understanding.

In practice, one of the main goals of geophysical investigations is to identify the main geomorphological features of an unknown medium, meaning the spatial location and concentration of geological features such as the transition between materials, discontinuities and material concentrations. This, in turn, implies the need to define a likely spatial distribution of the subsurface's stiffness/velocity properties. In the case of a vertical 1D profile, this requires the definition of the location of the sharp transitions between material properties (layer interfaces), and the characterization of the corresponding mechanical properties.

In a horizontally stratified earth model, prior to making an inference about the likely variation of the elastic parameters within the geological layers, an assumption must be made concerning the number of layers in a certain depth range of interest. This assumption defines the dimensionality (i.e., the number of unknowns) of the inverse problem. In reality, however, such information is rarely available for the dimension and definition of the parameter space to be fixed. Nevertheless, a subjective imposition of a certain model parametrization may strongly affect the validity of the inverted profile, as the inference might be founded on unrealistic assumptions about the "best approximation" to the truth.

To relax the hypothesis about the subsurface structure or spatial layering of the me-

dia's mechanical parameters, before the forward model is calibrated, it is proposed to define the number of layers, their locations, and their corresponding mechanical parameters as random variables. From a Bayesian perspective, this set up is closely associated with probabilistic model selection, where a collection of models with varying number of parameters are presented for inversion, and the task is to select the models that most likely describe the experimental observations.

To illustrate the applicability of the proposed probabilistic calibration method, a one dimensional horizontally stratified media is presented in terms of a Bayesian partition model (Denison *et al.*, 2002*b*). Partition models, also known as multiple change point problems, divides the parameter space into an unknown number of disjoint regions, where the distribution of the points in different regions is independent a-priori. Formulating the inverse medium problem in terms of a partition model may help reduce the dimensionality of the parameter space. Hence, regularizing the solution through specific prior distributions, which bears smoothness constraints (in a Bayesian inversion framework (Ulrych *et al.*, 2001; Dosso, 2002; Huang *et al.*, 2006)), or regularization terms (in deterministic optimization problems (Tikhonov, 1963; Na & Kallivokas, 2008; Epanomeritakis *et al.*, 2008)), is precluded.

A generalization of the simulation-based Markov Chain Monte Carlo methods, so called reversible jump (Green, 1995), is used to sample the posterior distribution of varying dimensionality. In this setting, the Markov chain is capable of undergoing dimension changes while moving among a number of candidate models. The key aspect of the reversible jump algorithm is the introduction of some auxiliary random variable to equalize the dimensionality of the parameter space across models. A series of one-to-one deterministic functions are defined to perform dimension matching such that the balance condition is satisfied. Balance condition is the necessary condition for a Markov chain to converge to the target density.

Since the introduction of Bayesian inference methods to the geophysical community, this has received a great deal of attention in a variety of applications (Duijndam, 1988*a*,*b*;

Gouveia & Scales, 1998; Ulrych *et al.*, 2001; Scales & Tenorio, 2001; Tarantola, 2005). However, a limited number of studies have addressed the subsurface parameter estimation as a model selection problem, many of which resort to approximate methods to fulfill the model determination (Dettmer *et al.*, 2009; Dosso & Dettmer, 2011). The varying dimensional formulation was first introduced to the geophysics literature by Malinverno (Malinverno, 2002) in a 1D-DC resistivity sounding inversion, and later implemented in a number of geophysical probing inverse problems such as (Sambridge *et al.*, 2006; Dettmer *et al.*, 2010; Agostinetti & Malinverno, 2010; Minsley, 2011).

The major impact of utilizing a probabilistic calibration via a Bayesian solution to solve inverse problems, is the systematic exploration of all combinations of the model parameters through a transparent definition of the impact of the participating uncertainty sources (Arson & Medina-Cetina, 2014). During such exhaustive parameter exploration, a probability metric is defined to assess the likelihood of selecting sets of parameters that serve to approximate the model predictions with the experimental observations (likelihood); but also a probability metric is defined to reflect the degree of knowledge on the model parameters (prior) before the model inversion. The combination of these two states of knowledge about the model of interest yields the following benefits: a transition from deterministic to probabilistic model parameters, assessment of the type and degree of correlation between the model parameters (e.g. linear or non-linear), measurement of the impact of the varying experimental observations (e.g. the effect of the number of observations on the prediction confidence levels), assessment of the model performance, and most importantly, that among a number of competing models to choose from, it is possible to select the best model which can describe the process that generated the observations. The latter is the key focus of the present study. The varying parameter dimensionality is formulated through a Bayesian inversion, to populate likely configurations of an heterogeneous elastic medium occupying a semi-infinite domain.

3.3 Forward Model

In this section we briefly introduce the forward model used in the model inversion. We are seeking to infer the elastic characteristics of a horizontally stratified semi-infinite soil model by leveraging the medium's response to interrogating waves. We also are interested in quantifying the inherent uncertainty of these estimates.

The forward physics describing the phenomenon can be described as a vertical propagation of compressional waves when the media is subjected to a uniform excitation $p(t)$ over the surface. This problem can be treated as a one dimensional problem along the depth direction. In a computational setting, a major issue associated with this geo-acoustic inverse problem is to model the semi-infinite physical domain. In order to arrive at a computationally finite region the medium must be truncated at some depth. If the truncated boundary is fixed or inadequately modeled, the propagating waves are (partially) reflected in the domain, and distort the inverted profile (Kang & Kallivokas, 2010a).

To address the issue, a Perfectly-Matched-Layer (PML) approach is adopted, and a PML buffer zone is introduced at the truncation interface (Kang & Kallivokas, 2010b). The PML enforces the rapid decay of the wave motion within the buffer zone, with ideally no reflection back into the domain. Figure 3.1 illustrates the schematic representation of the problem. We refer to the original work (Kang & Kallivokas, 2010b) for the extensive derivations of the model, however, for the sake of completeness we only include the governing wave equation: find $\nu(z,t)$ and $\sigma(z,t)$ such that

$$\begin{aligned}
\frac{\partial^2 \nu(z,t)}{\partial t^2} + c(z)\, g(z) \frac{\partial \nu(z,t)}{\partial t} - \frac{\partial \sigma(z,t)}{\partial z} &= 0, \quad \text{for } z \in (0, L_t),\ t \in (0, T], \\
\frac{\partial \sigma(z,t)}{\partial t} + c(z)\, g(z)\, \sigma(z,t) - c^2(z) \frac{\partial^2 \nu(z,t)}{\partial z \partial t} &= 0, \quad \text{for } z \in (0, L_t),\ t \in (0, T],
\end{aligned} \tag{3.1}$$

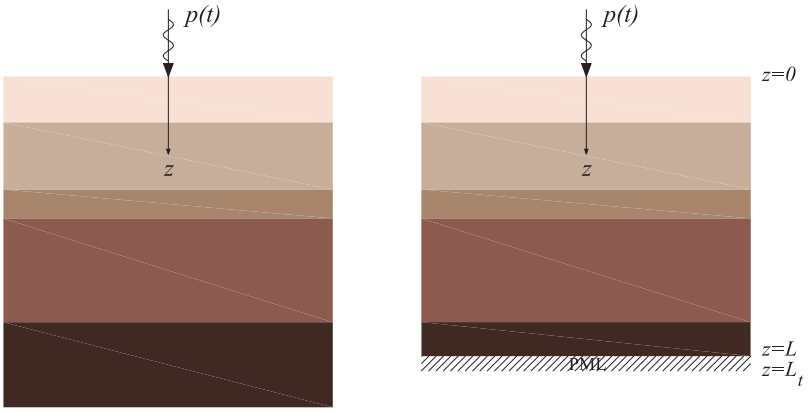

Figure 3.1: Schematic presentation of the 1D problem. (a) Original semi-infinite soil media (b) PML truncated domain

subject to

$$\begin{aligned} \nu\left(L_t, t\right) &= 0 \\ \sigma\left(0, t\right) &= p\left(t\right) \\ \nu\left(z, 0\right) &= 0 \\ \frac{\partial \nu}{\partial t}\left(z, 0\right) &= 0 \\ \sigma\left(z, 0\right) &= 0 \end{aligned} \tag{3.2}$$

where ν is the normalized displacement with respect to the soil's density ρ (i.e., $\nu = \rho u$). $g\left(z\right)$ is an attenuation function which accounts for the artificial dissipation of the wave motion within the buffer zone, and $c\left(z\right)$ is the 1D soil compressional wave velocity random field which is the inverse problem parameter. Equation 3.1 present the displacement (ν) - stress (σ) mixed equations governing wave propagation in a PML truncated one dimensional domain.

3.4 Bayesian Approach to Inverse Problems

An inverse problem is described as the process of estimating some characteristics of a physical system from a set of directly measurable responses of the system (observations) (Medina-Cetina & Arson, 2014). The model parameters $\boldsymbol{\theta}$, and the process of interest $\mathbf{d}$

are related through a so-called forward model. The forward operator G relies on a physical theory to predict the outcome of a possible experiment, or in other words to approximate the reality: $\mathbf{d}_{obs} \approx G(\boldsymbol{\theta})$, or

$$\mathbf{d}_{obs} = G(\boldsymbol{\theta}) + \boldsymbol{\epsilon} \tag{3.3}$$

where $\boldsymbol{\epsilon}$ is the random error component which quantifies the deviation between model prediction and data. This random term contains both theoretical and measurement errors (assuming the forward model is an unbiased estimate to the true physical process). Explicit distinction, however, could be made between model and observational errors in a full uncertainty quantification framework (UQ) (Medina-Cetina, 2006).

The basis of this UQ framework is founded on the definition of a 'true process' vector $\mathbf{d}$, which in general represents values of observable variables (in this case displacement time history response of earth at the surface level). Notice that in typical geomechanical problems or processes, $\mathbf{d}$ is not known a-priori. However, if the true process is assumed to be random, $\mathbf{d}$ can be defined as a vector of random variables. On the other hand, what the modeler can determine are: (1) a vector of physical observations $\mathbf{d}_{obs}$, and (2) a vector of model predictions $\mathbf{d}_{pred}$ (prescribed at the same control points in space and time). $\mathbf{d}_{pred}$ represents a vector of predictions stemming from the forward model, conditioned on a vector of control parameters $\boldsymbol{\theta}$. $\mathbf{d}_{pred}$ could deviate from the true process ($\mathbf{d}$) as a result of the model not fully capturing the underlying physics, due, for example to the fact that either the governing PDE is an inadequate idealization of the true process, initial/boundary conditions are insufficiently modeled, or due to the deficiency of the computational scheme or lack of resolution of the numerical solver. Physical random deviations between $\mathbf{d}$ and $\mathbf{d}_{obs}$ (observation error), and between $\mathbf{d}$ and $\mathbf{d}_{pred}$ (model error) are denoted by $\Delta\mathbf{d}_{obs}$ and $\Delta\mathbf{d}_{pred}$, respectively ($\Delta\mathbf{d}_{obs} = \mathbf{d} - \mathbf{d}_{obs}$ and $\Delta\mathbf{d}_{pred} = \mathbf{d} - \mathbf{d}_{pred} = \mathbf{d} - G(\boldsymbol{\theta})$).

Therefore the following relation holds

$$\mathbf{d}_{obs} = \mathbf{d}_{pred} + \Delta\mathbf{d}_{obs} + \Delta\mathbf{d}_{pred} \tag{3.4}$$

In general, the error components $\Delta\mathbf{d}_{obs}$ and $\Delta\mathbf{d}_{pred}$ are not identifiable, meaning several different combinations of values could be equally consistent with the observed data. However, this does not mean that all the possible values are equally likely (Koutsourelakis, 2009). For example, error trends that significantly deviate from zero most likely imply either a bias in the model or a mis-calibration of the data acquisition instrument. The Bayesian method provides a basis for quantifying a priori and a posteriori measures of plausibility of each type of error (Kennedy & O'Hagan, 2001). In this study, the model discrepancy term vanishes, since the data is synthesized by perturbing the model output. Therefore, the error component can be defined by a single uncertainty metric as shown in equation 3.3. Notice that this latter formulation is valid also when the model predictions are unbiased along the domain of interest (where $\mathbf{d}$ is defined). That is, when the probabilistic expectation $\mathbb{E}[\Delta\mathbf{d}_{obs} - \Delta\mathbf{d}_{pred}] = 0$ (Medina-Cetina, 2006).

In a Bayesian approach to inverse problems, a prior distribution $p(\boldsymbol{\theta})$ is incorporated in estimating each model unknown, which quantifies the initial uncertainty about the parameter. Ideally, this density limits the space of plausible parameters by giving higher probability to those which can help to describe the system's response more accurately. The objective of the inversion is to sample the posterior distribution $p(\boldsymbol{\theta}|\mathbf{d}_{obs})$, build to fully describe the model parameters in terms of a density function, given the data $\mathbf{d}_{obs}$ is observed. According to the Bayes theorem

$$p(\boldsymbol{\theta}|\mathbf{d}_{obs}) = \frac{p(\mathbf{d}_{obs}|\boldsymbol{\theta})\, p(\boldsymbol{\theta})}{\int_{\boldsymbol{\Theta}} p(\mathbf{d}_{obs}|\boldsymbol{\theta})\, p(\boldsymbol{\theta})\ \mathrm{d}\boldsymbol{\theta}} \tag{3.5}$$

where the likelihood function $p(\mathbf{d}_{obs}|\boldsymbol{\theta})$ is the probability that the observed realization $\mathbf{d}_{obs}$ is produced by model $\boldsymbol{\theta}$. Under the customary assumption that the random error components $\boldsymbol{\epsilon} = (\epsilon_1, \ldots, \epsilon_n)^T$ are such that $\boldsymbol{\epsilon} \overset{iid}{\sim} \mathcal{N}\left(\mathbf{0}, \sigma^2\mathbf{I}_n\right)$ (i.e., uncertainty associated with the data is multi-variate normal with mean zero and standard deviation σ, and data

points are independent of each other), the likelihood function is found with reference to a multivariate normal density

$$p\left(\mathbf{d}_{obs}|\boldsymbol{\theta}\right) = \frac{1}{\left[(2\pi)^n|\mathbf{C}_d|\right]^{1/2}} \exp\left[-\frac{1}{2}\left(G\left(\boldsymbol{\theta}\right) - \mathbf{d}_{obs}\right)^T \mathbf{C}_d^{-1}\left(G\left(\boldsymbol{\theta}\right) - \mathbf{d}_{obs}\right)\right] \tag{3.6}$$

where n is the number of observations, $\mathbf{I}_n$ is an $n \times n$ identity matrix, and $\mathbf{C}_d = \sigma^2\mathbf{I}_n$ is the covariance of the error term. The quantity in the denominator of equation 3.5 (the probability of observing the data $\mathbf{d}_{obs}$) is a normalizing constant, such that the posterior is integrated to one.

3.5 Bayesian Partition Models

As described in the preceding section, our geo-acoustic inverse problem requires the identification of the spatially-dependent coefficient of a PML augmented wave equation, given the probed medium's response to a known excitation. This describes a functional inverse problem where the unknown quantity is a function of the spatial coordinate. Hence, in our Bayesian probabilistic setup, the inverse problem parameter comprises a real-valued random field $c\left(\mathbf{z}\right)$ (of infinite dimensionality), which assigns a probability density function to the subsurface property of interest at each point in the spatial domain. In order to arrive at a computationally feasible problem, this random field (and the forward model) must be approximated by its discretized version. Hence the velocity field is approximated with an N-dimensional joint probability density $p(c_1(z_1), \ldots, c_N(z_N)|\mathbf{d}_{obs})$, with N being the number of grid blocks in the domain.

One way of treating the problem is to assign a prior to each random variable $\mathbf{c} = (c_1, \ldots, c_N)^T$, and directly apply the Bayesian formulation to form the posterior density of $\mathbf{c}|\mathbf{d}_{obs}$, and implement MCMC methods to explore the resulting, often high-dimensional, posterior density. Although MCMC methods converge to the posterior by definition as the number of samples grows, in such high dimensional, highly correlated target density configurations, slow chain mixing and serious lack of convergence arise, which render the whole inversion procedure almost computationally impractical.

Instead of exploring the value of $\mathbf{c}(z)$ at each of the N grid blocks, we opt for a varying dimensional Bayesian model to parameterize the velocity random field. We introduce a Bayesian partition model for which it is a-priori assumed that the underlying process that takes the form of a step function (Denison *et al.*, 2002*a*; Holmes *et al.*, 2005). This setting is well suited to our 1D heterogeneity assumption.

The Bayesian partition model can be defined by

$$c\left(z\right) = \mathbf{Z}\mathbf{c} + \boldsymbol{\varepsilon} \tag{3.7}$$

$$\mathbf{Z} = \begin{pmatrix} I\left(z^{(1)} \leq z_1\right) & I\left(z_1 < z^{(1)} \leq z_2\right) & \cdots & I\left(z^{(1)} > z_{k-1}\right) \\ I\left(z^{(2)} \leq z_1\right) & I\left(z_1 < z^{(2)} \leq z_2\right) & \cdots & I\left(z^{(2)} > z_{k-1}\right) \\ \vdots & \vdots & \ddots & \vdots \\ I\left(z^{(N)} \leq z_1\right) & I\left(z_1 < z^{(N)} \leq z_2\right) & \cdots & I\left(z^{(N)} > z_{k-1}\right) \end{pmatrix} \tag{3.8}$$

where $\mathbf{Z}$ is called the basis matrix, and where each column forms a basis function. This formulation states that the true layered profile is made up of a linear combination of these basis functions and the corresponding coefficients ($\mathbf{c}$). $\mathbf{c} = (c_1, \ldots, c_k)^T$ hold the value of partition weights (i.e. wave velocity at each layer), and $I\left(.\right)$ is the indicator function which assumes the value one, if its argument is true, and zero otherwise. The vector $(z_1, \ldots, z_{k-1})$ denotes the $k-1$ change point locations (position of the layer interfaces), where k is unknown number of partitions (layers). $z^{(1)}, \ldots, z^{(N)}$ are the coordinates of N prespecified grid points, which not necessarily coincide with the forward model discretization mesh. Figure 3.2 shows the partition model presentation of a 1D velocity random field. $\boldsymbol{\varepsilon}$ is the error component accounting for the deviation between the true stratified earth model and its partition model representation. Notice that this error term directly propagates to the misfit between observations and the physical model predictions.

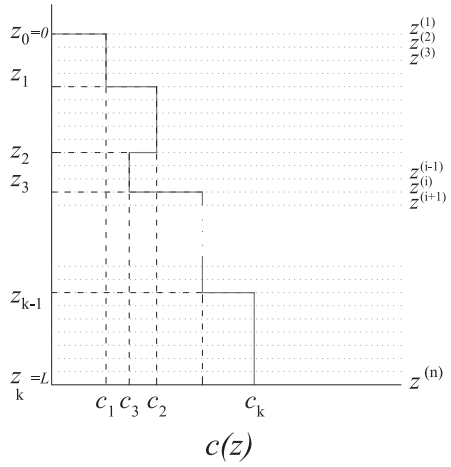

Figure 3.2: Partition model presentation of the 1D velocity random field

3.6 Bayesian Model Selection

In an inverse medum problem it is very common to find situations where there is very limited knowledge about the subsurface formations and stratifications available. Such processes call for a more general and usually broader set of models to be considered to reconstruct the subsurface characteristics.

The proposed Bayesian partition model is categorized within a special class of models namely variable dimension models. A variable dimension model is defined as a model with apriori unknown number of unknowns. This definition by nature pertains to the spatial case of a Bayesian model selection problems, where the competing models belong to the same family, with differing number of parameters, namely, nested models (Robert, 2007).

A Bayesian variable dimension model is defined as a set of plausible models $\mathcal{M}_k = \{f(\mathbf{d}_{obs}|\mathcal{M}_k, \boldsymbol{\theta_k})\,;\ \boldsymbol{\theta}_k \in \boldsymbol{\Theta}\}; k = 1, \ldots, K$, each reflecting a hypothesis about the data $\mathbf{d}_{obs} = (d_{1_{obs}}, \ldots, d_{n_{obs}})^T$. Each model $\mathcal{M}_k$ is defined by a set of model specific vector $\boldsymbol{\theta}_k$ of dimension k, and sampling density $f(\mathbf{d}_{obs}|\mathcal{M}_k, \boldsymbol{\theta_k})$. Having K such competing models, it is desired to find the model stratigraphy that best describes the observations. Oftentimes, due to the lack of knowledge about the true underlying process, the number of components,

k, can not be arbitrarily fixed to infer the parameters $\boldsymbol{\theta}$.

A variable dimension model can be formulated as an extension to the standard Bayesian modeling (see § 3.4), where a prior distribution is assigned on the model indicator $\mathcal{M}_k$, which implies extending the prior modeling from parameters to models. The parameter space associated with the set of models $\mathcal{M}_k$ is given by

$$\boldsymbol{\Theta} = \bigcup_{k \in \mathscr{K}} \{k\} \times \boldsymbol{\Theta}_k \tag{3.9}$$

Having defined priors π_k on the indicator parameter $\mathcal{M}_k$ (being considered now part of the parameters), and parameter subspace $\boldsymbol{\Theta}_k$, by virtue of Bayes's theorem

$$p\left(\mathcal{M}_k, \boldsymbol{\theta}_k | \mathbf{d}_{obs}\right) = \frac{p\left(\mathbf{d}_{obs} | \mathcal{M}_k, \boldsymbol{\theta}_k\right) p\left(\boldsymbol{\theta}_k | \mathcal{M}_k\right) \pi_k}{\sum_{k \in \mathscr{K}} \pi_k \int_{\Theta_k} p\left(\mathbf{d}_{obs} | \boldsymbol{\theta}_k, \mathcal{M}_k\right) p\left(\boldsymbol{\theta}_k | \mathcal{M}_k\right) \mathrm{d}\boldsymbol{\theta}_k} \tag{3.10}$$

Bayes factors in the Bayesian model selection context offers a thorough criteria to pairwise comparison of members in $\{\mathcal{M}_k\}$. The relative plausibility of model i versus model j having experimental observations $\mathbf{d}_{obs}$ is determined by the Bayes factor given by

$$BF\left[\mathcal{M}_i : \mathcal{M}_j\right] = \frac{p\left(\mathcal{M}_i | \mathbf{d}_{obs}\right) / p(\mathcal{M}_i)}{p\left(\mathcal{M}_j | \mathbf{d}_{obs}\right) / p(\mathcal{M}_j)} \tag{3.11}$$

This, by definition, is the posterior to prior odds ratio. Here $p\left(\mathcal{M}_i\right)$ and $p\left(\mathcal{M}_i | \mathbf{d}_{obs}\right)$ are the prior and the posterior probability of $\mathcal{M}_i$ being the true model, respectively. Equivalently

$$BF\left[\mathcal{M}_i : \mathcal{M}_j\right] = \frac{p\left(\mathbf{d}_{obs} | \mathcal{M}_i\right)}{p\left(\mathbf{d}_{obs} | \mathcal{M}_j\right)} \tag{3.12}$$

where $p\left(\mathbf{d}_{obs} | \mathcal{M}_i\right)$ is the marginal likelihood of data under model $\mathcal{M}_i$, which is the normalizing constant of the posterior density and defined as follows:

$$p\left(\mathbf{d}_{obs} | \mathcal{M}_i\right) = \int_{\boldsymbol{\Theta}_i} p\left(\mathbf{d}_{obs} | \mathcal{M}_i, \boldsymbol{\theta}_i\right) p\left(\boldsymbol{\theta}_i | \mathcal{M}_i\right) \mathrm{d}\boldsymbol{\theta}_i \tag{3.13}$$

The above quantity (equation 3.13) is the basis for the Bayesian method's natural

penalty against complex models, also known as Occam's razor. The Bayesian embodiment of Occam's razor is briefly explained in Appendix D. Note that in a frequentist hypothesis testing setup, the criteria to compare the relative merits of one model over another is the likelihood ratio statistics (Vuong, 1989). A more flexible model is able to describe the data better, hence, it gives rise to a higher likelihood measure. This is under the assumption of the error being i.i.d Gaussian, this criteria equates to comparing the response misfits, in a least square sense, which is always reduced by increasing the flexibility of the model. It is proved that a criterion solely based on the likelihood ratio test fails to chose a model if $\mathcal{M}_1 \subset \mathcal{M}_2$, and $\mathcal{M}_1$ is the true hypothesis (which is the case in our varying dimensional model) (Lehmann & Casella, 1998).

This is where terms are added to the (log)likelihood ratio to penalize the inclusion of unnecessary model dimensions. For instance, the Akaike Information Criteria (AIC) (Akaike, 1974), the Bayes Information Criteria (BIC) (Schwarz, 1978), or Jeffrey's variant of it are all based on such developments (Kass & Raftery, 1995). Despite all the modifications, all the latter methods still tend to overestimate the dimensionality of the model. For a further discussion the interested reader is referred to (Kass & Raftery, 1995).

3.7 Reversible Jump MCMC

A customary burden of using Bayes factors (equation 3.12) is the computation of, oftentimes, high dimensional marginal likelihood integrals (equation 3.13). To circumvent this difficulty, one may resort to alternative solutions such as Monte Carlo simulation based methods (e.g., pseudo-priors (Carlin & Chib, 1995; Chib & Jeliazkov, 2001)), or asymptotic approximation to Bayes factors (e.g., Schwartz's criteria also known as BIC) (Schwarz, 1978). The later is widely used in variety of application including geophysical modeling (e.g., see (Dosso & Dettmer, 2011; Dettmer *et al.*, 2009; Ulrych *et al.*, 2001)) due to the ease of its implementation. BIC provides a first-order approximation to the logarithm of the Bayes factor as the sample size grows. In contrast to what its name suggests, BIC is barely considered a Bayesian model selection protocol, as the method overlooks the dependence of the BF to the prior assumptions ((Robert, 2007), §7). Moreover, the

applicability of the approximation is restricted to models with regular likelihoods, and i.i.d. data structures. Also the method calls for the derivation of maximum likelihood estimates for the parameters of all models, which is an unfavorable fact when K is large. Due to the aforementioned shortcomings, reversible jump MCMC has recently become increasingly popular in geophysical inversion as a robust tool for subsurface modeling. A detailed introduction to geophysical transdimensional Bayesian inversion can be found in Sambridge et al. (Sambridge *et al.*, 2013).

3.7.1 Reversible Jump MCMC Algorithm

Suppose we want to generate samples from a varying dimensional target distribution $p(\boldsymbol{\theta}, k)$, where $k \in \mathfrak{K} = \{1, \ldots, K\}$ and $\boldsymbol{\theta} \in \boldsymbol{\Theta}_k$ ($\boldsymbol{\Theta}_k$ denotes the parameter space of the k dimensional model). k is also a random variable which denotes the dimension of random vector $\boldsymbol{\theta}$, and K is a finite integer. This joint probability density $p(\boldsymbol{\theta}, k)$ can be written in its conditional form

$$p(\boldsymbol{\theta}, k) = p(\boldsymbol{\theta}|k)\, p(k) \tag{3.14}$$

We seek to construct a reversible Markov chain $\{(\boldsymbol{\theta}, k)_n\}$ which has a stationary distribution $p(\boldsymbol{\theta}, k)$. At the (s)th iteration the chain state is $(\boldsymbol{\theta}^{(s)}, k^{(s)})$. A new model of (possibly different) dimension k^* is proposed with probability $q(k^*|k^{(s)}) = q_{k^{(s)},k^*}$, where $\sum_{k^* \in \mathfrak{K}} q_{k^{(s)},k^*} = 1$. The basis of Green's idea (Green, 1995) is to supplement each of the current parameter space $\boldsymbol{\Theta}_{k^{(s)}}$, and the candidate parameter space $\boldsymbol{\Theta}_{k^*}$, with adequate artificial spaces in order to create a bijection between them. To this end, given k^*, we draw a $d_{k^{(s)},k^*}$ dimensional auxiliary variable u from a proposal distribution $\psi_{k^{(s)},k^*}(u|\boldsymbol{\theta}^{(s)})$. The new state of the chain $\boldsymbol{\theta}^*$ is found from the transformation $\mathcal{T}$ such that $\boldsymbol{\theta}^* = \mathcal{T}_{k^{(s)},k^*}(\boldsymbol{\theta}^{(s)}, u)$. $\mathcal{T}_{k^{(s)},k^*}$ is a deterministic mapping, so called dimension matching transformation such that $\mathcal{T}_{k^{(s)},k^*} : \mathbb{R}^{k^{(s)}+d_{k^{(s)},k^*}} \rightarrow \mathbb{R}^{k^*}$, where $\mathbb{R}^{k^*}$ denotes the proposed parameter space of k^* dimension. This transformation ensures that the balance condition (necessary condition for Metropolis-Hastings algorithm to converge to the target density) holds in this setting

(Mondal *et al.*, 2010). The equality $k^{(s)} + d_{k^{(s)},k^*} = k^* + d_{k^*,k^{(s)}}$ must be satisfied, in order to perform reversible moves form $(\boldsymbol{\theta}^{(s)}, k^{(s)})$ to $(\boldsymbol{\theta}^*, k^*) = (\mathcal{T}_{k^{(s)},k^*}(\boldsymbol{\theta}^{(s)}, u), k^*)$ and conversely, from $(\boldsymbol{\theta}^*, k^*)$ to $(\boldsymbol{\theta}^{(s)}, k^{(s)}) = (\mathcal{T}_{k^*,k^{(s)}}(\boldsymbol{\theta}^*, u'), k^{(s)})$.

The proposed state $(\boldsymbol{\theta}^*, k^*)$ is accepted with probability $r_{k^{(s)},k^*}(\boldsymbol{\theta}^{(s)}, \boldsymbol{\theta}^*)$

$$r_{k^{(s)},k^*}(\boldsymbol{\theta}^{(s)}, \boldsymbol{\theta}^*) = \min\left\{1, \frac{p(\boldsymbol{\theta}^*, k^*)}{p(\boldsymbol{\theta}^{(s)}, k^{(s)})} \frac{q_{k^*,k^{(s)}}}{q_{k^{(s)},k^*}} \frac{\psi_{k^*,k^{(s)}}(u'|\boldsymbol{\theta}^*)}{\psi_{k^{(s)},k^*}(u|\boldsymbol{\theta}^{(s)})} \left|\frac{\partial \mathcal{T}_{k^{(s)},k^*}(\boldsymbol{\theta}^{(s)}, u)}{\partial \boldsymbol{\theta}^{(s)} \partial u}\right|\right\} \quad (3.15)$$

which states that the new state of the chain is $(\boldsymbol{\theta}^*, k^*)$ with probability $r_{k^{(s)},k^*}$, or $(\boldsymbol{\theta}^{(s)}, k^{(s)})$ with the complement probability $(1 - r_{k^{(s)},k^*})$.

The algorithm can be completed with additional steps within a given model $\mathcal{M}_k$, or about hyperparameters that are not model dependent, which is the case for our hierarchical Bayes model implementation. These additional states are presented in section 3.7.3. We implement the preceding algorithm to reconstruct the spatial distribution of the acoustic wave velocity random field $c(\mathbf{z})$.

3.7.2 Prior Elicitation

We dedicate this section to thoroughly examining the prior elicitation. This effort is justified considering the great sensitivity of Bayesian model selection results to the choice of priors. Since in an standard Bayesian point estimation, the influence of the prior distribution vanishes as the sample size grows, while in a model selection problem rich data availability dose not remedy adverse effects of poor prior specification (Berger & Pericchi, 1996).

The first step in a Bayesian data analysis setting is to specify prior densities to the model parameters $\boldsymbol{\theta}$ (given the model representation $(\mathcal{M})$ is chosen). The prior distribution $p(\boldsymbol{\theta})$ is basically a tool to summarize the initially available information on the process, and to quantify the uncertainty associated with this information. In a scientific inference problem, due to objectivity requirements, we tend to select standard vague or non-informative priors in order to base the inference merely on the experimental observations.

A number of techniques are currently available for constructing such standard priors (Kass & Wasserman, 1996). The use of these priors, however, is rather delicate for varying dimensional model settings, since the majority of non-informative priors are improper, defined up to a constant of proportionality. In general, improper priors can not be assigned to model specific parameters in Bayesian model determination, as the choice of the arbitrary normalizing constant will influence the Bayes factor (equation 3.12). Notice that the Bayes factor is a multiple of this normalizing constant (equations 3.12, 3.13). Proper vague priors (proper priors with large dispersion parameter) also do not address the difficulty, for they give rise to the so called Jeffreys-Lindley paradox (Lindley, 1957; Kass & Wasserman, 1995). The Jeffreys-Lindley paradox is a problem related to the stability of the Bayes factor, which causes the simplest model (which might be a very poor reflection of the data)to always be favored by the Bayes factor.

We address the aforementioned concerns in our choice of priors. We use a hierarchical Bayes approach to model the lack of information on the parameters of the prior distribution, by a second level of prior distributions on these parameters. Hence we refrain from using improper priors, yet avoiding any subjective input to the inference by introducing unground informative priors. The posterior kernel (of varying dimension) according to the Bayes rule is

$$p\left(\mathbf{m}_k, k|\mathbf{d}_{obs}\right) \propto p\left(\mathbf{d}_{obs}|\mathbf{m}_k, k\right) p\left(\mathbf{m}_k, k\right) \tag{3.16}$$

where $\mathbf{m}_k$ is the parameter vector associated to the k layer soil model. $\mathbf{d}_{obs}$ denotes a vector of experimental observations, which is the $n \times 1$ vector of normalized displacement response, recorded at the soil surface. Introducing the second layer of hierarchy will lead to

$$
\begin{aligned}
p\left(\mathbf{m}_k, k|\mathbf{d}_{obs}\right) &\propto p\left(\mathbf{d}_{obs}|\mathbf{m}_k, k\right) p\left(\mathbf{m}_k|k\right) p\left(k\right) \\
&\propto p\left(\mathbf{d}_{obs}|\mathbf{m}_k, k\right) p\left(\mathbf{c}|\sigma^2, v, k\right) p\left(\mathbf{z}|k\right) p(\sigma^2) p\left(v\right) p\left(k|\lambda\right) p\left(\lambda\right)
\end{aligned} \tag{3.17}
$$

For the ease of notation, we define vectors $\mathbf{m}_P$, and $\mathbf{m}_H$ which contain the model specific parameters, and the global hyperparameters, respectively. The global parameters are unknowns, which bear on parameters common to all models. Thus $\mathbf{m}_P = (\mathbf{c}_{k\times 1}^T, \mathbf{z}_{(k-1)\times 1}^T)^T$, $\mathbf{m}_H = (\sigma^2, v, \lambda)^T$, and $\mathbf{m}_k = (\mathbf{m}_P^T, \mathbf{m}_H^T)^T$, and $\mathbf{m} = (\mathbf{m}_k^T, k)^T$. Superscript T denotes transposition. The definition of the priors are

$$
\mathbf{c}|\sigma^2, v, k \sim \mathcal{N}\left(\mathbf{c}_0, \sigma^2 v \mathbf{I}_{k\times k}\right) \tag{3.18a}
$$

$$
\sigma^2 \sim \mathcal{IG}\left(\alpha_0, \delta_0\right) \tag{3.18b}
$$

$$
v \sim \mathcal{G}a\left(\zeta_0, \eta_0\right) = \frac{\eta_0^{\zeta_0}}{\Gamma\left(\zeta_0\right)}\, v^{(\zeta_0 - 1)} e^{(-\eta_0 v)} \tag{3.18c}
$$

$$
p\left(\mathbf{z}|k\right) \propto \binom{T}{k-1}^{-1} \tag{3.18d}
$$

$$
k|\lambda \sim \frac{1}{\sum_{i=1}^{K}\left(\lambda^i/i!\right)} \frac{\lambda^{k-1}}{(k-1)!}\,, \quad k = 1, \ldots, K \tag{3.18e}
$$

$$
\lambda \sim \mathcal{G}a\left(\iota_0, \kappa_0\right) \tag{3.18f}
$$

In the above, $\mathbf{c}$ represents the log-velocity random field. We, a priori, assume that the velocity field within each layer is populated from a log-normal type distribution. Hence, the log-velocity field has a multi-variate Gaussian prior density (equation 3.18a). This assumption ensures that velocity is a positive-valued random filed. We further suppose that $c_1, \ldots, c_k$ are a priori independent. The correlation structure of the layered elastic properties will be reconstructed a posteriori (if there exists any). $\mathbf{c}_0$ is set to $\ln(200)$, meaning that before the inversion, the media is assumed to be homogeneous. From here on $\mathbf{c}$ refers to the log-velocity of the soil layers.

The hyper parameters σ^2 and v are noise variance and precision parameter respectively. We opt for broadly non-informative priors for these parameters ($\alpha_0 = \delta_0 = 0.01$ and $\zeta_0 = \eta_0 = 0.01$), (equations 3.18b, and 3.18c). Setting v is not a trivial task, since an unground specification of this parameter (relatively large values) may lead to Jeffreys-Lindley's paradox (Denison *et al.*, 2002*b*). By considering it as a random variable we elevate the robustness of the method against poor choices of v.

Notice that there is no restriction in using improper priors for the global parameters (which are common among all the models), since in marginal likelihood calculation (equation 3.13) common parameters can be integrated out using the same prior, even when the prior is improper (Berger & Pericchi, 1998). Hence, the problem with the arbitrary proportionality constant, which brings about Lindley's paradox, is removed.

$\mathbf{z}$ is the position vector of the $k-1$ layer interfaces. $p(\mathbf{z}|k)$ (equation 3.18d) reflects the prior assumptions about the position of the material interfaces. We define an underlying grid of T points (which coincides with the finite element discretization of the physical domain). This prior suggests that given a k layer model is the true process, and there are T candidate nodes to locate $k-1$ interfaces, any combination of $(z_1, \ldots, z_{k-1})$ is equally likely. A prior of the form (equation 3.18d) does not place an explicit penalty on the model complexity. However, as stated earlier, the marginal likelihood contains a built-in penalty on the model dimension, which strongly depends on the prior variance v of the coefficients $\mathbf{c}$ (Denison *et al.*, 2002*b*).

We assign a hierarchical truncated Poisson prior on $k|\lambda$, with K being the maximum number of layers in partitioning (equation 3.18e). This setting controls the prior weights given to over-parameterized models, while avoiding to subjectively regularize the solution by freeing λ. λ is a hyperparameter to be elicited from the data. A natural choice of prior on this parameter is a flat Gamma distribution ($\iota_0 = \kappa_0 = 0.01$).

3.7.3 Reversible Jump MCMC Implementation as Birth-Death Process

In this section we extract the details involved in the RJMCMC algorithm for our specific inversion setup, once the prior densities are assigned to the model unknowns. In order to

traverse the varying dimensional posterior surface, we perform four types of move: Birth (B), Death (D), Move (M), and Perturb (P). Different search strategies have been designed depending on the application (e.g., see the original work by Green (Green, 1995), and Denison *et al.* (Denison *et al.*, 1998)). As long as the algorithm satisfies the balance condition, and the acceptance ratio remains computationally efficient, we assume that our approach offers a flexible design.

Let us suppose that at the (s)th step the chain is at $k^{(s)}, \mathbf{m}_P^{(s)}, \mathbf{m}_H^{(s)}$ (denoting number of layers, model specific parameters $\mathbf{c}^{(s)} = (c_1^{(s)}, \ldots, c_k^{(s)})^T, \mathbf{z}^{(s)} = (z_1^{(s)}, \ldots, z_{k-1}^{(s)})^T$, and hyper-parameters $\sigma^{2(s)}, v^{(s)}, \lambda^{(s)}$ respectively). The possible transitions are: (B) add an intersection at a random location with probability $p_{k^{(s)}}^{(B)}$. (D) Delete a randomly chosen intersection with probability $p_{k^{(s)}}^{(D)}$. (M) Swap a randomly chosen intersection for a randomly chosen available node in $\mathscr{T}$ with probability $p_{k^{(s)}}^{(M)}$, where $\mathscr{T}$ is the set of candidate node locations, and T is the size of the set $\mathscr{T}$ ($|\mathscr{T}| = T$). (P) Perturb velocity of a randomly chosen layer with probability $p_{k^{(s)}}^{(P)}$. Where $p_{k^{(s)}}^{(B)} + p_{k^{(s)}}^{(D)} + p_{k^{(s)}}^{(M)} + p_{k^{(s)}}^{(P)} = 1,\ \forall k^{(s)}$. Notice that (B) and (D) involve dimension changes in $\mathbf{m}_P^{(s)}$, while (M), and (P), proposes moves within the current dimension, hence the later proceeds similar to regular Metropolis-Hastings algorithm (Robert & Casella, 2004). Below is the definition of each transition:

- **Birth**

  $k^* = k^{(s)} + 1$

  With probability $p_{k^{(s)}}^{(B)} = q_{k^{(s)},k^*}$, a Birth move is proposed, and a layer interface i is added at an available random grid location. This random location is proposed from the probability $q_z(\mathbf{z}^*|\mathbf{z}^{(s)}, k^{(s)})$.

  Here $d_{k^{(s)},k^*} = 1$, and $d_{k^*,k^{(s)}} = 0$, so an auxiliary variable is needed for the dimension balance. We draw u from $\psi_{k^{(s)},k^*}(u|\mathbf{c}^{(s)})$.

  Next, we determine the proposed layer velocities $\mathbf{c}^*$ from the transformation $\mathcal{T}_{k^{(s)},k^*}(\mathbf{c}^{(s)}, u)$ given by

$$\mathcal{T}_{k^{(s)},k^*}(\mathbf{c}^{(s)},u)=\begin{cases} c_1^{k^{(s)}+1} &= c_1^{k^{(s)}} \\ &\vdots \\ c_{i-1}^{k^{(s)}+1} &= c_{i-1}^{k^{(s)}} \\ c_i^{k^{(s)}+1} &= c_i^{k^{(s)}}-\varsigma_c u \\ c_{i+1}^{k^{(s)}+1} &= c_i^{k^{(s)}}+\varsigma_c u \\ &\vdots \\ c_{k^{(s)}+1}^{k^{(s)}+1} &= c_{k^{(s)}}^{k^{(s)}} \end{cases} \tag{3.19}$$

This implies that the velocity of the chosen layer is perturbed from a Gaussian proposal to attain the velocity of the two emerged layers. ς_c is a variance measure, defining size of the search step. Notice that the hyperparameters remain unchanged in the Birth (also in Death) move. The candidate state is accepted with probability

$$\begin{aligned} r_{k^{(s)},k^*}(\mathbf{m}_P^{(s)},\mathbf{m}_P^*)=\min\Bigg\{1,\underbrace{\frac{p(\mathbf{m}_P^*,k^*)}{p(\mathbf{m}_P^{(s)},k^{(s)})}}_{\text{prior ratio}}\underbrace{\frac{p(\mathbf{d}|\mathbf{m}_P^*,\mathbf{m}_H^{(s)},k^*)}{p(\mathbf{d}|\mathbf{m}_P^{(s)},\mathbf{m}_H^{(s)},k^{(s)})}}_{\text{likelihood ratio}} \\ \times\underbrace{\frac{q_{k^*,k^{(s)}}\;\psi_{k^*,k^{(s)}}(u'|\mathbf{c}^*)\;q_z(\mathbf{z}^{(s)}|\mathbf{z}^*,k^*)}{q_{k^{(s)},k^*}\;\psi_{k^{(s)},k^*}(u|\mathbf{c}^{(s)})\;q_z(\mathbf{z}^*|\mathbf{z}^{(s)},k^{(s)})}}_{\text{proposal ratio}} \\ \times\underbrace{\left|\frac{\partial\mathcal{T}_{k^{(s)},k^*}(\mathbf{c}^{(s)},u)}{\partial\mathbf{c}^{(s)}\partial u}\right|}_{\text{Jacobian}}\Bigg\} \end{aligned} \tag{3.20}$$

where the prior ratio is

$$\frac{p(\mathbf{m}_P^*,k^*)}{p(\mathbf{m}_P^{(s)},k^{(s)})}=\frac{p(\mathbf{c}^*|\sigma^{2(s)},v^{(s)},k^*)p(\mathbf{z}^*|k^*)p(k^*|\lambda^{(s)})}{p(\mathbf{c}^{(s)}|\sigma^{2(s)},v^{(s)},k^{(s)})p(\mathbf{z}^{(s)}|k^{(s)})p(k^{(s)}|\lambda^{(s)})} \tag{3.21}$$

and

$$q_z(\mathbf{z}^{(s)}|\mathbf{z}^*, k^*) \propto \frac{1}{k^* - 1} \tag{3.22a}$$

$$q_z(\mathbf{z}^*|\mathbf{z}^{(s)}, k^{(s)}) \propto \frac{1}{T - \left(k^{(s)} - 1\right)} \tag{3.22b}$$

$$\psi_{k^*,k^{(s)}}(u'|\mathbf{c}^*) \propto 1 \tag{3.22c}$$

$$\psi_{k^{(s)},k^*}(u|\mathbf{c}^{(s)}) \sim \frac{1}{\varsigma_c}\mathcal{N}(0,1|u) \tag{3.22d}$$

$$q_{k^{(s)},k^*} = \begin{cases} 1/2 & k^{(s)} = 1 \\ 1/4 & \text{otherwise} \end{cases} \tag{3.22e}$$

$$q_{k^*,k^{(s)}} = \begin{cases} 1/3 & k^{(s)} = K \\ 1/4 & \text{otherwise} \end{cases} \tag{3.22f}$$

$$\left|\frac{\partial \mathcal{T}_{k^{(s)},k^*}(\mathbf{c}^{(s)}, u)}{\partial \mathbf{c}^{(s)} \partial u}\right| = 2\varsigma_c \tag{3.22g}$$

$p(\mathbf{d}|\mathbf{m}_P, \mathbf{m}_H, k)$ is the likelihood function, which is constructed according to equation 3.6.

- **Death**

  $k^* = k^{(s)} - 1$

  With probability $p_{k^{(s)}}^{(D)} = q_{k^{(s)},k^*}$, a Death move is proposed. A current interface i is randomly chosen from the probability $q_z(\mathbf{z}^*|\mathbf{z}^{(s)}, k^{(s)})$ and removed. The proposed velocity profile $\mathbf{c}^*$ is determined from the deterministic Death transformation (which is the reverse Birth transformation)

$$\mathcal{T}_{k^{(s)},k^*}(\mathbf{c}^{(s)},u) = \begin{cases} c_1^{k^{(s)}-1} & = c_1^{k^{(s)}} \\ & \vdots \\ c_{i-1}^{k^{(s)}-1} & = c_{i-1}^{k^{(s)}} \\ c_i^{k^{(s)}-1} & = \frac{1}{2}\left(c_i^{k^{(s)}} + c_{i+1}^{k^{(s)}}\right) \\ c_{i+1}^{k^{(s)}-1} & = c_{i+2}^{k^{(s)}} \\ & \vdots \\ c_{k^{(s)}-1}^{k^{(s)}-1} & = c_{k(s)}^{k^{(s)}} \end{cases} \tag{3.23}$$

The acceptance probability is the same as equation 3.20, with the following modifications

$$q_z(\mathbf{z}^{(s)}|\mathbf{z}^*,k^*) \propto \frac{1}{T-\left(k^{(s)}-1\right)} \tag{3.24a}$$

$$q_z(\mathbf{z}^*|\mathbf{z}^{(s)},k^{(s)}) \propto \frac{1}{k^*-1} \tag{3.24b}$$

$$\psi_{k^*,k^{(s)}}(u'|\mathbf{c}^*) \sim \frac{1}{\varsigma_c}\mathcal{N}(0,1|u) \tag{3.24c}$$

$$\psi_{k^{(s)},k^*}(u|\mathbf{c}^{(s)}) \propto 1 \tag{3.24d}$$

$$q_{k^{(s)},k^*} = \begin{cases} 1/3 & k^{(s)}=1 \\ 1/4 & \text{otherwise} \end{cases} \tag{3.24e}$$

$$q_{k^*,k^{(s)}} = \begin{cases} 1/2 & k^{(s)}=K \\ 1/4 & \text{otherwise} \end{cases} \tag{3.24f}$$

$$\left|\frac{\partial \mathcal{T}_{k^{(s)},k^*}(\mathbf{c}^{(s)},u)}{\partial \mathbf{c}^{(s)}\partial u}\right| = \frac{1}{2\varsigma_c} \tag{3.24g}$$

- **Move**

$k^* = k^{(s)}$

With probability $p^{(M)}_{k^{(s)}} = q_{k^{(s)},k^*}$, a "Move" move is proposed. A layer interface in randomly chosen from a uniform probability, and moved to an available knot location. A new set of hyper parameters $\mathbf{m}^*_H$ is drawn from the probability $q(\mathbf{m}^*_H|\mathbf{m}^{(s)}_H)$. Log-normal proposals are used to update all the hyperparameters.

In a Move step, as the number of material layers is fixed, the algorithm reduces to the regular Metropolis-Hastings MCMC with the acceptance probability of the following form: (Notice that the hyperparameters of the model are also updated in Move and Perturb).

$$r_{k^{(s)},k^*}(\mathbf{m}^{(s)},\mathbf{m}^*) = \min\left\{1, \underbrace{\frac{p(\mathbf{m}^*)}{p(\mathbf{m}^{(s)})}}_{\text{prior ratio}} \underbrace{\frac{p(\mathbf{d}|\mathbf{m}^*_P,\mathbf{m}^*_H,k^{(s)})}{p(\mathbf{d}|\mathbf{m}^{(s)}_P,\mathbf{m}^{(s)}_H,k^{(s)})}}_{\text{likelihood ratio}} \underbrace{\frac{q(\mathbf{m}^{(s)}_H|\mathbf{m}^*_H)}{q(\mathbf{m}^*_H|\mathbf{m}^{(s)}_H)}}_{\text{proposal ratio}}\right\} \tag{3.25}$$

- **Perturb**

  $k^* = k^{(s)}$

  With probability $p^{(P)}_{k^{(s)}} = q_{k^{(s)},k^*}$, a Perturb move is proposed. A layer is randomly picked from a uniform density, and its material property is perturbed with a Gaussian proposal. It is also attempted to update the model hyperparameters from log-normal proposal densities (similar to the M move). The probability of accepting the candidate state is found from equation 3.25. Notice that the uniform and Gaussian proposals to update $\mathbf{m}_P$ do not appear in this ratio (also in the M step), for reasons of symmetry.

3.8 Application to a Synthetic Case

The inversion scheme outlined in the preceding sections is applied to a synthetic data set to deduce the subsurface elastic properties of a soil model. We consider the horizontally stratified semi-infinite soil medium depicted in figure 3.3. The medium is modeled as a one-

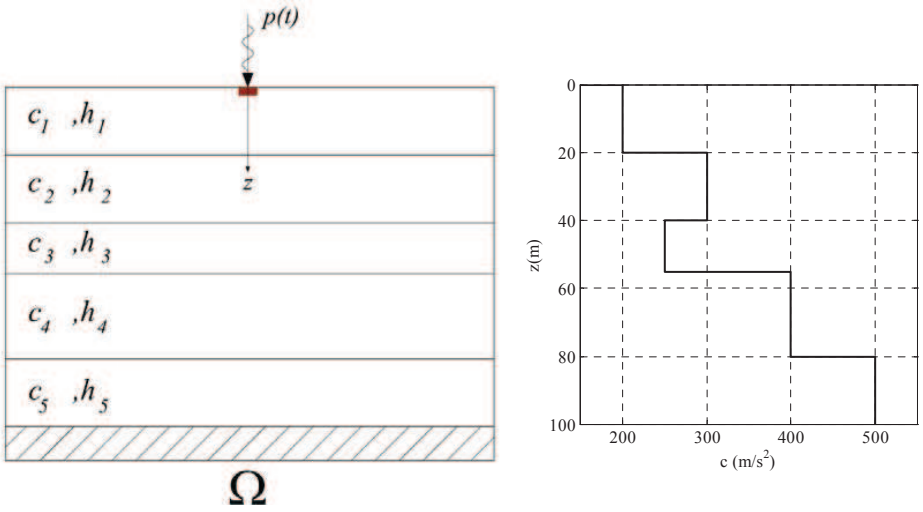

Figure 3.3: Benchmark soil velocity profile

dimensional PML-truncated domain, with the regular domain extending to $z = 100$m, and the PML buffer zone thickness being 10m. Figure 3.3 illustrates the target wave velocity profile, which reflects sharp transitions between different materials in depth. The medium is probed with a Gaussian pulse-type excitation $p(t)$ applied at the soil surface as shown in figure 3.4a. Figure 3.4b depicts the frequency spectrum of the excitation.

Figure 3.5a shows the displacement time history response of the medium given the soil model depicted in figure 3.3, which is obtained by solving the forward problem 3.1 and 3.2 using a mixed finite element method. 220 elements of length 0.5m are used in the analysis. Displacement response, as a measurable characteristic of the wave field, will serve as the input to our inversion scheme. We generate the synthetic data by perturbing the displacement response $v(0,t)$ of the soil model with 20% Gaussian noise. Figure 3.5b illustrates this data set. The attenuation effect is disregarded in this study, and the soil density is assumed to be known a priori ($\rho = 2000\,\mathrm{kg/m^3}$).

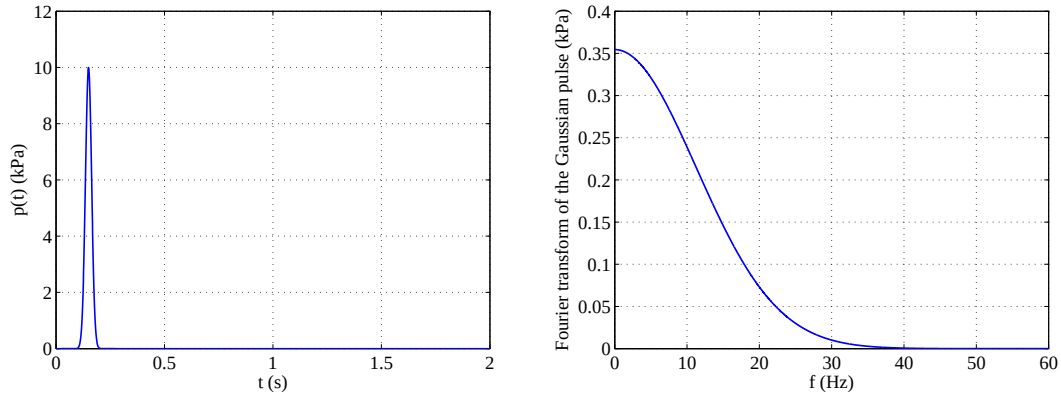

(a) (b)

Figure 3.4: (a) Time history of the applied stress $p(t)$ (b) Frequency spectrum of the applied stress $p(t)$

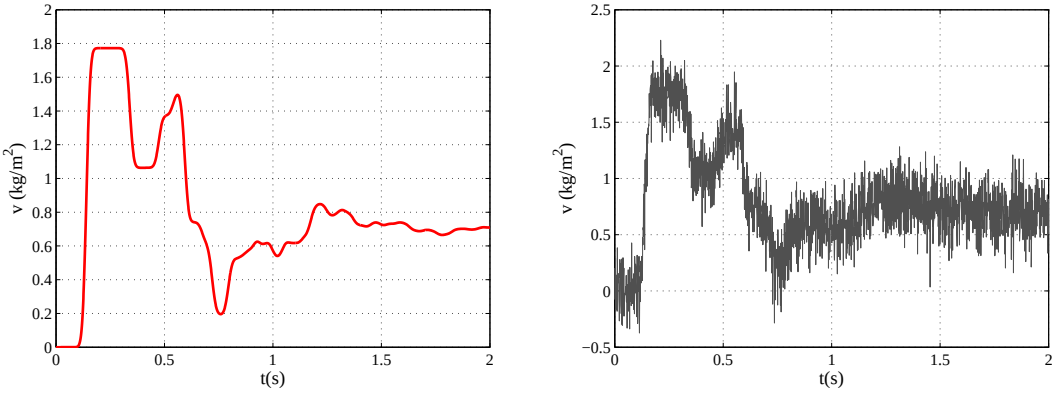

(a) (b)

Figure 3.5: (a) Measured displacement response at the surface (b) Synthetic data: Measured displacement response at $z = 0$ perturbed with 20% Gaussian noise

3.9 Results

In this section, we give a demonstration of the Bayesian varying dimensional inversion, and model determination using the methodology introduced in the preceding sections. The inversion allowed for the maximum of 40 soil layers (up to the truncation interface), which indicates maximum number of 83 model unknowns. This maximum resolution is attributed to the frequency of the exerted load (maximum frequency 40 Hz). The simplest earth model is $k = 1$, which corresponds to the state of a homogenous medium. No additional assumption is made concerning the regularization of the deduced velocity profile.

We started the inversion with homogenous initial guess ($k = 1, c = \ln(200^{\mathrm{m/s}})$). The RJMCMC sampler was run, and a total of 100K iterations were stored as the generated samples. The first 20K samples were discarded as burn-in iterations. Every fifth visited sample was kept in the chain as high dependency is expected, especially between successive values of k, since the difference between the current and the proposed k values could be at most one. Figure 3.6 illustrates the first 300 RJMCMC sampling sequence for the model index (number of layers), starting from $k = 1$. This figure shows that k increases rapidly up to $k = 10$ and in about 200 iterations, then it settles down to the five layer target model. This figure also implies that even though our sampling strategy dose not force the model to undergo dimension changes at every iteration (we are pointing to M, and P moves) the waiting time at a single model is not long. Hence the sampler promptly explores the space of plausible models until it converges to the target model $k = 5$. The rest of the simulation effort is committed to arriving at the stationary condition in sampling the parameters of the few favored models. This observation confirms the efficiency of the algorithm design and of the proposal density formulations.

Figure 3.7a depicts the full sampling history for the same parameter, to further emphasize the stability of the RJMCMC chain. The marginal posterior probability mass function of k is shown in figure 3.7b, which quantifies the level of certainty in accepting each hypothesis. According to this figure, 6 layer profile is also a likely model to describe the observations with much less probability. The figure manifests the Bayesian inversion

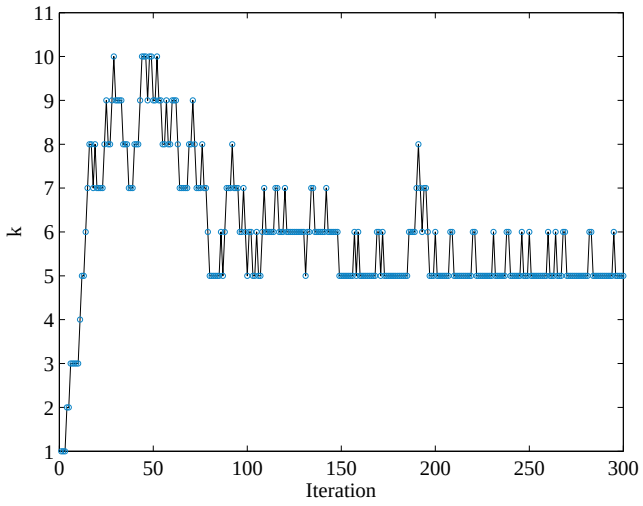

Figure 3.6: Number of basis functions (layer interfaces) variation in first 300 RJ-MCMC iterations

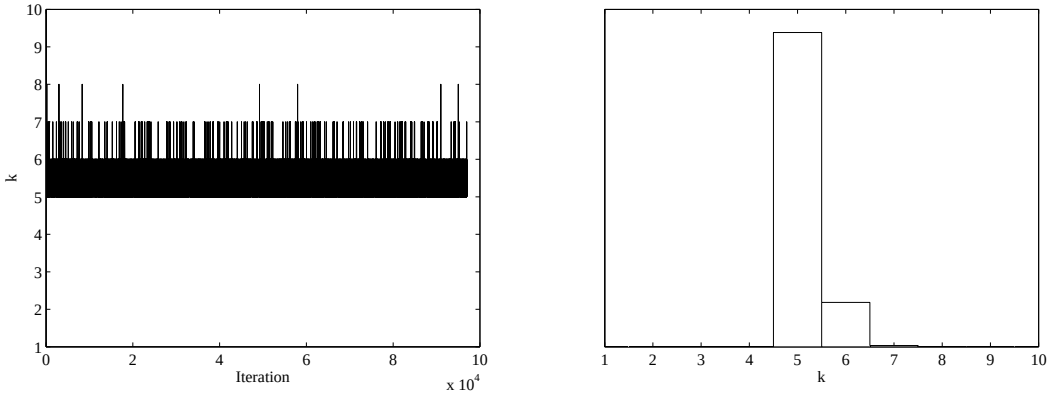

(a) Posterior samples of k

(b) Posterior mass function of k

Figure 3.7: Number of layers (k) in the partition model

capability to deduce the true nature of the underlying process without imposing any regularization constraint to penalize overly complex models.

Figures 3.8 and 3.9 illustrate the marginal posterior densities of the model specific parameters, given the true model $k = 5$. Figure 3.8 shows the posterior estimates for the layer thicknesses $p(\mathbf{z}|\mathbf{d}_{obs}, k = 5)$, and their associated uncertainties. The target values are also superimposed on each histogram (dashed lines). The figure indicates the ability of the inversion scheme to deduce the target parameters. Notice that the deviation of the posterior mean from the target values are about one to two element dimensions. The thickness of the fifth layer is not included here, as it is considered semi-infinite. Theoretically, the PML is assumed to be located at a depth beyond which homogeneity is ascertained. Figure 3.9 shows the inverted acoustic soil velocities of the true model $p(\mathbf{c}|\mathbf{d}_{obs}, k = 5)$, together with the target values.

Figure 3.10 shows inference for model hyperparameters. Although these parameters might not be incorporated directly in model predictions, they are highly influential in attaining reliable parameter estimates. In figure 3.10a the standard deviation of the observational error term σ^2 is displayed, which is relatively centered around the target added Gaussian noise (signal to noise ratio, SNR= 5).

Figure 3.10b depicts the dispersion parameter v. This parameter is of crucial significance in our model determination framework, since fixing v to small values (choice of relatively sharp priors on $\mathbf{c}$) limits the flexibility of each basis function coefficient, therefore many partitions (layers) are required to adequately model the target process ($\mathbb{E}(k|\mathbf{d}_{obs})$ grows). The definition of the basis functions in a Bayesian partition model is given in equation 3.8. By contrast, large v (relatively diffuse prior on $\mathbf{c}$) results in a more flexible regression function posterior mean $\tilde{c}(z)$ (see equation 3.7), which can accommodate wilder oscillations in its behavior. Hence, fewer basis functions are needed to reflect the true underlying process ($\mathbb{E}(k|\mathbf{d}_{obs})$ becomes increasingly small), as each basis function has more degrees of freedom. Notice that here we did not choose to set up a fixed value for v, rather this parameter is considered as a random variable (equation 3.18c), and its value is

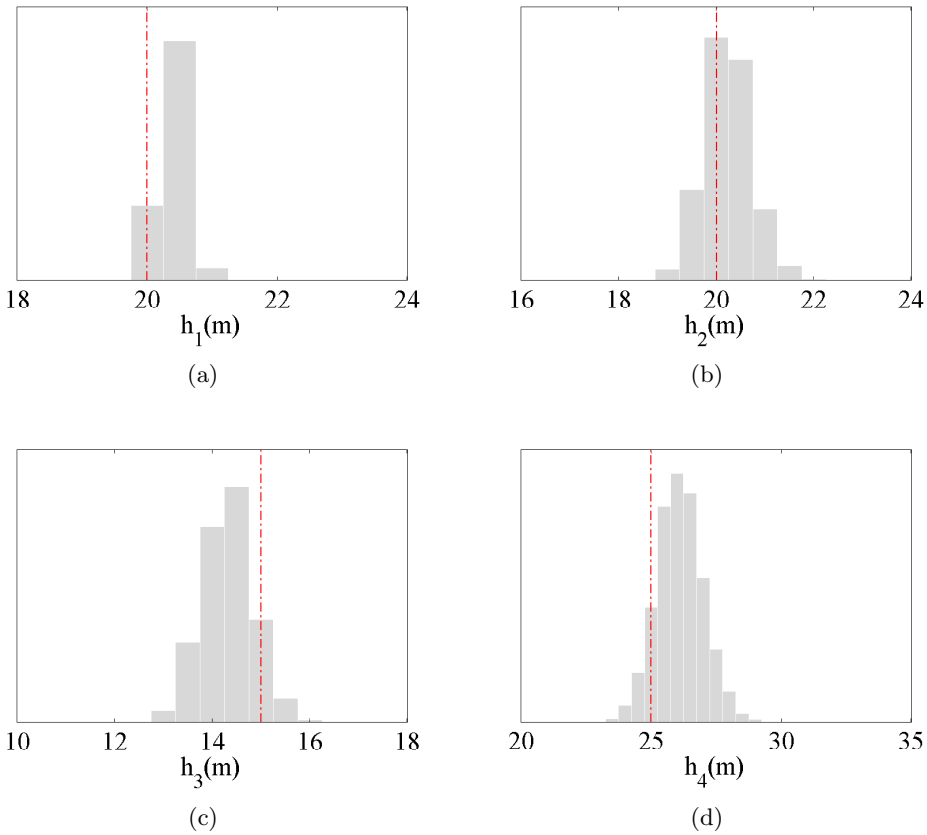

Figure 3.8: Marginal posterior density of the layer thicknesses given $k = 5$ and the corresponding target values (dashed line)

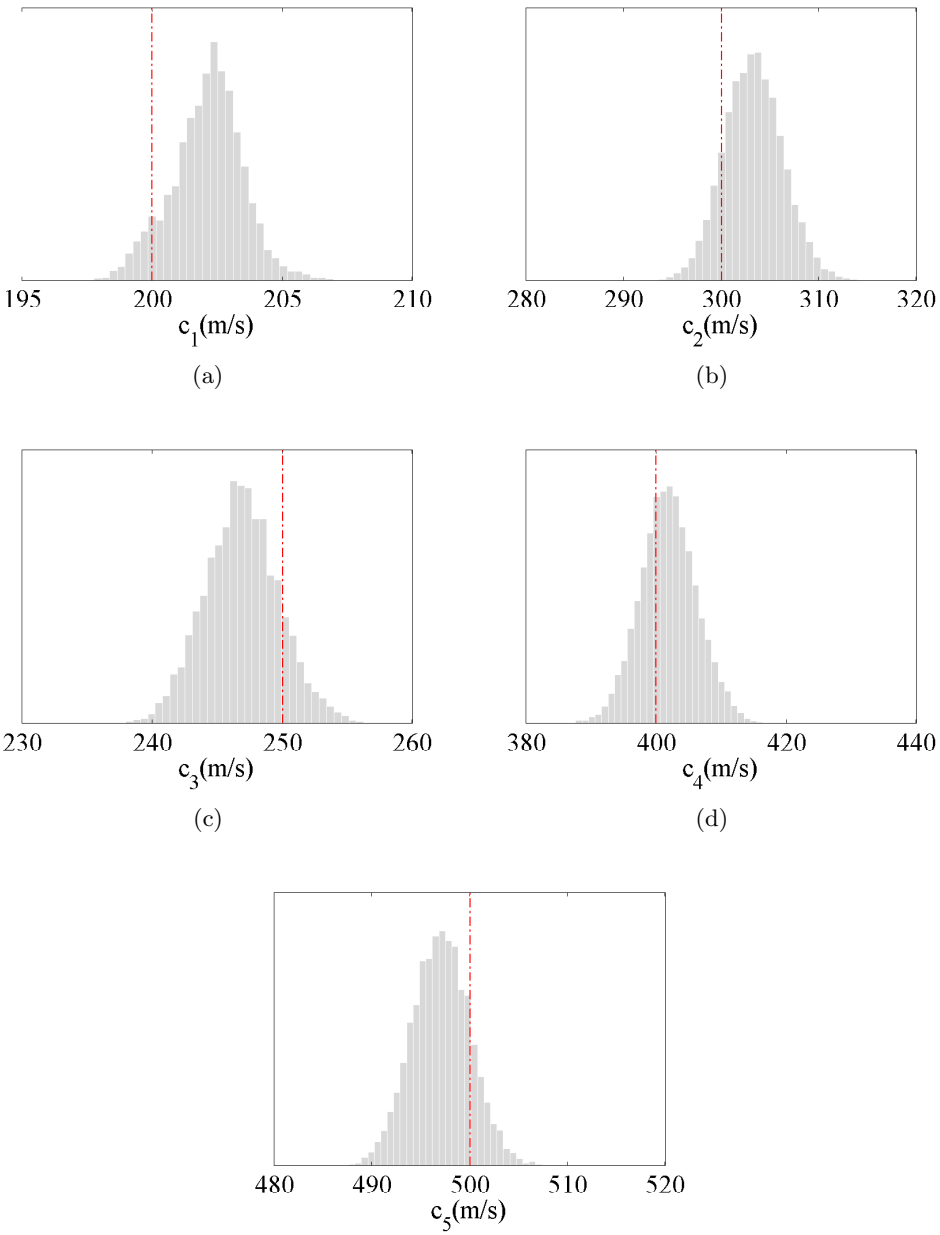

Figure 3.9: Marginal posterior density of the layer velocities given $k = 5$ and the corresponding target values (dashed line)

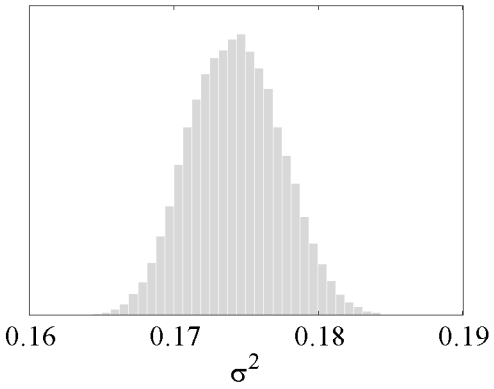

(a) Noise standard deviation (σ)

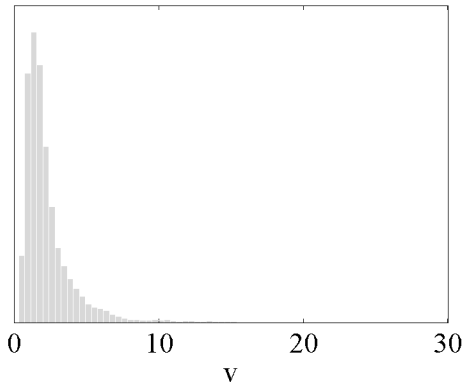

(b) Precision parameter (v)

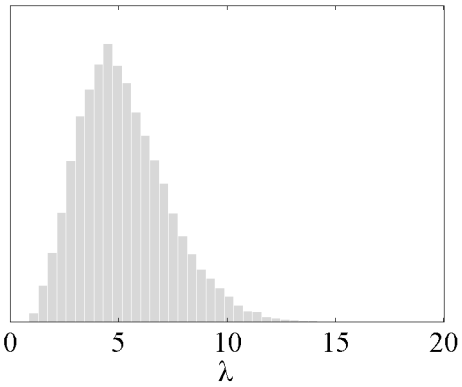

(c) Rate parameter in poisson prior (λ)

Figure 3.10: Marginal posterior density for model hyper-parameters

deduced from the data such that the marginal likelihood is maximized.

The marginal posterior density of the rate parameter λ in the Poisson prior (equation 3.18e) is provided in figure 3.10c. We can see that the Bayesian point estimate for λ is closely approximated by $\hat{\lambda} \approxeq 5$. This parameter is the mean of the Poisson prior equation 3.18e, which reflects the numbers of layers k accommodated in the model $c(z)$.

Figure 3.11 demonstrates the essence of Bayesian updating and uncertainty reduction as a result of introducing the experimental observations. Figure 3.11a presents 5×10^2 superimposed likely prior soil models (equation 3.7), with the coefficients of each curve drawn directly from the definition of the priors (equation 3.18). These curves show the state of minimum knowledge about the subsurface structure. No stratification and velocity measure is discernible at this initial state. Figure 3.11b depicts 5×10^3 posterior soil model realizations, which mimic accurately the general trend of the target process.

Figure 3.12 quantifies the observations of the previous figure. The posterior mean soil profile $\tilde{c}(z)$ (black solid curve) is illustrated together with 95% credible intervals for the posterior predictions (dark shaded area). The prior credible region is also included in the figure (light shaded area), which occupies the entire space (and extends to infinity). The mean posterior prediction of the displacement time history response of the media $v(z = 0, t)$ is pictured in figure 3.13. The figure also provides a measure of uncertainty around the posterior mean estimate $\tilde{v}(0, t)$. This plot accentuates the high fidelity of the posterior estimates to the experimental observations.

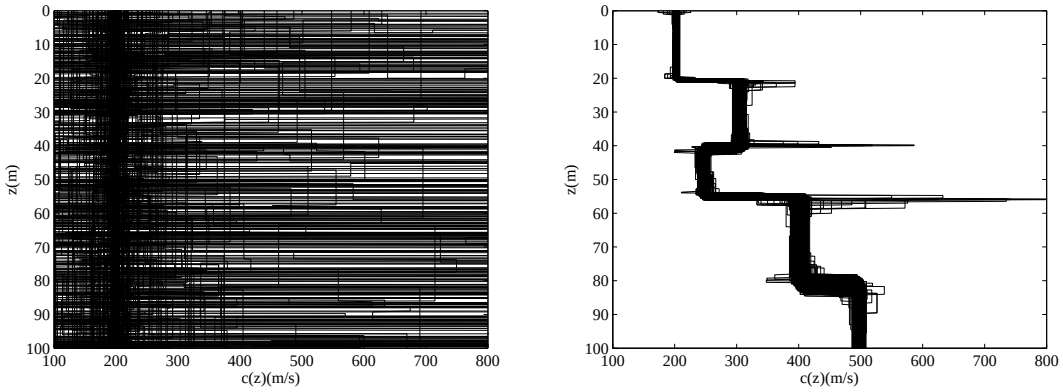

(a) Superimposed $5e2$ likely prior soil models (b) Superimposed $5e3$ likely posterior soil models

Figure 3.11: Prior and posterior model predictions

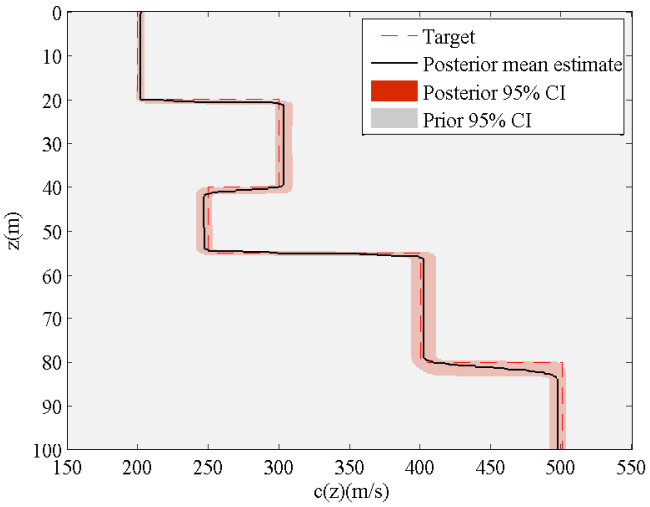

Figure 3.12: Posterior mean estimate together with 95% credible intervals for the mean posterior and the mean prior

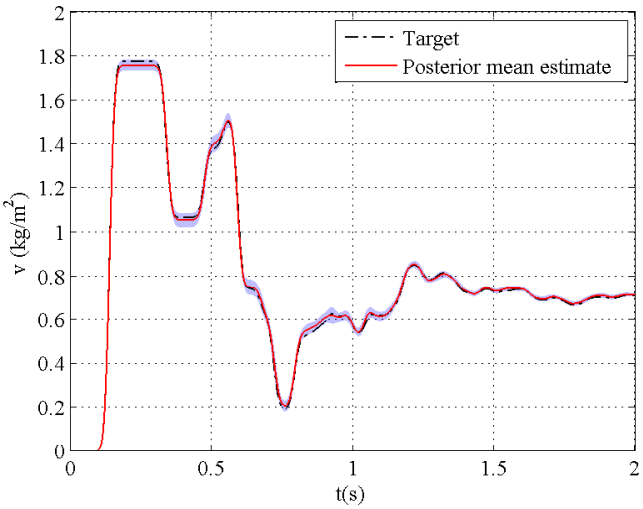

Figure 3.13: Posterior displacement prediction together with 95% credible intervals around the mean

3.10 Concluding Remarks

This paper introduces a probabilistic calibration approach via a Bayesian formulation for the solution of inverse problems, defined by the random field characterization of heterogeneous media, for an acoustic one-dimensional velocity field with horizontally layered structure. A self-regularized varying structure forward model is formulated based on the notion of Bayesian partition models in order to parameterize the acoustic wave velocity random field. The method offers a reduced dimensional inversion technique by dividing the velocity random field into an unknown number of soil layers within a certain depth interval. Number of layers, their velocities and thicknesses are inverse deduced, conditioned on the observations. The reward of the approach is that the explicit regularization of the inverted profile by global damping procedures or even through imposition of priors, which carry smoothness constraints, (and might introduce subjectivity to the inference process), is not required. The reversible jump MCMC algorithm was implemented to carry out the simulation of the resulting varying dimensional posterior density. The provided synthetic case indicates significant functionality of the inversion scheme to retrieve the benchmark

subsurface profile.

4. VARIABLE DIMENSIONAL BAYESIAN FULL WAVEFORM INVERSION FOR 2D SEMI-INFINITE HETEROGENEOUS MEDIA

4.1 Overview

This paper introduces a methodology to infer the spatial variation of soil elastic characteristics of a heterogeneous unbounded medium, via a probabilistic calibration approach, given a prescribed sequence of loading and the corresponding time history response registered at the ground level. This involves solution of an inverse medium problem, where the object of inference constructs a continuous spatial random field. The shear wave velocity field is presented on a discrete grid as a proxy for the continuous model. In a grid-based inversion, the pointwise values of the field is explored at each of the grid-blocks with a Monte Carlo search, leading to a very high dimensional parameter space. This, in turn, gives rise to major complications in posterior sampling. In order to reduce the dimensionality of the inverse problem, we opt for partition model description of the velocity field. That is, the field is decomposed into a number of non-overlapping subregions, so called Voronoi tessellations, where the number of tessellations, their geometry, and weights dynamically change to adapt to the features of the target model. A Gaussian Markov Random field prior formalizes the correlation structure among the tessellations. The idea of treating the number of tessellations (number of unknowns) as an unknown itself, is closely related to Bayesian model selection, where the likely dimensionality of the inverse problem is inferred conditional on the experimental observations. A reversible jump Markov chain Monte Carlo (RJMCMC) scheme is applied to sample the posterior distribution of varying dimension. The governing forward physics consist of propagation of 2D scalar (SH) waves travelling in the heterogeneous Earth, where in order to model the semi-infinite extent of the physical domain, a perfectly matched layer (PML) is introduced at the truncation boundary. Synthetic data examples are set to illustrate the capabilities of the proposed methodology.

4.2 Introduction

Methods of constructing subsurface images of the Earth's internal structure and composition has been actively developed in variety of fields such as geophysical probing applications, geotechnical site characterization, oil and mineral resource assessment, groundwater remediation and non-destructive testing, among others. This imaging process essentially involves solution of an inverse problem. An inverse problem is described as the process of estimating some characteristics of a physical system from a set of directly measurable responses of the system (observations). The basis of all the above applications is stimulating the domain by a physical/mechanical excitation and recording the response as the observable parameter which is fed to the inverse solver to reconstruct the spatially variable characteristic of interest. In this article the aim is to infer the elastic characteristics/shear wave velocity field of a two dimensional arbitrarily heterogeneous Earth model from surficial measurements of displacement time history response of the domain to prescribed dynamic excitation also located at the ground level.

Full waveform inversion consists in a data fitting procedure based on modeling the propagation of wave-field through subsurface earth to extract quantitative images of elastic moduli (and/or density and/or attenuation properties) where the entire information embedded in the waveform from the onset of the wave to the final recognisable oscillations in the wave train (typically recorded directly in the time-domain and on the probed domain's surface) is exploited (Fichtner, 2010). Full waveform inversion was introduced to the geophysical community by the early work of Bamberger et al. (Bamberger *et al.*, 1977) and has been pursued afterwards in wide range of disciplines as diverse as geophysical exploration, medical imaging, oil and gas exploration, etc. in both frequency-domain and time-domain for nearly four decades now. The majority of the literature, however, has focused on deterministic approaches. More recently, owing to the advances in computational power of the computers, statistical inversion methods has been emerged to address the essential need for incorporating the various sources of uncertainty stemming from measurement errors, aleatory formations, and limited theoretical understanding.

Waveform inversion could be classified as migration velocity analysis methods (MVA) (Plessix *et al.*, 1998; Chavent & Jacewitz, 1995) or full waveform based schemes (Plessix, 2008). MVA is based on the analysis of the kinematic of reflections and is an iterative process of the following two-step workflow: (1) the data are migrated by prestack migration and (2) the velocity profile is updated based on the migration output. The iteration is repeated until the optimal migration velocity that best flattens the reflection "Common Image Gathers" (CIG) is achieved (Biondi, 2006).

Symes (Symes, 2008) in a comparative discussion reviewed the superiority of the MVA over deterministic full waveform approaches. Despite the remarkable ability of the full waveform inversion techniques to reconstruct detailed models of subsurface structure, they tend to become trapped in local minima associated with the waveform misfit function, as the misfit function is highly nonlinear with respect to the changes in velocity model. Hence, the solution is overly sensitive to the initial estimate of velocity structure. On the other hand, MVA requires decomposition of the sought properties into the, so-called, background and reflectivity components, followed by a fairly complex forward modeling, and an expensive optimization process in order to recover the reflectivity. The reader is referred to Virieux and Operto and Plessix (Virieux & Operto, 2009; Plessix, 2008) for a review of available (deterministic) full waveform inversion techniques in exploration geophysics.

The information contained in seismic measurements are naturally limited, sparse and noise-contaminated. These observations are used to retrieve essentially infinite number of unknowns (pointwise values of the velocity field), where generally no information is available on spatial variability of the property of interest. These lead to the inherent non-uniqueness of the reconstructed image. That is, the reconstructed image is highly uncertain, acknowledging that infinite solutions are equally compatible with the data. On the other hand, the validity of the constructed image is highly dependent on how accurately the propagation of waves through strongly heterogeneous Earth is simulated (does the model captures all the physics that contribute to the data?). Therefore, deterministic

estimation of the velocity model could be considered of limited use considering all the sources of uncertainty. The straightforward recognition of the noted uncertainties has led to introduction of probabilistic inverse theory, and the Bayesian method to be specific, to the geophysical literature (Keilis-Borok & Yanovskaya, 1967; Press, 1968; Tarantola, 2005) where each plausible solution is assigned a probability of representing the true Earth.

We refer to some of major earlier geophysical literature on the subject of Bayesian inversion. Duijdnam (Duijndam, 1988*a*,*b*) presents an excellent introduction and reference to the subject, specifically in seismic applications. Scales and Tenorio (Scales & Tenorio, 2001) gives a overview on fundamental concepts of uncertainty based data fitting and model parameter estimation with a comparative discussion on Bayesian and frequentist methodologies with specific emphasis on means of formalizing the prior density. Ulrych etal (Ulrych *et al.*, 2001) gives a tutorial on concepts central to the Bayesian approach to inverse problems. Some standard references on applied probability theory and Bayesian data analysis are (Box & Tiao, 1992; Gelman *et al.*, 2003; Jaynes & Bretthorst, 2003).

We consider Bayesian formulation of a nonlinear inverse problem in which the object of inference constructs a spatial random field. Two major modelling and computational challenges are involved in this construction. First, the number of unknowns (i.e., pointwise values of the field) is essentially infinite (Rechenmacher & Medina-Cetina, 2007). Hence, the unknown field is approximated by its spatial discretization. This discretization is often according to the resolution of the forward solver leading to an often very high dimensional parameter space. Large dimensionality of the input space with a nonlinear forward mapping lead to multimodal, strongly correlated and skewed posteriors, which in turn gives rise to major complications in the posterior sampling. Moreover, grid based parametrization of the unknown field artificially enforce a minimum length scale of variability which is generally imposed by the discretization size of the governing PDE (Lee *et al.*, 2002). If the scale of variation of the unknown spatial field is higher than the resolution of the mesh, the scheme constitutes a waste of computational resources, since the forward model has to run on a unnecessarily fine mesh. Moreover, as the number of unknowns increases (at times, higher

than the number of data) overfitting the data might occur, which generates spurious large fluctuations in the inverted material property values. This results could be completely erroneous and yet very well fit the data. Such solutions also perform poorly in terms of prediction (Koutsourelakis, 2009). In a deterministic setup, eliminating such solution somewhat becomes a subjective choice. A popular option to select the best model is to impose an auxiliary constraint on the model parameters in order to minimize the norm of the solution. This produces the smallest model that minimizes the misfit function (also referred to as minimum norm solution) (Everett, 2013).

Secondly, Simulation based inference schemes (Monte Carlo methods) usually requires a high number of forward model calls in order to arrive at stationary state of the chain and approximate the estimators. Repeated evaluation of the forward model, particularly when faced with large-scale inverse problems, even though possible in theory, could be computationally intractable, rendering the inference impractical in real applications.

Three key approaches might be adopted to cope with the addressed challenges: (1) reducing the dimensionality of the parameter space, (2) reducing the computational cost of the forward simulations, and (3) increasing the acceptance rate of the sampling algorithm (reducing the number of forward model calls required to infer the estimators of interest) (Frangos *et al.*, 2010). This article particularly focuses on the first approach, while the proposed prior setup stabilizes the inverse problem, such that an increased acceptance rate in Monte Carlo sampling is obtained.

A number of techniques have been developed based on reducing dimensionality of the model. As noted earlier, in a gridded parametrization of a spatial inverse problem, the dimensionality of the parameter space is basically tied to the dimensionality of the numerical discretization (Koutsourelakis, 2009). That is, if finite element method is used to discretize the equation of motion, the vector of unknowns is of same dimension as the number of elements. More efficient basis could be adopted, in case there is a knowledge of smoothness or specific structure in the material field. A popular means of reducing dimensionality of the unknown field is via Karhunen-Loeve (KL) expansion based on the random field prior.

This transforms the inverse problem to inference on a truncated sequence of weights of the KL modes (Marzouk & Najm, 2009). In a work by Li and Cripka (Li & Cirpka, 2006) KL expansion is employed in a geostatistical inverse problem adopted on an unstructured grid for the identification of transport parameters. In a number of articles (e.g. Effendiev et al (Efendiev *et al.*, 2006) and Mondal etal (Mondal *et al.*, 2010)) KL is used to parameterize the permeability field in a porous media model. The primary emphasis is on a two-stage MCMC scheme that utilizes upscale models and multi-scale data that poses constraints among the KL weights in order to match known values of the permeability at the specific locations. Higdon (Higdon, 2002) proposed another alternative to arrive at a lower dimensional representation of the field via a process convolution prior for the underlying image (given the filed is stationary Gaussian process).

If the variability of the parameter field is not smooth enough to be adequately described through a simple geostatistical model with a given variogram, different methods has been proposed. Cardiff and Kitanidis (Cardiff & Kitanidis, 2009) suggested a Bayesian level set inversion protocol framework for imaging of zoned parameter fields with abrupt changes (jumps) in the parameter values which reduces the problem to the estimation of "metaparameters" that control the shape and location of the geological facies. That is, the deformation of the level set function leads to evolution of the boundaries between zoned geologic units.

We opted for a relatively new choice of parametrization, based on Bayesian partition modeling (BPM) (Denison *et al.*, 2002a,b), which is especially suitable when dealing with earth models with sharp material interfaces. Partition modeling involves in discretizing the spatial/temporal random field into a number of disjoint regions, so-called Voronoi tessellations, where the number of tessellations and their geometry dynamically vary during the inversion to adapt to the structure and properties of the target model. Therefore, the number, geometry (shape, size and position), and the weight of the tessellations (describing the intensity of the parametric field of interest) are inversion parameters, directly determined by the data. The idea of treating the number of partitions (number of param-

eters) as a parameter itself is closely associated with probabilistic model selection, where a collection of models with varying number of parameters are presented for inversion, and the task is to select the model that most likely describes the experimental observations. The greatest advantage of treating an inverse problem as a Bayesian model selection is the notion of Bayesian parsimony, also known as "Occam's razor", stating that the simplest model consistent with the data should be favored over more complex models, and optimum complexity of the model must be inferred from the data. As a result, the smallest model (less parameters) that adequately describes the data is chosen, without sacrificing the accuracy of the recovered image. This capacity owes to the flexibility provided by the mobile number, size, shape and position of the Voronoi cells.

Reducing dimensionality of the parameter space means that regularizing the solution through global damping procedures (in deterministic optimization problems, e.g. (Na & Kallivokas, 2008; Epanomeritakis *et al.*, 2008; Tahvildari & Kaihatu, 2011)) or specific prior distributions which bears smoothness constraints (in a Bayesian inversion framework e.g. (Ulrych *et al.*, 2001; Dosso, 2002; Huang *et al.*, 2006)), is precluded.

A generalization of the simulation-based Markov Chain Monte Carlo methods, so called reversible jump (Green, 1995), is used to sample the posterior distribution of varying dimensionality. In this setting, the Markov chain is capable of undergoing dimension changes while moving among a number of candidate models. The key aspect of the reversible jump algorithm is the introduction of some auxiliary random variable to equalize the dimensionality of the parameter space across models. A series of one-to-one deterministic functions are defined to perform dimension matching such that the balance condition is satisfied. Balance condition is the necessary condition for a Markov chain to converge to the target density.

The varying dimensional (transdimensional) formulation in a 1D application was first introduced to the geophysics literature by Malinverno (Malinverno, 2002) in a DC resistivity sounding inversion, and later implemented in a number of geophysical probing inverse problems such as (Sambridge *et al.*, 2006; Dettmer *et al.*, 2010; Agostinetti & Malinverno,

2010; Minsley, 2011). Partition modeling in two dimensions has been used in Earth sciences with applications in geostatistics (Stephenson *et al.*, 2004), thermochronology (Stephenson *et al.*, 2006), paleoclimatology, climate variation reconstruction (Hopcroft *et al.*, 2007, 2009), transport in porous media and reservoir modeling (Efendiev *et al.*, 2011). These applications are substantially different from our development, in that, in all these previous studies, following the original work of Denison et.al (Denison & Holmes, 2001), the BPM is applied for fitting a surface throughout a set of spatially distributed observational data. That is, the Voronoi tessellations are utilised to partition the spatial data field, not the parameter/unknown model space. The former is a more standard application of BPM, as the geometry, concentration, and weight of the partitions are directly guided by the information carried by the spatially distributed data. Hence, the regions are defined such that the points nearby in the data space have the same distributions. Central to this approach is the ability to assign conjugate priors within the partitions, which significantly eases the posterior inference.

We propose partitioning the unknown velocity field (as a dimensionality reduction tool) in the absence of any direct observation of spatially distributed velocity values. Probably the closest development to this work is that of Bodin and Sambridge (Bodin & Sambridge, 2009) where they adopted the transdimensional framework in a seismic travel time tomography application. The work later extended to include the data noise as an unknown parameter (Bodin *et al.*, 2012). In their study, the use of BPM was motivated by heterogenous nature and uneven spatial distribution of data, such that cell concentration and the discretization resolution is led by intensity of seismic rays.

Motivated by the computationally intensive nature of the forward model (which strictly limits the number of calls to the forward solver), instead of a uniform prior model (as suggested in previous studies, e.g. (Bodin & Sambridge, 2009; Bodin *et al.*, 2012)), a proper Gaussian Markov Random field (GRMF) (Ferreira & Oliveira, 2007) prior is assigned within the disjoint regions, to alleviate the inherent ill-posedness and enhance the stability of the inverse problem. The GMRF model formalizes the correlation structure among the

tessellations, which implies that the measure of velocity at a particular cell depends only on the velocity value at the neighboring cells. We adopt a Hierarchical Bayes approach where intensity of the correlation (level of smoothness) is tuned by random variables to be inferred from the data. In a hierarchical approach, the lack of information on the parameters of the prior distribution is modeled by a second level of priors. This way, any subjective input through explicit regularization of the model parameters is avoided.

The numerical solution of the equations of motion is a key defining characteristic of full waveform inversion. The governing forward physics involves in propagation of 2D scaler (SH) waves travelling in the heterogeneous Earth, when the medium is probed by a stress load on the surface. In order to model the semi-infinite extent of the physical domain, a perfectly matched layer (PML) (Kang & Kallivokas, 2010*b*) is introduced at the truncation boundary to emulate the infiniteness of the Earth's structure. A displacement-stress mixed finite element scheme is used for numerical solution of PML-augmented wave PDE.

4.3 The Forward Model

In this section we introduce the forward wave propagation problem, originally appeared in (Kang & Kallivokas, 2010*b*). The forward model represents the mathematical relation which maps the parameter space (velocity field) into the predicted observation values (domain's displacement response to the prescribed source condition).

We are seeking to recover the spatial variation of soil elastic characteristics of a heterogenous unbounded medium, given a prescribed sequence of loading and the corresponding time history response registered at the ground level. The forward physics involves in propagation of 2D scaler (SH) waves travelling in the soil when the medium is probed by a stress load $p(t)$ on the surface.

A major challenge involved in radiation problems is to sufficiently model the open boundaries of the physical domain. Computational tools based on domain discretization require the unbounded domain be reduced to finite. Hence, the physical domain must be truncated at some distance from the source. If the truncated interface simply fixed or insufficiently modeled, the outgoing radiations reflect back to the computational domain

and contaminate the solution, which in turn affect the viability of the inverted image.

To avoid spurious reflections caused by the truncation, a so called Perfectly-Matched-Layer (PML) buffer zone is enforced at the edge of the computational domain that absorbs the incident radiation with ideally no reflection into the domain. The introduced boundary enforces the rapid attenuation of the wave motion within the absorbing layer. The PML has been widely used among other numerical radiation boundary conditions, since it has proved excellent absorbtion over a wide range of incident angles and not particularly sensitive to the shape of the wave front and the frequency of the excitation (Basu & Chopra, 2003, 2004).

Two dimensional scalar wave equation over a heterogenous un-bounded Earth is

$$\nabla.\left(\mu\nabla u\right)=\rho\frac{\partial^2 u}{\partial t^2} \tag{4.1}$$

where $u(\mathbf{x},t)$ is anti-plane displacement, $\mu(\mathbf{x})$ is the shear modulus, and $\rho(\mathbf{x})$ is the soil density. Numerical solution of equation 4.1 is obtained by truncating the semi-infinite domain, and surrounding the finite computational domain by PML slabs, as illustrated in figure 4.1. The full derivation of the governing wave equation in a PML-truncated domain can be found in the original work (Kang & Kallivokas, 2010*b*), also briefly included here for the sake of completeness.

The construction of PML is based on the concept of physical coordinate stretching, such that the space in the absorbing layer is stretched by a complex function, and attenuation of motion is enforced within the PML. This leads the transient propagating waves to exponentially decay as they enter the PML zone. The stretched coordinates are defined as

$$\tilde{x}_j=\int_0^{x_j}\left[\left\{1+f_j^e\left(s\right)\right\}-i\frac{f_j^p\left(s\right)}{a_0}\right]\mathrm{d}s,\quad j=1,2. \tag{4.2}$$

where $a_0=k_s b$ is the non-dimensional frequency and b is the characteristic length of the system. $k_s=\omega/c_s$ is the wave number, with $c_s=\sqrt{\mu/\rho}$ denoting the phase velocity of the wave. f_j^p and f_j^e are the attenuation functions, which serve to decay propagating and

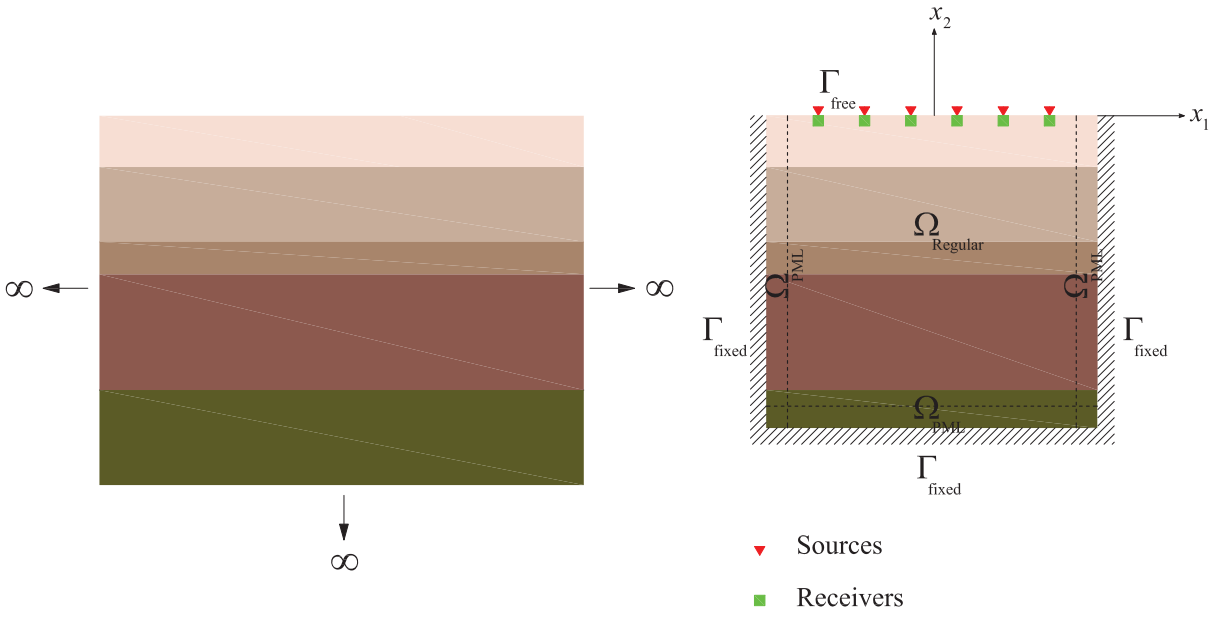

Figure 4.1: Benchmark soil velocity profile

evanescent waves, respectively, along $(x_j, \ \ j = 1, 2)$ directions, and are defined as follows

$$f_j^{p,e}(\mathbf{x}) = \begin{cases} 0, & |x_j| < |x_j^{\text{itf}}| \\ \frac{3b}{2L_j^{\text{PML}}} \log\left(\frac{1}{|R|}\right) \left(\frac{x_j - x_j^{\text{itf}}}{L_j^{\text{PML}}}\right)^2, & |x_j| \geq |x_j^{\text{itf}}| \end{cases}; \quad j = 1, 2. \tag{4.3}$$

which suggests a positive attenuation within the PML, and zero value in the regular domain. L_j^{PML} and x_j^{itf} are thickness of the PML and coordinate of the PML-regular domain interface in x_j direction, as shown in figure 4.2. R denotes the reflection coefficient which tunes the amount of reflection from the edge of the fixed boundary into the regular domain. By virtue of equations 4.2 and 4.3, the stretched and the original coordinates match at the regular domain-PML boundary which ensures no reflection of the outgoing waves occurs at the edge of the absorber.

The governing 2D scalar wave equation within a PML truncated domain is given by:

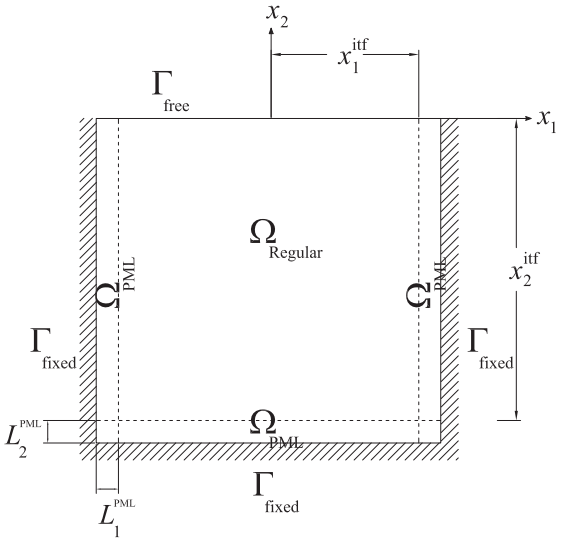

Figure 4.2: Schematic of a 2D computational domain surrounded by a PML absorbing boundary

$$f_m\ddot{v} + c_s g_c \dot{v} + c_s^2 g_k v - \nabla.\left(\tilde{\mathbf{F}}^e \dot{\mathbf{s}} + \tilde{\mathbf{F}}^p \mathbf{s}\right) = 0, \tag{4.4a}$$

$$\mathbf{F}^e \ddot{\mathbf{s}} + \mathbf{F}^p \dot{\mathbf{s}} - c_s^2 \nabla \dot{v} = 0, \tag{4.4b}$$

$$\text{in } \Omega \times (0, T],$$

subject to

$$v(\mathbf{x}, t) = 0 \qquad \text{on } \Gamma_{\text{fixed}} \times (0, T], \tag{4.5a}$$

$$\dot{s}_2(\mathbf{x}, t) = p(\mathbf{x}, t) \qquad \text{on } \Gamma_{\text{free}} \times (0, T], \tag{4.5b}$$

$$v(\mathbf{x}, 0) = 0 \qquad \text{on } \Omega, \tag{4.5c}$$

$$\dot{v}(\mathbf{x}, 0) = 0 \qquad \text{on } \Omega, \tag{4.5d}$$

$$\mathbf{s}(\mathbf{x}, 0) = 0 \qquad \text{on } \Omega, \tag{4.5e}$$

$$\dot{\mathbf{s}}(\mathbf{x}, 0) = 0 \qquad \text{on } \Omega. \tag{4.5f}$$

$v(\mathbf{x},t)=\rho u(\mathbf{x},t)$ is normalized displacement with respect to the material's density with u being the anti-plane displacement. $\mathbf{x}$ and t denote location and time, respectively. $\mathbf{s}(\mathbf{x},t)$ is stress memories and is given by:

$$\mathbf{s}(\mathbf{x},t)=\int_0^t \boldsymbol{\sigma}(\mathbf{x},\tau)\,\mathrm{d}\tau \tag{4.6}$$

where $\mathbf{s}=[s_1 \;\; s_2]^T$. Hence

$$\dot{\mathbf{s}}(\mathbf{x},t)=\boldsymbol{\sigma}(\mathbf{x},t), \tag{4.7a}$$

$$\ddot{\mathbf{s}}(\mathbf{x},t)=\dot{\boldsymbol{\sigma}}(\mathbf{x},t). \tag{4.7b}$$

$\boldsymbol{\sigma}=[\sigma_{31},\sigma_{32}]$ is the vector of shear stress components. f_m, g_c and g_k are PML attenuation functions, given by

$$f_m=[1+f_1^e][1+f_2^e], \tag{4.8a}$$

$$g_c=g_2^p[1+f_1^e]\,g_1^p[1+f_2^e], \tag{4.8b}$$

$$g_k=g_1^p g_2^p. \tag{4.8c}$$

where $g_1^p=f_1^p/b$ and $g_2^p=f_2^p/b$ are normalized attenuation functions. $\tilde{\mathbf{F}}^e$, $\tilde{\mathbf{F}}^p$, $\mathbf{F}^e$, and $\mathbf{F}^p$ are stretch tensors given by

$$\tilde{\mathbf{F}}^e = \begin{bmatrix} 1+f_2^e & 0 \\ 0 & 1+f_1^e \end{bmatrix}, \tag{4.9a}$$

$$\tilde{\mathbf{F}}^p = \begin{bmatrix} c_s g_2^p & 0 \\ 0 & c_s g_1^p \end{bmatrix}, \tag{4.9b}$$

$$\mathbf{F}^e = \begin{bmatrix} 1+f_1^e & 0 \\ 0 & 1+f_2^e \end{bmatrix}, \tag{4.9c}$$

$$\mathbf{F}^p = \begin{bmatrix} c_s g_1^p & 0 \\ 0 & c_s g_2^p \end{bmatrix}. \tag{4.9d}$$

Equations 4.4 present the mixed displacement (v) -stress memory ($\mathbf{s}$) equations governing the propagation of the SH waves in the PML-truncated domain.

4.4 Methodology

We are seeking to recover the heterogeneous shear wave velocity profile c_s (appeared in equation 4.4) within the PML-truncated domain. This involves solution of an inverse medium problem, described as the task of inferring the spatial variability of a physical characteristic of the medium from limited and noisy measurements/observations. The uncertainty stemming from lack of data, its random nature and the model error (i.e. the discrepancy between the true process from which the data is generated and the theory approximating the reality, so-called the forward model) renders point estimates of limited use. Moreover, it is essential to built the confidence intervals for the generated estimates which quantify the inferential uncertainties about the unknowns. Most importantly, the predictive ability of the retrieved model must be assessed. We adopt a Bayesian perspective to inference, in which the model unknowns are treated as random variables. As a result, the solution to the inverse problem is not point estimates but probability density/mass functions. Furthermore, Bayesian approach sets out as a way to facilitate the integration

of geo-evidence, since it allows for a translation of information content (observational, theoretical, experts judgment) in form of a probability function (Tarantola, 2005).

4.4.1 Hierarchical Bayesian Inverse Modeling

Consider a n dimensional vector of observable quantities-data $\mathbf{d}_{\text{obs}}$ and a k dimensional vector of model parameters-inputs $\boldsymbol{\theta}$, both assumed to be real valued and finite-dimensional, and $\mathbf{G}$ being the forward model, mapping $\boldsymbol{\theta}$ into $\mathbf{d}_{\text{obs}}$. Here, $\mathbf{G}$ is the discretized version of the initial boundary value problem presented in equations 4.4 and 4.5. The following relationship holds:

$$\mathbf{d}_{\text{obs}} = \mathbf{G}\left(\boldsymbol{\theta}\right) + \boldsymbol{\epsilon} \tag{4.10}$$

where $\boldsymbol{\epsilon}$ is the random error component which quantifies the deviation between model prediction and measurements. This random term encompass both theoretical and measurement errors (assuming the forward model is an unbiased estimate to the true physical process). Explicit distinction, however, could be made between model and observational errors in a full uncertainty quantification framework (UQ) (Medina-Cetina, 2006).

In a Bayesian approach to inverse problems, a prior distribution $p\left(\boldsymbol{\theta}\right)$ is incorporated in estimating each model unknown, which quantifies the initial uncertainty about the parameter. Ideally, this density limits the space of plausible parameters by giving higher probability to those which can help to describe the system's response more accurately. The objective of the inversion is to sample the posterior distribution $p\left(\boldsymbol{\theta}|\mathbf{d}_{\text{obs}}\right)$, built to fully describe the model parameters in terms of a density function, given the data $\mathbf{d}_{\text{obs}}$ is observed. According to Bayes theorem

$$p\left(\boldsymbol{\theta}|\mathbf{d}_{\text{obs}}\right) = \frac{p\left(\mathbf{d}_{\text{obs}}|\boldsymbol{\theta}\right)p\left(\boldsymbol{\theta}\right)}{\int_{\boldsymbol{\Theta}} p\left(\mathbf{d}_{\text{obs}}|\boldsymbol{\theta}\right)p\left(\boldsymbol{\theta}\right)\ \mathrm{d}\boldsymbol{\theta}} \tag{4.11}$$

The likelihood function $p\left(\mathbf{d}_{\text{obs}}|\boldsymbol{\theta}\right)$ is the conditional probability that the observed realization $\mathbf{d}_{\text{obs}}$ is produced by model $\boldsymbol{\theta}$. Given the errors ϵ_i are identically distributed Gaussian random variables with mean zero and covariance matrix $\mathbf{C}_d$, (i.e., $\boldsymbol{\epsilon} \sim \mathcal{N}\left(\mathbf{0}, \mathbf{C}_d\right)$), the

likelihood function is found with reference to a multivariate normal density

$$p\left(\mathbf{d}_{\text{obs}}|\boldsymbol{\theta}\right)=\frac{1}{\left[(2\pi)^{n}|\mathbf{C}_{d}|\right]^{1/2}}\exp\left[-\frac{1}{2}\left(\mathbf{G}\left(\boldsymbol{\theta}\right)-\mathbf{d}_{\text{obs}}\right)^{T}\mathbf{C}_{d}^{-1}\left(\mathbf{G}\left(\boldsymbol{\theta}\right)-\mathbf{d}_{\text{obs}}\right)\right] \tag{4.12}$$

where n is the number of observations and $\mathbf{C}_d$ is the covariance of the error term. The quantity in the denominator of equation 4.11 (the probability of observing the data $\mathbf{d}_{\text{obs}}$) is a normalizing constant, such that the posterior is integrated to one. If further assumption is made such that random error components $\boldsymbol{\epsilon}=\left(\epsilon_1,\ldots,\epsilon_n\right)^T$ are $\boldsymbol{\epsilon}\overset{iid}{\sim}\mathcal{N}\left(\mathbf{0},\sigma_d^2\mathbf{I}_n\right)$, the likelihood function will be reduced to the following form

$$p\left(\mathbf{d}_{\text{obs}}|\boldsymbol{\theta}\right)=\frac{1}{\sigma_d^n}\exp\left\{\frac{\|\mathbf{d}_{\text{obs}}-\mathbf{G}\left(\boldsymbol{\theta}\right)\|^2}{2\sigma_d^2}\right\} \tag{4.13}$$

where $\mathbf{I}_n$ is an $n\times n$ identity matrix and $\|\mathbf{d}_{\text{obs}}-\mathbf{G}\left(\boldsymbol{\theta}\right)\|^2=\sum_{i=1}^{n}\left(d_{\text{obs}_i}-\mathbf{G}\left(\boldsymbol{\theta}\right)\right)^2$. If there is a knowledge of spatial dependence between the data points (due to specific events such as sensor miscalculation), these could naturally be incorporated in formulating the likelihood. The level of data uncertainty is difficult to quantify a-priori, therefore, the noise variance σ_d is considered a random variable being inferred from the data. By assigning a conjugate Gamma prior for σ_d^{-2} (i.e., $\sigma_d^{-2}\sim\mathcal{G}a\left(\delta_d,\eta_d\right)$) we are able to integrate out the variance term from equation 4.13 which leads to the following simplified expression for the likelihood:

$$p\left(\mathbf{d}_{\text{obs}}|\boldsymbol{\theta}\right)\propto\frac{\Gamma\left(\delta_d+n/2\right)}{\left(\eta_d+\frac{1}{2}\|\mathbf{d}_{\text{obs}}-\mathbf{G}\left(\boldsymbol{\theta}\right)\|^2\right)^{\delta_d+n/2}} \tag{4.14}$$

where $\Gamma\left(.\right)$ is the Gamma function. It is also of interest to determine σ_d whether as an estimator of the data uncertainty, as a type of measure of validity of the forward model or for predictive purposes. The posterior for σ_d, $p\left(\sigma_d^{-2}|\boldsymbol{\theta},\mathbf{d}_{\text{obs}}\right)$, will also be Gamma, due to the conjugate specification, with the following updated parameters

$$p\left(\sigma_d^{-2}|\boldsymbol{\theta}, \mathbf{d}_{\text{obs}}\right) = \mathcal{G}a\left(\delta_d + \frac{n}{2}, \delta_d + \frac{1}{2}\|\mathbf{d}_{\text{obs}} - \mathbf{G}\left(\boldsymbol{\theta}\right)\|^2\right) \tag{4.15}$$

A Monte Carlo method will be used to draw samples of $\boldsymbol{\theta}$ from $p\left(\boldsymbol{\theta}|\mathbf{d}_{\text{obs}}\right)$. Once a samples of $\boldsymbol{\theta}$ collected the above equation could be applied to directly generate samples of σ_d.

4.4.2 Velocity Field Parameterization Using Voronoi Tessellations

The velocity field comprise a continuous infinite dimensional function of spatial coordinate: $c_s\left(\mathbf{x}\right)$. This infinite dimensional stochastic field can be adequately described by a certain collocation points $\mathbf{x}_i$ to render the parameter space finite. In a regular treatment of an inverse medium problem (grid-based inversion), the pointwise value of $\mathbf{c}_s\left(\mathbf{x}\right)$ is explored at each of the N discretized blocks with a Monte Carlo search. This proves computationally exhaustive (practically infeasible) task, and explicit regularization of the solution is required.

Here, we opted for a mobile irregular type of discretization. We partition the velocity field into a number of disjoint regions through a set of Voronoi tessellations. Given a set of k nuclei (center) with spatial coordinates denoted by $\{\mathbf{x}_{c_1}, \ldots, \mathbf{x}_{c_k}\}$ where $\mathbf{x}_{c_i} \in \mathbb{R}^2$, the Voronoi tessellations (also referred to as Dirichlet tessellations) define k non-overlapping regions denoted by $\{\mathcal{R}_1, \ldots, \mathcal{R}_k\}$, where all the points nearest to $\mathbf{x}_{c_i}$ belongs to region $\mathcal{R}_i$ so that

$$\mathcal{R}_i = \{\mathbf{x} \in \mathbb{R}^2 : \|\mathbf{x} - \mathbf{x}_{c_i}\| < \|\mathbf{x} - \mathbf{x}_{c_j}\| \text{ for all } j \neq i\}$$

where $\|.\|$ denotes Euclidian distance defined for all points $\mathbf{x} \in \mathbb{R}^2$. Boundaries between the tessellations are defined by straight lines. The splits are defined only via the coordinates of its nucleus, and a constant weight denoting the shear wave velocity for the region. For a velocity field described by a Voronoi diagram the following expression holds:

$$\mathbf{c}_s(\mathbf{x}) = \sum_{i=1}^{k} I_{\mathcal{R}_i}(\mathbf{x})\ c_{s_i} \tag{4.16}$$

where $I_{\mathcal{R}}(\mathbf{x})$ is an indicator function of the tessellation region $\mathcal{R}$, which assumes $I_{\mathcal{R}}(\mathbf{x}) = 1$ if $\mathbf{x} \in \mathcal{R}$ and $I_{\mathcal{R}}(\mathbf{x}) = 0$ otherwise. This representation basically states that $\mathbf{c}_s(\mathbf{x})$ made up of a linear combination of constant basis functions $\mathbf{I}_{\mathcal{R}}$ with the corresponding coefficients $(c_{s_1}, \ldots, c_{s_k})$ denoting the velocities of the k cells. Within each tessellation region the velocity field is assumed to be constant. Higher order polynomials (a linear, quadratic, etc.) can be assumed at the cost of added complexity and computational burden, as this requires additional unknowns for each partition. Figure 4.3 shows an example of a Voronoi diagram where partitions $\mathcal{R}_1$ and $\mathcal{R}_2$ are characterized by their nuclei $\mathbf{x}_{c_1}$ and $\mathbf{x}_{c_2}$. The number of unknowns, therefore, reduces to $2k$ (k discrete parameters describing the coordinates of the nuclei in the plane plus k velocity values assigned to each partition). As the inversion proceeds, the number of partitions, their geometry, and the corresponding velocities varies dynamically to adapt the shape and physical properties of the subsurface features with possibly sharp boundaries between geologic units.

4.4.3 The Choice of Priors

The first step in Bayesian inverse modeling is to formulate a prior distribution for each participating parameter. That is, formalizing any information about the model's variables, available through expert's judgement, historical evidence or prior beliefs by choosing functional forms of probability and estimating the parameters of the prior density. In this section we give a brief summary of the Gaussian Markov random field (GMRF) as a standard model used to describe spatial fields. GMRFs have widely been adopted to model sampling distribution of spatial data involved in variety of applications such as image precessing, (blur and noise removal, detection of boundaries of an object), remote sensing and disease mapping (Besag *et al.*, 1991; Cressie & Chan, 1989). GMRFs have been also used to formalize the prior beliefs about the (unknown) structure of a spatially varying random field, as appears in an inverse problem. The latter application is the focus of this section.

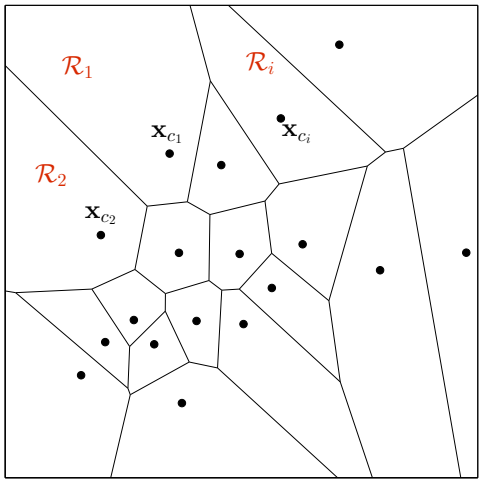

Figure 4.3: An example of Voronoi tessellation formed about 18 pseudo random points on the plane populated from a bivariate normal density. The boundary of two neighboring tessellations is the perpendicular bisector of the line connecting their nuclei.

We choose to model the log-velocity field to ensure the inferred velocity is a positive valued field, where the log-velocity field is decomposed into a number of subregions represented by a Voronoi cell. A GMRF model is used to formalize the correlation structure among the tessellations, implying that the measure of velocity at a particular cell depends only on the velocity value at the neighboring cells.

Typically, Markov random fields are defined over a regular lattice, where the specification of the neighboring system is rather standard. In our application there is an added difficulty associated with the irregular areal units. Again, consider the Voronoi diagram partitioned the unknown field composed of k tessellations indexed $1, \ldots, k$ in a domain of interest Ω_{Regular}. We assume the neighborhood set N_i of partition i is constituted by its immediately adjacent cells sharing a common border with i. More extended neighborhood structures are possible depending on the specifics of the problem and user choices. Figure 4.4 depicts the presentation of the neighborhood system for a given region. Having denoted the log-velocity measures corresponding to the spatial locations $\mathbf{x}_c = \{x_{c_i}\}_{i=1}^{k}$ by

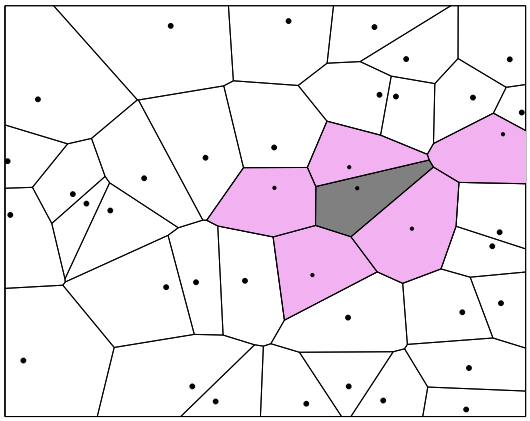

Figure 4.4: Definition of the neighborhood set for a given tessellation: In a Markov Random field the distribution of the spatial process at a given location depends only on the attributes of the process at the neighboring cells

$\mathbf{c}_s = \{c_{s_i}\}_{i=1}^{k}$, a proper Gaussian Markov random field prior model for $\mathbf{c}_s$ is defined by the joint distribution (Ferreira & Oliveira, 2007)

$$p\left(\mathbf{c}_s | c_{s_0}, k, \tau, \phi\right) \sim \mathcal{N}_k\left(c_{s_0}\mathbf{1}_k, \tau^{-1}\Sigma_\phi\right) \tag{4.17}$$

Vector $\mathbf{x}_c$ holds the coordinates of the cells nuclei. c_{s_0} is a location parameter. Naturally, any prior information on the mean of the velocity random field could be incorporated in this parameter. $\mathbf{1}_k$ is a k-dimensional vector of ones, and $\tau > 0$ ia a scale parameter. $\Sigma_\phi^{-1} = (\phi\mathbf{I}_k + \mathbf{H})$, where $\mathbf{I}_k$ is a $k \times k$ identity matrix. $\phi \geq 0$ is a spatial parameter which controls the measure of correspondence between velocities of different partitions (Ferreira & Lee, 2007), and controls the smoothness of process $\mathbf{c}_s$.

$\mathbf{H}$ is defined as follows

$$H_{ji} = \begin{cases} h_i & j = i, \\ -g_{ji} & j \in N_i, \\ 0 & \text{otherwise}, \end{cases} \tag{4.18}$$

where $g_{ji} = g_{ij}$ is a positive scalar denoting the measure of similarity between regions j and i. N_i is the collection of tessellations j comprising the neighborhood set of region i, and $h_i = \sum_{j \in N_i} g_{ji}$. Here, g_{ji} is assumed to be one. Equation 4.18 indicates that a diagonal elements H_{ii} equals the number of neighbors of cell i, and an off-diagonal element H_{ij} is -1 if i and j are neighbors and zero otherwise.

A familiar reader may realize that as ϕ approaches zero, the GMRF model of equation 4.17 reduces to a so called intrinsic Gaussian Markov random field (IGMRF): $\mathcal{N}_k \left(c_{s_0} \mathbf{1}_k, \tau^{-1} \mathbf{H}^{-1} \right)$ (Besag *et al.*, 1991). This type is very popular prior for spatial fields, however their use is rather delicate for a varying dimensional problem. $\mathbf{H}$ is a rank deficient matrix, therefore, not positive definite. Hence, an IGMRF prior density is improper (priors which are not integrable or their constant of proportionality is unknown). The use of improper priors for varying dimensional inverse problems and Bayesian model selection is restricted as this may result in an identifiability issue. An interested reader is referred to (Bilancia *et al.*, 2013) for more details. Further details on Bayesian model selection and unidentifiable Bayes factor is provided in appendix E.

On the other hand as ϕ grows very large, model of equation 4.17 reduces to a simple Gaussian process with constant covariance structure, stating that the component of $\mathbf{c}_s = \{c_{s_i}\}_{i=1}^k$ are independent random variables with mean c_{s_0} and constant variance τ^{-1}.

τ and ϕ appeared in equation 4.17 are random variables. We propose a Gamma prior for the both variables:

$$p\left(\tau | \delta_\tau, \eta_\tau\right) \sim \mathcal{G}a\left(\delta_\tau, \eta_\tau\right) = \frac{\eta_\tau^{\delta_\tau}}{\Gamma\left(\delta_\tau\right)} \tau^{\delta_\tau - 1} \exp\left(-\eta_\tau \tau\right) \tag{4.19}$$

and

$$p\left(\phi|\delta_\phi,\eta_\phi\right)\sim\mathcal{G}a\left(\delta_\phi,\eta_\phi\right) \tag{4.20}$$

To allow for higher flexibility and robustness of the inference, we avoid fixing the hyper-parameters of the Gamma densities $\delta_\tau,\eta_\tau,\delta_\phi,\eta_\phi$. Thus, another level of hierarchy is added by introducing hyper-priors to these parameters. Consider the Gamma prior appeared in equation 4.19. In order to avoid any subjective inputs to the inference, mean of the Gamma density is assumed to be a random variable. The quantity $\mu_\tau=\eta_\tau/\delta_\tau$ is defined where μ_τ is a location parameters to which an exponential prior is assigned such that $p\left(\mu_\tau|a_{\mu_\tau}\right)=\frac{1}{a_{\mu_\tau}}\exp\left(-\mu_\tau/a_{\mu_\tau}\right)$. The hyper-parameter of the exponential density a_{μ_τ} could be chosen to be a very small value ($a_{\mu_\tau}=10^{-4}$) to constitute a non-informative density. Noting that $p\left(\tau,\mu_\tau|\delta_\tau,a_{\mu_\tau}\right)\propto p\left(\tau|\mu_\tau,\delta_\tau\right)p\left(\mu_\tau|a_{\mu_\tau}\right)$, integrating out μ_τ from the joint density in the left hand side of the latter proportionality leads to the following prior

$$p\left(\tau|\delta_\tau,a_{\mu_\tau}\right)=\frac{\Gamma\left(\delta_\tau+1\right)}{\Gamma\left(\delta_\tau\right)}\delta_\tau^{\delta_\tau}\frac{\tau^{(\delta_\tau-1)}}{a_{\mu_\tau}\left(\delta_\tau\tau+a_{\mu_\tau}^{-1}\right)^{(\delta_\tau+1)}} \tag{4.21}$$

If similar derivation repeated considering equation 4.20 one could obtain

$$p\left(\phi|\delta_\phi,a_{\mu_\phi}\right)=\frac{\Gamma\left(\delta_\phi+1\right)}{\Gamma\left(\delta_\phi\right)}\delta_\phi^{\delta_\phi}\frac{\phi^{\left(\delta_\phi-1\right)}}{a_{\mu_\phi}\left(\delta_\phi\phi+a_{\mu_\phi}^{-1}\right)^{\left(\delta_\phi+1\right)}} \tag{4.22}$$

$\mathbf{x}_c$ is the position vector of the k Voronoi nuclei. We wish to specify an non-informative prior for $\mathbf{x}_c$. An underlying grid is defined which coincides with the finite element discretization of the physical domain. Having k Voronoi cells, and N elements in the regular domain Ω_{Regular}, there are $\binom{N}{k}=\frac{N!}{k!(N-k)!}$ possible configurations to position the Voronoi nuclei. Given that any of these configurations is equally likely, the discrete uniform prior for the nuclei positions is obtained

$$p\left(\mathbf{x}_c|k\right)\propto\binom{N}{k}^{-1} \tag{4.23}$$

A prior of the above form does not place an explicit penalty on the model complexity.

However, as stated earlier, the marginal likelihood contains a built-in penalty on the model dimension, which strongly depends on the prior variance $\tau^{-1}\Sigma_\phi$ of the coefficients $\mathbf{c}_s$.

An assumption that significantly contributes to the expressivity and flexibility of the model to recover the shape and structure of subsurface formations is that the size of the model (number of tessellations) could vary. Having assumed that this number is unknown a priori, in the absence of any specific information concerning the optimum number of cells, a hierarchical truncated Poisson prior is proposed for $k|\lambda$:

$$p\left(k|\lambda\right) = \frac{e^{-\lambda}\lambda^k}{k!\left(1-e^{-\lambda}\right)} \qquad k = 1, \ldots, K \tag{4.24}$$

The truncation term K is the maximum allowable number of cells which could simply set equal to the number of regular domain elements. This setting controls the prior weights given to over-parameterized models, while avoiding to subjectively regularize the solution by freeing λ. λ is a hyperparameter to be elicited from the data. An exponential hyper-prior is used for λ:

$$p\left(\lambda|\delta_\lambda, \eta_\lambda\right) \sim \mathcal{G}a\left(\delta_\lambda, \eta_\lambda\right) \tag{4.25}$$

Hyper-parameters $\delta_\lambda, \eta_\lambda$ could be chosen such that the above prior becomes flat ($\delta_\lambda = \eta_\lambda = 0.01$). The overall prior for the model becomes:

$$\begin{aligned} p\left(\boldsymbol{\theta}, k\right) &= p\left(k, \mathbf{c}_s, \mathbf{x}_c, \lambda, \tau, \phi\right) = p\left(k, \{c_{s_i}\}_{i=1}^k, \{x_{c_i}\}_{i=1}^k, \lambda, \tau, \phi\right) \\ &= p\left(k|\lambda\right) p\left(\lambda|\delta_\lambda, \eta_\lambda\right) p\left(\mathbf{c}_s|k, c_{s_0}, \tau, \phi\right) p\left(\tau|\delta_\tau, a_{\mu_\tau}\right) p\left(\phi|\delta_\phi, a_{\mu_\phi}\right) p\left(\mathbf{x}_c|k\right) \end{aligned} \tag{4.26}$$

The components of the above equation are given in equations 4.17 and 4.21-4.25. The posterior kernel, therefore, is given by

$$p\left(\boldsymbol{\theta}, k|\mathbf{d}_{\text{obs}}\right) \propto p\left(\boldsymbol{\theta}, k\right) p\left(\mathbf{d}_{\text{obs}}|\boldsymbol{\theta}\right) \tag{4.27}$$

where $p(\mathbf{d}_{\text{obs}}|\boldsymbol{\theta})$ is defined in equation 4.14.

4.4.4 Bayesian Computation

Bayesian inference relies on the ability to estimate probabilities and statistical quantities associated with the posterior distribution. The posterior distribution derived above (equation 4.27) is known up to a proportionality constant which cannot be expressed in a convenient analytical form. Monte Carlo methods provide essentially the only accurate mean of inferring the posterior which does not depend on the knowledge of the proportionality. Markov Chain Monte Carlo (MCMC) is an iterative stochastic method, designed to generate samples from the posterior kernel. The methods consist of generating Markov chain according to the transition function which asymptotically converges to the target as the sample size grows. A sequence of models generates the Markov chain where each model is a perturbation of the last. The perturbations are proposed according to an easy-to-sample proposal distribution, and are accepted or rejected in accordance with a prescribed criteria such as Metropolis Hastings scheme (see for example (Sivia, 1996)). The sampling is continued until specific convergence conditions are met (Cowles & Carlin, 1996).

Although theoretical convergence is assured under weak condition (Liu, 2001), slow chain mixing and lack of convergence often arise in high dimensional, highly correlated, multi-modal target density configurations. As a result exuberant number of likelihood computation and hence repeated forward simulation is required. This might render the inference impractical, especially when dealing with large scale forward solvers.

In this work there is an added difficulty related to the varying dimensionality of the target distribution, that is the dimension of the model space is unknown depending on the number of Voronoi cells k. We opted a generalization of MCMC, so-called the Reversible Jump MCMC (RJMCMC) framework introduced by Green (Green, 1995), which is utilized to move Markov chains among different dimensions. The key aspect of the reversible jump algorithm is the introduction of some auxiliary random variable to equalize the dimensionality of the parameter space across models. A series of one-to-one deterministic functions are defined to perform dimension matching such that the balance condition is satisfied.

Balance condition is the necessary condition for a Markov chain to converge to the target density. A detailed introduction to geophysical transdimensional Bayesian inversion can be found in Sambridge et al. (Sambridge *et al.*, 2013).

Suppose, $p(\boldsymbol{\theta}, k) \propto p(\boldsymbol{\theta}|k)\, p(k)$ is the target distribution up to a proportionality constant, where $k \in \mathfrak{K} = \{1, \ldots, K\}$ and $\boldsymbol{\theta} \in \boldsymbol{\Theta}_k$ ($\boldsymbol{\Theta}_k$ denoting the parameter space of the k dimensional model), and K is a finite integer. In a transdimensional configuration, k is also an unknown which denotes the dimension of vector of parameters $\boldsymbol{\theta}$. Hence, the support of the target density $p(\boldsymbol{\theta}, k)$ lies on $\cup_{k=1}^{K}\{k\} \times \boldsymbol{\Theta}_k$.

We seek to construct a reversible Markov chain $\{(\boldsymbol{\theta}, k)_n\}$ which has a stationary distribution $p(\boldsymbol{\theta}, k)$. At the (s)th iteration the chain state is $(\boldsymbol{\theta}^{(s)}, k^{(s)})$. Two proposals are needed to traverse the posterior surface when a dimension change is involved: one to move from $\boldsymbol{\Theta}_{k^{(s)}} \rightarrow \boldsymbol{\Theta}_{k^*}$ another for $\boldsymbol{\Theta}_{k^*} \rightarrow \boldsymbol{\Theta}_{k^{(s)}}$. That is, any transit from current state of the chain $\boldsymbol{\Theta}_{k^{(s)}}$ to the candidate space $\boldsymbol{\Theta}_{k^*}$ must have a degenerate density for the reverse move from $\boldsymbol{\Theta}_{k^*}$ to $\boldsymbol{\Theta}_{k^{(s)}}$. A new model of (possibly different) dimension k^* is proposed with probability $q(k^*|k^{(s)}) = q_{k^{(s)},k^*}$, where $\sum_{k^* \in \mathfrak{K}} q_{k^{(s)},k^*} = 1$. The basis of Green's idea (Green, 1995) is to supplement each of $\boldsymbol{\Theta}_{k^{(s)}}$ and $\boldsymbol{\Theta}_{k^*}$ with adequate artificial spaces in order to create a bijection between them.

Suppose a proposal from $(k^{(s)}, \boldsymbol{\theta}^{(s)})$ to $(k^*, \boldsymbol{\theta}^*)$ that increases the dimension by one ($\boldsymbol{\Theta}_{k^{(s)}}$ is nested within $\boldsymbol{\Theta}_{k^*}$; $k^* = k^{(s)} + 1$), and $q_{k^{(s)},k^*}$ the probability that such candidate is proposed, and $q_{k^*,k^{(s)}}$ probability that the reverse candidate is proposed. In order to account for $d_{k^{(s)},k^*} = \dim(\boldsymbol{\Theta}_{k^*}) - \dim(\boldsymbol{\Theta}_{k^{(s)}})$ dimension difference, $\boldsymbol{\theta}^{(s)}$ is augmented with $d_{k^{(s)},k^*}$ dimensional auxiliary variable $\mathbf{u}$ drawn form a proposal distribution $\psi(\mathbf{u})$. The new state of the chain $\boldsymbol{\theta}^*$ is found from the transformation $\mathcal{T}$ such that $\boldsymbol{\theta}^* = \mathcal{T}_{k^{(s)},k^*}(\boldsymbol{\theta}^{(s)}, \mathbf{u})$. $\mathcal{T}_{k^{(s)},k^*}$ is a deterministic mapping, so called dimension matching transformation such that $\mathcal{T}_{k^{(s)},k^*} : \mathbb{R}^{k^{(s)}+d_{k^{(s)},k^*}} \rightarrow \mathbb{R}^{k^*}$, where $\mathbb{R}^{k^*}$ denotes the proposed parameter space of k^* dimension. This transformation ensures that the detailed balance condition maintains (Mondal *et al.*, 2010).

The proposed state $(\boldsymbol{\theta}^*, k^*)$ is accepted with probability

$$r = \min\left\{1, \frac{p(\boldsymbol{\theta}^*, k^*)}{p(\boldsymbol{\theta}^{(s)}, k^{(s)})} \frac{q_{k^*,k^{(s)}}}{q_{k^{(s)},k^*}} \frac{1}{\psi(\mathbf{u})} \left| \frac{\partial \boldsymbol{\theta}^*}{\partial(\boldsymbol{\theta}^{(s)}, \mathbf{u})} \right| \right\} \tag{4.28}$$

where $\left|\frac{\partial \boldsymbol{\theta}^*}{\partial(\boldsymbol{\theta}^{(s)},\mathbf{u})}\right|$ is the Jacobian of the dimension matching transformation $\mathcal{T}$. This states that the new state of the chain is $(\boldsymbol{\theta}^*, k^*)$ with probability r, or $(\boldsymbol{\theta}^{(s)}, k^{(s)})$ with the complement probability $1 - r$. Similarly, the acceptance ratio of the reverse move, which involves lowering the dimension, is defined below

$$r = \min\left\{1, \frac{p(\boldsymbol{\theta}^{(s)}, k^{(s)})}{p(\boldsymbol{\theta}^*, k^*)} \frac{q_{k^{(s)},k^*}}{q_{k^*,k^{(s)}}} \psi(\mathbf{u}) \left| \frac{\partial \boldsymbol{\theta}^*}{\partial(\boldsymbol{\theta}^{(s)}, \mathbf{u})} \right|^{-1} \right\} \tag{4.29}$$

The algorithm can be completed with additional steps within a given space $\boldsymbol{\Theta}_k$, or about hyperparameters that are not model dependent, which is the case for our hierarchical Bayes model implementation. We implement the preceding algorithm to reconstruct the spatial distribution of the shear wave velocity random field $\mathbf{c}_s(\mathbf{x})$. For a more detailed discussion on the reversible jump algorithm, definition of the dimension matching transformation and its Jacobian the reader is referred to (Denison *et al.*, 2002*b*).

4.4.4.1 Reversible Jump MCMC Algorithm as Birth and Death Process

This section sets out the details of the RJMCMC move steps we employ to traverse the transdimensional posterior surface, specific to our waveform inversion. Firstly, for ease of notation two vectors $\boldsymbol{\theta}_M$ and $\boldsymbol{\theta}_H$ are defined which hold the model specific and global hyper-parameters, respectively. The global parameters are those which bear on parameters common to all the competing models. Hence, $\boldsymbol{\theta}_M = \{\mathbf{c}_s, \mathbf{x}_c\}$, $\boldsymbol{\theta}_H = \{\lambda, \tau, \phi\}$ and $\boldsymbol{\theta} = \{k, \boldsymbol{\theta}_M, \boldsymbol{\theta}_H\}$. The proposed search algorithm consists of four types of moves: Birth (B), Death (D), Move (M), and Perturb (P). Different search strategies have been designed depending on the application (e.g., see the original work by Green (Green, 1995), and Denison *et al.* (Denison *et al.*, 1998)). As long as the algorithm satisfies the detailed balance condition, the acceptance ratio remains computationally efficient and moves are simulated suitably, the algorithm design could be flexible.

Let us suppose that at the (s)th step, the chain is at $k^{(s)}, \boldsymbol{\theta}_M^{(s)}, \boldsymbol{\theta}_H^{(s)}$ (denoting number of cells, model specific parameters $\mathbf{c}_s^{(s)} = \{c_s^{(s)}\}_{i=1}^{k^{(s)}}$ and $\mathbf{x}_c^{(s)} = \{x_c^{(s)}\}_{i=1}^{k^{(s)}}$ and hyper-parameters $\lambda^{(s)}, \tau^{(s)}, \phi^{(s)}$, respectively). Notice that σ_d was integrated out from the posterior and will not be sampled from by MCMC search.

The possible RJMCMC transitions are: (B) add a new generating point (nucleus) to the tessellation with probability $p_{k^{(s)}}^{(B)}$. (D) Delete a randomly chosen nucleus with probability $p_{k^{(s)}}^{(D)}$. (M) Swap a randomly chosen nucleus for a randomly chosen available node in $\mathscr{T}$ with probability $p_{k^{(s)}}^{(M)}$, where $\mathscr{T}$ is the set of candidate node locations, and T is the size of the set $\mathscr{T}$ ($|\mathscr{T}| = T$). (P) Perturb velocity of a randomly chosen cell with probability $p_{k^{(s)}}^{(P)}$. Where $p_{k^{(s)}}^{(B)} + p_{k^{(s)}}^{(D)} + p_{k^{(s)}}^{(M)} + p_{k^{(s)}}^{(P)} = 1, \ \forall\, k^{(s)}$. Notice that (B) and (D) propose moves between different dimensions while (M) and (P) propose moves within the current dimension, hence no dimension change takes place, and the latter proceeds similar to the regular Metropolis-Hastings algorithm (Robert & Casella, 2004). Below is the definition of each transition:

- **Birth**

  $k^* = k^{(s)} + 1$

  With probability $p_{k^{(s)}}^{(B)} = q_{k^{(s)},k^*}$, a Birth move is proposed, and a nucleus i is added at an available grid location. This random location is proposed from a uniform discrete probability $q_x(\mathbf{x}_c^*|\mathbf{x}_c^{(s)}, k^{(s)})$ (having N elements in the regular domain and $k^{(s)}$ current partitions $N - k^{(s)}$ knots are available to chose from). A velocity value must be assigned to the generated cell centered at $x^*_{c_{k^{(s)}+1}}$. This is obtained by perturbing the existing velocity value where the birth takes place from a Gaussian proposal $q_c(\mathbf{c}_s^*|\mathbf{c}_s^{(s)}, k^{(s)})$ (i.e., $c^*_{s_{k^{(s)}+1}} = c_{s_i}^{(s)} + \zeta_c u_c$ where $u_c \sim \mathcal{N}(0,1)$). ζ_c is a variance measure, defining size of the search step, and is a user tuned parameter. Notice that the dimension difference between the current and proposed states equal to two, therefore, two auxiliary variables are needed for dimension balance). The hyperparameters remain unchanged in the Birth (also in Death) move. The candidate

state is accepted with probability

$$
\begin{aligned}
r_{k^{(s)},k^*}(\boldsymbol{\theta}_M^{(s)}, \boldsymbol{\theta}_M^*) = \min\Bigg\{ 1, & \underbrace{\frac{p(\boldsymbol{\theta}_M^*, k^*)}{p(\boldsymbol{\theta}_M^{(s)}, k^{(s)})}}_{\text{prior ratio}} \underbrace{\frac{p(\mathbf{d}_{\text{obs}}|\boldsymbol{\theta}_M^*, \boldsymbol{\theta}_H^{(s)}, k^*)}{p(\mathbf{d}_{\text{obs}}|\boldsymbol{\theta}_M^{(s)}, \boldsymbol{\theta}_H^{(s)}, k^{(s)})}}_{\text{likelihood ratio}} \\
& \times \underbrace{\frac{q_{k^*,k^{(s)}}}{q_{k^{(s)},k^*}} \frac{q_c(\mathbf{c}_s^{(s)}|\mathbf{c}_s^*, k^*)}{q_c(\mathbf{c}_s^*|\mathbf{c}_s^{(s)}, k^{(s)})} \frac{q_x(\mathbf{x}_c^{(s)}|\mathbf{x}_c^*, k^*)}{q_x(\mathbf{x}_c^*|\mathbf{x}_c^{(s)}, k^{(s)})}}_{\text{proposal ratio}} \\
& \times \underbrace{\left| \frac{\partial \mathcal{T}_{k^{(s)},k^*}(\mathbf{c}^{(s)}, u_c)}{\partial \mathbf{c}^{(s)} \partial u_c} \right|}_{\text{Jacobian}} \Bigg\}
\end{aligned}
\tag{4.30}
$$

where the prior ratio is

$$
\frac{p(\boldsymbol{\theta}_M^*, k^*)}{p(\boldsymbol{\theta}_M^{(s)}, k^{(s)})} = \frac{p(\mathbf{c}_s^*|\tau^{(s)}, \phi^{(s)}, k^*) p(\mathbf{x}_c^*|k^*) p(k^*|\lambda^{(s)})}{p(\mathbf{c}_s^{(s)}|\tau^{(s)}, \phi^{(s)}, k^{(s)}) p(\mathbf{x}_c^{(s)}|k^{(s)}) p(k^{(s)}|\lambda^{(s)})} \tag{4.31}
$$

$p(\mathbf{c}_s|\tau, \phi, k)$, $p(\mathbf{x}_c|k)$ and $p(k|\lambda)$ are given in equations 4.17, 4.23 and 4.24, respectively. The precision matrix $\mathbf{H}$ (equation 4.18) needs to be updated at each step, since those elements of $\mathbf{H}$ which corresponds to the regions belonging to the neighborhood set of the new born tessellation changes during the Birth. The components of the proposal ratio are as follows

$$q_x(\mathbf{x}_c^*|\mathbf{x}_c^{(s)}, k^{(s)}) \propto \frac{1}{T - k^{(s)}} \tag{4.32a}$$

$$q_x(\mathbf{x}_c^{(s)}|\mathbf{x}_c^*, k^*) \propto \frac{1}{k^*} \tag{4.32b}$$

$$q_c(\mathbf{c}_s^*|\mathbf{c}_s^{(s)}, k^{(s)}) \sim \mathcal{N}(c^*_{s_{k^{(s)}+1}}|c^{(s)}_{s_i}, \zeta_c) = \frac{1}{\zeta_c\sqrt{2\pi}} \exp\left\{-\frac{1}{2\zeta_c^2}\left(c^*_{s_{k^{(s)}+1}} - c^{(s)}_{s_i}\right)^2\right\} \tag{4.32c}$$

$$q_c(\mathbf{c}_s^{(s)}|\mathbf{c}_s^*, k^*) \propto 1 \tag{4.32d}$$

$$q_{k^{(s)},k^*} = \begin{cases} 1/2 & k^{(s)} = 1 \\ 1/4 & \text{otherwise} \end{cases} \tag{4.32e}$$

$$q_{k^*,k^{(s)}} = \begin{cases} 1/3 & k^{(s)} = K \\ 1/4 & \text{otherwise} \end{cases} \tag{4.32f}$$

$$|\mathbf{J}|_{\text{Birth}} = \left|\frac{\partial \mathcal{T}_{k^{(s)},k^*}(\mathbf{c}^{(s)}, u)}{\partial \mathbf{c}^{(s)} \partial u}\right| = 1 \tag{4.32g}$$

$p(\mathbf{d}_{\text{obs}}|\boldsymbol{\theta}_M, \boldsymbol{\theta}_H, k)$ is the likelihood function, which is constructed according to equation 4.14. Equation 4.32a gives the probability of generating a cell centered at $x^*_{c_{k^{(s)}+1}}$ and equation 4.32b is the probability of deleting the cell centered at $x^*_{c_{k^{(s)}+1}}$. The probability that the new born cell is assigned a velocity value $c^*_{s_{k^{(s)}+1}}$ is given by equation 4.32c, and equation 4.32d is the probability of the reverse proposal: removing a velocity when cell is deleted. According to equations 4.32e and 4.32f the probability of proposing each of Birth, Death, Move and Perturb is chosen to be equal (i.e., $\frac{1}{4}$). The only exceptions are $k^{(s)} = 1$ and $k^{(s)} = K$. If $k^{(s)} = 1$, only Birth and Perturb moves are allowed, each with equal probability of $\frac{1}{2}$ and $k^{(s)} = K$. If $k^{(s)} = K$, the Birth proposal is prohibited so other search types are conducted with equal probability of $\frac{1}{3}$. The Jacobian term $|\mathbf{J}|_{\text{Birth}}$ accounts for the change in scale

when moving to a different dimension. A short derivation is provided in F where we show for the problem considered here $|\mathbf{J}|_{\text{Birth}} = 1$. More detailed discussion could be found in (Robert & Casella, 2004) and (Denison *et al.*, 2002*b*).

- **Death**

  $k^* = k^{(s)} - 1$

  With probability $p^{(D)}_{k^{(s)}} = q_{k^{(s)},k^*}$, a Death move is proposed. A current Voronoi nucleus i is randomly chosen from the probability $q_x(\mathbf{x}^*_c|\mathbf{x}^{(s)}_c, k^{(s)})$ and removed. The Death move is the exact reverse of the Birth move.

  The acceptance ratio for the Death proposal is the same as equation 4.30 where the components are defined bellow:

$$q_x(\mathbf{x}^*_c|\mathbf{x}^{(s)}_c, k^{(s)}) \propto \frac{1}{k^{(s)}} \tag{4.33a}$$

$$q_x(\mathbf{x}^{(s)}_c|\mathbf{x}^*_c, k^*) \propto \frac{1}{T - k^*} \tag{4.33b}$$

$$q_c(\mathbf{c}^*_s|\mathbf{c}^{(s)}_s, k^{(s)}) \propto 1 \tag{4.33c}$$

$$q_c(\mathbf{c}^{(s)}_s|\mathbf{c}^*_s, k^*) \sim \mathcal{N}(c^{(s)}_{s_{k^*+1}}|c^*_{s_i}, \zeta_c) = \frac{1}{\zeta_c\sqrt{2\pi}} \exp\left\{-\frac{1}{2\zeta_c^2}\left(c^{(s)}_{s_{k^*+1}} - c^*_{s_i}\right)^2\right\} \tag{4.33d}$$

$$q_{k^{(s)},k^*} = \begin{cases} 1/3 & k^{(s)} = 1 \\ 1/4 & \text{otherwise} \end{cases} \tag{4.33e}$$

$$q_{k^*,k^{(s)}} = \begin{cases} 1/2 & k^{(s)} = K \\ 1/4 & \text{otherwise} \end{cases} \tag{4.33f}$$

$$|\mathbf{J}|_{\text{Death}} = \left|\frac{\partial \mathcal{T}_{k^{(s)},k^*}(\mathbf{c}^{(s)}, u)}{\partial \mathbf{c}^{(s)} \partial u}\right| = 1 \tag{4.33g}$$

- **Move**

$k^* = k^{(s)}$

With probability $p^{(M)}_{k^{(s)}} = q_{k^{(s)},k^*}$, a "Move" move is proposed. A Voronoi cell nucleus $\mathbf{x}_{c_i}$ in randomly chosen from a uniform probability, and moved to an available knot location found by perturbing the coordinates of its current position vector according to a bivariate normal distribution.

$$q_x(\mathbf{x}^*_{c_i}|\mathbf{x}^{(s)}_{c_i}) = \frac{1}{2\pi\zeta_x^2}\exp\left\{-\frac{1}{2\zeta_x^2}(\mathbf{x}^*_{c_i}-\mathbf{x}^{(s)}_{c_i})^T(\mathbf{x}^*_{c_i}-\mathbf{x}^{(s)}_{c_i})\right\} \tag{4.34}$$

where ζ_x determines the amount that the nucleus i is displaced with respect to its original location. A new set of hyper parameters $\boldsymbol{\theta}^*_H$ is drawn from probability $q(\boldsymbol{\theta}^*_H|\boldsymbol{\theta}^{(s)}_H)$. To sample the hyper-parameters τ, ϕ and λ we use a log-normal proposal based on the current values of the chain using a properly tuned variance parameters (search step size) $\varsigma_\tau, \varsigma_\phi$ and ς_λ, respectively. According to a log-normal proposal, the log of the candidate parameter is centered on the log of the current value such that

$$q_\tau(\tau^*|\tau^{(s)}) = \frac{1}{\tau^*\varsigma_\tau\sqrt{2\pi}}\exp\left\{-\frac{1}{2\varsigma_\tau^2}\left(\ln\tau^* - \ln\tau^{(s)}\right)^2\right\} \tag{4.35}$$

The proposal densities for $q_\phi(\phi^*|\phi^{(s)})$ and $q_\lambda(\lambda^*|\lambda^{(s)})$ are constructed in a same fashion as equation 4.35. In a Move step, as the number of Voronoi cells is fixed, the algorithm reduces to the regular Metropolis-Hastings MCMC with the acceptance probability of the following form:

$$r_{k^{(s)},k^*}(\boldsymbol{\theta}^{(s)},\boldsymbol{\theta}^*) = \min\left\{1, \underbrace{\frac{p(\boldsymbol{\theta}^*)}{p(\boldsymbol{\theta}^{(s)})}}_{\text{prior ratio}} \underbrace{\frac{p(\mathbf{d}_{\text{obs}}|\boldsymbol{\theta}^*_M,\boldsymbol{\theta}^*_H,k^{(s)})}{p(\mathbf{d}_{\text{obs}}|\boldsymbol{\theta}^{(s)}_M,\boldsymbol{\theta}^{(s)}_H,k^{(s)})}}_{\text{likelihood ratio}} \underbrace{\frac{q(\boldsymbol{\theta}^{(s)}_H|\boldsymbol{\theta}^*_H)}{q(\boldsymbol{\theta}^*_H|\boldsymbol{\theta}^{(s)}_H)}}_{\text{proposal ratio}}\right\} \tag{4.36}$$

The prior ratio is $\frac{p(\boldsymbol{\theta}^*)}{p(\boldsymbol{\theta}^{(s)})} = \frac{p(k^*|\lambda^*)p(\lambda^*|\delta_\lambda,\eta_\lambda)p\left(\mathbf{c}^{(s)}_s|c_{s_0},\tau^*,\phi^*\right)p(\tau^*|\delta_\tau,a_{\mu_\tau})p\left(\phi^*|\delta_\phi,a_{\mu_\phi}\right)}{p\left(k^{(s)}|\lambda^{(s)}\right)p\left(\lambda^{(s)}|\delta_\lambda,\eta_\lambda\right)p\left(\mathbf{c}^{(s)}_s|c_{s_0},\tau^{(s)},\phi^{(s)}\right)p\left(\tau^{(s)}|\delta_\tau,a_{\mu_\tau}\right)p\left(\phi^{(s)}|\delta_\phi,a_{\mu_\phi}\right)}$.
The velocity parameter assigned to the displaced cell moves with the cell, therefore, the velocity vector remains unchanged ($\mathbf{c}^*_s = \mathbf{c}^{(s)}_s$). The precision matrix $\mathbf{H}$ needs to

be updated accordingly, as the tessellation geometry changes in the vicinity of the moved cell. The proposal ratio is given by $\frac{q(\boldsymbol{\theta}_H^{(s)}|\boldsymbol{\theta}_H^*)}{q(\boldsymbol{\theta}_H^*|\boldsymbol{\theta}_H^{(s)})} = \frac{q_\tau(\tau^{(s)}|\tau^*)}{q_\tau(\tau^*|\tau^{(s)})}\frac{q_\phi(\phi^{(s)}|\phi^*)}{q_\phi(\phi^*|\phi^{(s)})}\frac{q_\lambda(\lambda^{(s)}|\lambda^*)}{q_\lambda(\lambda^*|\lambda^{(s)})}$. Notice that the proposal made to move a nucleus (equation 4.34) is symmetrical, that is $q_x(\mathbf{x}_{c_i}^*|\mathbf{x}_{c_i}^{(s)}) = q_x(\mathbf{x}_{c_i}^{(s)}|\mathbf{x}_{c_i}^*)$, and hence cancels out from the proposal ratio.

- **Perturb**

  $k^* = k^{(s)}$

  With probability $p_{k^{(s)}}^{(P)} = q_{k^{(s)},k^*}$, a Perturb move is proposed. A Voronoi cell i is randomly picked from a uniform density, and its velocity parameter is perturbed with a Gaussian proposal $q_c(c_{s_i}^*|c_{s_i}^{(s)})$:

$$q_c(c_{s_i}^*|c_{s_i}^{(s)}) = \frac{1}{\zeta_c\sqrt{2\pi}}\exp\left\{-\frac{1}{2\zeta_c^2}\left(c_{s_i}^* - c_{s_i}^{(s)}\right)^2\right\} \tag{4.37}$$

  It is also attempted to update the model hyperparameters from log-normal proposal densities (same as the M move, equation 4.35). The probability of accepting the candidate state is found from equation 4.36, with prior ratio defined such that $\frac{p(\boldsymbol{\theta}^*)}{p(\boldsymbol{\theta}^{(s)})} = \frac{p(k^*|\lambda^*)p(\lambda^*|\delta_\lambda,\eta_\lambda)p\left(\mathbf{c}_s^*|c_{s_0},\tau^*,\phi^*\right)p(\tau^*|\delta_\tau,a_{\mu_\tau})p\left(\phi^*|\delta_\phi,a_{\mu_\phi}\right)}{p\left(k^{(s)}|\lambda^{(s)}\right)p\left(\lambda^{(s)}|\delta_\lambda,\eta_\lambda\right)p\left(\mathbf{c}_s^{(s)}|c_{s_0},\tau^{(s)},\phi^{(s)}\right)p\left(\tau^{(s)}|\delta_\tau,a_{\mu_\tau}\right)p\left(\phi^{(s)}|\delta_\phi,a_{\mu_\phi}\right)}$. The precession matrix $\mathbf{H}$ remains unchanged in a Perturb, since the geometry of the cells are not affected. The proposal ratio is the same as the Move step. Again, the Gaussian proposal to update c_{s_i} (equation 4.37) dose not appear in this ratio, for reasons of symmetry.

4.5 Numerical Results

In this section, the numerical results of the transdimensional Bayesian material profile inversion scheme outlined in the preceding sections will be discussed.

We will look into the inversion of four shear waves velocity profiles. We tend to introduce more complexity into the synthesized profiles as we proceed, by adding inclined layers and/or inclusion of a buried object. A 60m by 30m heterogeneous half-plane is considered where the computational domain is surrounded by PMLs on the sides and the bottom. The

medium is probed with a Gaussian pulse-type stress load $p(t)$ applied on the entire surface of the regular domain. The maximum frequency of the excitation is 15Hz and the peak amplitude is 10kPa. The readings are recorded every 0.0025 seconds. Figure 4.5 illustrates the time history and the frequency spectrum of the excitation applied in all four cases.

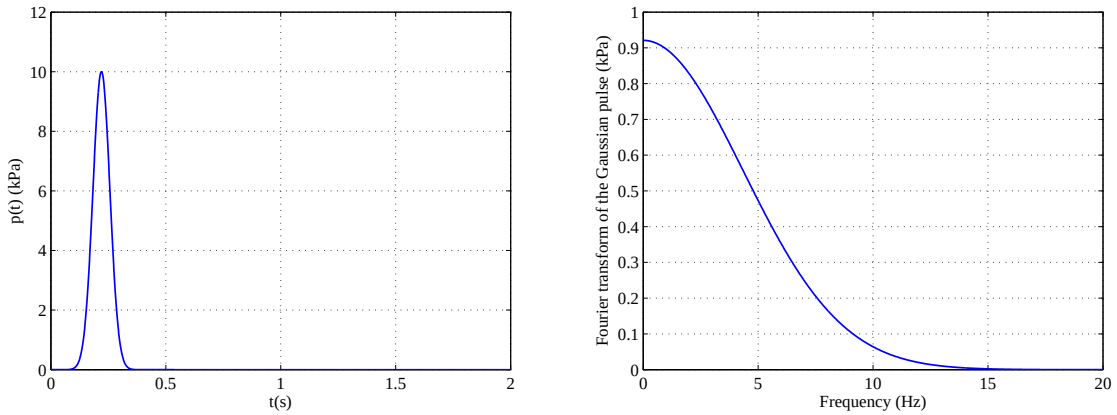

(a) Time history (b) Frequency spectrum

Figure 4.5: (a) Source time signal $p\,(t)$ (b) Frequency spectrum of the time signal $p\,(t)$ with $f_{\max} = 15$ Hz

The first velocity profile (profile A), shown in figure 4.6, is composed of three horizontal layers with shear wave velocities 100m/s, 115m/s, and 130m/s from top to bottom. The soil density is assumed to be 2000kg/m^3 for all the layers. Notice that the layers are extended into the PML zone, such that the shear wave velocity remains constant in a direction perpendicular to the regular domain-PML interface, with a value equal to the velocity at the interface. In theory, the PML is to be located at a point beyond which homogeneity is ascertained perpendicular to the interface. The forward model (equations 4.4 and 4.5) is solved numerically using a mixed finite element scheme (Kang & Kallivokas, 2010*b*). The domain is discretized by biquadratic elements of of size 1.5m and 0.75m for the regular domain and the PML zone, respectively. The user tuned reflection coefficient (shown in

equation 4.3) is set to $|R| = 10^{-8}$.

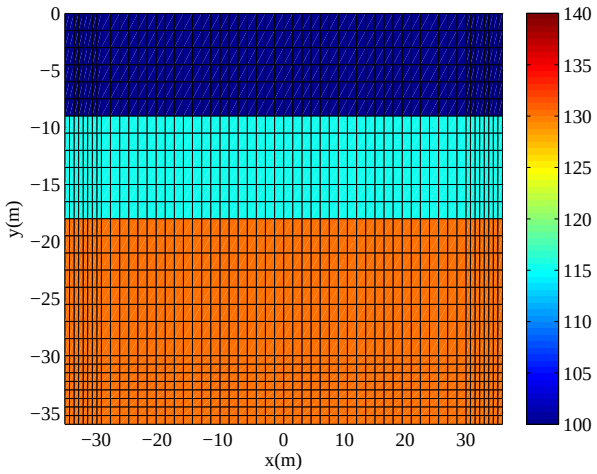

Figure 4.6: Target shear wave velocity profile A (c_s = 110 m/s, c_s = 115 m/s and c_s = 130 m/s from top to bottom)

The displacement time history measurements $v(\mathbf{x}, t)$ are collected at the ground level, where one reading is made every 1.5m of the regular domain. The synthetic data is generated by perturbing the forward model solution under the target velocity profile, with 10% Gaussian noise (10% of the average observed displacement). Figure 4.7 depicts the displacement time history response of Earth to the prescribed excitation together with the synthesized data set. Displacement response, as a measurable characteristic of the wave field, will serve as the input to our inversion scheme.

No constraint is placed on the maximum allowable number of cells in the Voronoi diagram, allowing the number of cells to increase as many as the number of elements of the regular domain ($K = 800$). This indicates maximum number of $2K + 3 = 1603$ unknowns. Notice that each Voronoi cell is identified by two numbers: a discrete value corresponding to the element number which includes the nucleus and a velocity value. In addition, τ, ϕ, and λ are to be sampled by the MCMC search.

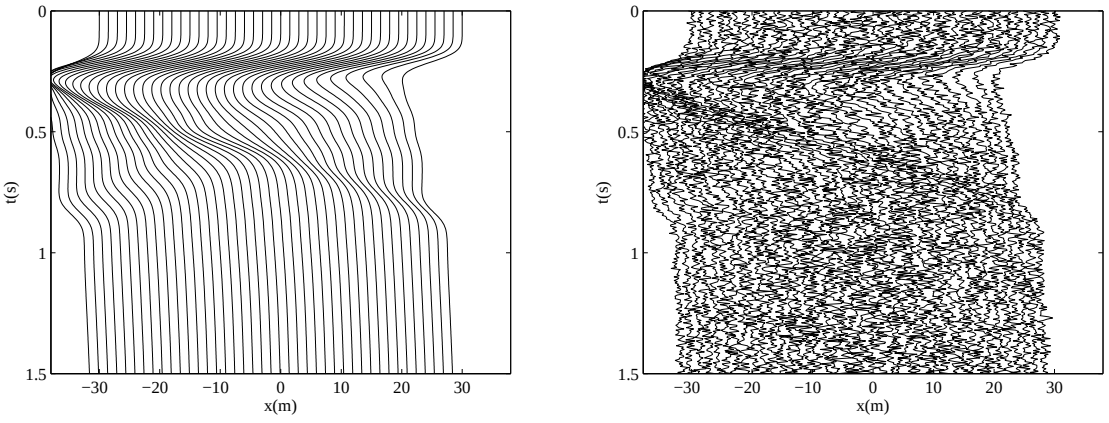

Figure 4.7: (a) Displacement responses $u(\mathbf{x}, t)$ measured over the surface. Data is obtained by applying a uniformly-distributed Gaussian pulse with $f_{\max} = 15$ Hz over the entire surface of profile A. (b) Synthetic data: Measured displacement response at the ground level perturbed with 10% Gaussian noise

The constants of the prior density (equation 4.26) need to be specified. The following values are assigned to the hyperparameters: $c_{s_0} = 100$ (equation 4.17); $\delta_\tau = 1$, $a_{\mu_\tau} = 10^{-4}$ (equation 4.21); $\delta_\phi = 1$, $a_{\mu_\phi} = 10^{-4}$ (equation 4.22); $\delta_\lambda = \eta_\lambda = 0.01$ (equation 4.25); $\delta_d = \eta_d = 0.01$ (equation 4.14). These values are chosen to construct fairly flat hyperpriors. These specifications encourage complexity of the recovered model (defined by the number of basis functions/Voronoi tessellations, and smoothness parameters) be specified only by the data.

Posterior inference for the unknowns of the target profile A is made based on ensemble of 3500 collected RJMCMC samples. We started the inversion from homogenous initial guess $c_s = 100$m/s (one tessellation $k = 1$, nucleus of which positioned at a randomly chosen knot). The first 1000 samples were discarded as burn-in iterations, only after which the chain is guaranteed to sample from the posterior. Every third visited sample was kept in the chain as high dependency is expected, especially between successive values of k, since the difference between the current and the proposed k values could be at most one.

MCMC trace plot for k is shown in figure 4.8a (only first 400 samples are presented). This figure shows that k raises up to $k = 5$ and in about 150 iterations it settles down to the $k = 3$ Voronoi cells, which is the minimum number of partitions that could recover the three layer target profile. This clearly manifests how the Bayesian model selection adheres to the principle of parsimony, also known as Bayesian Occam's Razor, indicating Bayes rule's natural penalty against unnecessarily complex models. This figure also implies that even though our sampling strategy dose not force the model to undergo dimension changes at every iteration (in Move and Perturb k remains unchanged), the waiting time at a single model is not long. Hence, the sampler promptly explores the space of plausible models until it converges to the simplest model that retrieves the structure. The rest of the simulation effort is devoted to arriving at the stationary condition in sampling the parameters of the few favored models. This observation confirms the efficiency of the algorithm design and of the proposal density formulations.

Figures 4.8b and 4.8c depict cumulative mean and standard deviation trace plots for an ensemble of 400 pointwise velocity values. Visual inspection of the sampling sequence and cumulative first and second order statistics traces of parameters are easy non-convergence checks. This, however, only applies to output of variables that do not change dimension. In practice we expect to see the cumulative traces tending toward a constant value and not drifting in any direction. A thorough review of the MCMC convergence diagnostic techniques could be found in (Brooks & Roberts, 1998; Cowles & Carlin, 1996). These techniques, however, apply only to situations which the dimension of the parameter space is fixed. Brooks and Guidici (Brooks & Giudici, 1999) have proposed a convergence assessment specifically for transdimensional samplers.

The posterior mean velocity model is displayed in figure 4.9a which precisely recovers the target. This is obtained by averaging the post burn-in velocity values at every grid location. The best partitioned velocity model which maximizes the posterior is also shown in figure 4.9b. The cell geometry and nuclei positioning constructing the optimal solution are superimposed on the inverted image. The nuclei are arranged such that the three

layer structure is formed after only about 150 samples are collected. Posterior inference on the number of tessellations needed to construct the velocity model $p\left(k|\mathbf{d}_{\text{obs}}\right)$ is shown in figure 4.9c which quantifies the level of certainty in accepting each model configuration. No models with more than 5 partition have been accepted, given that the upper limit for k is set to 800. This presents the capability of Bayesian inversion to deduce the true nature of the underlying process without imposing any regularization constraint to penalize overly complex models. An error map for the inverted velocity image could be constructed. This map, displayed in figure 4.9d, assigns an error estimate (which is the pointwise standard deviation of an ensemble of post burn-in velocity models) to each grid location. This type of error estimation provides information to make precise statement about the degree of confidence in the inference about the Earth's interior. According to this figure maximum uncertainty occurs at the interface of the first two layers. An overall trend of increasing uncertainty with depth is apparent.

In figure 4.10 the the posterior mean velocity profile are plotted for three vertical cross section lines positioned at $x = -21.75$, $x = 0.75$ and $x = 11.25$ m of the regular domain. The target profile together with the 95% credible intervals for the posterior predictions are also superimposed. This figure highlights the capability of the reversible jump algorithm in recovering earth models with sharp material interfaces. Figure 4.12 illustrates the marginal posterior densities of pointwise velocity values at six selected locations $p\left(c_s|\mathbf{d}_{\text{obs}}\right)|_{x=x_i,y=y_i}$. The configuration of the selected elements is shown in figure 4.11. The target values are also superimposed on each histogram (dashed lines). The figure indicates the ability of the inversion scheme to deduce the target parameters. Notice that instead of having a single velocity value at each spatial location indicating the optimal solution, a density function is obtained which summarizes all the plausible solutions with the corresponding probability of occurrence. Hence, the inherent ill-posedness (solution non-uniqueness) of the inverse medium problem is resolved. Posterior cumulative density function (cdf) of the shear wave velocities at the same bench mark locations are provided in figure 4.13. This figure also indicates that the uncertainty of the inferred wave velocity slightly increases with depth.

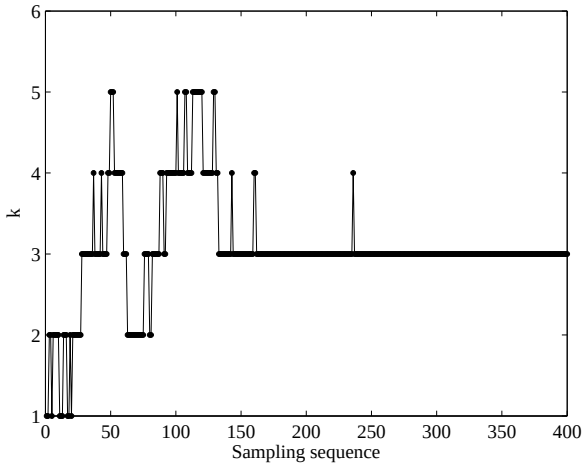

(a)

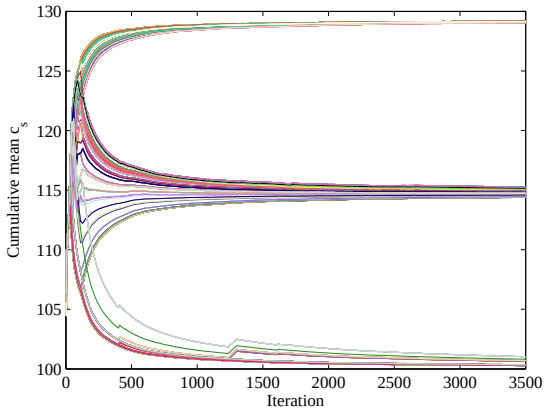

(b) Cumulative mean of the sampling history

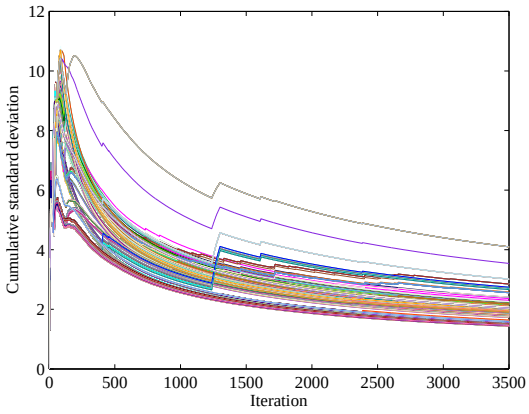

(c) Cumulative standard deviation of the sampling history

Figure 4.8: (a) RJ-MCMC sampling sequence of the number of cells in the Voronoi diagram k; (b) and (c) Convergence diagnosis: plots the cumulative mean and standard deviation (over iterations) for element-wise velocities corresponding to target profile A.

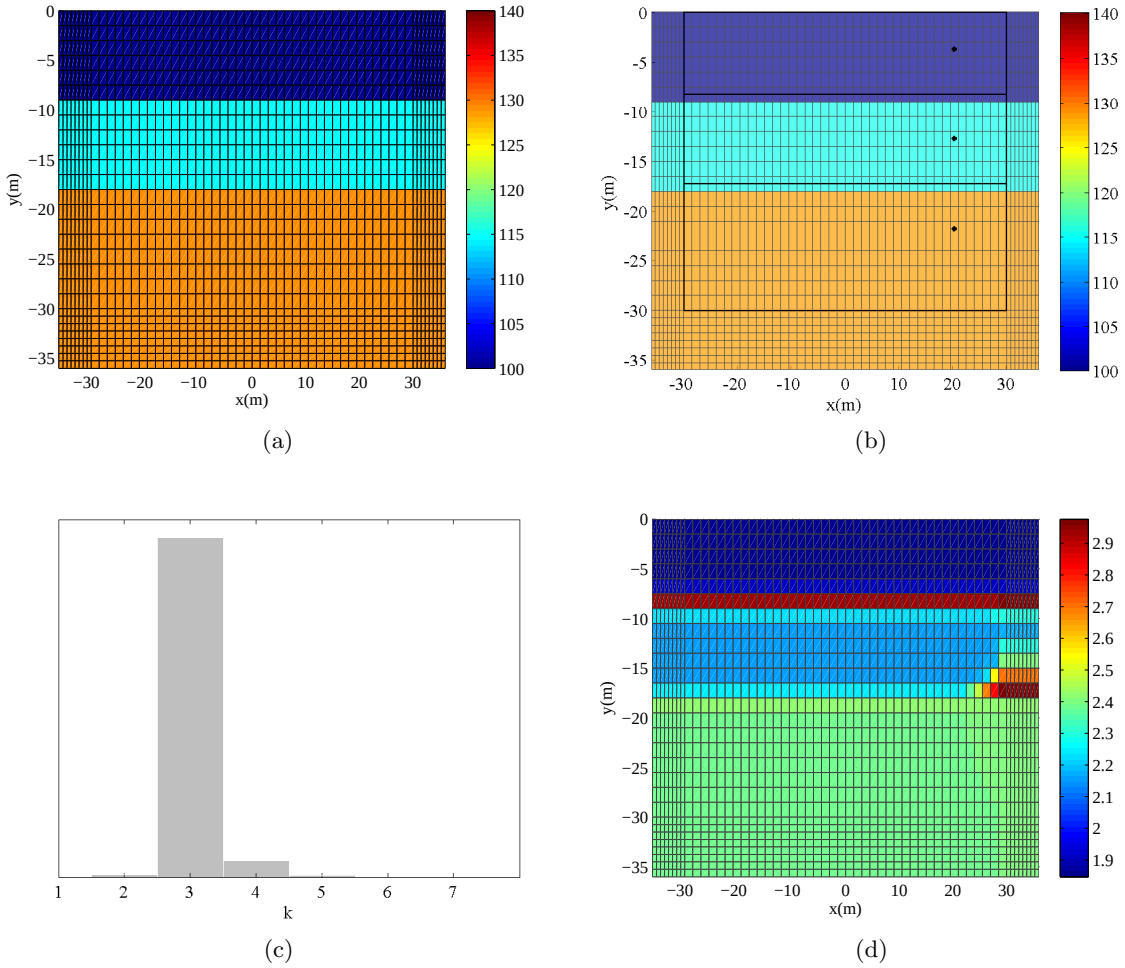

Figure 4.9: Reversible jump MCMC output for target profile A: (a) Average solution (posterior mean velocity field estimate) (b) Best solution which maximizes the posterior density (c) Posterior mass function $p(k|\mathbf{d}_{\text{obs}})$ of the number of cells in the Voronoi diagram (d) Estimated error map showing the pointwise variability of the post burn-in velocity draws.

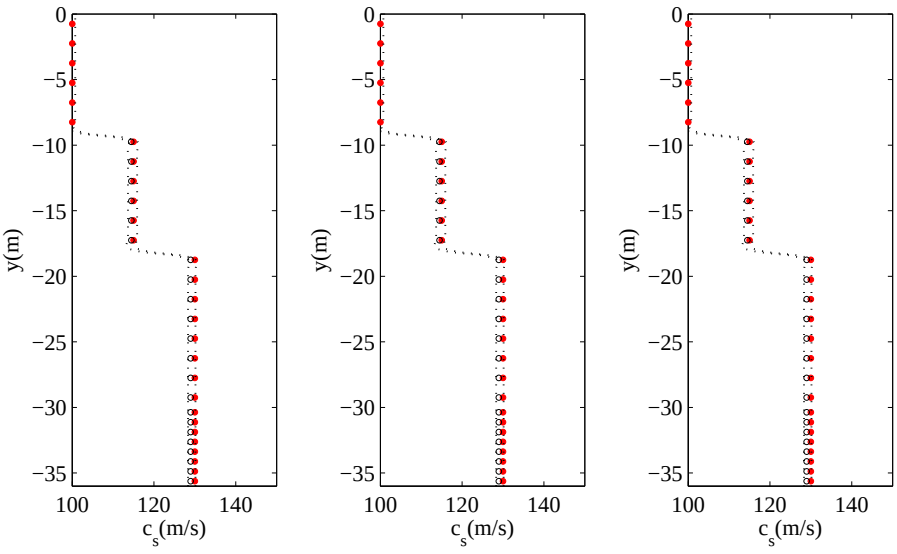

(a) $x = -21.75$ m (b) $x = 0.75$ m (c) $x = 11.25$ m

Figure 4.10: Cross-section profiles showing the true models (solid res dots), posterior mean estimates (black hollow dots) and 95% credible intervals for the posterior mean (black dotted line) corresponding to profile A.

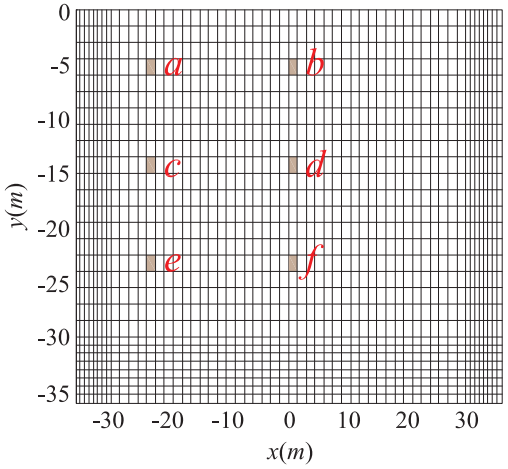

Figure 4.11: Configuration of the six benchmark elements for target shear wave velocity profile A.

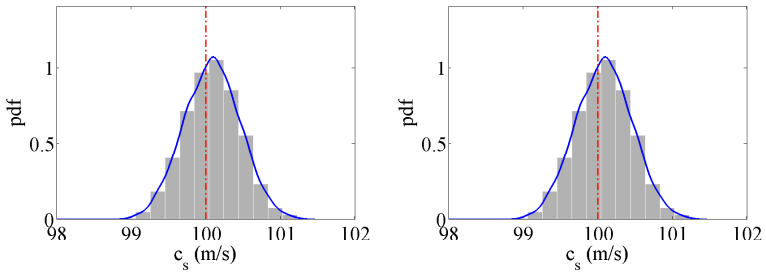

(a) $c_s\,(-23.25, -5.25)$

(b) $c_s\,(0.75, -5.25)$

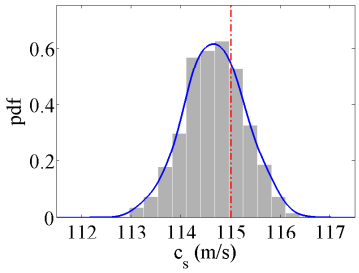

(c) $c_s\,(-23.25, -14.25)$

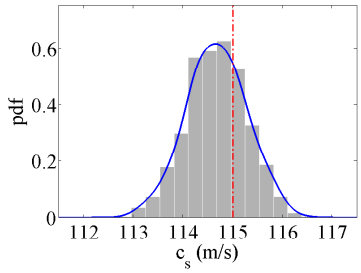

(d) $c_s\,(0.75, -14.25)$

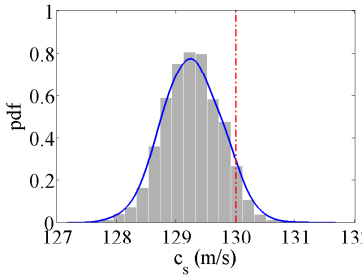

(e) $c_s\,(-23.25, -23.25)$

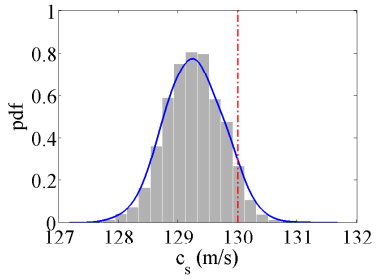

(f) $c_s\,(0.75, -23.25)$

Figure 4.12: Marginal posterior density of the shear wave velocities and the corresponding target values (dashed line) at six selected elements a, b, c, d, e, and f (profile A).

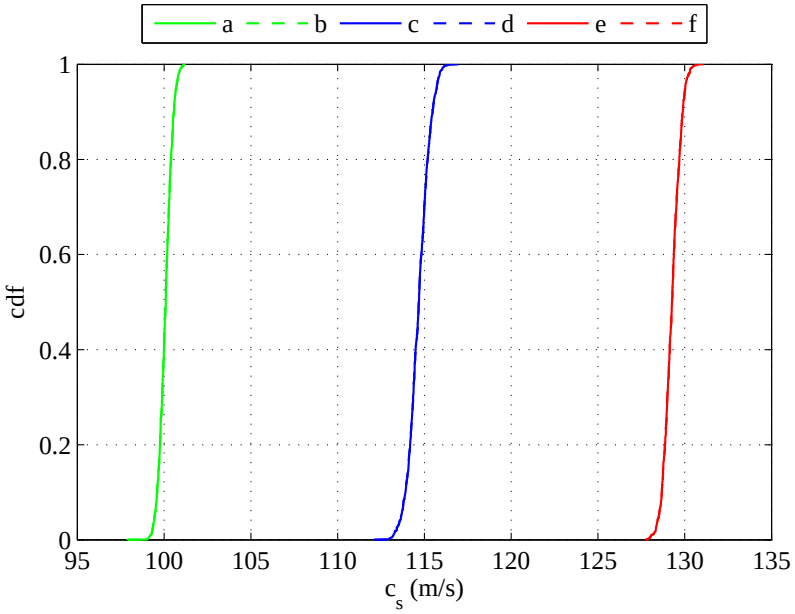

Figure 4.13: Posterior cumulative density function (cdf) of the shear wave velocities at six selected elements a, b, c, d, e, and f (profile A).

Figure 4.14 depicts the posterior densities of the inferred hyper-parameters. In figure 4.14a the variance of the observational error term σ_d^2 is displayed, which is relatively centered around the target added Gaussian noise (signal to noise ratio, SNR=10). The marginal posterior histogram of the rate parameter λ in the truncated Poisson prior (equation 4.24) is provided in figure 4.14b. We can see that the this parameter is centered around 3 (Bayesian point estimate for λ). This parameter is the mean of the Poisson prior, which reflects the numbers of cells k constructing the model $\mathbf{c}_s$. Figure 4.14c depicts the marginal posterior histograms of ϕ, which is a spatial parameter that controls the measure of correspondence between velocities of different cells and tunes the smoothness of the velocity field. The lower values of ϕ result in stronger dependence between the velocity of the neighbouring cells, hence, represents smoother models.

Figure 4.14d depicts the dispersion parameter τ. This parameter is of crucial significance in our transdimensional framework, since fixing τ to large values (choice of relatively sharp priors on $\mathbf{c}_s$) limits the flexibility of each basis function coefficient, therefore many tessellations are required to adequately model the target process (i.e., $\mathbb{E}\left(k|\mathbf{d}_{\text{obs}}\right)$ grows). The definition of the basis functions in a Bayesian partition model is given in equation 4.16. By contrast, small values of τ (relatively diffuse prior on $\mathbf{c}_s$) results in a more flexible mean posterior velocity field $\mathbb{E}\left(\mathbf{c}_s|\mathbf{d}_{\text{obs}}\right)$, which can accommodate wilder oscillations in its behavior. Hence, fewer basis functions are needed to reflect the true underlying process (i.e., $\mathbb{E}\left(k|\mathbf{d}_{\text{obs}}\right)$ becomes increasingly small), as each basis function has more degrees of freedom. Notice that here we did not choose to set up a fixed value for τ. Rather, this parameter is considered as a random variable which is assigned a Gamma prior (equation 4.19), and its value is deduced from the data. A second level of hierarchical prior (an exponential prior) is assigned to the parameters of the Gamma prior for increased robustness and flexibility. Figure 4.14e displays the scatter plot of τ against ϕ. A strong inverse correlation between these two quantities is observed.

Next, we consider a profile composed of two layers with an inclined interface depicted in figure 4.15 (profile B). The size of the computational domain, the PML zone and the

discretization are the same as profile A. The layer velocities are $c_s = 110$ m/s and $c_s = 135$ m/s from top to bottom. The domain is illuminated with the stress load shown in figure 4.5. The sources and receivers are distributed on the entire surface of the domain, and the readings are collected at every 1.5 m intervals for 2 seconds, where the time step is 0.0025 sec. The soil's density is 2000kg/m^3 for the entire domain. Figure 4.16b shows the synthetic data generated by perturbing the forward solver output (figure 4.16a) with a Gaussian random noise (SNR=10). The RJMCMC algorithm is run and every 3 visited model is collected. The first 1000 samples are withdrawn as burn-in and the posterior inference is made using an ensemble of 3000 models. The convergence is checked by inspecting the cumulative mean and standard deviation traces of point wise velocities in the regular domain plotted in figure 4.17. Figures 4.18a and 4.18b depict the average solution velocity map and the best sampled model which maximizes the posterior. The target is precisely recovered by four Voronoi cells in average (figure 4.18c). An error map for the inverted velocity image is presented in figure 4.18d.

The target and the inverted velocity profiles are plotted together over three vertical sections in figure 4.19. The credible regions are also included showing a very narrow range of variability around the mean profile. Marginal posterior histograms of wave velocity at six grid locations are plotted in figure 4.21. The benchmark grid blocks are marked in figure 4.20. Posterior cdf of the shear wave velocities at the same bench mark locations are presented in figure 4.22. Figure 4.23 shows marginal posterior histograms of model hyperparameters.

In figure 4.24 target profile C is displayed, showing an elliptical object ($c_s = 150$ m/s) in a background velocity of $c_s = 115$ m/s. The synthetic data is presented in figure 4.25. The recovered average profile is shown in figure 4.26. The location, shape, and the velocity of the inclusion are detected fairly well. The optimal solution is comprised of 14 "mobile" tessellations (figure 4.26b) making the total number of unknowns equal to 31 instead of 800 (number of elements in the 40 $\times$ 20 mesh) in a grid based inversion approach. Again, in the transdimensional approach, overcomplex models are not penalized by global damping

parameters; instead the algorithm smoothens the model in response to the data. Hence, the number of basis functions increases until a reasonable saturation is reached. From that point on, adding more basis functions has strongly diminishing return, as this reduces the marginal likelihood (see appendix E for discussion on Bayesian model selection and definition of the marginal likelihood).

The posterior mean inverted profile is plotted along three vertical cross-sections together with the target and estimated 95% credible regions (figure 4.27). Mild discrepancy could be seen between the target and retrieved velocity values, however the location of the object is obtained pretty well. Figures 4.29 and 4.30 present the inference on the wave velocity of six selected grid blocks (presented in figure 4.28). Figure 4.31 shows marginal posterior histograms of model hyperparameters.

In the last profile (profile D), depicted in figure 4.32, the same elliptical inclusion as profile C is added to profile B. The inversion setup is the same as the previous cases. The initial guess is homogenous with $c_s = 125$ m/s. The data is shown in figure 4.33. The mean inverted solution shown in figure 4.34a recovers the shape and the location of the inclusion fairly good. By adding more complexity to the target the number of cells required to form the features increases. This could be observed from figure 4.34b where the optimum solution is constructed by 20 tessellations (total of 43 inversion parameters). The posterior mass function $p\left(k|\mathbf{d}_{\text{obs}}\right)$ presented in figure 4.34c shows the average number of Voronoi cells is nearly $\mathbb{E}\left(k|\mathbf{d}_{\text{obs}}\right) = 21$. The standard deviation for the inverted velocity image is presented in figure 4.9d, which assigns an error estimate to each grid location.

The cross-sectional profiles (figure 4.35) illustrates deviation of the mean solution from the target, and quantifies the amount of variation around the mean. Although the quality of the recovered image degrades as more complexity is introduced into the target, except for a few sections, the credible regions include the true velocities. A similar observation could be made from figures 4.37 and 4.38, where marginal posterior histogram and posterior cdf of shear wave velocity are depicted at the 9 benchmark elements presented in figure 4.36. Finally figure 4.39 depicts the posterior densities of hyper-parameters σ_d^2, λ, τ, and ϕ.

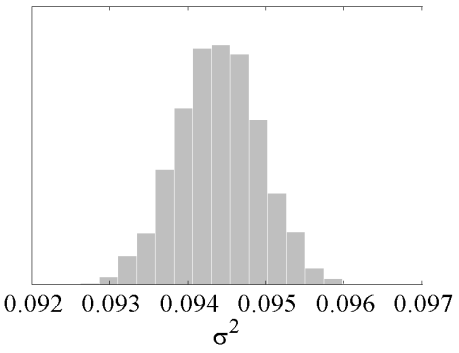

(a) Noise variance $p\left(\sigma_d^2|\mathbf{d}_{\text{obs}}\right)$

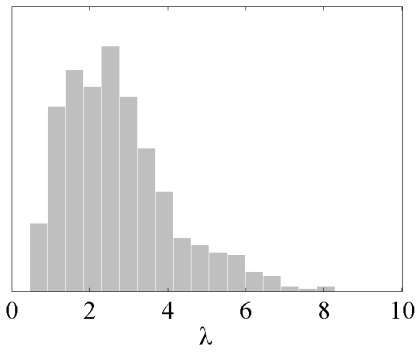

(b) Rate parameter in Poisson prior $p\left(\lambda|\mathbf{d}_{\text{obs}}\right)$

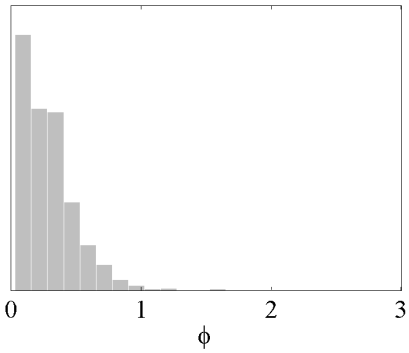

(c) $p\left(\phi|\mathbf{d}_{\text{obs}}\right)$

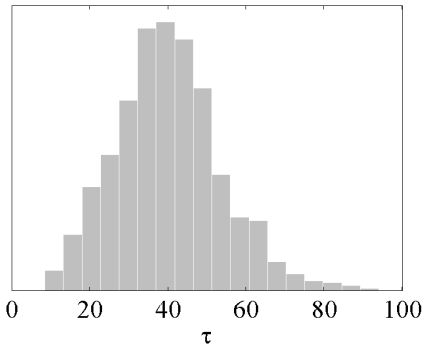

(d) Scale parameter of the Gaussian Markov random field prior $p\left(\tau|\mathbf{d}_{\text{obs}}\right)$

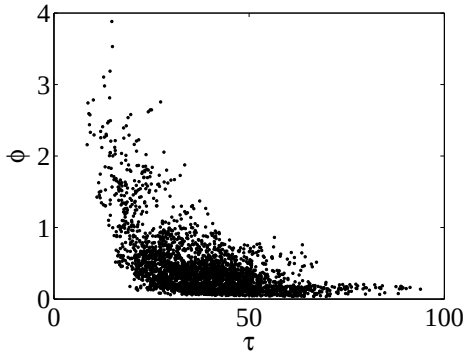

(e)

Figure 4.14: (a)-(d) Marginal posterior density for model hyper-parameters. (e) Scatter plot of τ and ϕ MCMC samples, displaying the correlation structure between the two hyper-parameters (profile A).

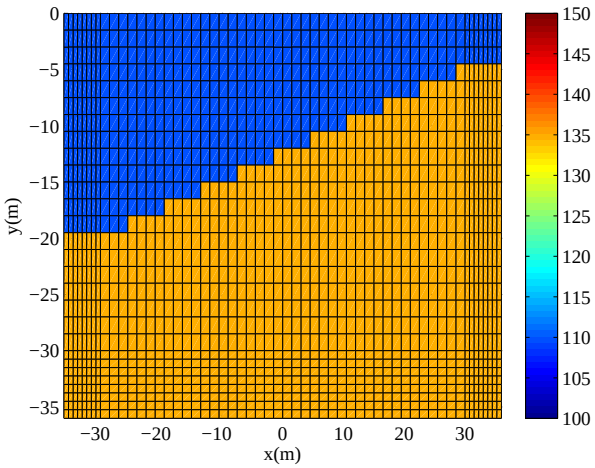

Figure 4.15: Target shear wave velocity profile B (c_s = 110 m/s and c_s = 135 m/s from top to bottom)

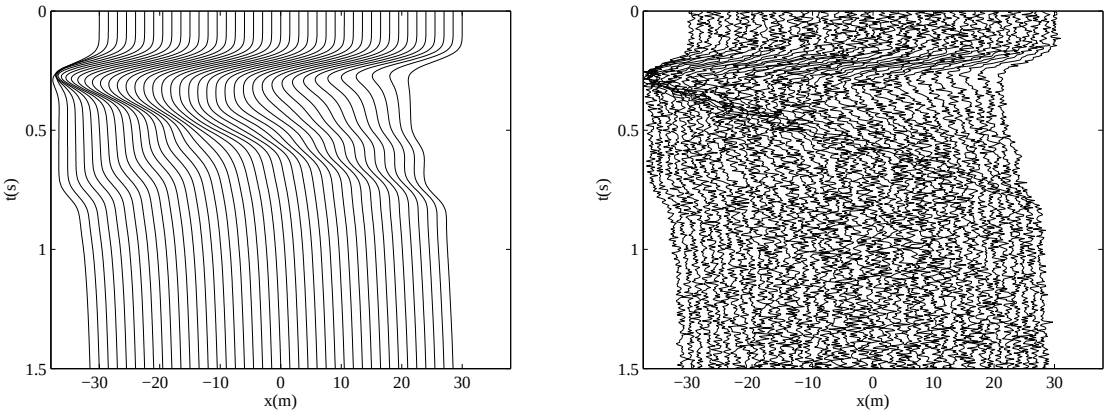

(a) (b)

Figure 4.16: (a) Displacement responses $u(\mathbf{x}, t)$ measured over the surface. Data is obtained by applying a uniformly-distributed Gaussian pulse with $f_{\max}$ = 15 Hz over the entire surface of profile B. (b) Synthetic data: Measured displacement response at the ground level perturbed with 20% Gaussian noise

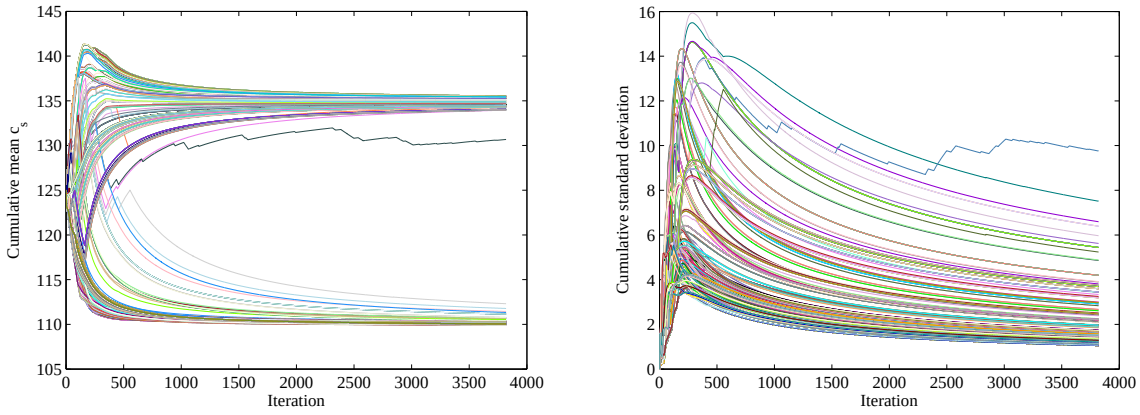

(a) Cumulative mean of the sampling history

(b) Cumulative standard deviation of the sampling history

Figure 4.17: Convergence diagnosis: plots the cumulative mean and standard deviation (over iterations) for element-wise velocities corresponding to target profile B.

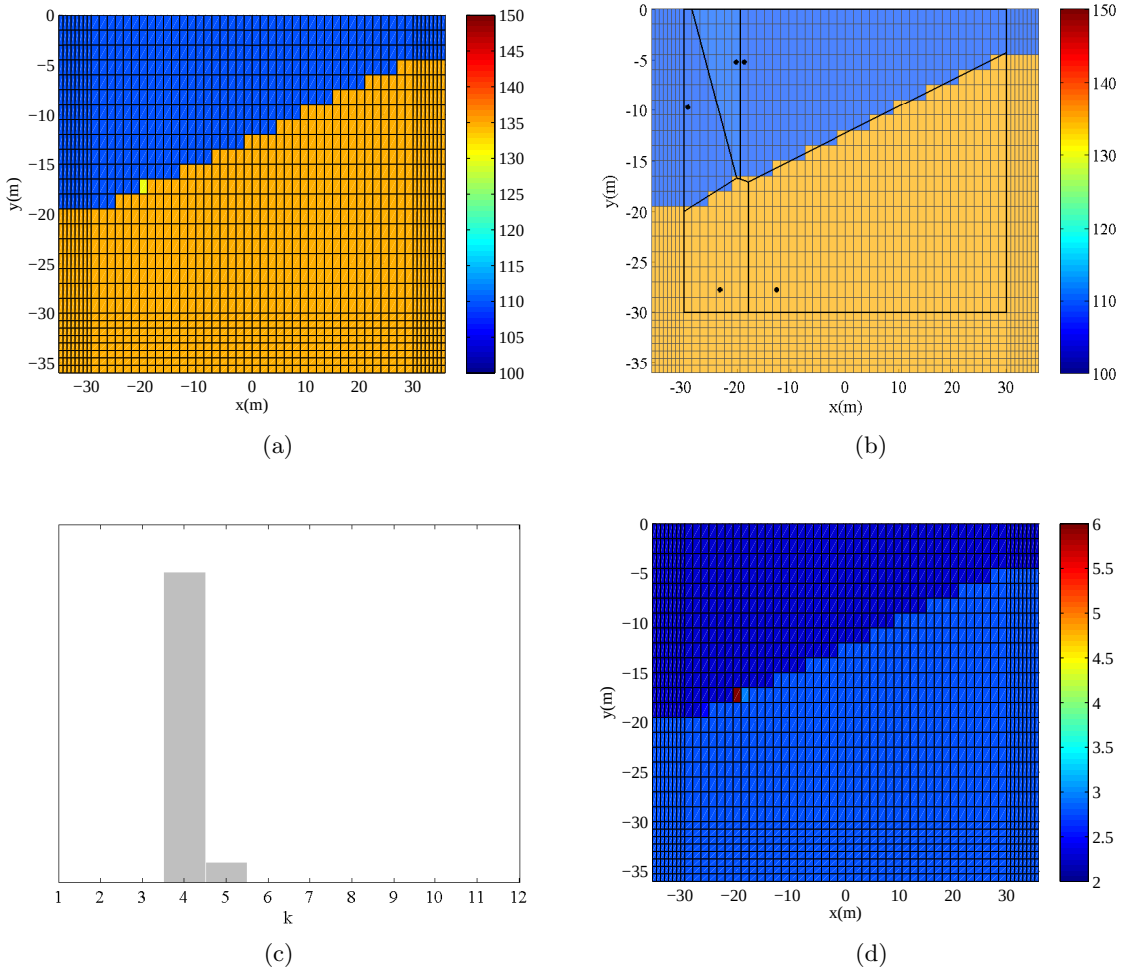

Figure 4.18: Reversible jump MCMC output for target profile B: (a) Average solution (posterior mean velocity field estimate) (b) Best solution which maximizes the posterior density (c) Posterior mass function $p(k|\mathbf{d}_{\text{obs}})$ of the number of cells in the Voronoi diagram (d) Estimated error map showing the pointwise variability of the post burn-in velocity draws.

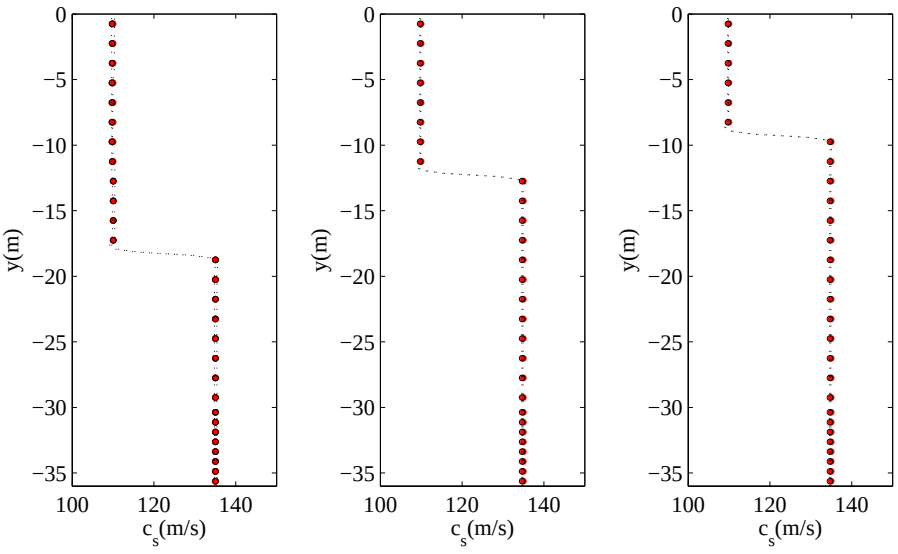

(a) $x = -21.75$ m (b) $x = 0.75$ m (c) $x = 11.25$ m

Figure 4.19: Cross-section profiles showing the true models (solid res dots), posterior mean estimates (black hollow dots) and 95% credible intervals for the posterior mean (black dotted line) corresponding to profile B.

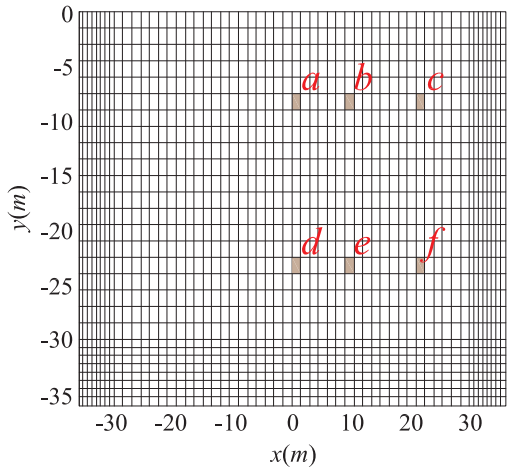

Figure 4.20: Configuration of the six benchmark elements for target shear wave velocity profile B.

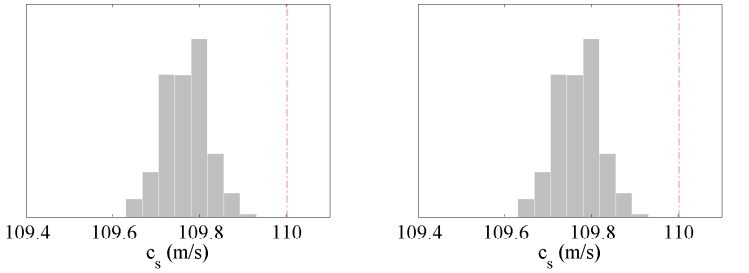

(a) c_s $(0.75, -8.25)$ (b) c_s $(9.75, -8.25)$

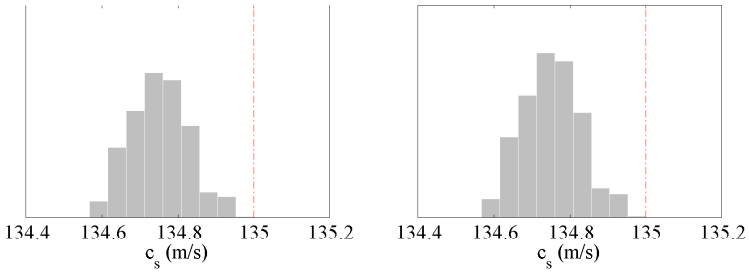

(c) c_s $(21.75, -8.25)$ (d) c_s $(0.75, -23.25)$

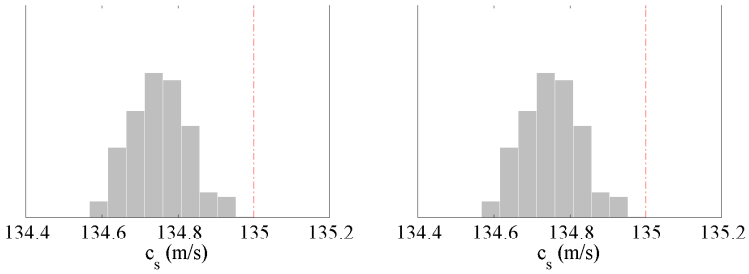

(e) c_s $(9.75, -23.25)$ (f) c_s $(21.75, -23.25)$

Figure 4.21: Marginal posterior density of the shear wave velocities and the corresponding target values (dashed line) at six selected elements a, b, c, d, e, and f (profile B).

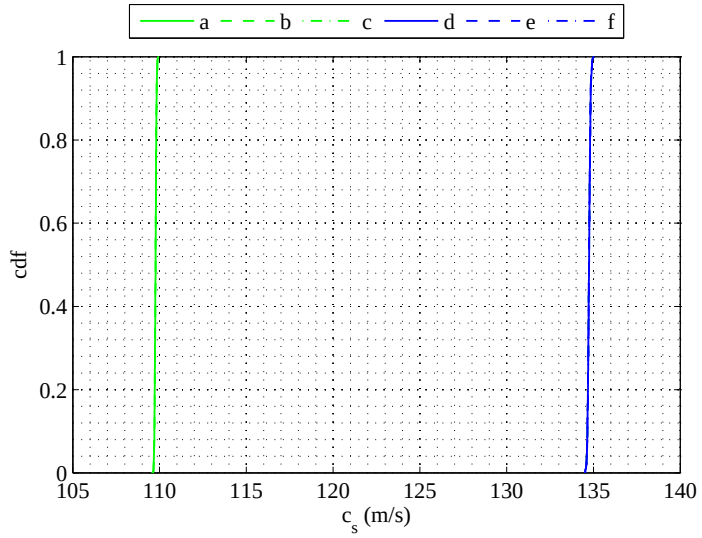

Figure 4.22: Posterior cumulative density function (cdf) of the shear wave velocities at six selected elements a, b, c, d, e, and f (profile B).

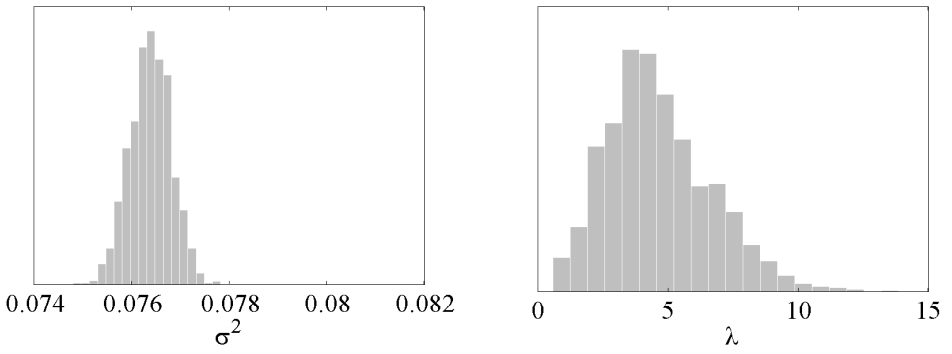

(a) Noise variance $p\left(\sigma_d^2|\mathbf{d}_{\text{obs}}\right)$

(b) Rate parameter in Poisson prior $p\left(\lambda|\mathbf{d}_{\text{obs}}\right)$

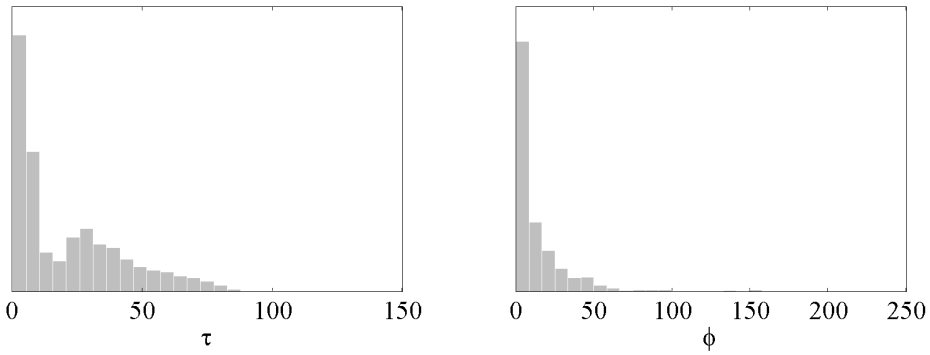

(c) Scale parameter of the Gaussian Markov random field prior $p\left(\tau|\mathbf{d}_{\text{obs}}\right)$

(d) $p\left(\phi|\mathbf{d}_{\text{obs}}\right)$

Figure 4.23: Marginal posterior density for model hyper-parameters (profile B).

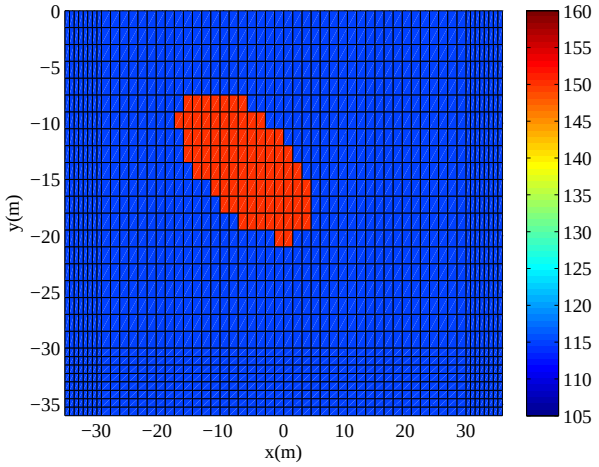

Figure 4.24: Target shear wave velocity profile C (the background velocity is $c_s = 115$ m/s and velocity of the ellipsoidal anomaly is $c_s = 150$ m/s)

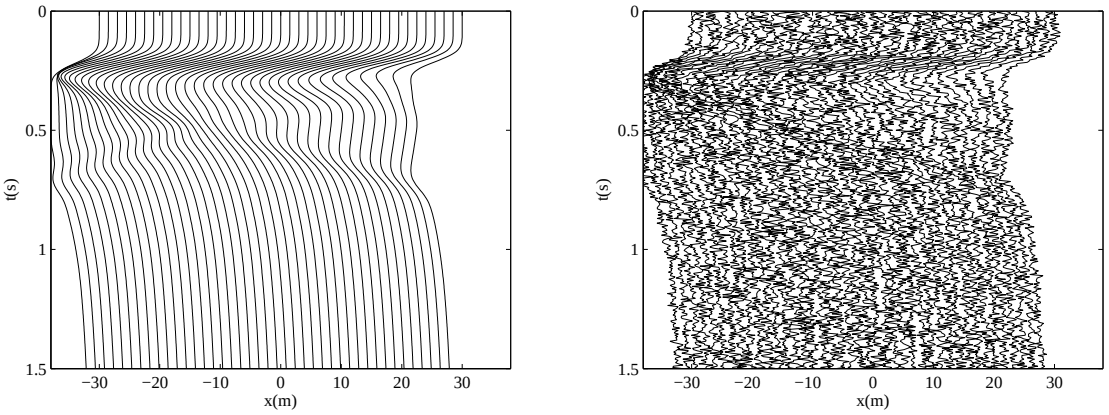

(a) (b)

Figure 4.25: (a) Displacement responses $u(\mathbf{x}, t)$ measured over the surface. Data is obtained by applying a uniformly-distributed Gaussian pulse with $f_{\max} = 15$ Hz over the entire surface of profile C. (b) Synthetic data: Measured displacement response at the ground level perturbed with 20% Gaussian noise

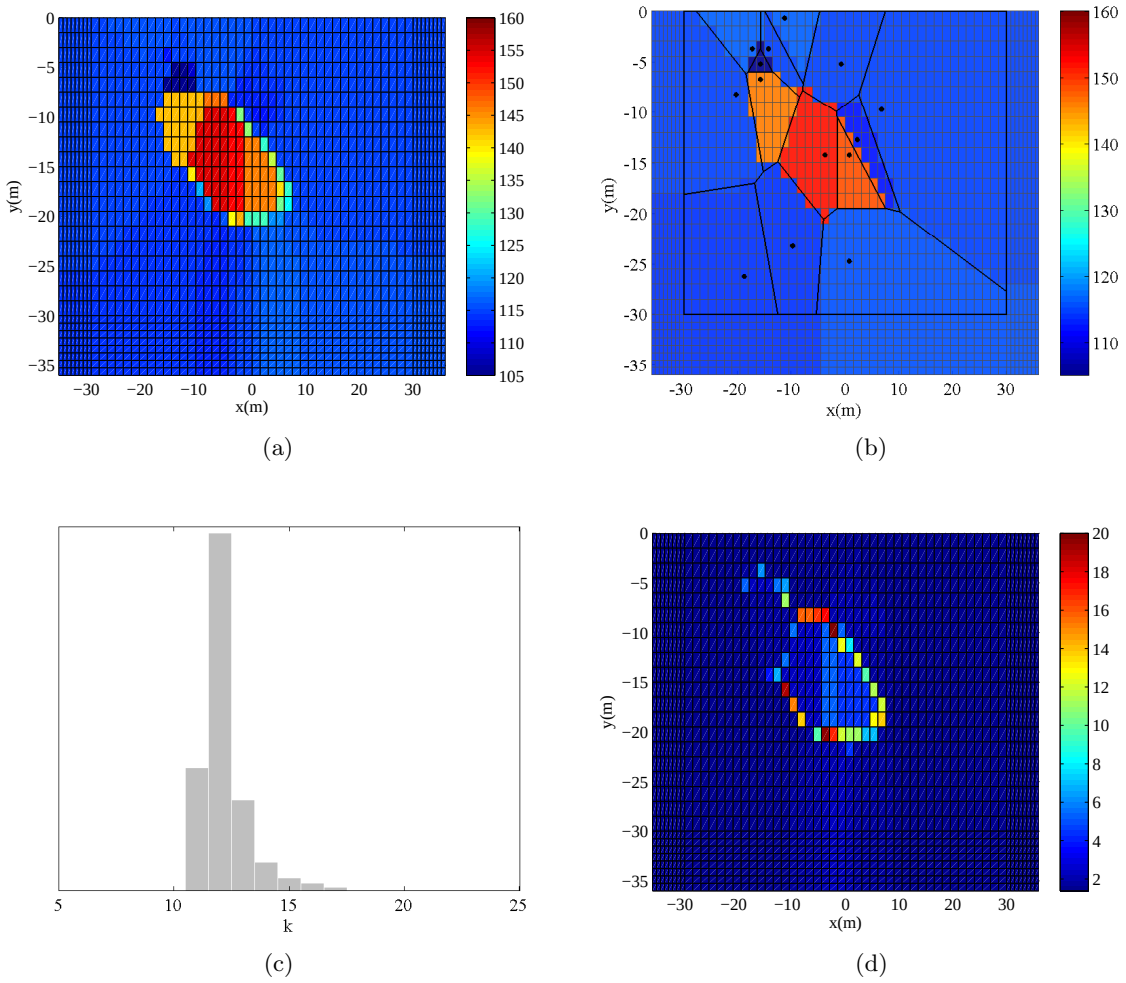

Figure 4.26: Reversible jump MCMC output for target profile C: (a) Average solution (posterior mean velocity field estimate) (b) Best solution which maximizes the posterior density (c) Posterior mass function $p(k|\mathbf{d}_{\text{obs}})$ of the number of cells in the Voronoi diagram (d) Estimated error map showing the pointwise variability of the post burn-in velocity draws.

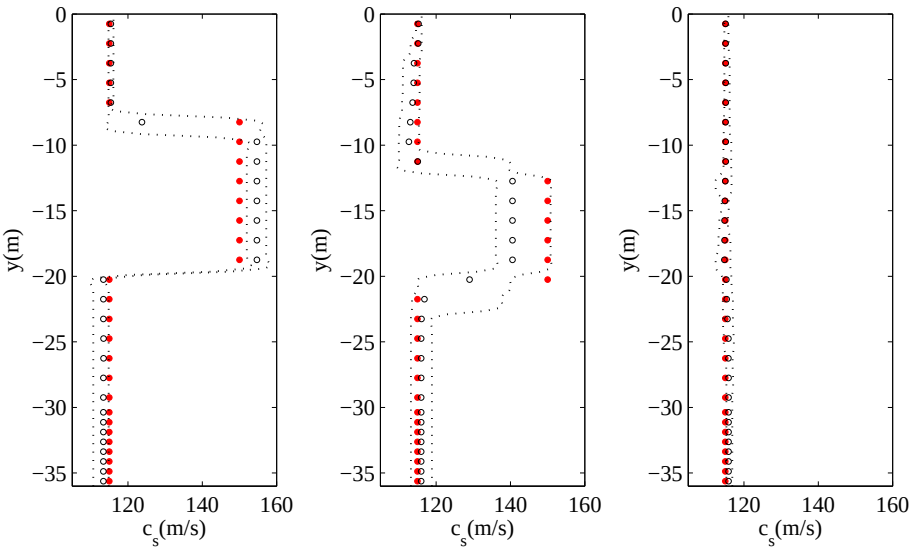

(a) $x = -6.75$ m (b) $x = 0.75$ m (c) $x = 11.25$ m

Figure 4.27: Cross-section profiles showing the true models (solid res dots), posterior mean estimates (black hollow dots) and 95% credible intervals for the posterior mean (black dotted line) corresponding to profile C.

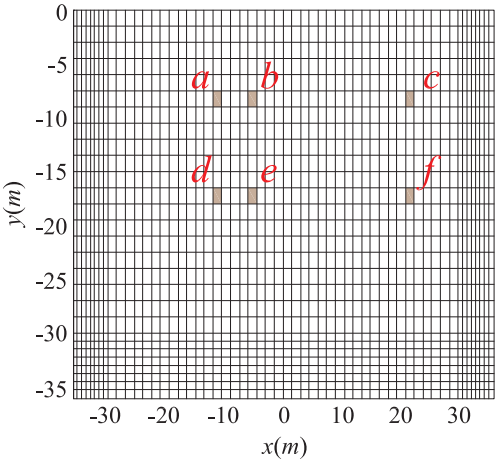

Figure 4.28: Configuration of the six benchmark elements for target shear wave velocity profile C.

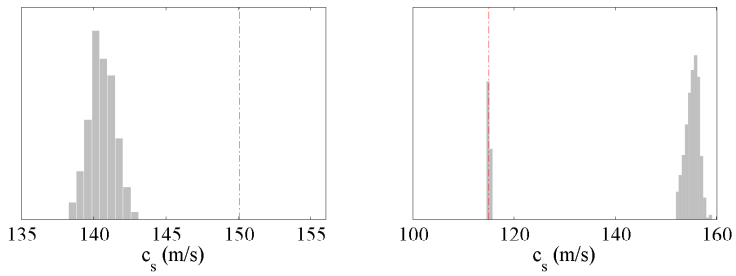

(a) c_s $(-11.25, -8.25)$ (b) c_s $(-5.25, -8.25)$

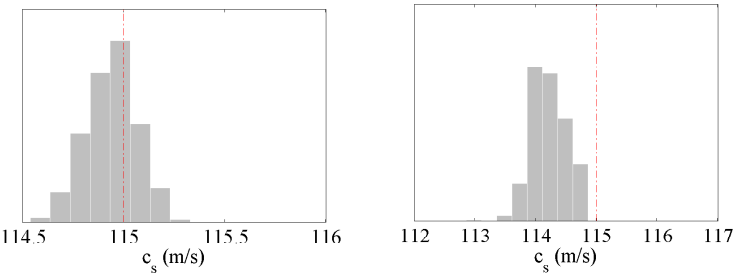

(c) c_s $(21.75, -8.25)$ (d) c_s $(-11.25, -17.25)$

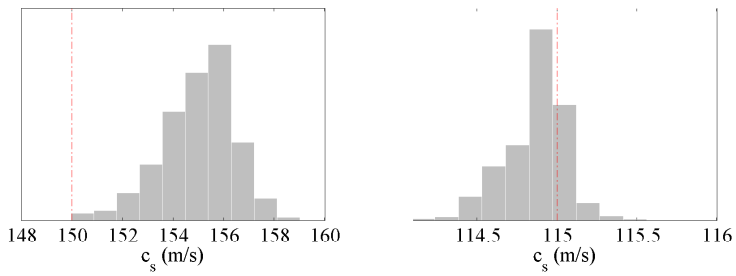

(e) c_s $(-5.25, -17.25)$ (f) c_s $(21.75, -17.25)$

Figure 4.29: Marginal posterior density of the shear wave velocities and the corresponding target values (dashed line) at six selected elements a, b, c, d, e, and f (profile C).

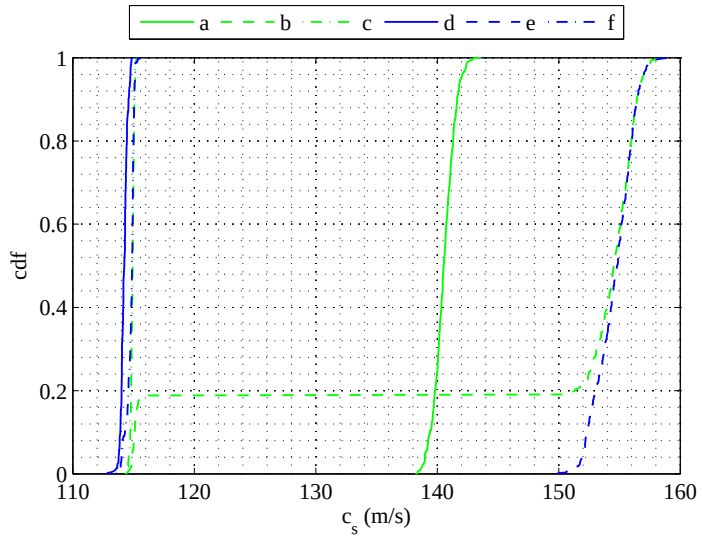

Figure 4.30: Posterior cumulative density function (cdf) of the shear wave velocities at six selected elements a, b, c, d, e, and f (profile C).

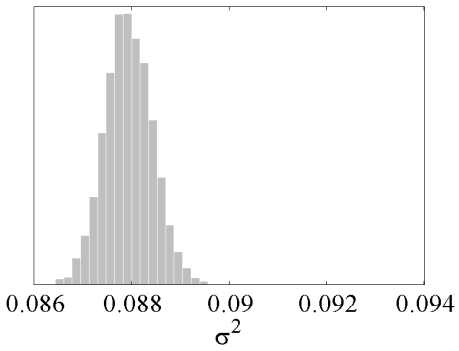

(a) Noise variance $p\left(\sigma^2|\mathbf{d}_{\text{obs}}\right)$

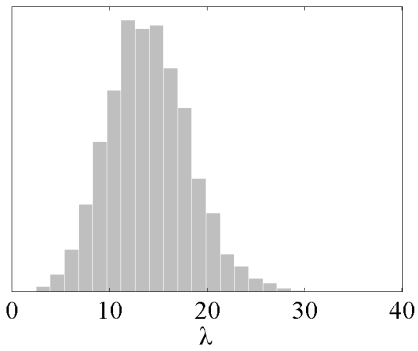

(b) Rate parameter in Poisson prior $p\left(\lambda|\mathbf{d}_{\text{obs}}\right)$

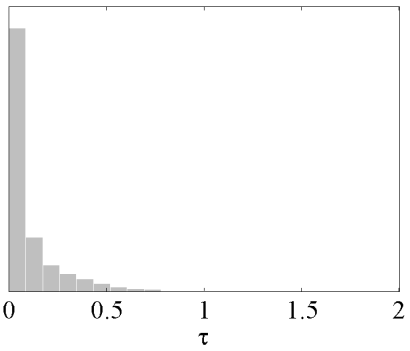

(c) Scale parameter of the Gaussian Markov random field prior $p\left(\tau|\mathbf{d}_{\text{obs}}\right)$

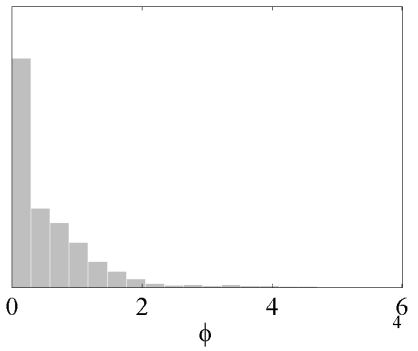

(d) $p\left(\phi|\mathbf{d}_{\text{obs}}\right)$

Figure 4.31: Marginal posterior density for model hyper-parameters (profile C).

4.6 Concluding Remarks

A Bayesian framework has been introduced for the identification of the spatially varying soil elastic characteristics of a heterogeneous unbounded earth. This defines an inverse medium problem in which the object of inference constructs a continuous random field. That is, an essentially infinite dimensional parameter space is to be deduced from a finite dimensional, sparse and noisy measurements, resulting in the ill-posed nature of the problem. A self-regularized dynamic parametrization of the shear wave velocity field is formulated based on the notion of Bayesian partition modeling. The method offers a reduced dimensional inversion technique by partitioning the velocity random field into a number of disjoint regions through a set of Voronoi tessellations. The number of tessellations, their geometry and weights (defining the intensity of the velocity field) dynamically vary during the inversion, in order to recover the subsurface formations. The method is specifically suitable when modeling subsurfaces with zoned structures and sharp material interfaces, where the field is not smooth enough to be adequately described by a correlation function, and common dimensionality reduction techniques such as Karhunen-Loève expansion. The reward of the approach is that the explicit regularization of the inverted profile by global damping procedures or even through imposition of priors, which carry smoothness constraints, (and might introduce subjectivity to the inference process), is not required. We further stabilize the inverse problem by assigning a proper Gaussian Markov random field prior within the tessellations. The prior constitutes the correlation structure across the tessellations stating the velocity value at a particular cell depends only on the velocity of the neighboring cells. A hierarchical structure is defined such that the level of correlation (smoothness of the process) is merely controlled by the data. The reversible jump MCMC algorithm was implemented to carry out the simulation of the resulting varying dimensional posterior density. The provided synthetic case indicates significant functionality of the inversion scheme to retrieve the benchmark subsurface profiles.

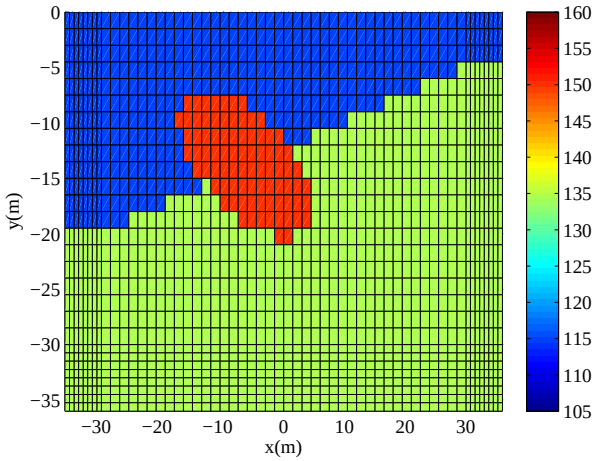

Figure 4.32: Target shear wave velocity profile D (the background velocities are c_s = 115 m/s and c_s = 135 m/s from top to bottom and velocity of the ellipsoidal anomaly is $c_s = 150$ m/s).

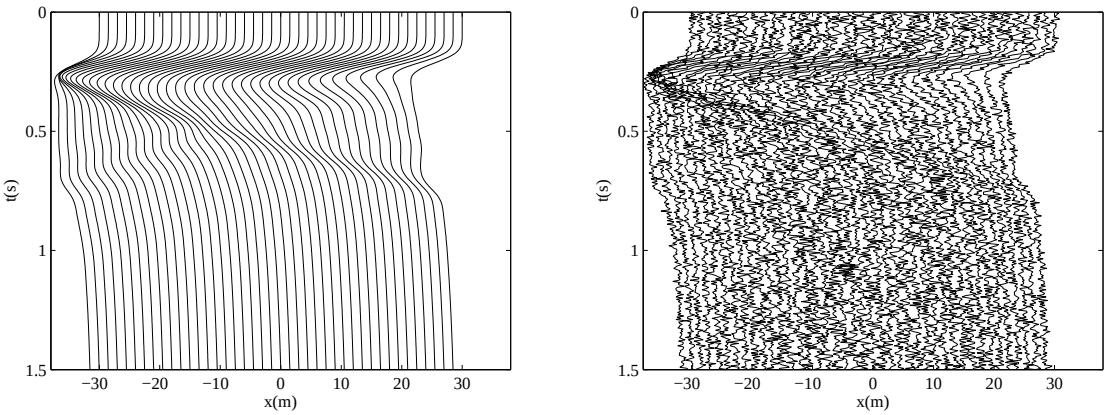

(a) (b)

Figure 4.33: (a) Displacement responses $u(\mathbf{x}, t)$ measured over the surface. Data is obtained by applying a uniformly-distributed Gaussian pulse with $f_{\max}$ = 15 Hz over the entire surface of profile D. (b) Synthetic data: Measured displacement response at the ground level perturbed with 20% Gaussian noise

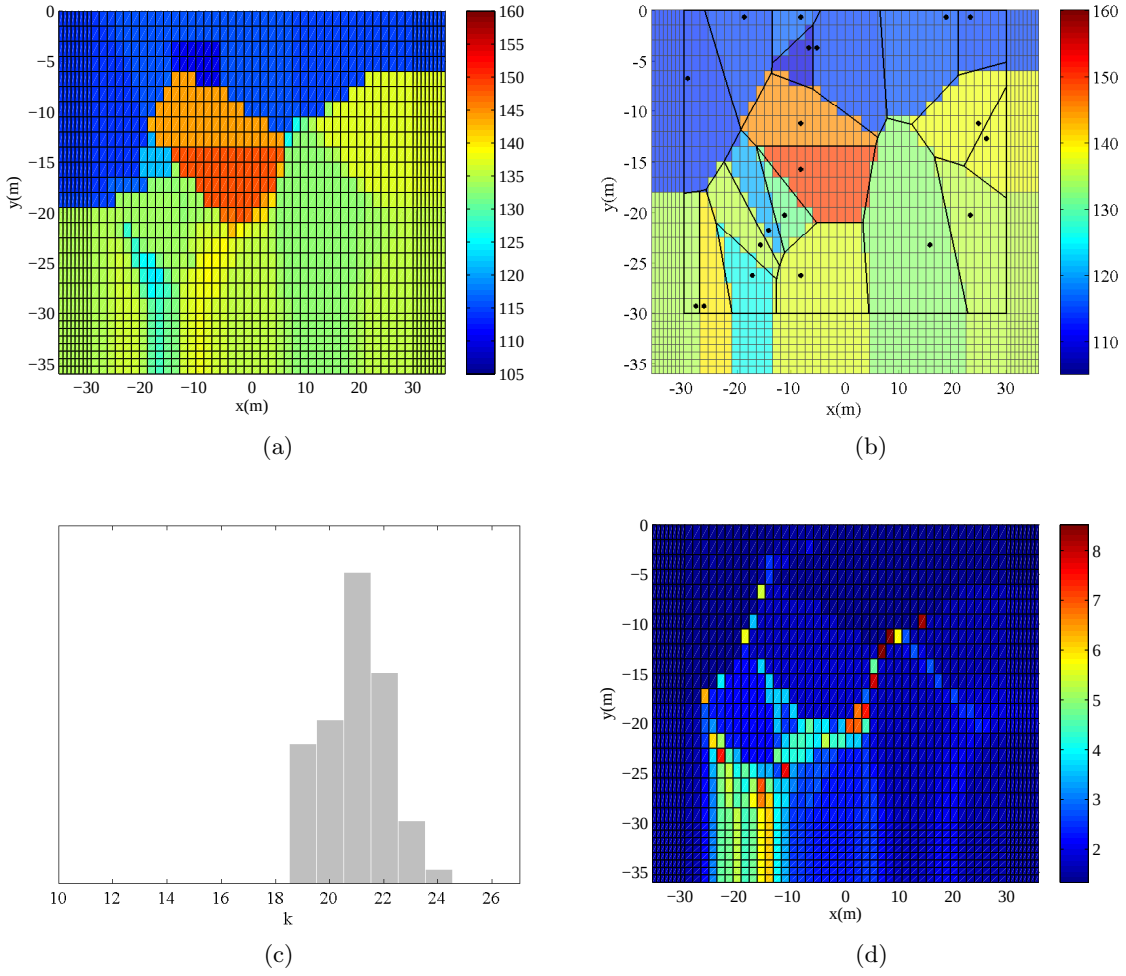

Figure 4.34: Reversible jump MCMC output for target profile D: (a) Average solution (posterior mean velocity field estimate) (b) Best solution which maximizes the posterior density (c) Posterior mass function $p(k|\mathbf{d}_{\text{obs}})$ of the number of cells in the Voronoi diagram (d) Estimated error map showing the pointwise variability of the post burn-in velocity draws.

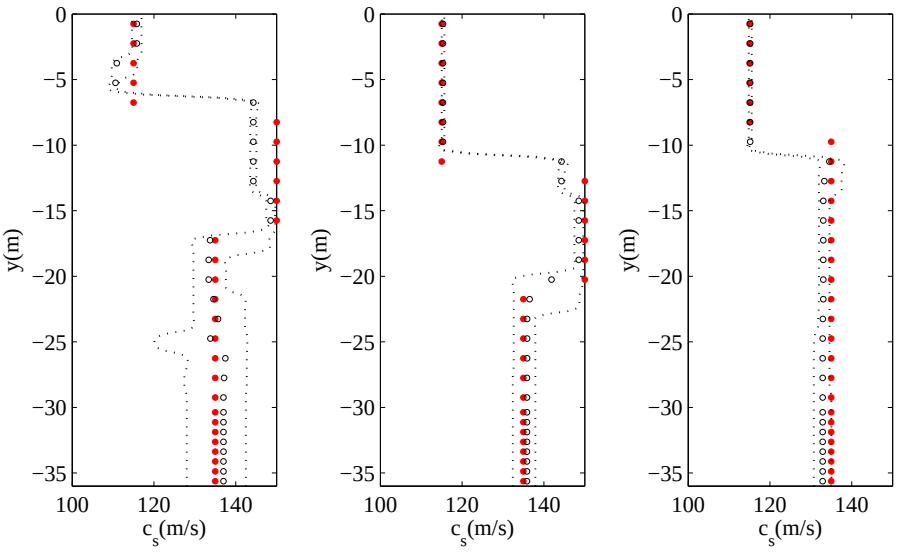

(a) $x = -11.25$ m (b) $x = 0.75$ m (c) $x = 11.25$ m

Figure 4.35: Cross-section profiles showing the true models (solid res dots), posterior mean estimates (black hollow dots) and 95% credible intervals for the posterior mean (black dotted line) corresponding to profile D.

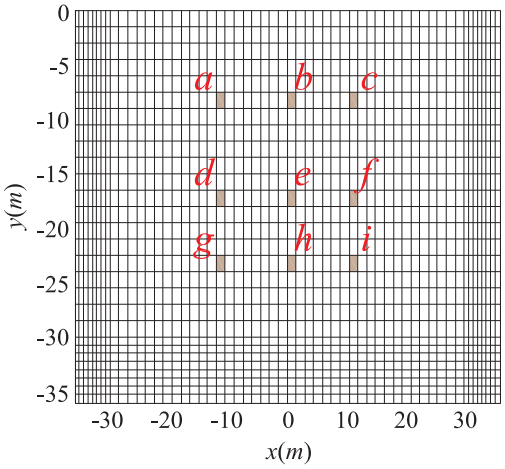

Figure 4.36: Configuration of the nine benchmark elements for target shear wave velocity profile D.

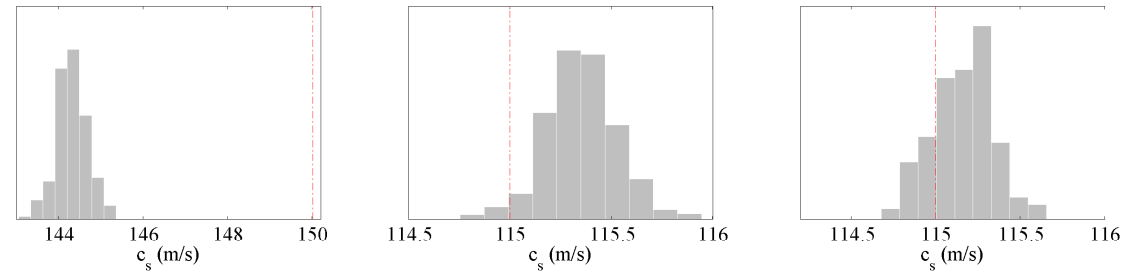

(a) c_s $(-11.25, -8.25)$ (b) c_s $(0.75, -8.25)$ (c) c_s $(11.25, -8.25)$

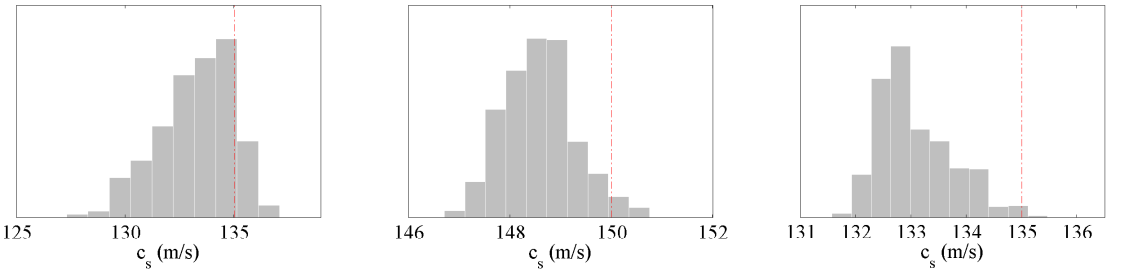

(d) c_s $(-11.25, -17.25)$ (e) c_s $(0.75, -17.25)$ (f) c_s $(11.25, -17.25)$

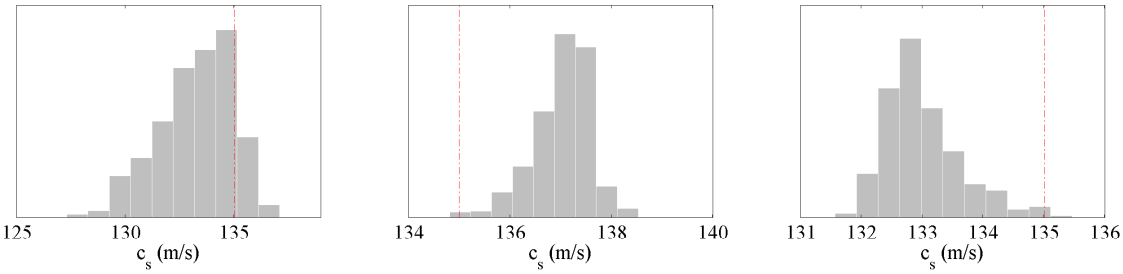

(g) c_s $(-11.25, -23.25)$ (h) c_s $(0.75, -23.25)$ (i) c_s $(11.25, -23.25)$

Figure 4.37: Marginal posterior density of the shear wave velocities and the corresponding target values (dashed line) at nine selected elements a, b, c, d, e, f, g, h and i (profile D).

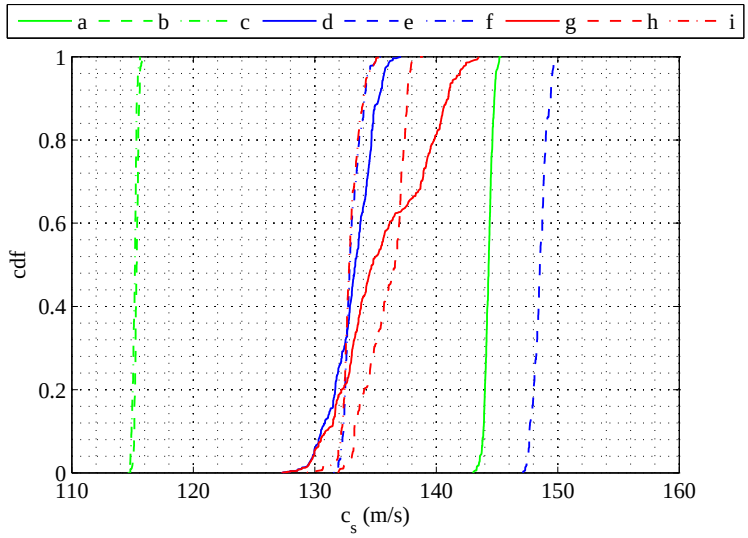

Figure 4.38: posterior cumulative density function (cdf) of the shear wave velocities at nine selected elements a, b, c, d, e, f, g, h and i (profile D).

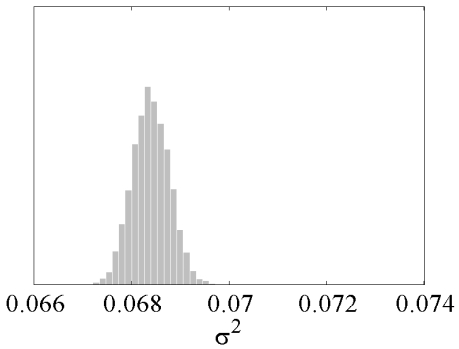

(a) Noise variance $p\left(\sigma_d^2|\mathbf{d}_{\text{obs}}\right)$

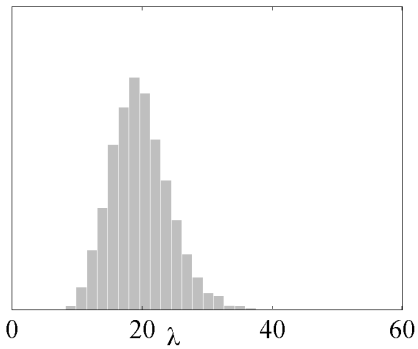

(b) Rate parameter in Poisson prior $p\left(\lambda|\mathbf{d}_{\text{obs}}\right)$

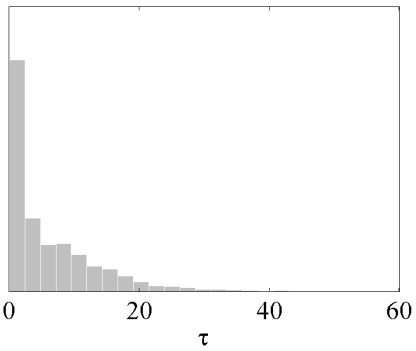

(c) Scale parameter of the Gaussian Markov random field prior $p\left(\tau|\mathbf{d}_{\text{obs}}\right)$

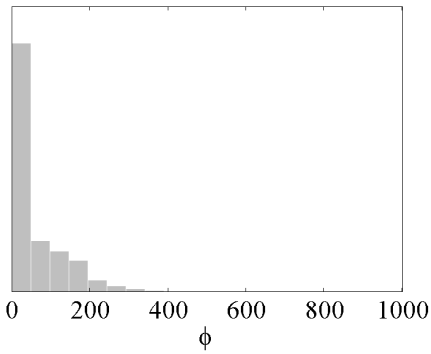

(d) $p\left(\phi|\mathbf{d}_{\text{obs}}\right)$

Figure 4.39: Marginal posterior density for model hyper-parameters (profile D).

5. JOINT STATES OF INFORMATION FROM DIFFERENT PROBABILISTIC GEO-PROFILE RECONSTRUCTION METHODS

5.1 Overview

Development of technologies for site characterization has grown at a faster pace compared to the development of decision-making methods required for the assimilation of inferences they generate. In the case of geophysical surveying, such dephase adds to the dependency on the use of expert's judgment in the interpretation of geophysical mappings. A systematic assimilation of this type of geo-surveying evidence is required, in particular for the integration of spatial geomorphological information (i.e. stratigraphy), characterized from different geophysical methods. This paper presents a methodology to address this challenge by the use of a probabilistic approach. A set of synthetic geophysical mappings are used to illustrate the applicability of the proposed methodology and its potential extrapolation to other scientific imaging disciplines.

5.2 Introduction

This paper introduces a methodology for integrating multiple types of evidence (i.e. theoretical, experimental and experts' beliefs), and multiple sources of geo-surveying information (e.g. image profiles from different geophysical methods), for the systematic assimilation of states of evidence into the mechanistic characterization of a given site. The same approach can be extrapolated to any other similar scientific imaging settings.

The overarching objective of the present work is to improve the number and quality of inferences related to site characterization based on geophysical site investigation. This aligns with the new scientific paradigm that asks for developing a scheme of work that can expedite the process of systematic evidence assimilation to significantly enhance the expert's judgment (i.e. "big data" paradigm). That means, to provide effective theoretical methods and computational applications to improve the expert's ability to systematically assimilate scientific evidence (Hey, 2009).

Here, better expert judgment means better decision-making, which translates into improved scientific and engineering practices (Kaynia *et al.*, 2008). This is particularly relevant on geo-engineering applications, where the challenge is to integrate geological, geophysical, geochemical, hydrogeological and geotechnical evidence, with varying spatial and time scales, and sometimes with varying sampling and modeling conditions. This integrated approach is required before, during, and after the design/analysis/instllation of engineering structures, or during the development of mid to long-term geo-processes.

Probability, in particular Bayesian theory, stands out as a way to facilitate the integration of geo-evidence since it allows for a translation of information content into the probability space, where this can be fully operated. In fact, Bayesian theory is revolutionizing the way in which science generate scientific inferences because of its ability to integrate, in a logical manner, a) experimental observations (data), b) model predictions and c) experts judgment (Robert, 2007).

Furthermore, investigations on the combination of logic and probability by Jaynes and Tarantola (Jaynes & Bretthorst, 2003; Tarantola, 2005) helped to define a generalization of the Bayes' theorem and created a beautiful, yet complex, mathematical "collaboration models", on which this paper is based. Where the Bayes' paradigm is now defined as only one possibility on a sounder framework to integrate scientific evidence. To be fair, it should be acknowledged that the promising use of advanced probability logic investigations depends on efficient computations. This, in fact, may become a limitation, particularly when the number of parameters required as part of the computational assimilation of evidence grows, since it requires the numerical sampling of multidimensional probability distributions (Gentle *et al.*, 2004).

The proposed methodology relies on the current expertise on probabilistic geophysical inversions found elsewhere (Tarantola & Valette, 1982; Cary & Chapman, 1988; Gouveia & Scales, 1998; Ulrych *et al.*, 2001; Malinverno, 2002; Dosso, 2002; Dettmer *et al.*, 2009; Medina-Cetina *et al.*, 2013), which allows for populating probability density functions of a material property at every point within the domain of interest. That is, representing the

solution to the inverse medium problem as a random field of mechanical parameters.

Therefore, by having this approach, the inherent ill-posed nature of the geophysical inversion problem is resolved (i.e. multiple mappings may generate the same 'measured' site response). But the major benefit of the probabilistic inversion is that it provides a measure of the spatial correlation structure of the resulting stratigraphy, and of the uncertainty associated to the inferences, something that cannot be achieved by typical optimization-based inversions. This approach provides a measure of the uncertainty on the geophysical estimates stemmed from the use of a mechanically-based forward model.

From the probabilistic definition of the geophysical inversion, it is thus possible to sample multiple likely realizations of the site's spatially varying material properties (considering that the solution to an inverse problem is not unique, and that several likely material profiles may be the 'true' image of the soil). From the sampling of this likely combinations, a probability map defining each 'geo-morphological' feature of interest can be populated (i.e. location and concentration of faults, soil layers, gas hydrates, salt layers, bottom rock, etc.).

This paper introduces a methodology to populate probability maps of geomorphological features that can be applied to characteristics observed in different geophysical investigations at the same location, and it introduces a methodology to operate across these maps to improve (or enrich) the resulting mechanistic stratigraphy representing the geological 'earth model'. A set of theoretically-based synthetic cases are presented to illustrate the applicability of the proposed method.

5.3 Rationale

This work focuses on geophysical investigations that generate soil images (or soil profiles) via the probabilistic solution of the inverse problem. This is defined by a collection of realizations of media properties $\mathbf{m}(\mathbf{x})$ representing mechanical parameters, distributed within the spatial domain of interest $\mathcal{D}$, where $\mathbf{x} = (x_1, x_2, x_3)^T$ is the position vector. The probabilistic solution of the inverse problem allows for defining full probability density functions of the vector of material property a, at any point $\mathbf{m}_a\left(\mathbf{x}^i\right)$, and for defining

the correlation structure between material properties at varying points (i.e., $\mathbf{m}_k\left(\mathbf{x}^i\right)$ and $\mathbf{m}_b\left(\mathbf{x}^j\right)$. Indexes a and b represent distinct material properties (e.g. electrical conductivity and P-wave velocity) and superscripts i and j represent distinct points in space.

The probabilistic inversion can be obtained by the use of the Bayesian paradigm, which maps a set of observations $\mathbf{d}_{\text{obs}}(\mathbf{y}, t)$ onto the random field $\mathbf{m}(\mathbf{x})$ (i.e. probabilistic solution of the inverse problem). The set of observations $\mathbf{d}_{\text{obs}}(\mathbf{y}, t)$ are the series of ground responses at different locations $\mathbf{y}$ and times t to a given excitation $P(\mathbf{z}, t)$, where $\mathbf{y}$ and $\mathbf{z}$ are typically located in the upper boundary of the domain $\mathcal{D}$ (figure 5.2). In a probabilistic setup, the process to define the mapping from $\mathbf{d}_{\text{obs}}(\mathbf{y}, t)$ to $\mathbf{m}(\mathbf{x})$ relies on the sampling of realizations of the medium's mechanical properties $\mathbf{m}(\mathbf{x})$ via a Marcov-Chain Monte-Carlo MCMC approach, and the use of a selection rule such as Metropolis-Hastings (Robert & Casella, 2004), which guarantees convergence to a stationary condition as the number of samples grows to infinite.

The MCMC sampling process consists in proposing realizations of $\mathbf{m}(\mathbf{x})$ that serve as input for the simulation of the forward problem defined by $\mathbf{d}_{\text{pred}}(\mathbf{y}, t) = g(P(\mathbf{z}, t), \mathbf{m}(\mathbf{x}))$, such that the model predictions $\mathbf{d}_{\text{pred}}(\mathbf{y}, t)$ can be evaluated at the same locations $\mathbf{y}$ and times t as the experimental observations $\mathbf{d}_{\text{obs}}(\mathbf{y}, t)$. $g(P(\mathbf{z}, t), \mathbf{m}(\mathbf{x}))$ is called the forward problem, which is typically a nonlinear mapping that transforms an earth model $\mathbf{m}(\mathbf{x})$ into a unique set of observations $\mathbf{d}_{\text{obs}}(\mathbf{y}, t)$. g is a mathematical/empirical operator that reflects the governing physics of the forward model (e.g. elastic wave propagation, diffusion of electrical potential, etc). According to Metropolis-Hastings rule, the probability of accepting the proposed earth model $\mathbf{m}(\mathbf{x})$ increases as the sampler moves toward the true earth model that generated the observations. The sampling is continued until specific convergence conditions are met (Cowles & Carlin, 1996).

As pointed out earlier, in a geophysical inverse modeling the unknown quantity of interest comprise a real-valued random field $\mathbf{m}(\mathbf{x})$, denoting the spatial variation of a material property. This signifies that the number of unknowns (i.e., pointwise values of the unknown field) is essentially infinite. In a computational setting, to construct a finite-

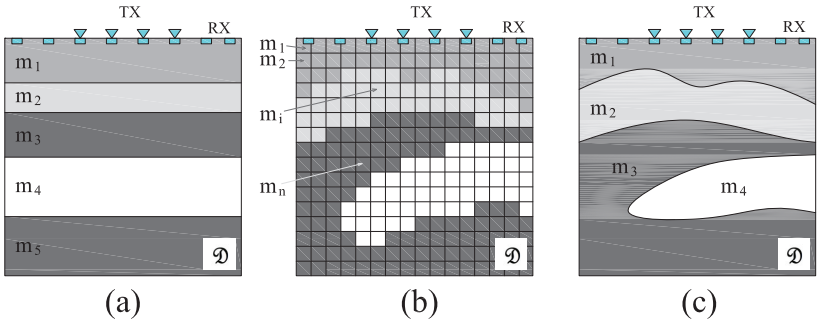

Figure 5.1: Parametrization of the material field (i.e. forming model vector $\mathbf{m}(\mathbf{x})$): (a) Layered model (b) Gridded model (c) Parametric model

dimensional (n dimensional) parameter vector $\mathbf{m}(\mathbf{x}) \simeq \{m_1, m_2, \ldots, m_k\}^T$ as a proxy for the continuous model, the unknown field must be effectively parameterized.

In a one dimensional earth model, where the material properties are assumed to only vary with depth (a reasonable assumption in near surface geotechnical investigation), the subsurface might be partitioned into a number of layers where the location of the interfaces and the corresponding material properties are defined as unknowns or random variables. As an example, a set of resistivity measurements might be interpreted in terms of a layered earth with k electrical resistivities and $k-1$ layer thicknesses (e.g. (Dettmer *et al.*, 2010; Minsley, 2011; Malinverno, 2002)). This parametrization pattern is referred to as a layered model as presented in figure 5.1a.

In case of two-dimensional heterogeneity, where the medium is no longer assumed horizontally stratified, the portion of the earth model under investigation might be gridded into rectangular blocks at a specified resolution, such that $\mathbf{m}(\mathbf{x})$ can be adequately represented at this finite set of grid blocks (see Figure 5.1b). The inverse problem, therefore, reduces to inferring the material properties at each grid location (e.g. (Mosegaard & Tarantola, 1995; Gouveia & Scales, 1998)). In a gridded parametrization, however, the dimensionality of the parameter space is generally tied to the dimensionality of the numerical discretization (Koutsourelakis, 2009). That is, if finite element method is used to discretize the forward

equation, the vector of unknowns is of the same dimension as the number of elements. Hence, depending on the resolution of the forward solver mesh, the number of parameters might rise up to thousands, which are to be estimated from the inherently sparse noisy data. This condition leads to ill-posed nature (solution non-uniqueness) of the inverse problem. Grid-based formulation, therefore, requires imposition of additional assumptions about the parameter field to alleviate the solution non-uniqueness. This is performed by global damping procedures which might introduce subjectivity to the inference process.

In a more efficient treatment of the inverse problem, instead of imposing regularity assumptions on large number of parameters, the problem is reduced to the estimation of a few parameters that controls the shape and location of the subsurface structures. In this type of models, known as "parametric models", definition of the subsurface geomorphological features is directly defined by a few inversion parameters (e.g. (Cardiff & Kitanidis, 2009; Bodin & Sambridge, 2009; Mondal *et al.*, 2010)). Methods of boundary detection and shape reconstruction such as level set protocol have been used in earth science applications such as hydrological mapping (Cardiff & Kitanidis, 2009) and reservoir modeling (Mondal *et al.*, 2010).

Notice that within an Uncertainty Quantification approach (UQ), such as by the use of the Bayesian paradigm for the solution of the probabilistic inversion discussed above, it is also possible to measure the influence of a set of hyper-parameters associated to the experimental observations and the model predictions (Medina-Cetina & Rechenmacher, 2010) (e.g., the amount and location of data, influence of boundary conditions, and even numerical parameters such as mesh resolution, time step integration, etc). A schematic representation of a probabilistic geophysical inversion is shown in Figure 5.2.

Once the probabilistic inversion is completed, it follows to define the geomorphological features of interest lying within the domain $\mathcal{D}$. This relies on the ability to delineate the subsurface geomorphological formations from inverted images of material properties $\mathbf{m}(\mathbf{x})$.

Let $h_q(\mathbf{x})$ be a function of spatial coordinates defining a geomorphological event q (e.g. a function representing stratigraphic characteristics such as location of layer inter-

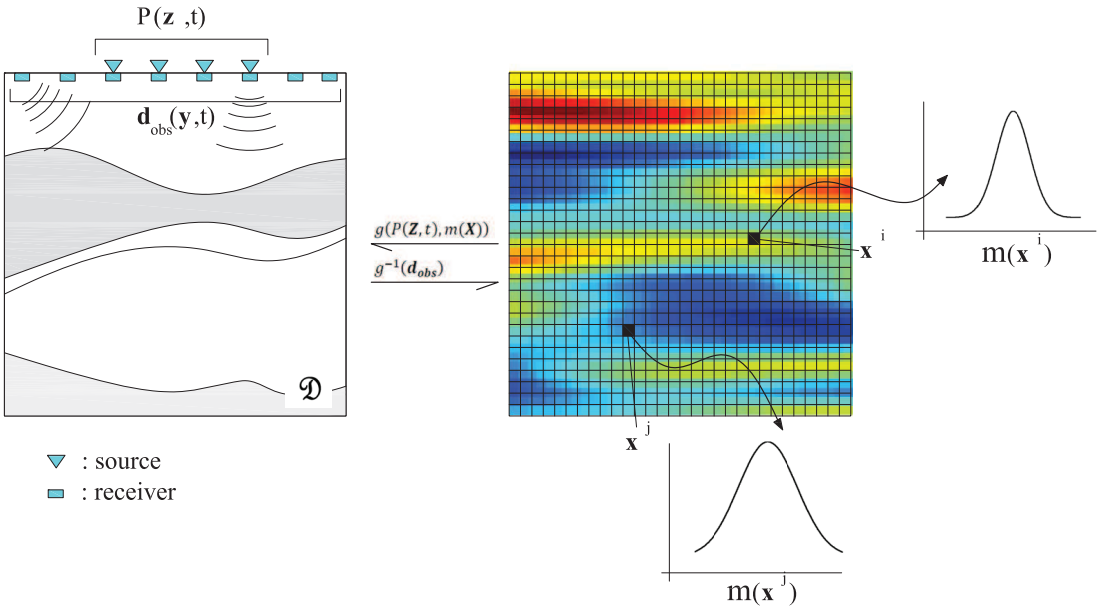

Figure 5.2: Schematic representation of a probabilistic geophysical inversion. Right to left (the forward problem): $\mathbf{d}_{\text{obs}} = g\left(P\left(\mathbf{z},t\right),\mathbf{m}\left(\mathbf{x}\right)\right)$ denotes the forward modeling: the process of obtaining the seismic response of earth to a given excitation $P\left(\mathbf{z},t\right)$ given the spatial variation of the subsurface material properties $\mathbf{m}\left(\mathbf{x}\right)$ is fully known. Left to right (the inverse problem): $g^{-1}\left(\mathbf{d}_{\text{obs}}\right)$. The inverse deduction of the spatial distribution of the subsurface material properties, given the data $\mathbf{d}_{\text{obs}}$ is observed over the surface. The solution to an inverse problem is not unique. i.e., at each point $\mathbf{x}^i$ in space $\mathcal{D}$, the value of the material property $\mathbf{m}\left(\mathbf{x}^i\right)$ is not certain. This uncertainty is fully quantified by a probability density function.

faces, boundary between different geological facies, location of faults, etc.). The proposed methodology, requires that the mapping from $\mathbf{m}(\mathbf{x})$ to $h_q(\mathbf{x})$ be systematized. Imaging the geomorphological structure from the reconstructed spatial variability of the property of interest (the mapping from $\mathbf{m}(\mathbf{x})$ to $h_q(\mathbf{x})$) requires the use of a classifier. This means, if the aim is to reconstruct the boundaries between geological facies, the classifier establishes the membership of each point in space in a given facies. Classification process is conducted by assigning values to an indicator function corresponding to each geomorphological feature q at each point $\mathbf{x}$. The indicator function $I_q(\mathbf{x})$ will assume a "zero" value if the geomorphological feature q is absent at point $\mathbf{x}$, and "one" if it is present.

For instance, consider a case of detecting concentration of gas hydrates (denoted by material D_1). From a single realization of $\mathbf{m}(\mathbf{x})$, a scanning of each point $\mathbf{x}$ for the feature q defined by the location of gas hydrates, $I_q(\mathbf{x})$ will yield regions of zeros and ones, where the sets of 'ones' will indicate the presence of gas hydrates:

$$I_q(\mathbf{x}) = \begin{cases} 1, & \mathbf{x} \in D_1 \\ 0, & \mathbf{x} \notin D_1 \end{cases} \tag{5.1}$$

The same approach could then be applied to delineate all the q geomorphological features of interest (e.g., transition between the soil units, concentration of materials, faults, etc.) using the same realization drawn from $\mathbf{m}(\mathbf{x})$. This is performed by properly defining the indicator function corresponding to each feature.

Defining the indicator function is not always a trivial task, specifically if the material properties are strongly heterogeneous. Numerous mathematical algorithms (e.g., k-means clustering algorithm, expectation-maximization algorithm, minimum-variance algorithm, etc.) are available to assign values of indicator function to poorly differentiated material fields (Wohlberg & Tartakovsky, 2009). Defining the identification function completes the classification process for a single realization of the material field, since pointwise values of the field are available at each grid location. In general classification problems, however,

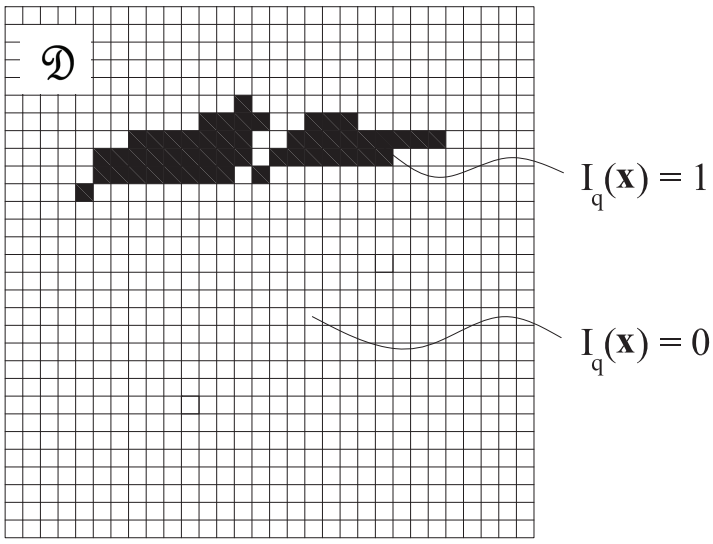

Figure 5.3: Schematic representation of the classification process; defining the identifier function.

there is an additional step to assign the value of the indicator function at points where measurements are not available. The definition of the optimal classifier is out of the scope of this work, but not the fundamental step on the proposed methodology to translate the expert's knowledge into a systematic identification of geomorphological features. A schematic representation of the classification process is shown in Figure 5.3. Details on how to perform a standard probabilistic classification can be found in (Denison *et al.*, 2002*b*).

Also, notice that in terms of computational accuracy, the higher the resolution of the media (i.e. discretization of the spatial domain in the forward model), the finer the definition of the topological features of interest. Here, it is worth mentioning that if a layered or parametric model is used, since the shape of the subsurface structure of interest (e.g. boundaries between material zones and geologic facies) is directly modeled as an inversion

parameter, the classification step is skipped. The case study presented in this paper is parameterized as a layered model.

Since the resulting classification (binary) mapping can be repeated n times by drawing different realizations from $\mathbf{m}(\mathbf{x})$, every time that a realization is presented to the classifier, a new binomial mapping $I_q(\mathbf{x})$ is computed (see figure 5.4). After sampling sufficient n realizations, a smooth description of the topological regions can be retrieved in the form of relative frequency measures at each point $\mathbf{x}$, leading to the definition of a probability distribution $f(h_q(\mathbf{x}))$, the integral of which equals to one. This distribution leads the probability of finding the geomorphological feature q at a point $\mathbf{x}$, which can be simply defined as the result of a 'probabilistic classification' (Duda *et al.*, 2001). The described procedure to construct $f(h_q(\mathbf{x}))$ is summarized in the workflow presented in figure 5.5. A schematic representation of the probabilistic classification process is shown in Figure 5.4.

Provided that r geophysical investigations are performed at the same site and within the same domain $\mathcal{D}$, it is anticipated that distinct geomorphological features will be defined. In fact, some will be able to identify specific features better than others, and some will identify some features that the others will not, since the 'physics' behind each profile's reconstruction method are different. However, when implementing the methodology described above, it is not only the identification of the geomorphological feature q what is relevant, but the degree of certainty to find it. Consequently, it is possible to generate r distinct probability maps of the q feature $f(h_q(\mathbf{x}))_r$, which can now be operated in the probability space to produce joint states of information based on the use of different geophysical methods. As a result, an 'enriched' spatial geological model can be produced with uncertainty measures. Below, two basic operators are proposed to operate the mappings $f(h_q(\mathbf{x}))_r$, and later these are illustrated when applied to a couple of synthetic cases.

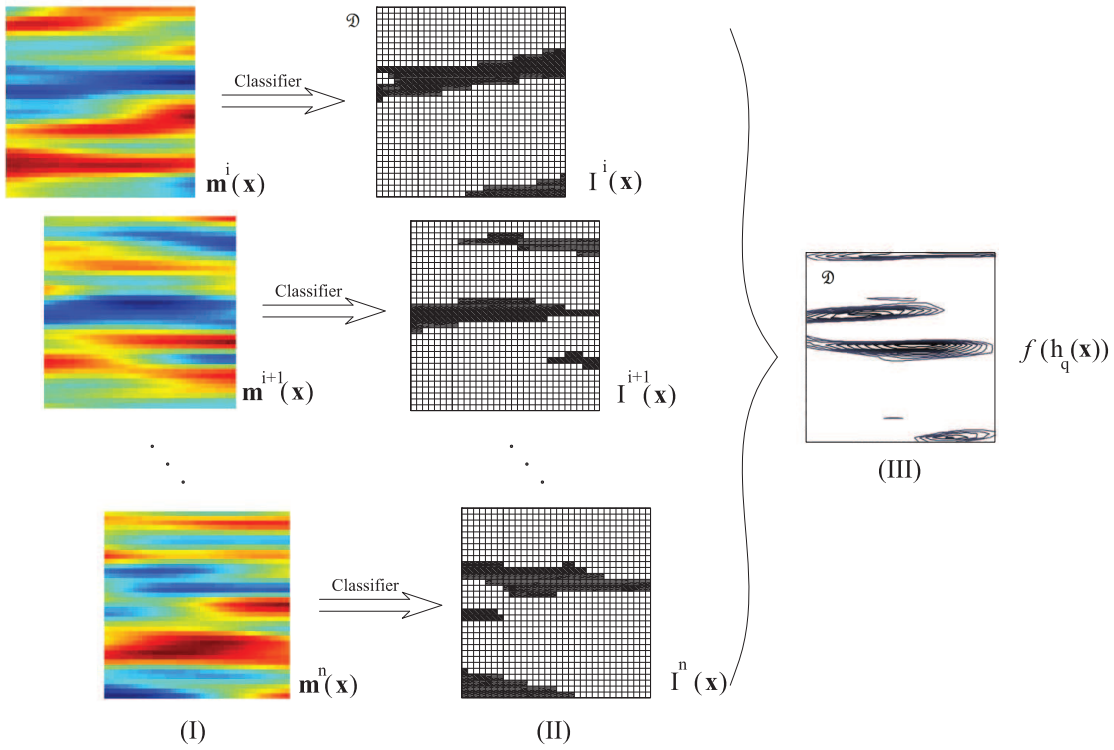

Figure 5.4: Schematic representation of the probabilistic classification process:
(I): Random realizations from $\mathbf{m}(\mathbf{x})$,
(II): Corresponding binomial mappings (defining the identifier function for each realization of the material random field) $h_q(\mathbf{x})$,
(III): Joint probability distribution $f(h_q(\mathbf{x}))$ which gives the probability of occurrence of geomorphological event h_q at point $\mathbf{x}$

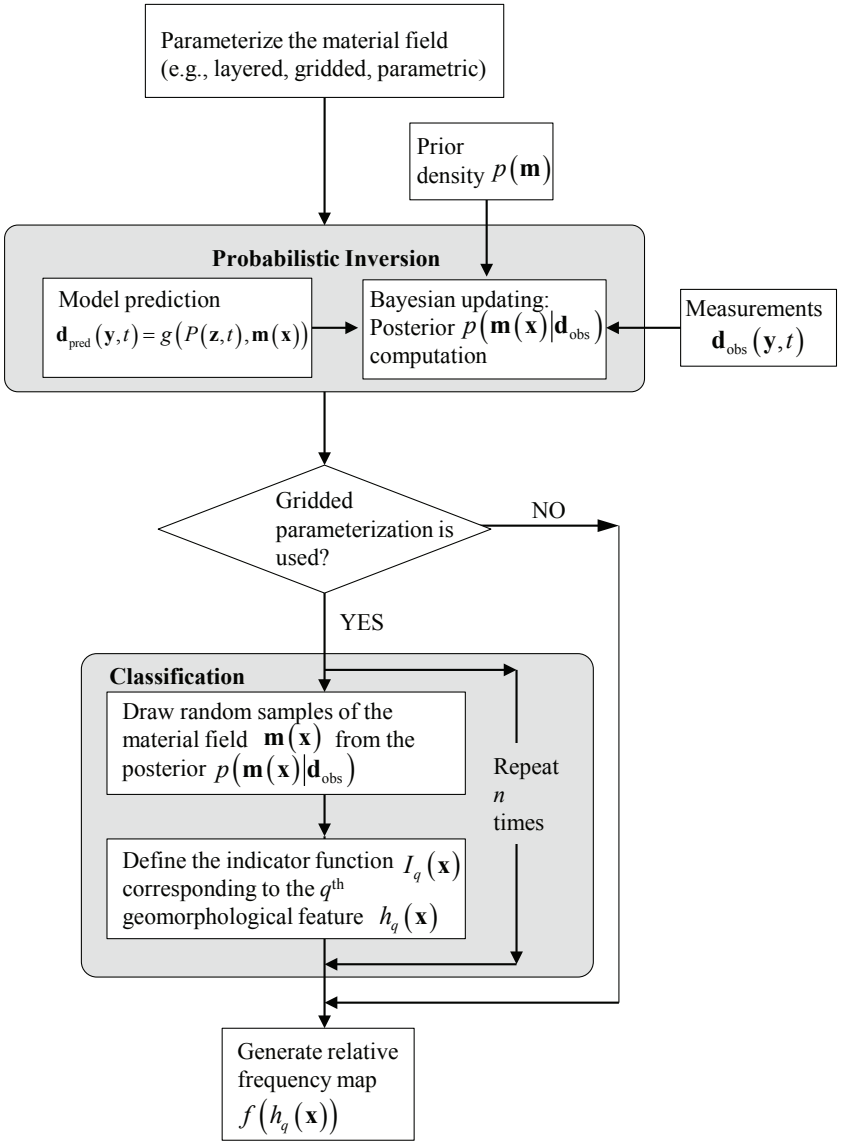

Figure 5.5: Workflow of computing the probability of finding geomorphological event q at point $\mathbf{x}$: $f(h_q(\mathbf{x}))$

5.4 Fundamentals of the Bayesian Approach to Inverse Problems

A Bayesian inversion consists in generating a probabilistic mapping of a set of observations $\mathbf{d}_{\text{obs}}(\mathbf{y}, t)$ onto a random field $\mathbf{m}(\mathbf{x})$. The inverse deduction of the earth model (i.e., full descriptions of both the location of the geomorphological features and spatially variable material properties) calls for a 'probabilistic calibration', which consists in mapping the ground response to a geophysical excitation $\mathbf{d}_{\text{obs}}$ onto governing physical parameters $\mathbf{m} = \mathbf{m}(\mathbf{x})$, embedded in each forward mechanical model. The following relationship holds:

$$\mathbf{d}_{\text{obs}} = g(\mathbf{m}(\mathbf{x})) + \boldsymbol{\epsilon} \tag{5.2}$$

where $g(\mathbf{m})$ (presented as $g(P(\mathbf{z}, t), m(\mathbf{x}))$ in the previous section) is the mathematical operator which captures the physics of the forward model. $\boldsymbol{\epsilon}$ is the random error component which quantifies the deviation between model prediction and measurements. This random term encompass both measurement and theoretical errors, where the latter is defined as the discrepancy between the model predictions and the true process due to the model not fully capturing the governing physics.

The Bayesian paradigm stands out as a suitable tool to define the proposed mapping. Because, it combines the prior knowledge about the model parameters (i.e. expert's judgment), the evidence carried by the data (i.e. experimental observations), and the evidence provided by the physical theory (i.e. model predictions), in order to define the posterior density. The posterior represents the full description of the model parameters in terms of a density function $p(\mathbf{m}|\mathbf{d}_{\text{obs}})$ (Robert, 2007). It also reflects any interventions in the solution of the inverse problem (e.g. via changes on the experimental observations, model predictions and expert's beliefs), by updating the probabilistic solution to the inverse problem. The Bayesian formulation for the solution to an inverse problem is defined as

$$p(\mathbf{m}|\mathbf{d}_{\text{obs}}) = \frac{p(\mathbf{d}_{\text{obs}}|\mathbf{m})\, p(\mathbf{m})}{\int_{\mathcal{M}} p(\mathbf{d}_{\text{obs}}|\mathbf{m})\, p(\mathbf{m})\ \mathrm{d}\mathbf{m}} \tag{5.3}$$

where $p(\mathbf{m})$ is called the prior density, which quantifies the initial uncertainty about the

material parameters. Ideally, this density limits the space of plausible parameters by giving higher probability to those which describe the data more closely. The likelihood function $p\left(\mathbf{d}_{\text{obs}}|\mathbf{m}\right)$ characterizes the data random behavior with respect to the model predictions, and is the probability that the observed realization $\mathbf{d}_{\text{obs}}$ is produced by model $\mathbf{m}$. $\mathcal{M}$ denotes the space of admissible model parameters.

By assuming that the random error components $\boldsymbol{\epsilon} = (\epsilon_1, \ldots, \epsilon_n)^T$ are such that $\boldsymbol{\epsilon} \overset{iid}{\sim} \mathcal{N}\left(\mathbf{0}, \sigma^2\mathbf{I}_n\right)$, the likelihood function is defined with reference to a multivariate normal density as

$$p\left(\mathbf{d}_{\text{obs}}|\mathbf{m}\right) = \frac{1}{\left[(2\pi)^n|\mathbf{C}_d|\right]^{1/2}} \exp\left[-\frac{1}{2}\left(g\left(\mathbf{m}\right) - \mathbf{d}_{\text{obs}}\right)^T \mathbf{C}_d^{-1}\left(g\left(\mathbf{m}\right) - \mathbf{d}_{\text{obs}}\right)\right] \tag{5.4}$$

n is the number of observations, and $\mathbf{I}_n$ is an $n \times n$ identity matrix, and $\mathbf{C}_d = \sigma^2\mathbf{I}_n$ is the covariance of the error term. More complex likelihood models which could account for the spatial dependence of the data, non-Gaussian error structures or capture events such as sensor miscalibration could also be formulated. The quantity in the denominator of equation 5.3, called the marginal likelihood, (the probability of observing the data $\mathbf{d}_{\text{obs}}$) is a normalizing constant, such that the posterior is integrated to one.

As it was mentioned earlier, due to the inherent high-dimensional nature of the problem (i.e. the finer the discretization of the problem the higher the resolution of the geophysical imaging), computing posterior moments normally requires performing high-dimensional integrations. This poses a major computational challenge for the Bayesian formulation of inverse problems. The computation of the posterior requires most of the times a numerical solver such as the Markov-Chain Monte-Carlo method MCMC, along with a decision rule (e.g., the Metropolis-Hastings M-H algorithm). These guarantee convergence to the target posterior as the number of samples grows (Robert & Casella, 2004). A summary of the MCMC-MH approach is included in the Appendix for further reference. In this study probabilistic inversion is carried out for two sets of geophysical data; seismic and electrical

resistivity. The next two sections are dedicated to introduce the basics of the forward model and formulation of the inverse problem for each geophysical survey.

5.5 Vertical Electrical Sounding (VES)

The electrical resistivity sounding is comprised of inverse deduction of the spatially variable resistivity of the subsurface $\rho(z)$ from a set of four-electrode (two transmitter-two potential) readings placed on the ground. The two current electrodes are deployed to introduce an electrical circuit into the earth and the induced potential difference (voltage) is recorded by the two potential electrodes. On the surface of a horizontally layered soil the electrical potential $V(x)$ at a distance x from a grounded electrode carrying direct current I is given by (Koefoed, 1979): (Figure 5.6)

$$V(x) = \frac{I_{\mathtt{DC}}}{2\pi} \int_0^\infty T(\lambda)\, J_0(\lambda x)\, \mathrm{d}\lambda \tag{5.5}$$

where $T(\lambda) = \rho_1[1 + 2K(\lambda)]$ is known as the transfer function of resistivities and layer thicknesses of the model. $K(\lambda)$ is called the Stefanesco kernel function (Stefanesco *et al.*, 1930) of resistivity which is a function of layer parameters and identifies the departure in response of a homogeneous half space from the horizontally layered earth. ρ_1 is the resistivity of the upper layer, λ is the integration variable (wavenumber), and J_0 is the Bessel function of the the first kind of zeroth order.

With the measurements of voltage, the apparent resistivity (i.e., the resistivity of an electrically homogeneous and isotropic half space which generates the actual measurements) ρ_a can be found for any type of electrode configuration. The Schlumberger arrangement is well suited for the purpose of this 1D profiling, since it can achieve high penetration depth with current electrode separation sufficiently large (Parasnis, 1997).

Resistivity sounding survey data is presented as a smooth apparent resistivity curve plotted on a log-log graph. The field procedure for Schlumberger sounding consists of centering the potential probes at a fixed location, while the current electrodes are shifted apart in steps. The voltage readings are made successively as the separation between the

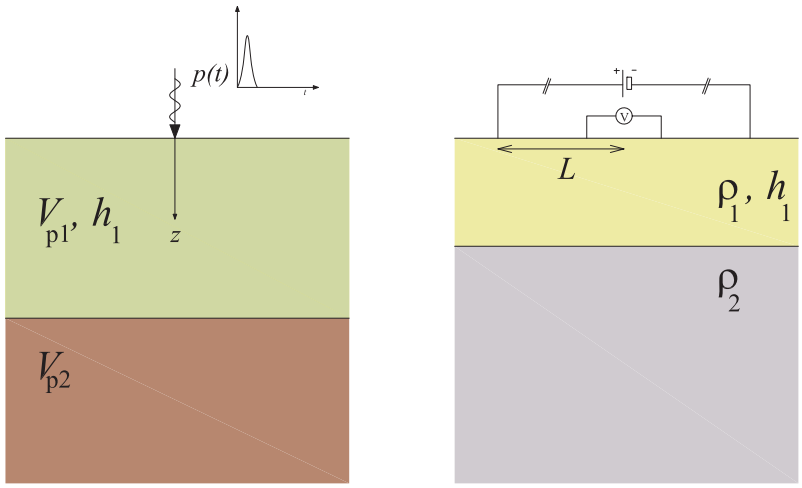

Figure 5.6: Problem configuration (benchmark).
Left: Acoustic imaging with a Gaussian pulse type load excitation over the surface.
Right: Vertical electrical sounding with Schlumberger electrode configuration.

current electrodes expands. Assuming that conductivity varies with depth only, as the separation between the potential and current electrodes grows, the current lines samples from increasingly deeper levels in the subsurface, resulting in observed variations in the apparent resistivity readings.

Given the spatial variation of the layer resistivities with depth, the forward model returns the predicted vector of apparent resistivity denoted by ρ_a. The apparent resistivity for the Schlumberger configuration is given by (Koefoed, 1979):

$$\rho_a(L) = L^2 \int_0^\infty T(\lambda)\, J_1(\lambda x)\, \lambda \mathrm{d}\lambda \tag{5.6}$$

where L is the one-half of the current electrode separation and J_1 is the first order Bessel function. Transform $T(\lambda)$ constructed by recurrence formulae for $k-1$ layers resting on an kth layer (infinite substratum) is given by:

$$T_j(\lambda) = \begin{cases} \rho_j \frac{1-\kappa_j \upsilon_j}{1+\kappa_j \upsilon_j} & \text{if } j = k-1 \\ \frac{W_j(\lambda)+T_{j+1}(\lambda)}{1+W_j(\lambda)T_{j+1}(\lambda)/\rho_j^2} & \text{if } j = k-2, k-3, \ldots, 1 \end{cases} \tag{5.7}$$

where $\kappa_j = \frac{\rho_j - \rho_{j+1}}{\rho_j + \rho_{j+1}}$, $W_j(\lambda) = \rho_j \frac{1-\upsilon_j}{1+\upsilon_j}$,and $\upsilon_j = \exp(-2h_j\lambda)$ in equation 5.7. h_j and ρ_j denote layer thickness and resistivity of the jth layer, respectively. The transform $T(\lambda) = T_1(\lambda)$ in equation 5.6 is found by recursive application of equation 5.7, starting from $j = k - 1$. More details on the VES formulation can be found in (Parasnis, 1997).

The integral in equation 5.6 (called Hankel J_1 transform), can be carried out numerically using the method of digital linear filtering (Ghosh, 1971*a*,*b*; Guptasarma & Singh, 1997). The Hankel J_1 transform is solved by a 140-point filter proposed in (Guptasarma & Singh, 1997).

The inverse electrical resistivity problem is constructed according to equation 5.3:

$$p\left(\mathbf{m}_{\texttt{VES}}|\mathbf{d}_{\text{obs}}^{\texttt{VES}}\right) \propto p\left(\mathbf{d}_{\text{obs}}^{\texttt{VES}}|\mathbf{m}_{\texttt{VES}}\right) p\left(\mathbf{m}_{\texttt{VES}}\right) \tag{5.8}$$

where $\mathbf{d}_{\text{obs}}^{\texttt{VES}} = (\rho_{a_1}, \rho_{a_2}, \ldots, \rho_{a_{n_{\texttt{VES}}}})^T$ is the vector of noisy apparent resistivity measurements collected successively as the separation between the current electrodes expands in steps, and $n_{\texttt{VSS}}$ is the number of data points. $\mathbf{m}_{\texttt{VES}} = (\rho_1, \rho_2, \ldots, \rho_k, h_1, h_2, \ldots, h_{k-1}, \sigma_{\texttt{VES}})^T$ is the parameter vector associated to the a k layer soil model. Hyper-parameter $\sigma_{\texttt{VES}}$ is the variance of the resistivity data which is appears in the likelihood function:

$$p\left(\mathbf{d}_{\text{obs}}^{\texttt{VES}}|\mathbf{m}_{\texttt{VES}}\right) \propto \frac{1}{\sigma_{\texttt{VES}}^{n_{\texttt{VES}}}} \exp\left\{ \frac{\sum_{i=1}^{n_{\texttt{VES}}} \left(d_{\text{obs}_i}^{\texttt{VES}} - g\left(\mathbf{m}_{\texttt{VES}}\right)\right)^2}{2\sigma_{\texttt{VES}}^2} \right\} \tag{5.9}$$

The above equation is a simplified representation of equation 5.4, given the assumption that uncertainty associated with the data is multi-variate normal with constant variance, and data points are independent of each other. $g\left(\mathbf{m}_{\texttt{VES}}\right)$ is defined in equation 5.6. The prior density is defined as $p\left(\mathbf{m}_{\texttt{VES}}\right) \propto \frac{1}{\sigma_{\texttt{VES}}^2}$. This prior signifies that the prior on parameters $(\rho_1, \rho_2, \ldots, \rho_k, h_1, h_2, \ldots, h_{k-1})^T$ and $\log(\sigma_{\texttt{VES}})$ are uniform in $(0, \infty)$.

5.6 Vertical Seismic Sounding (VSS)

The objective of the vertical seismic sounding is to infer the elastic characteristics of a horizontally stratified semi-infinite soil model by leveraging the medium's response to the interrogating waves. The forward physics describing the phenomenon is vertical

propagation of compressional waves when the media is subjected to a uniform mechanical excitation $p(t)$ over the surface (Figure 5.6). This problem is one dimensional along the direction of the symmetry (Fichtner, 2010).

In a computational setting a major issue associated with the seismic inverse problem is to model the semi-infinite spatial domain. In order to arrive at a computationally finite region, the media must be truncated at some depth. If the truncated boundary is fixed or inadequately modeled, the propagating waves are (partially) reflected in the domain, and distort the inverted profile (Kang & Kallivokas, 2010*a*). To address the issue, Perfectly-Matched-Layer (PML) wave absorbing boundaries are introduced at the truncation interface (Kang & Kallivokas, 2010*b*). The introduced boundary enforces the rapid decay of the wave motion within the buffer zone, with ideally no reflection to the domain. Figure 5.7 illustrates the schematic representation of the problem. The forward model definition shows detailed derivations of the computational implementation (Kang & Kallivokas, 2010*b*), including the finite element formulation of the derived PDEs. However, for the sake of completeness only the governing wave equation is included here: find $\nu(z,t)$ and $\sigma(z,t)$ such that

$$\begin{aligned} \frac{\partial^2 \nu}{\partial t^2} + V_p(z)\zeta\frac{\partial \nu}{\partial t} - \frac{\partial \sigma}{\partial z} &= 0, \quad \text{for } z \in (0, L_t),\ t \in (0, T], \\ \frac{\partial \sigma}{\partial t} + V_p(z)\zeta\sigma - V_p^2(z)\frac{\partial^2 \nu}{\partial z \partial t} &= 0, \quad \text{for } z \in (0, L_t),\ t \in (0, T], \end{aligned} \tag{5.10}$$

subject to

$$\begin{aligned} \nu(L_t, t) &= 0 \\ \sigma(0, t) &= p(t) \\ \nu(z, 0) &= 0 \\ \frac{\partial \nu}{\partial t}(z, 0) &= 0 \\ \sigma(z, 0) &= p(t) \end{aligned} \tag{5.11}$$

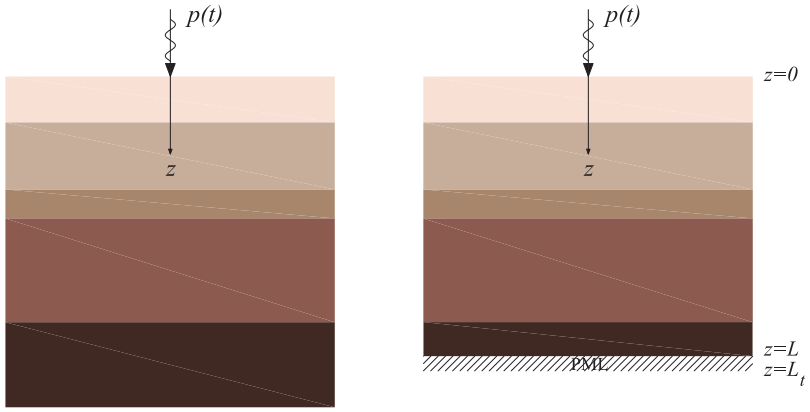

Figure 5.7: Schematic presentation of the 1D problem. (a) Original semi-infinite soil media (b) PML truncated domain.

where $\nu = \gamma u$ is the normalized displacement (with u the measurable vertical displacement). γ denotes the soil density which is assumed to be a known constant in this study; and the attenuation effect is disregarded. σ denotes stress (not to be confused with the standard deviation; σ denoting stress only appears in this section). $\zeta(z)$ is an attenuation function which accounts for the artificial decay of the wave motion within the PML buffer zone, and L_t is the depth of the fixed end of the PML. $V_p(z)$ indicates the 1D soil compressional wave velocity random field which is the inverse problem parameter. Equation 5.10 presents the displacement (ν) - stress (σ) mixed equations governing wave propagation in a PML truncated one dimensional domain.

The inverse compressional wave propagation problem (VSS) consists in deduction of the subsurface elastic properties of a horizontally stratified semi-infinite soil medium from noisy surficial vertical displacement measurements. The posterior density is

$$p\left(\mathbf{m}_{\mathtt{VSS}}|\mathbf{d}_{\text{obs}}^{\mathtt{VSS}}\right) \propto p\left(\mathbf{d}_{\text{obs}}^{\mathtt{VSS}}|\mathbf{m}_{\mathtt{VSS}}\right) p\left(\mathbf{m}_{\mathtt{VSS}}\right) \tag{5.12}$$

where $\mathbf{d}_{\text{obs}}^{\mathtt{VSS}} = (u_1, u_2, \ldots, u_{n_{\mathtt{VSS}}})^T$ is the vector of noisy vertical displacement measurements. $\mathbf{m}_{\mathtt{VSS}} = (V_{p_1}, V_{p_1}, \ldots, V_{p_k}, h_1, h_2, \ldots, h_{k-1}, \sigma_{\mathtt{VSS}})^T$ is the parameter vector associated to the a k layer soil model, where $V_{p_1}, V_{p_1}, \ldots, V_{p_k}$ and $h_1, h_2, \ldots, h_{k-1}$ denote the p-wave velocities and heights of the soil layers, respectively. $\sigma^2_{\mathtt{VSS}}$ is the variance of the seismic data. The

likelihood function forms similar to the equation 5.9:

$$p\left(\mathbf{d}_{\text{obs}}^{\mathtt{VSS}}|\mathbf{m}_{\mathtt{VSS}}\right) \propto \frac{1}{\sigma_{\mathtt{VSS}}^{n_{\mathtt{VSS}}}} \exp\left\{\frac{\sum_{i=1}^{n_{\mathtt{VSS}}}\left(d_{\text{obs}_i}^{\mathtt{VSS}} - g\left(\mathbf{m}_{\mathtt{VSS}}\right)\right)^2}{2\sigma_{\mathtt{VSS}}^2}\right\} \tag{5.13}$$

$n_{\mathtt{VSS}}$ is number of data points and $g\left(\mathbf{m}_{\mathtt{VSS}}\right)$ is defined in equations 5.10 and 5.11, which is numerically solved using a mixed finite elements scheme. Similar to the resistivity problem, a non-informative prior $p\left(\mathbf{m}_{\mathtt{VSS}}\right) \propto \frac{1}{\sigma_{\mathtt{VSS}}^2}$ is assigned to the model parameters.

5.7 Basic Probability Operators

Once the probabilistic calibration is completed for each geophysical method (as described in the preceding sections) it is now possible to integrate the multiple states of information following a premise of "collaboration". The theoretical basis for achieving the claims discussed above are based on the definition of the spaces of probability distributions portrayed by Kolmogorov's axioms, through the use of two basic operations called AND and OR (Tarantola, 2005). These are symbolically denoted by $\wedge$ and $\vee$ respectively. The operations 'conjunction' (AND) and 'disjunction' (OR) for any subset $\mathcal{A}$, and for any two probability distributions P_1 and P_2 are defined to satisfy the set of axioms below:

$$\begin{aligned}
\left(\mathsf{P}_1 \vee \mathsf{P}_2\right)(\mathcal{A}) \neq 0 \quad &\Rightarrow \quad \mathsf{P}_1(\mathcal{A}) \neq 0 \text{ or } \mathsf{P}_2(\mathcal{A}) \neq 0 \\
\left(\mathsf{P}_1 \wedge \mathsf{P}_2\right)(\mathcal{A}) \neq 0 \quad &\Rightarrow \quad \mathsf{P}_1(\mathcal{A}) \neq 0 \text{ and } \mathsf{P}_2(\mathcal{A}) \neq 0
\end{aligned} \tag{5.14}$$

The first axiom means that if any event is possible for P_1 *OR* P_2 the event is either possible for each of the distributions. The second one states if an event is possible for P_1 *AND* P_2, the event is possible for both P_1 and P_2. Also a probability distribution M, namely homogenous measure distribution exists to satisfy for any P

$$\mathsf{P} \wedge \mathsf{M} = \mathsf{P} \tag{5.15}$$

M is the neutral element for the conjunction operator, which is interpreted as a proba-

bility distribution that bears no information. If $f_1(\mathbf{x}), f_2(\mathbf{x}), \ldots, f_n(\mathbf{x})$ and $\mu(\mathbf{x})$ are the probability densities associated with $\mathsf{P}_1, \mathsf{P}_2, \ldots, \mathsf{P}_n$, and M, the following equalities holds:

$$\begin{aligned} (f_1 \vee f_2 \vee \ldots \vee f_n)(\mathbf{x}) &= \frac{1}{n}\left(f_1(\mathbf{x}) + f_2(\mathbf{x}) + \ldots + f_n(\mathbf{x})\right) \\ \frac{(f_1 \wedge f_2 \wedge \ldots \wedge f_n)(\mathbf{x})}{\mu(\mathbf{x})} &= \frac{1}{\eta}\,\frac{f_1(\mathbf{x})}{\mu(\mathbf{x})}\,\frac{f_2(\mathbf{x})}{\mu(\mathbf{x})}\cdots\frac{f_n(\mathbf{x})}{\mu(\mathbf{x})} \end{aligned} \tag{5.16}$$

where η is a normalization constant $\eta = \int_{\mathfrak{X}} \frac{f_1(\mathbf{x})}{\mu(\mathbf{x})}\,\frac{f_2(\mathbf{x})}{\mu(\mathbf{x})}\cdots\frac{f_n(\mathbf{x})}{\mu(\mathbf{x})}$, and the integration is carried out over a finite dimensional space of all parameters $\mathfrak{X}$. The aforementioned axioms constitute what is called the inference space.

Interpretation of Tarantola's operators is illustrated in Figure 5.8 by the use of two distinct states of information (e.g. two different experts' opinions, or same material property evaluated from different geophysical methods at the same point in space, etc.). The available evidence regarding a specific event is defined by a "First" probability density function of Gaussian shape, with mean $-\alpha_0$ and standard deviation σ (Figure 5.8a). Similarly, a "Second" probability density function is defined with mean α_0 and standard deviation σ (Figure 5.8b). Figure 5.8c shows how the AND operator follows the Bayesian approach, defining the combination of states of information as an updating process, which is applied only when the sampling of both distributions comes from the same population. This results in a Gaussian distribution with zero mean and a standard deviation $\sigma_{AND} < \sigma$, meaning that what is common to the First and Second distribution is emphasized, with a reduction on the new representation of the information uncertainty. The OR operator (Figure 5.8d) on the other hand, applies when the sampling of both distributions comes from different populations. It then preserves the original modes at $-\alpha_0$ and α_0 respectively, and shows zero mean (since both distributions are symmetric with respect to zero) but penalizes the new scheme of information with higher uncertainty, $\sigma_{OR} > \sigma$. Notice that if the modes of the First and Second states of information approach to each other, they will tend to become the same distribution with no uncertainty penalty ($\sigma_{OR} \geq \sigma$).

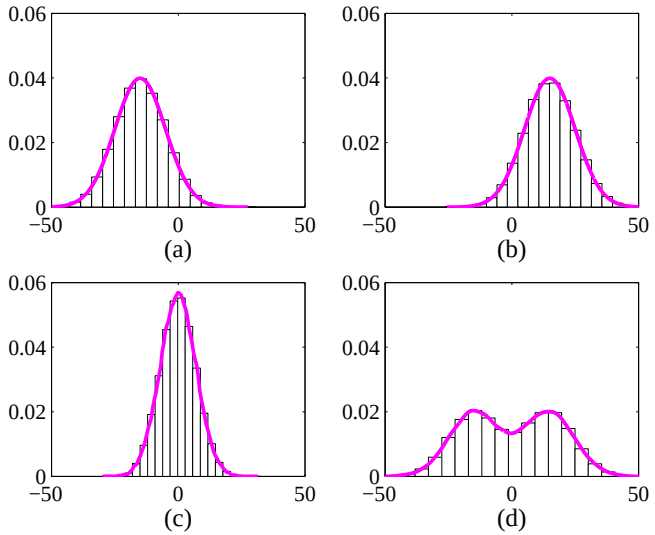

Figure 5.8: Conjunction and disjunction in a 1D probability space; (a),(b): Input probabilities, (c): Conjunction, (d): Disjunction.

In many respects, the use of both the AND and the OR operators resembles distinct natures of collaboration: the enhancement of what is of interest for two information contents with a reduction of uncertainty, and the preservation of different modes, in exchange for a relaxation on the collaborative uncertainty. Same principle applies for jointing geomorphological information derived from each geophysical inversion outlined in sections 5.5 and 5.6. By substituting f_1 and f_2 (equation 5.16) with the marginal posterior densities of the layer depths $p\left(h_1, h_2, \ldots, h_k | \mathbf{d}_{\text{obs}}^{\texttt{VES}}\right)$ and $p\left(h_1, h_2, \ldots, h_k | \mathbf{d}_{\text{obs}}^{\texttt{VSS}}\right)$ inferred from VES and VSS, respectively, the operators conjunction and disjunction provide the joint description of soil stratification:

$$
\begin{aligned}
p\left(h_1, h_2, \ldots, h_k | \mathbf{d}_{\text{obs}}^{\texttt{VES}}\right) \vee p\left(h_1, h_2, \ldots, h_k | \mathbf{d}_{\text{obs}}^{\texttt{VSS}}\right) = \\
\frac{1}{2}\left[p\left(h_1, h_2, \ldots, h_k | \mathbf{d}_{\text{obs}}^{\texttt{VES}}\right) + p\left(h_1, h_2, \ldots, h_k | \mathbf{d}_{\text{obs}}^{\texttt{VSS}}\right)\right] \\
p\left(h_1, h_2, \ldots, h_k | \mathbf{d}_{\text{obs}}^{\texttt{VES}}\right) \wedge p\left(h_1, h_2, \ldots, h_k | \mathbf{d}_{\text{obs}}^{\texttt{VSS}}\right) \propto \\
p\left(h_1, h_2, \ldots, h_k | \mathbf{d}_{\text{obs}}^{\texttt{VES}}\right) \times p\left(h_1, h_2, \ldots, h_k | \mathbf{d}_{\text{obs}}^{\texttt{VSS}}\right)
\end{aligned}
\tag{5.17}
$$

μ in equation 5.16 (the homogeneous density function) is proportional to the unity.

5.8 Application to a 1D Tomography Study

5.8.1 Integration of Evidence Among Different Physics: VES-VSS

A case study is presented to illustrate the application of the probability "collaboration" operators presented above when introduced to multiple geophysical survey data collected over the same site but based on fundamentally different underlying physics. The main argument here is that different geophysical methods are able to sense different physical properties which usually contain complementary information about the site's stratigraphy. The goal of this synthetic exercise is to make use of the probability operators to combine the inherent complementary information from different geophysical inversion and to define a single and 'richer' stratigraphy description.

While the existing joint inversion schemes (e.g., (Hering *et al.*, 1995; Manglik & Verma, 1998)) rely on the fact that the structures described by each of the geophysical methods are congruent (full agreement and similarity between the interpreted subsurface structures is the inherent assumption to jointly invert the multiple data sets), no restriction is placed here on the features deduced from the different physics being concurrent. No relationship of any type (e.g., empirical petrophysical relationships or statistical correlations (Lelièvre *et al.*, 2012)) are imposed between physical parameters of the different models.

The collaboration inversion scheme outlined in the preceding section is applied to a synthetic 1D tomography problem. A simplified two layer horizontally stratified semi-infinite soil media is considered as the target stratigraphy. The study is formulated by the joint

application of a 1D vertical electrical sounding and by an elastic full-waveform inversion. The probabilistic inversion scheme, presented in sections 5.5 and 5.6, is applied to a set of synthetic seismic-electrical resistivity data set, for deducing the subsurface elastic properties, electrical conductivity measures, and stratification of the soil (i.e. location of the transition between soil units). The two-layer Earth model considered as the benchmark is presented in Figure 5.6, with the target velocity and resistivity profiles defined as follows: the p-wave velocity values for the top layer and the stratum are 250 and 520 m/s respectively, and the thickness of the top layer is assumed to be 18 m. As for the resistivity profile, ρ_1, ρ_2, and h are 10 Ωm, 390 Ωm, and 15 m, respectively.

In the seismic setting, the media is modeled as a one-dimensional PML-truncated domain, with the regular domain extended to $z = 100$ m, and PML buffer zone thickness being 10m ($L_t = 110$m). The domain is probed with a Gaussian pulse-type mechanical excitation $p(t)$ applied at the soil surface with a maximum frequency equal to $f_{max} = 40$ Hz, and the peak amplitude of 10 kPa. The time signal $p(t)$ and its frequency spectrum are shown in Figure 5.9. The attenuation effect is disregarded in this study, and the soil density is assumed to be known a priori ($\gamma = 2000$ kg/m^3).

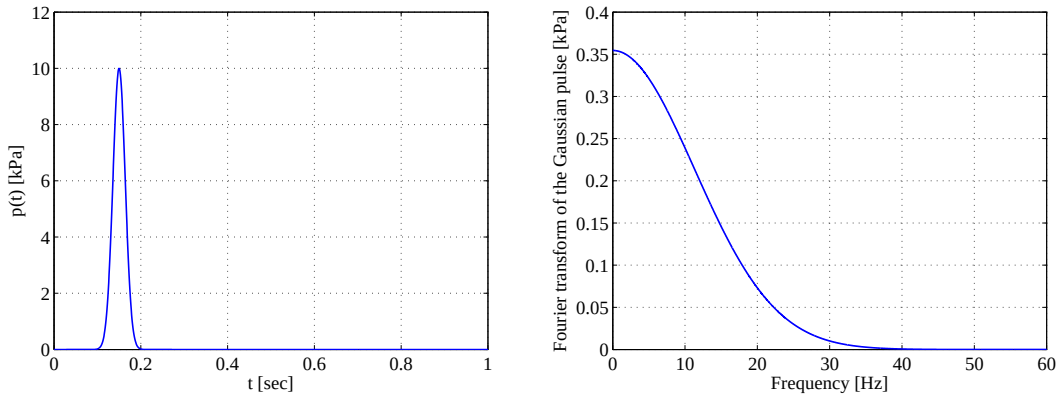

(a) Gaussian pulse time history (b) Gaussian pulse frequency spectrum

Figure 5.9: Excitation time signal and its Fourier spectrum.

Figure 5.10a illustrates the displacement time history response of media given the benchmark soil model, found by solving the forward problem (equations 5.10 and 5.11), and by using a mixed finite element technique (Kang & Kallivokas, 2010*b*). The displacements response, is used as a measurable characteristic of the wave field, and will serve as the input to the inversion scheme. Synthetic seismic data was fabricated by perturbing the model response with 20% Gaussian noise (shown in Figure 5.10a). The data is comprised of 101 data points recorded every 0.02 seconds for total of 2 seconds.

The synthetic resistivity data (the apparent resistivity readings made at different electrode separations collected with a Schlumberger electrode array) is shown in Figure 5.10b. The data consist of 60 measurements of apparent resistivity values in the electrode separation range of L ∼1-10000 m, where 15 readings are made per decade. The synthetic data is generated by adding 15% Gaussian noise to the predicted model response obtained from equation 5.6, where the benchmark resistivity model is introduced to equation 5.7.

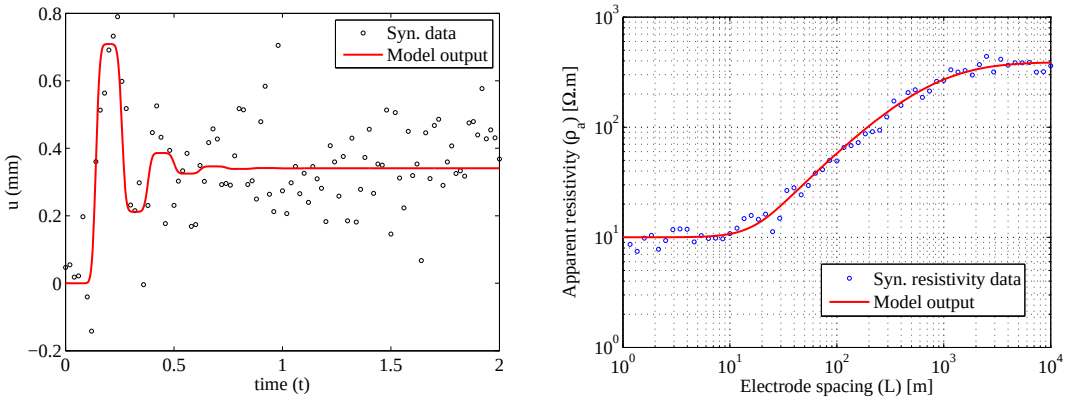

(a) (b)

Figure 5.10: Synthetic data. a) Measured displacement response at the surface (solid line) perturbed with 20% Gaussian noise. b) Theoretical apparent resistivity curve generated for the benchmark two layer Earth model (solid line) perturbed with 15% Gaussian random noise.

First, the Bayesian inversion methodology introduced above was applied to the seismic

and the resistivity data independently. In this case, each model consists of 4 parameters: two resistivity values, one thickness (thickness of the top layer), and a hyper-parameter $\sigma^2_{\mathtt{VES}}$ denoting the variance of the data noise for the VES; and two p-wave velocities, one thickness, and a hyper-parameter $\sigma^2_{\mathtt{VSS}}$ corresponding to the variance of the data noise for the VSS. Notice that, here, it is assumed that the true number of soil layers is known. In a horizontally stratified earth model, prior to making an inference about the likely variation of the material properties within the geological layers, an assumption must be made concerning the number of layers in a certain depth range of interest. This assumption defines the dimensionality (i.e., the number of unknowns) of the inverse problem. In reality, however, such information is rarely available for the dimension and definition of the parameter space to be fixed. In this synthetic study, our main focus is dedicated to demonstrate the outlined framework of jointing states of geophysical information using the introduced probability operators, hence, we avoid adding complexity to the probabilistic inversion step. However, to relax the hypothesis about the number of soil layers prior to inversion, it is possible to define the number of layers, as well as their locations, and their corresponding material properties as random variables. From a Bayesian perspective, this set up is closely associated with probabilistic model selection, where a collection of models with varying number of parameters are presented for inversion, and the task is to select the models that most likely describe the experimental observations. This type of inverse problems are referred to as trans-dimensional (varying-dimensional) inverse problems since the number of unknowns is an unknown itself. Recently, a Monte Carlo method, so-called reversible jump Markov chain Monte Carlo (RJMCMC) algorithm (Green, 1995) has been introduced to the earth science literature, which is applied to sample the posterior distribution of varying dimension. More details on the RJMCMC algorithm or alternative asymptotic techniques of Bayesian model class selection could be find in (Malinverno, 2002; Minsley, 2011; Cao & Wang, 2013; Wang *et al.*, 2013).

A uniform non-informative prior (defined in sections 5.5 and 5.6) was specified to all the model parameters, denoting that no information was available about the earth model

parameters prior to the 'field data collection', founding the inference merely on the experimental observations. The likelihood function reflects the observational tradeoff between the experimental observations and the model predictions, which in this case is populated from a Gaussian model (equations 5.9 and 5.13).

The solution of the numerical integration of the posterior, the simple multiplicity of the uniform prior and the Gaussian likelihood (equations 5.8 and 5.12), was obtained after 10,000 MCMC simulations where convergence was guaranteed. The first 2000 samples were discarded as burn-in iterations. The runtime to draw 10000 (accepted) samples on a 2.4 GHz Quad-Core AMD Opteron machine are 201 and 284 minutes for the VES and VSS, respectively.

Figure 5.11 presents the estimated probability marginal distributions for the 1-D earth model parameters (ρ_1, ρ_2, and the thickness of the top layer) from the electrical resistivity sounding. Figures 5.11a and 5.11b show the marginal posterior probability density of the resistivity of each layer (ρ_1, ρ_2). The probability density function for the location of the transition between layers (i.e. the geomorphological feature) is shown in Figure 5.11c. These distributions provide a measure of uncertainty about the materials and the location of the geomorphological feature of interest. The variance of the induced ground response $\sigma^2_{\texttt{VES}}$ is also considered as a random variable here, which indicates a direct influence of the data, which converges to the measure of the added 15% noise used to populate it (Figure 5.11d). Notice that the probability estimates vary closely around the target values (dashed lines).

Results of the seismic inversion are presented in Figure 5.12. The marginal posterior densities of the two layer soil model parameters (p-wave velocities V_{p1}, V_{p2}, and the thickness of the upper layer) are shown in Figures 5.12a-5.12c, respectively. Similarly to the resistivity inversion, material properties and the geomorphological feature of interest coincide with the benchmark values, and provide a measure of uncertainty on their estimates.

Table 5.1 presents the statistics defined for the independent inversions of both VES and VSS. This shows that the standard deviation of the electrical resistivity grows with respect

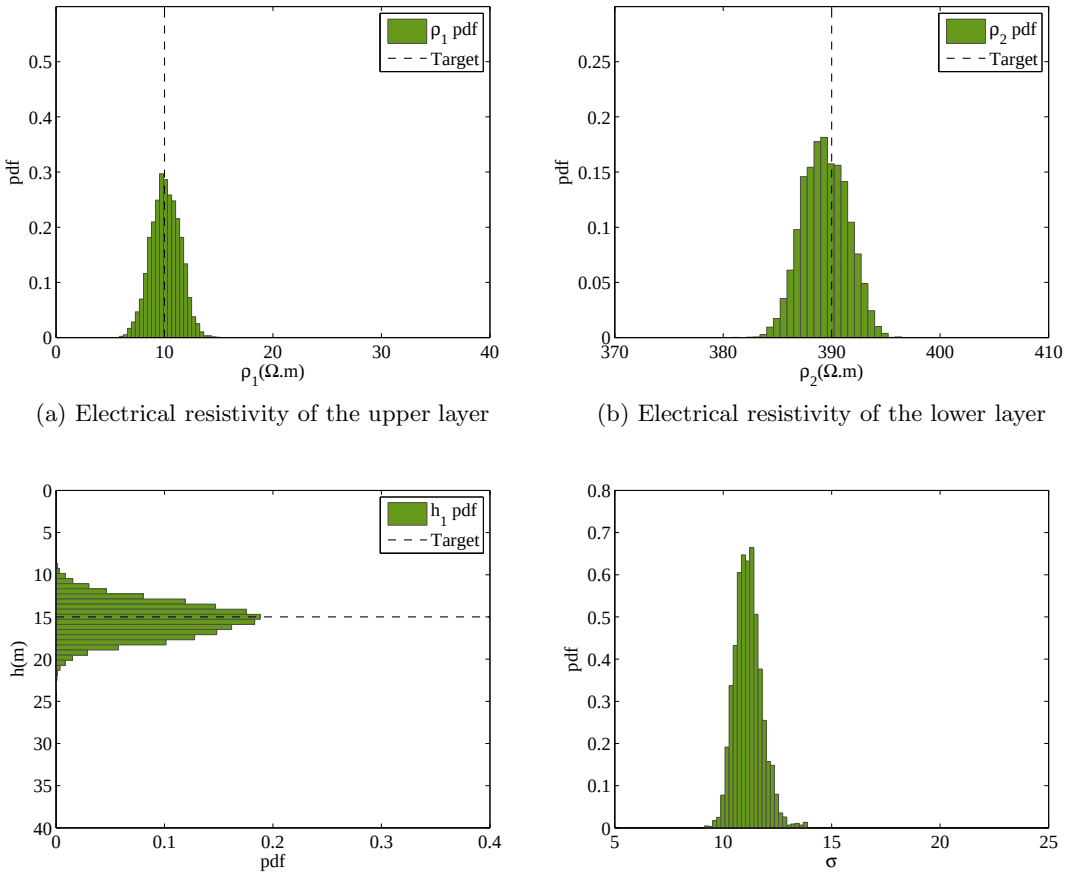

(a) Electrical resistivity of the upper layer

(b) Electrical resistivity of the lower layer

(c) Depth of the interface

(d) Pdf of the likelihood's standard deviation

Figure 5.11: Marginal posterior densities regarding the vertical electrical sounding, together with the target values (dashed line).

to depth about 55% from the upper to the lower layer. That is not the case for the wave velocities, where the uncertainty is slightly lower for the bottom layer (about 3.6%). This is hypothesized to be due to the disregard for the viscosity effect of the soil in the VSS forward model (i.e soil is modeled as a perfectly elastic media). In reality, however, the viscous characteristic of the soil results in the attenuation of wave energy as it propagates in depth. The poor quality of the seismic recordings retrieved from the higher depths is attributed to this effect. This means the slight change in the uncertainty of the inferred wave speed could be related to a numerical effect rather than a physical phenomenon.

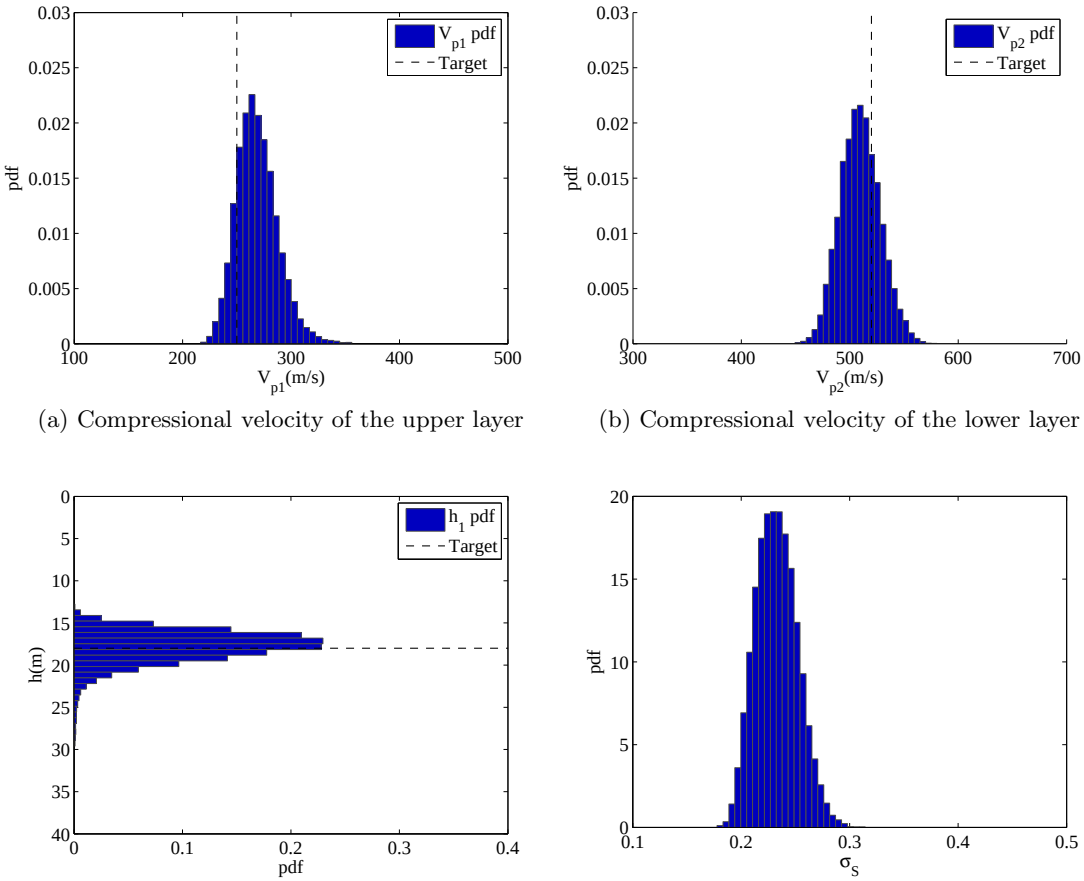

(a) Compressional velocity of the upper layer

(b) Compressional velocity of the lower layer

(c) Depth of the interface

(d) Pdf of the likelihood's standard deviation

Figure 5.12: Marginal posterior densities regarding the seismic inversion, together with the target values (dashed line).

Second, results from the coupled or joint probabilistic inversion between the VES and VSS are presented in figure 5.13. This shows the inverted material properties of the two-layer earth model obtained from the the coupled or joint inversion of both data sets. The formulation of this inversion considered the existence of a single transition between soil layers, as opposed to the two distinct locations retrieved from the independent probabilistic inversions of VES and VSS discussed above. Table 5.2 presents the statistics corresponding to this inversion, indicating that the material properties' mean estimates of the coupled inversion converge to about the same estimates from the independent inversions. Figures

Table 5.1: Statistics of the posterior parameters of the independent resistivity and seismic inversions.

		Mean	Standard deviation
VES	ρ_1 (Ωm)	10.093	1.332
	ρ_2 (Ωm)	389.381	2.069
	h_1 (m)	15.357	2.049
	σ	11.157	0.625
VSS	V_{p1} (m/s)	268.679	19.292
	V_{p2} (m/s)	509.608	18.618
	h_1 (m)	17.857	1.922
	σ	0.233	0.019

5.13a and 5.13c show a reduced uncertainty on the retrieved elastic-resistivity properties of the upper layer compared with the independent inversions illustrated in Figures 5.11a and 5.12a respectively (72.7% reduction for the electrical resistivity and 29.8% for the wave velocity). On the other hand, the uncertainty change was moderate on the inverted properties of the lower layer (35.3% reduction for the electrical resistivity and 1.38% increase for the wave velocity). Estimates of the location of the soil interface lied between the two known reference depths (15m and 18m) for resistivity and seismic inversions respectively (Figure 5.13g). These show a significant reduction with respect to the independent soil transitions, between 65% and 55% with respect to VES and VSS respectively. However, this contradicts 'reality' as imposed by construction of the case study, since the inversion of each physics showed above its ability to find their 'true' distinct geomorphological features. Figures 5.13e, 5.13f show $\sigma_{\texttt{VES}}$ and $\sigma_{\texttt{VSS}}$, denoting the variability of resistivity and seismic data respectively, which converge to about the same values obtained in the independent inversions. Indeed, coupling VES and VSS converge to the same standard deviation assumed for the generation of each individual data set.

A major advantage of the probabilistic model calibration is that it makes it feasible to retrieve the correlation structure defining the degree of association between the regression parameters, something that cannot be achieved by typical deterministic calibrations, where a single vector of optimal parameters is retrieved. Figure 5.14 introduces the correlation

Table 5.2: Statistics of the posterior parameters of the coupled resistivity and seismic inversion.

		Mean	Standard deviation
Joint VES & VSS	ρ_1 (Ωm)	10.837	0.764
	ρ_2 (Ωm)	389.466	2.071
	V_{p1} (m/s)	257.195	14.260
	V_{p2} (m/s)	507.640	18.885
	h_1 (m)	16.986	1.241
	σ_{VES}	11.277	0.666
	σ_{VSS}	0.233	0.022

among the resistivity-velocity properties of the upper and the lower layer respectively. The relevance of these figures is to emphasize the capability of a probabilistic inversion to quantify the cross-correlation structure of the model parameters. In the case of the coupled probabilistic inversion, a clear linear correlation among the properties of the upper layer V_{p1} and ρ_1 can be observed (Figure 5.14a). A slight negative V_{p2} and ρ_2 correlation can be detected in Figure 5.14b.

Third, once the independent probabilistic calibration is completed for all participating geo-mappings, it is then possible to merge information content from each geophysical inversion now making use of Tarantola's 'collaboration' probability operators. For the 1D soil modeling, the geomorphological information extracted from both geophysical data is the definition of the location of the transition between layers. In general, this step is carried out following the proposed classification method described in section 5.3. For this specific 1D example the location of the interface is retrieved as an inversion parameter (i.e. for this case there is no need to complete the classification analysis).

Figure 5.15 shows the merging of geomorphological information via the AND conjunction operator, which shows an enhanced location of the resulting layer boundary. These figures are obtained by direct application of equations 5.17, where $p\left(h|\mathbf{d}_{\text{obs}}^{\texttt{VES}}\right)$ and $p\left(h|\mathbf{d}_{\text{obs}}^{\texttt{VSS}}\right)$ denote the marginal posterior probability density of the depth of the layer interface, captured from independent seismic and resistivity modelings.

Following the assumption that each geophysical method detects distinct characteristics

of the soil media, it can be stated that the findings of each physics belong to distinct populations. Following this rationale, the AND-conjunction operation showed in Figure 5.15 cannot be interpreted as the distribution of the location of a single transition between soil units, which in this case shows further reduction of uncertainty compared to the joint inversion (it would be misleading). On the other hand, the probability distribution describing the OR-disjunction operation can be interpreted as the existence of two distinct geomorphological features showing their corresponding modes, which spans a region (after merging both distributions) indicating the probability of finding two distinct geomorphological features (or one) that will represent more accurately the stratigraphy description. It is therefore hypothesized that this approach will improve the identification of geomorphological features, for which the OR-disjunction operator would be more suitable.

5.8.2 Integration of Evidence Among the Same Physics

A case study is presented to illustrate further the application of the probability 'collaboration' operators, when introduced to multiple geophysical survey data stemmed from the 'same physics' collected over the same site. This case was designed to represent the scenario of merging evidence belonging to the same population, consisting on a seismic survey conducted using two different pulse-type stress sources with max frequencies $f_{\max} = 20$Hz and $f_{\max} = 70$Hz respectively (Figure 5.16). That is, to maximize the inferences that can be populated by making use of a previous low resolution seismic available at the same site (meaning the merging of two independent field investigations with low and high resolutions using the AND operator).

The field experimental observations (synthetic) are generated by solving the forward problem under the target velocity profile ($V_{p1} = 250$m/s, $V_{p2} = 520$m/s, and depth of the interface $h = 15$m) with an added 20% Gaussian random noise. The synthesized sensor readings are plotted in Figure 5.17, indicating the inclusion of 101 data points. Figures 5.18a and 5.18b show the velocity measures retrieved from the independent calibration of the two sensor readings, with a more certain (narrower) pdf defined by the high frequency survey data (Figure 5.18a). This shows also the density function of material properties

obtained by the application of the AND-conjunction operator. These results aim at quantifying the confidence gained from using low to high resolution seismic, and to outline the local differences from the lower to the upper soil layers, showing a consistent confidence gain in the upper soil layer with respect to the lower soil layer.

The use of the AND operator for updating the probability distributions of both the material properties and the geomorphological features, corroborates the proper use of the AND operator. It shows an improved estimate of the 'true' material properties and the corresponding reduction of uncertainty on the material estimates and in the location of the materials boundary.

Table 5.3: Statistics of the seismic inversion where the media is probed with two sources of different frequencies

		$f_{\max} = 20$Hz	$f_{\max} = 70$Hz	Conjunction
101 Data points	$\mathbb{E}[V_{p1}]$	259.868	250.205	253.086
	$\mathbb{E}[V_{p2}]$	505.243	544.403	523.623
	$\mathbb{E}[h_1]$	14.406	14.544	14.512
	std$[V_{p1}]$	14.217	9.267	7.763
	std$[V_{p2}]$	12.024	12.785	8.759
	std$[h_1]$	1.330	0.729	0.640
202 Data points	$\mathbb{E}[V_{p1}]$	261.775	252.877	255.561
	$\mathbb{E}[V_{p2}]$	520.850	532.687	527.233
	$\mathbb{E}[h_1]$	14.969	15.216	15.161
	std$[V_{p1}]$	10.128	6.656	5.562
	std$[V_{p2}]$	9.647	8.917	6.548
	std$[h_1]$	0.923	0.492	0.434

Moreover, when increasing the data sampling intensity from the ground response to 202 data points (twice as in the previous case), further uncertainty reductions can be observed. Figure 5.19c presents similar plots to those discussed for 5.18c. These show a consistent reduction on uncertainty for both the material properties and the location of the transition between soil units. Table 5.3 presents the statistics defined for this inversion, where uncertainty reductions are observed between 30 to 40%.

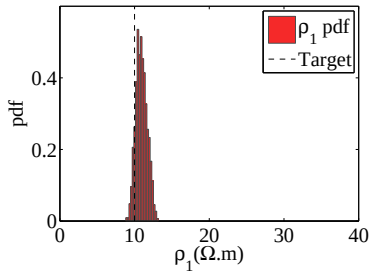

(a) Electrical resistivity of the upper layer

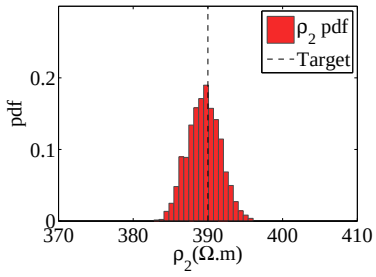

(b) Electrical resistivity of the lower layer

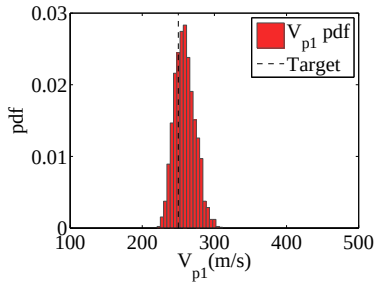

(c) Compressional velocity of the upper layer

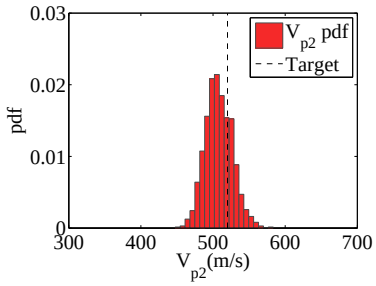

(d) Compressional velocity of the lower layer

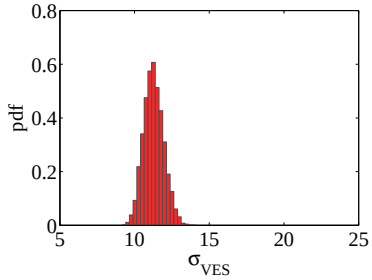

(e) Standard deviation of the resistivity data

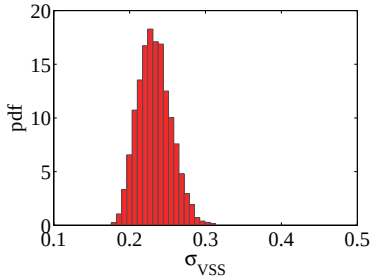

(f) Standard deviation of the seismic data

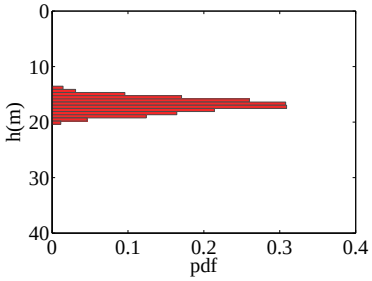

(g) Depth of the interface

Figure 5.13: Marginal posterior densities regarding the joint seismic-electrical resistivity inversion, together with the target values (dashed line).

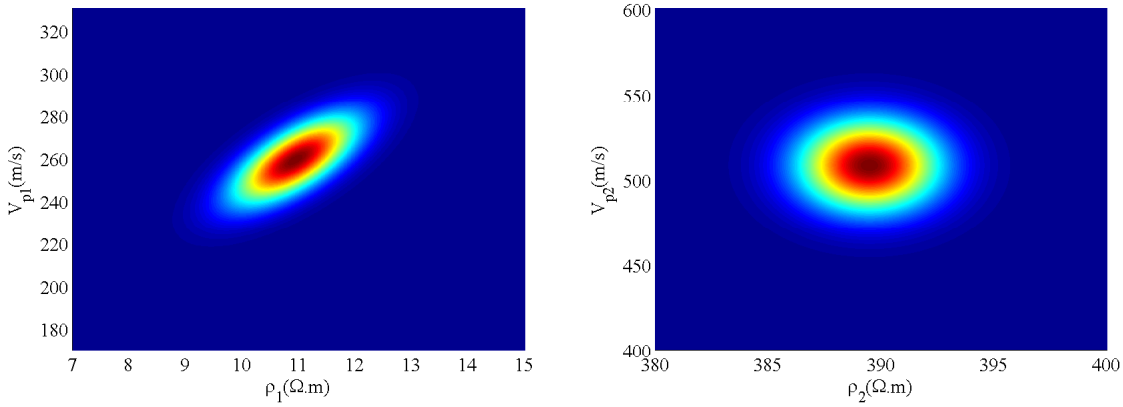

(a) (b)

Figure 5.14: Correlation structure between compressional wave velocity and electrical resistivity. Posterior probability projections of the p-wave velocity vs resistivity for a) top layer and b) bottom layer.

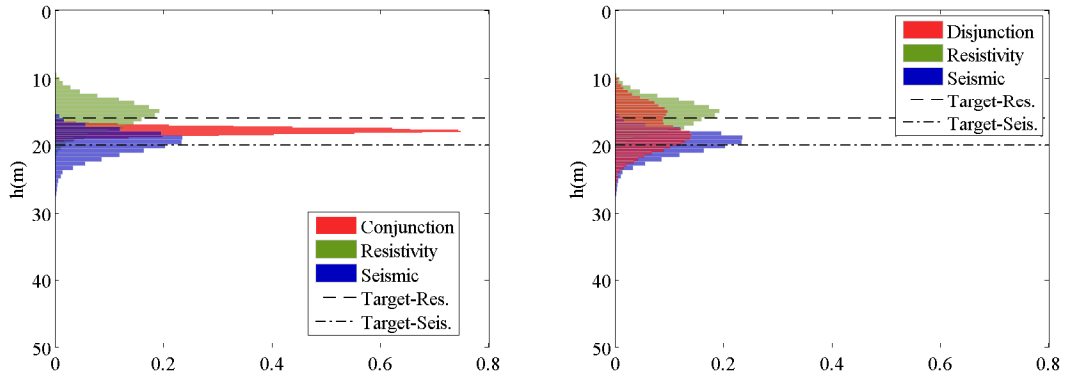

(a) (b)

Figure 5.15: Seismic-electrical resistivity inversion of depth of the layer interface for a 2-layer Earth model, superimposed with multi-physics reconstructed soil profile via a) Conjunction operator and b) Disjunction operator.

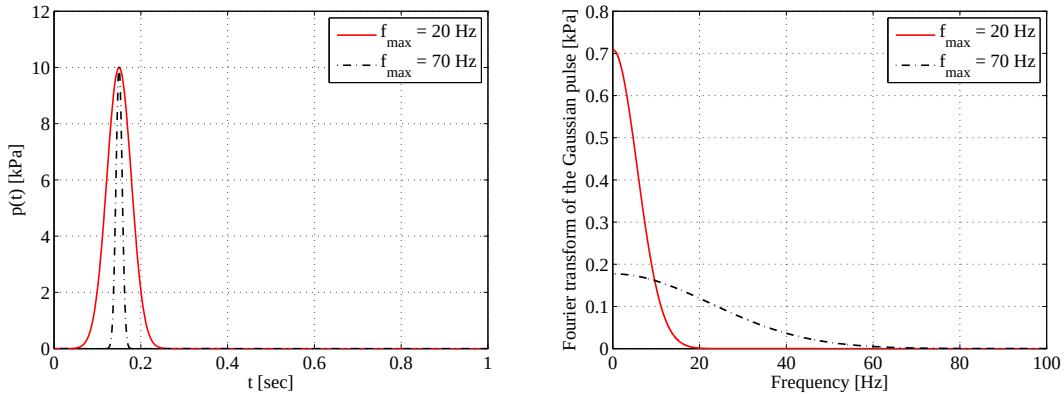

(a) Gaussian pulse time history (b) Gaussian pulse frequency spectrum

Figure 5.16: Excitation time signals and their Fourier spectrum.

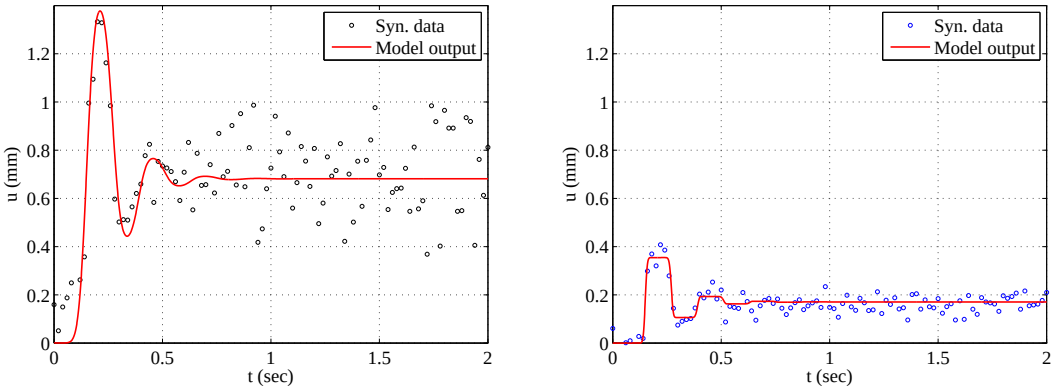

(a) $f_{max} = 20$Hz source (b) $f_{max} = 50$Hz source

Figure 5.17: Synthetic data generated by perturbing the model response with 20% Gaussian noise (SNR=5) together with the measured displacement response at the ground level (solid curve).

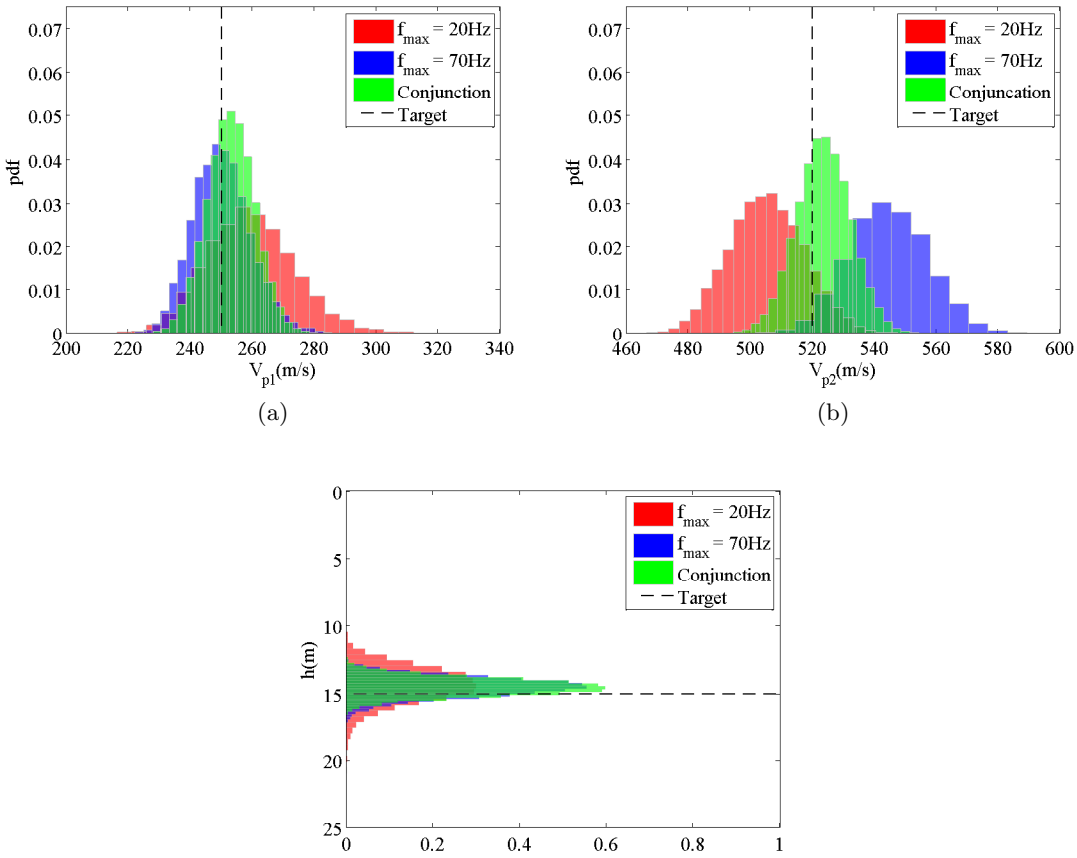

Figure 5.18: Inverted compressional wave velocities (a and b) and inverted depth of the boundary (c) of a 2-layer earth model corresponding to sources with f_{max} = 20 Hz and f_{max} = 70 Hz, together with the target values (dashed line). The measurements are made every 0.02 sec (101 data points).

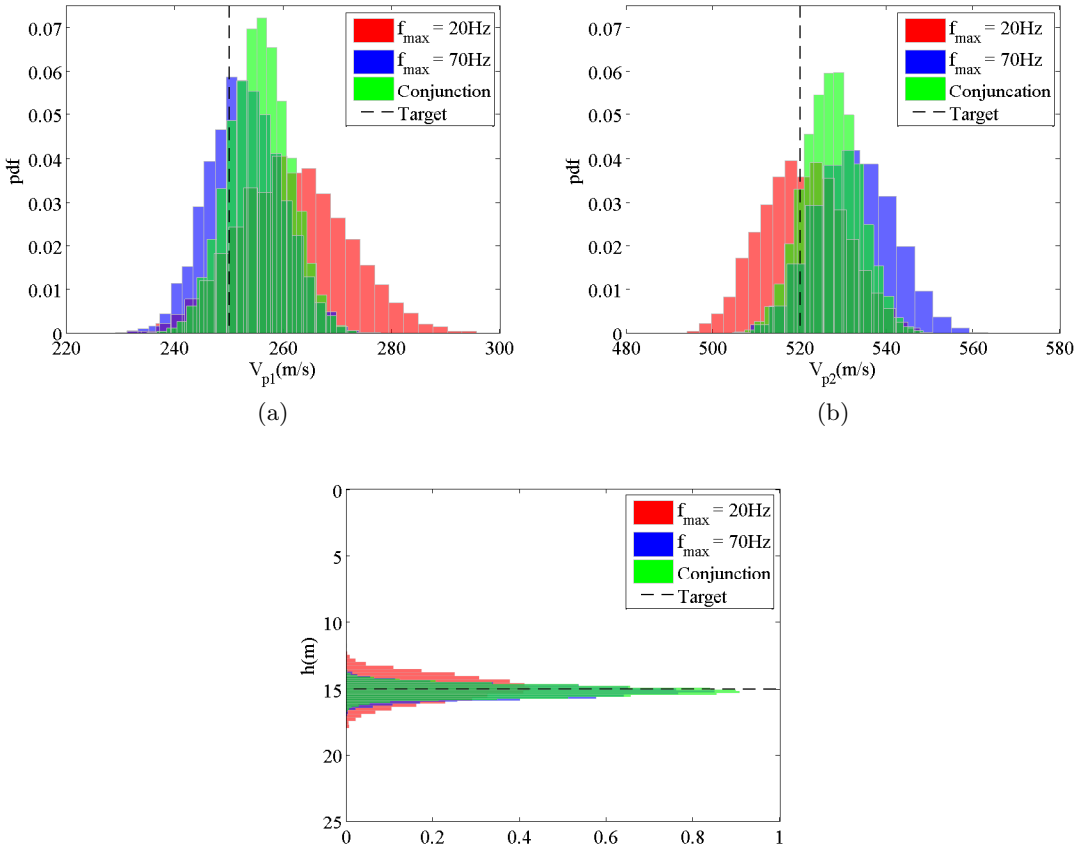

(a) (b)

(c)

Figure 5.19: Inverted compressional wave velocities (a and b) and inverted depth of the boundary (c) of a 2-layer earth model corresponding to sources with f_{max} = 20 Hz and f_{max} = 70 Hz, together with the target values (dashed line). The measurements are made every 0.01 sec (202 data points).

5.9 Concluding Remarks

The sequence a) probabilistic geophysical inversion, b) geomorphological classification, and c) probabilistic calibration, set the basis for the use of two basic probability operators, AND-Conjunction and OR-Disjunction, for defining joint states of evidence from different geo-profile reconstruction methods. Once these three steps are completed for a given q geomorphological feature of interest, it is then possible to enrich the geo-spatial geological model when two or more probabilistic geophysical reconstruction mappings are available. The use of the AND-conjunction operator is shown to be the same as of the Bayesian paradigm, based on the principle of conjunction of information, which applies to evidence sampled from the same population that anticipates a resulting reduction on the uncertainty of both the material properties and the location of the geomorphological features. The use of the OR-disjunction operator, is an alternative when information from the parenting probability mappings are sampled from different populations, which then facilities the integration of complementary evidence for the location of geomorphological features, resulting on the enrichment of the stratigraphical description or earth model. When the degree of complementary information between parenting probability mappings is not significant, the OR-disjunction operator simply reflects the convergence between methods to the same state of information.

From the discussion of the applicability of the proposed method to the synthetic cases discussed above, it is observed that the use of the AND-conjunction operator (Bayesian paradigm), may be utilized for objectives different to what it may be required. Such as in the case of having a true collaborative operator (OR-disjunction operator), that can make distinctions between the differences of maps describing the same object based on different information source or knowledge.

6. BAYESIAN MODEL SELECTION FOR VIRIAL EQUATIONS OF STATE

6.1 Overview

This paper introduces a generic model selection methodology to define the most likely order of the virial Equation of State (EOS) for describing a set of $P\rho T$ experimental observations. Current practice on the deterministic model calibration techniques applied to EOS and its corresponding standard statistical inferences overlooks model uncertainty. Hence, typical EOS parameterizations make use of subjective or optimization-based selections of a truncation term in the virial expansion model. Emphasis is given solely to a qualitative curve fitting to the data, without questioning the potential influence of the aleatory and epistemic uncertainties involved in the process. Bayesian model selection through the use of the Bayes Factors (BF) provide a coherent and reproducible framework for accounting for all participating sources of uncertainty while penalizing any over-fitting effects. The aim is to adopt a formal prior selection to avoid subjective assumptions. Consequently, the favored virial model shows a full probabilistic description of its regression-type coefficients in the form of a joint probability density function, namely the posterior density or the probabilistic solution to the inverse problem. Therefore, improved statistical inferences can be generated from the sampling of the posterior, by sampling likely combinations of the virial coefficients and estimating descriptive statistics about the response of the EOS model. To illustrate the applicability of the proposed methodology, the virial EOS model is applied to isothermal experimental curves of pure Argon (Ar) measurements.

6.2 Introduction

The use of gas models of equations of state (EOS) in industrial applications requires the proper characterization of its model parameters. The lack of an uncertainty quantification approach may translate into significant economical loses, due to the deterministic point estimation approaches used to define the model parameters, and because of the large trading volumes involved. In practice, the parametrization of advanced models commonly appears

as an optimization problem, where an objective function minimizes the deviation between experimental observations and the corresponding model predictions (Edgar & Himmelblau, 1988). The result is a single vector of the model parameters: the optimal.

In addition, most of the current calibration processes imply that the data used to define the optimal set of model parameters is fully certain, or represents the mean or the statistical trend of the experimental observations. Also, the amount and location of data used for the calibration is typically assumed to have no impact on the selection of the model parameters. These two related assumptions imply discarding the effect of the aleatory uncertainty in the calibration process, not to mention the epistemic uncertainty related to the data collection.

Moreover, it is common to disregard the uncertainty carried by the model generation, which is known a-priori to contain limitations as to accurately predict the process of interest, either because of limited knowledge about the physics of the problem (i.e. in physically based models), or because of low model fidelity (i.e. low order empirical models). This later model related assumption implies discarding the effect of the model epistemic uncertainty in the calibration process.

Nevertheless, the most common assumption made during the calibration of EOS models, is the belief that only one combination of the model parameters exists to generate model predictions that best approximate the experimental observations. This assumption is exacerbated when calibrating multivariate models. The calibration of EOS models is ill-posed.

Use of a probabilistic calibration or solution to the inverse problem (Tarantola, 2005) can overcome this difficulty, because it allows a systematic exploration of all combinations of the model parameters within a transparent definition of the impact of the participating uncertainty sources. During such exhaustive parameter exploration, a probability metric can assess the likelihood of selecting sets of parameters that approximate the model predictions of the experimental observations (likelihood function). In addition, a probability metric can reflect the degree of a-priori knowledge for the model parameters (prior probability density). By the virtue of Bayes theorem, the combination of these two states

of knowledge about the model of interest yields the following benefits: a transition from deterministic to probabilistic model parameters, assessment of the type and degree of correlation between the model parameters (e.g. linear or non-linear), measurement of the impact of the varying experimental observations and hyper-parameters (e.g., varying number of parameters, varying variance, etc.), and consequently the assessment of the model performance (Robert, 2007).

This work extends this approach for the probabilistic selection of competing models, where the aim is to select the best model to describe the process that generated a given set of observations, based on the state of uncertainty of the participating evidence (i.e. experimental observations, EOS model, and even expert's judgment). This approach is defined as a probabilistic model selection (Kass & Raftery, 1995), which provides a coherent and reproducible methodology for the optimal selection of EOS models. Results of this work will show the benefits of a full probabilistic calibration and selection of EOS for Argon model parameters, when presented to the experimental database generated by Gilgen *et al.* (Gilgen *et al.*, 1994*a*).

The canonical regression model for the virial EOS is proposed to illustrate the applicability of the probabilistic model selection methodology. This procedure uses Bayesian hypothesis testing and model selection when conducted through the definition of Bayes Factors (BF), which were first introduced by Jeffreys (Jeffreys, 1935, 1998). In order to compute BFs, a prior distribution must be assigned to the parameters of each model. In the absence of some closely related data to construct a proper prior distribution, as in the case of this study, a key concern is how to opt for a prior distribution that best represents the available information. This selection becomes a challenge in the case of BFs because they are more sensitive to the choices of priors on the model parameters (Robert, 2007)-§7.

In standard Bayesian point estimation, the influence of the prior distribution vanishes as the sample size grows, but that is not the case in model selection (Berger & Pericchi, 1996). Furthermore, the goal is to define a systematic scheme for prior determination to (ideally) avoid any subjective input to the inference process. In the case of non-informative priors,

used whenever little knowledge exists about the variability of the given model parameters, these are typically constructed by standard formal rules that generate so called improper priors up to a constant of proportionality (Kass & Wasserman, 1996). The problem with these is that the improper priors cannot be used in a model selection setting, because choice of the normalizing constant influences the BF, which is a multiple of this arbitrary constant.

To circumvent the difficulty of choosing a relevant prior to compute the BF, one may rely upon non-Bayesian model selection approaches such as Akaike Information Criterion (AIC) (Akaike, 1974). This method introduces ad hoc terms in the model selection criteria to penalize inclusion of unnecessary model dimensions. However these methods do not fully incorporate the "Occam's razor" principle, noting that among two equally possible theories, a simpler is favored over a more complex model, to better adapt to varying data conditions within the same data population (Jefferys & Berger, 1992). This notion prohibits choosing over-fitted models that perform poorly, particularly in terms of prediction. Another possibility is to exploit asymptotic approximations to BFs, such as Schwartz's criterion, also called Bayes Information Criterion (BIC) (Schwarz, 1978; Kass & Raftery, 1995). Although this will lead to an appropriate determination for sufficiently large samples in regular well-behaved models, the criterion does not work for irregular likelihoods. Therefore, the challenge is posed in the prior selection for the optimal probabilistic model selection and in the computational implementation of the Bayesian framework to take advantage of the benefits of BFs.

6.3 Virial Equation of State

The virial Equation of State (EOS) has special relevance in industrial applications because of its precise basis in statistical mechanics that provides coefficients in terms of molecular properties (Lucas, 1991). Kammerlingh Onnes in 1901 introduced the virial EOS presenting the molar compressibility factor Z for a fluid as an infinite power series in the molar density ρ (Privat *et al.*, 2009).

$$
\begin{aligned}
Z\left(T,\rho\right) &= \frac{P}{\rho RT} = 1 + \beta_1(T)\rho + \beta_2(T)\rho^2 + \ldots \\
&= 1 + \sum_{i=1}^{+\infty} \beta_i(T)\rho^i
\end{aligned}
\tag{6.1}
$$

in which ρ, P, T, and R denote the molar density, pressure, thermodynamic temperature, and the universal gas constant respectively. The β_i parameters are virial coefficients depending only on temperature. The first virial coefficient, β_0 must be unity to to satisfy the ideal gas limit. This equation encapsulates the departure from the ideal gas behavior into the infinite summation terms. The second virial coefficient β_1 is proved to be explicitly related to the interaction energy between a pair of molecules. Analogously, β_2 is associated with the influence of interaction between triples of molecules and so on. Normally, the credibility of the virial equation is restricted to relatively low density systems. Including higher order terms in the expansion extends the range of applicability of the virial equation to higher densities. Analytical evaluation of the higher order virials are intractable for common intermolecular interaction potentials, hence, these coefficients are commonly calibrated by fitting to volumetric data gathered isothermally. However, from the statistical point of view, there is no real limitation for extending the proposed methodology to the calibration of surface-type models.

The virial coefficients, as with any other regression-type model parameters, can come from fitting experimental data. However, the full formulation of the virial EOS as an infinite series is computationally infeasible and may not be justifiable. Therefore, the virial EOS requires truncation after a definite number of terms to proceed with the model calibration. Having a probabilistic calibration of each model (i.e. model expansions with varying terms) and using the same isothermal dataset makes it possible to assess the uncertainty of the model performance, yielding a probabilistic measure of how good one model is with respect to others (including models different from the virial EOS).

Least squares-type methods have been utilized to parameterize virial EOS for conditions with varying experimental setups (e.g. (Gilgen *et al.*, 1994*a*,*b*; Dymond & Alder, 1971), and review article on methodologies used for calculating the virial coefficients (Masters, 2008)). Some of these include gas factor measurements (e.g. using the Burnett apparatus), direct density measurements (e.g. weighing methods), and energy determinations (e.g. heats of formation and vaporization, heat capacity determinations, and Joule-Thomson coefficients) (Ewing & Marsh, 1979; McElroy *et al.*, 1989; Stewart & Jacobsen, 1989). For the former, when parameterizing models from volumetric techniques, numerical procedures have involved direct polynomial fits. For the latter, it is known that less accurate values result because the procedure involves a simplified inverse problem and different indirect models. Best results so far showing the lowest deviations between data and model predictions, are the direct polynomial correlations of data gathered with the Burnett apparatus, and by more sophisticated weighing methods like those based upon the Magnetic Suspension Densitometry (MSD) (Kleinrahm & Wagner, 1986; Patil *et al.*, 2007). It is worth noting that all existing parameterizations of the virial EOS are deterministic.

The use of a probabilistic approach to quantify the uncertainty involved in the solution of the inverse problem is necessary for proper qualification of model performance. This work focuses upon the uncertainty quantification of the virial parameters to determine the optimal number of terms for the model, by considering the effect of the number of data points used, and the local variability of the experimental observations. Truncation of the polynomial model occurs via implementation of a probabilistic model selection methodology, conditioned to available experimental observations and to the model capabilities to capture the data trend. This methodology outlines a standard, systematic, and objective methodology to determine the optimum number of terms for a virial EOS. In particular, the Bayesian model selection approach offers a robust tool to achieve this goal (Key *et al.*, 1999).

6.4 Bayesian Model Selection

Defining a number of terms for the virial EOS determines a single model. That is, varying the number of terms of the polynomial model monotonically defines a number of competing models to describe a given set of experimental observations. Having i's of such competing models $\mathscr{M}_1, \mathscr{M}_2, \ldots, \mathscr{M}_i$, it is desired to find the model that best describes the existing data. The Bayes Factor (BF) (Kass & Raftery, 1995), within the Bayesian model selection framework offers a sound criteria to compare performance of a set of competing models. This approach requires specifying priors on the unknowns (model parameters) for each competing model, and updating prior probabilities of models according to the Bayes' theorem (Liang *et al.*, 2008). This procedure identifies the model with the highest probability of capturing the data trend. By the virtue of the Bayes theorem the posterior probability that the observed data is generated from the model indexed by k is:

$$p\left(\mathscr{M}_k|\mathbf{y}\right) = \frac{p(\mathscr{M}_k)p(\mathbf{y}|\mathscr{M}_k)}{\sum_k p(\mathscr{M}_k)p(\mathbf{y}|\mathscr{M}_k)} \tag{6.2}$$

where $\mathbf{y}$ denotes data and $\boldsymbol{\theta}_k$ is the vector of model parameters corresponding to model $\mathscr{M}_k$, and $p(\mathscr{M}_k)$ is the prior probability of $\mathscr{M}_k$ being the reference model. $p\left(\mathbf{y}|\mathscr{M}_k\right)$ is called the marginal likelihood, and given by:

$$p\left(\mathbf{y}|\mathscr{M}_k\right) = \int_{\boldsymbol{\Theta}_k} p\left(\mathbf{y}|\boldsymbol{\theta}_k, \mathscr{M}_k\right) p\left(\boldsymbol{\theta}_k|\mathscr{M}_k\right) \mathrm{d}\boldsymbol{\theta}_k \tag{6.3}$$

The marginal likelihood provides the probability of model $\mathscr{M}_k$ being the true model given the observed data and prior information. In a Bayesian model selection setup, the criteria to compare the relative merits of one model over another is the BF. The BF for model i relative to model j is:

$$BF\left[\mathscr{M}_i : \mathscr{M}_j\right] = \frac{p\left(\mathbf{y}|\mathscr{M}_i\right)}{p\left(\mathbf{y}|\mathscr{M}_j\right)} \tag{6.4}$$

Indeed, the above expression for BF does not require the two models to be nested

(and belong to a same class of models), as opposed to its non-Bayesian counterpart, the Likelihood Ratio Test (LRT) (Casella & Berger, 2002), in which the null hypothesis must always reside within the alternative hypothesis (Robert, 2007). Jeffreys (Jeffreys, 1998) and with slight modification Kass and Raftery (Kass & Raftery, 1995) proposed the following guideline to interpret results of BFs: (table 6.1)

Table 6.1: Bayes Factor interpretation: grades of evidence corresponding to values of the BF against $\mathscr{M}_j$

B_{ij}	Evidence against $\mathscr{M}_j$
1 to 3	Not worth more than a bare mention
3 to 20	Positive
20 to 150	Strong
>150	Decisive

To make the preceding BF definition explicit for choosing from a set of virial EOS, let the model $\mathscr{M}_i$ be a virial EOS truncated to p terms (equation 6.1). This equation is a linear regression of $\mathbf{X}$ on $\mathbf{y}$ according to:

$$\mathbf{y} = \mathbf{X}_{n\times p}\boldsymbol{\beta}_{p\times 1} + \boldsymbol{\epsilon} \tag{6.5}$$

where $\boldsymbol{\epsilon}$ is the error term representing the deviation between the data and the model prediction. n and p are the sample size and the order of the virial expansion, respectively.

6.5 Bayesian Linear Regression

The general formulation for Bayesian linear regression (for which the virial EOS is a suitable representation) is:

$$\mathbf{y} = \mathbf{X}\boldsymbol{\beta} + \boldsymbol{\epsilon} \tag{6.6}$$

where response vector $\mathbf{y} = (y_1, \ldots, y_n)^T$ is normally distributed, with mean (expected model) vector $\mathbf{X}\boldsymbol{\beta}$ and covariance matrix $\sigma^2\mathbf{I}_n$, in which σ^2 is the variance of error term

$\boldsymbol{\epsilon}$, and $\mathbf{I}_n$ is a $n \times n$ identity matrix. $\mathbf{X}$ is a set of predictor variables arranged in a $n \times p$ design matrix. $\boldsymbol{\beta}$ is the vector of regression parameters, and $\boldsymbol{\epsilon} = (\epsilon_1, \ldots, \epsilon_n)^T$ is a vector of random error components such that $\boldsymbol{\epsilon} \overset{iid}{\sim} \mathscr{N}\left(\mathbf{0}, \sigma^2 \mathbf{I}_n\right)$.

To proceed with the implementation of the Bayesian regression, a prior distribution $\pi(\boldsymbol{\theta})$ must be incorporated for representing the known variability of the model parameters $\boldsymbol{\theta} = \left(\boldsymbol{\beta}, \sigma^2\right)^T$. Notice that here it is assumed that σ^2 is also a random variable which is to be inferred from the data. According to the Bayes' paradigm, the most general solution to the above regression problem is cast in the form of a density function namely the posterior distribution $\pi\left(\boldsymbol{\theta}|\,\mathbf{y}\right)$ which results from the product of the prior distribution for the parameters $\pi\left(\boldsymbol{\theta}\right)$ and the likelihood function $f\left(\mathbf{y}|\boldsymbol{\theta}\right)$ normalized by its marginal (Box & Tiao, 1992):

$$\pi\left(\boldsymbol{\theta}|\,\mathbf{y}\right) = \frac{f\left(\mathbf{y}|\boldsymbol{\theta}\right)\pi(\boldsymbol{\theta})}{\int_{\boldsymbol{\Theta}} f\left(\mathbf{y}|\boldsymbol{\theta}\right)\pi(\boldsymbol{\theta})\,\mathrm{d}\boldsymbol{\theta}} \tag{6.7}$$

where the integration is carried out over the parameter space $\boldsymbol{\Theta}$. The likelihood function $f\left(\mathbf{y}|\boldsymbol{\theta}\right)$ describes the data-error statistics. That is, the probability that the observed realization $\mathbf{y}$ is produced by model $\boldsymbol{\theta} \in \boldsymbol{\Theta}$. In particular, the likelihood for a linear model defined within a multivariate normal density (which proves to be the case for the data under study) takes the form:

$$f\left(\mathbf{y}|\boldsymbol{\beta}, \sigma^2\right) = \left(2\pi\sigma^2\right)^{-n/2} \exp\left(\frac{-1}{2\sigma^2}\left(\mathbf{y} - \mathbf{X}\boldsymbol{\beta}\right)'\left(\mathbf{y} - \mathbf{X}\boldsymbol{\beta}\right)\right) \tag{6.8}$$

where the prime denotes transpose here and throughout the text.

6.5.1 Selection of Priors

A fundamental phase in Bayesian modeling is the selection of priors. The use of standard objective selection of priors helps to minimize subjective inputs into a scientific inference problem, such as the probabilistic calibration of a given virial EOS. Opting for non-informative priors is a convenient choice, when little information exists about the variability of the model parameters. This type of priors gives stronger relevance to the

interaction between the experimental observations and the model predictions. However, a majority of non-informative priors, constructed by semi-automatic schemes, are improper defined up to a constant of proportionality (Kass & Wasserman, 1996). In general improper priors for model specific parameters (parameters which are not common to all compared models) cannot be used in model selection setting because the choice of the normalizing constant (the denominator in equation 6.7) influences the computation of the BF. Moreover, proper vague priors (proper priors with a large dispersion parameters) also do not solve the problem, as they give rise to the so called Jeffreys-Lindley paradox (Robert, 2007). The paradox is a problem related to the stability of the BF which causes the most parsimonious model (which might be a very poor reflection of the data) always been favored by the BF.

In normal regression models, a convenient choice of proper prior is a conjugate prior from the normal inverse-gamma family (Denison *et al.*, 1998, 2002*b*), in which the exact analytic assessment of all marginal likelihoods is feasible (equation 6.3). In particular, Zellner's G-prior (Zellner, 1986) provides a conjugate prior on regression coefficients which allows for constructing the prior covariance structure directly from the observed data through the design matrix $\mathbf{X}$. Zellner's G-prior on regression coefficients and dispersion parameter are given by

$$\boldsymbol{\beta}|\sigma^2, c, \mathbf{X} \sim \mathscr{N}\left(\boldsymbol{\mu_0}, c\sigma^2\left(\mathbf{X}'\mathbf{X}\right)^{-1}\right) \tag{6.9}$$

$$\sigma^2|\mathbf{X} \sim \mathscr{IG}\left(\alpha_0, \delta_0\right) \tag{6.10}$$

Definition of the priors is therefore reduced to choosing $\boldsymbol{\mu_0}$ and the inverse-gamma parameters α_0, δ_0. The prior mean $\boldsymbol{\mu_0}$ in the present study is set to zero, and $\alpha_0 = \delta_0 = 0$ without loss of generality. The choice of $\alpha_0 = \delta_0 = 0$ reflects the well-known improper Jeffreys prior (Jeffreys, 1946; Kass & Wasserman, 1996) for σ^2. It should be noted that that improperness of the prior on σ^2 does not make the BF indeterminate, as σ^2 is common

to all the competing models. c is a dispersion hyper-parameter reflecting the amount of information available in the prior relative to the observations. In this sense, as c goes to infinity, the influence of the prior tends to vanish at the rate of $1/c$. When setting $c = 1$, the prior is given the same weight as the data.

Herein, it is stressed that the value of c cannot be fixed as BF is highly sensitive to the choice of c. Several works provide recommendations on the relevant uniform choices of c (Kass & Wasserman, 1995; Foster & George, 1994). However, a more natural alternative is to treat c as a random hyper-parameter in the model which is elicited from the analysis. A proper prior is specified on c, which accordingly leads to a mixture of G-priors for the regression parameters $\boldsymbol{\beta}$, resulting in a more reliable inference and model selection. The proposed approach is based on a family of priors for c introduced by Liang *et al.*, so called hyper-g priors (Liang *et al.*, 2008):

$$\pi(c) = \frac{a-2}{2}(1+c)^{-a/2}, \quad c > 0 \tag{6.11}$$

This prior is proper for $a > 2$ and hence provides the possibility of comparing the linear virial EOS to any other family of models that does not contain c. Even though a choice of $1 < a \leq 2$ is plausible as it results in a proper posterior density, the issue of arbitrary constant of proportionality of the prior gives rise to indeterminate BFs, and hence should be avoided in a model selection setup. Setting $a = 3$ and $a = 4$ is a recommendation in (Liang *et al.*, 2008).

It is often convenient to present the prior density as a product of its conditional distributions as follows:

$$\pi\left(\boldsymbol{\beta}, \sigma^2\right) = \pi\left(\boldsymbol{\beta}|\sigma^2, c, \mathbf{X}\right)\ \pi\left(\sigma^2|\mathbf{X}\right)\ \pi(c) \tag{6.12}$$

with

$$\begin{aligned}\pi\left(\boldsymbol{\beta},\sigma^2|\,c,\mathbf{X}\right) &= \pi\left(\boldsymbol{\beta}|\,\sigma^2,c,\mathbf{X}\right)\,\pi\left(\sigma^2|\mathbf{X}\right)\\ &= \frac{\left(\frac{\delta_0}{2}\right)^{\alpha_0/2}}{(2\pi)^{p/2}\left|\mathbf{V}_0\right|^{1/2}\Gamma\left(\frac{\alpha_0}{2}\right)}\\ &\quad\times\left(\sigma^2\right)^{-\left(\frac{\alpha_0+p+2}{2}\right)}\exp\left[-\left(\frac{\left(\boldsymbol{\beta}-\boldsymbol{\mu}_0\right)'\mathbf{V}_0^{-1}\left(\boldsymbol{\beta}-\boldsymbol{\mu}_0\right)+\delta_0}{2\sigma^2}\right)\right]\end{aligned} \tag{6.13}$$

with Γ being the Gamma function, and $\mathbf{V}_0 = c\left(\mathbf{X}'\mathbf{X}\right)^{-1}$. $|.|$ denotes the determinant. Hence the quantity

$$\frac{\left(\frac{\delta_0}{2}\right)^{\alpha_0/2}}{(2\pi)^{p/2}\left|\mathbf{V}_0\right|^{1/2}\Gamma\left(\frac{\alpha_0}{2}\right)}$$

is the proportionality constant for the $\mathscr{NIG}$ prior. This normalizing constant is of great significance to develop Bayesian testing by constructing closed form BFs. The constant for the posterior density assumes the exact same functional form because of conjugacy, with prior parameters substituted by updated parameters.

6.5.2 Bayesian Point Estimation

By introducing the expressions derived for the prior density and the likelihood function, (equations 6.13, and 6.8), into the Bayes formula (equation 6.7), one can determine the form of the posterior up to a constant term. Using a conjugate prior structure, which is a normal inverse-gamma $\pi\left(\boldsymbol{\beta},\sigma^2|\mathbf{X},c\right) = \mathscr{NIG}\left(\boldsymbol{\mu}_0,\mathbf{V}_0,\alpha_0,\delta_0\right)$, the posterior distribution maintains the same functional form, except that the prior parameters are updated conditioned on the observed data. Hence, conditional on c, the posterior probability distribution is of the form:

$$\pi\left(\boldsymbol{\beta},\sigma^2|\mathbf{X},\mathbf{y},c\right) = \mathscr{NIG}\left(\boldsymbol{\mu}^\star,\mathbf{V}^\star,\alpha^\star,\delta^\star\right) \tag{6.14}$$

in which updated parameters are indicated by an asterisk. Setting $\alpha_0 = \delta_0 = 0$, $\boldsymbol{\mu_0} = \mathbf{0}_p$, $\mathbf{V}_0 = c\left(\mathbf{X}'\mathbf{X}\right)^{-1}$ simplifies the updated parameters to:

$$\begin{aligned}
\boldsymbol{\mu}^{\star} &= \left(\frac{c}{c+1}\right)\hat{\boldsymbol{\beta}} \\
\mathbf{V}^{\star} &= \left(\frac{c}{c+1}\right)\left(\mathbf{X}'\mathbf{X}\right)^{-1} \\
\delta^{\star} &= \mathbf{y}'\mathbf{y} - \frac{c}{c+1}\,\mathbf{y}'\mathbf{X}\left(\mathbf{X}'\mathbf{X}\right)^{-1}\mathbf{X}'\mathbf{y} \\
\alpha^{\star} &= n
\end{aligned} \tag{6.15}$$

in which $\hat{\boldsymbol{\beta}}$ is the maximum likelihood estimate for $\boldsymbol{\beta}$, and equals to:

$$\hat{\boldsymbol{\beta}} = \left(\mathbf{X}'\mathbf{X}\right)^{-1}\mathbf{X}'\mathbf{y} \tag{6.16}$$

The standard updating procedure for the normal inverse-gamma model appears elsewhere (Denison *et al.*, 2002*b*; Bernardo & Smith, 2009). Notice that the preceding expression for the posterior density is conditional on c. In order to appraise the posterior density for c, one may exploit Monte Carlo methods (Robert & Casella, 2004) to sample from the marginal posterior $\pi\left(c|\mathbf{y}\right) = f\left(\mathbf{y}|c\right)\pi\left(c\right)$. Having noted that the closed form expression for $f\left(\mathbf{y}|c\right)$ exists (see equation 6.20), any simulation-based method is easy to apply.

6.5.3 Bayesian Linear Model Comparison

Having determined the modeling representation, and the corresponding proper-informative priors, the Bayesian model selection problem reduces to treating some often high-dimensional integrations (equation 6.3). In general these integrations cannot be carried out with common numerical methods. However, full analytical calculations of the BF and other statistics of interest are available for a linear regression with the considered conjugate prior setting because the marginal likelihood of the data under each model $p\left(\mathbf{y}|\mathscr{M}_k\right)$ can be evaluated analytically (see equation 6.17). However, one may also marginalize the posterior density first by integrating out all the model unknowns $\boldsymbol{\theta} = \left(\boldsymbol{\beta}, \sigma^2\right)^T$ conditionally on c, leaving a

one dimensional integral over c. In this sense, the marginal likelihood of the data under model $\mathscr{M}_k$ is:

$$p\left(\mathbf{y}|\mathscr{M}_k\right) = \int_0^\infty f\left(\mathbf{y}|\mathbf{X}_k, c\right) \pi(c)\, \mathrm{d}c \tag{6.17}$$

where $f\left(\mathbf{y}|\mathbf{X}_k, c\right)$ comes from the following integration:

$$f\left(\mathbf{y}|\mathbf{X}_k, c\right) = \iint\limits_{\boldsymbol{\Theta}} f\left(\mathbf{y}|\boldsymbol{\beta}, \sigma^2, c, \mathbf{X}_k\right) \pi\left(\boldsymbol{\beta}, \sigma^2|\, c, \mathbf{X}_k\right) \mathrm{d}\boldsymbol{\beta}\mathrm{d}\sigma^2 \tag{6.18}$$

Substituting equations 6.8 and 6.13 into equation 6.18 provides:

$$f\left(\mathbf{y}|\mathbf{X}_k, c\right) = \frac{\left|\mathbf{V}^\star\right|^{1/2} \left(\delta_0\right)^{\alpha_0/2} \Gamma\left(\frac{\alpha^\star}{2}\right)}{\left|\mathbf{V}_0\right|^{1/2} \left(\pi\right)^{n/2} \Gamma\left(\frac{\alpha_0}{2}\right)} \left(\delta^\star\right)^{-\alpha^\star/2} \tag{6.19}$$

Under the assumed prior setting and using equations 6.15, $f\left(\mathbf{y}|\mathbf{X}_k, c\right)$ is proportional to:

$$f\left(\mathbf{y}|\mathbf{X}_k, c\right) \propto (c+1)^{-p_k/2} \left[\mathbf{y}'\mathbf{y} - \left(\frac{c}{c+1}\, \mathbf{y}'\mathbf{X}_k(\mathbf{X}_k'\mathbf{X}_k)^{-1}\mathbf{X}_k'\mathbf{y}\right)\right]^{-n/2} \tag{6.20}$$

The resulting one dimensional integration is easy to perform using standard numerical or Laplace approximation methods (Tierney & Kadane, 1986; Kass & Steffey, 1989). Having calculated the marginal likelihoods, equation 6.4 determines a BF of any two competing virial models:

$$BF\left[\mathscr{M}_i : \mathscr{M}_j\right] = \frac{\int_0^\infty (c+1)^{-p_i/2} \left[\mathbf{y}'\mathbf{y} - \left(\frac{c}{c+1}\, \mathbf{y}'\mathbf{X}_i(\mathbf{X}_i'\mathbf{X}_i)^{-1}\mathbf{X}_i'\mathbf{y}\right)\right]^{-n/2} \pi(c)\, \mathrm{d}c}{\int_0^\infty (c+1)^{-p_j/2} \left[\mathbf{y}'\mathbf{y} - \left(\frac{c}{c+1}\, \mathbf{y}'\mathbf{X}_j(\mathbf{X}_j'\mathbf{X}_j)^{-1}\mathbf{X}_j'\mathbf{y}\right)\right]^{-n/2} \pi(c)\, \mathrm{d}c} \tag{6.21}$$

6.5.4 Posterior Statistics

In addition to the entire posterior presentation (equation 6.14), statistics of the posterior are desired. Posterior location parameter and variation summaries for a normal linear model are all closed-form as the posterior is of a known family. Here the Bayesian estimates

of $\boldsymbol{\beta}$ and σ^2 are derived based on the rules of calculating means and variances of conditional distributions (Gelman *et al.*, 2003)-§1. Accordingly, the posterior mean of $\boldsymbol{\beta}|\mathbf{y}$ comes from averaging the conditional mean $\boldsymbol{\beta}|\mathbf{y}, c$ over the marginal distribution of c:

$$\mathbb{E}[\boldsymbol{\beta}|\mathbf{y}, \mathbf{X}] = \mathbb{E}\left[\mathbb{E}(\boldsymbol{\beta}|\mathbf{y}, \mathbf{X}, c)|\mathbf{y}, \mathbf{X}\right]$$

where $\mathbb{E}$ denotes the expectation operator. In the inner expectation, averaging occurs over $\boldsymbol{\beta}|\mathbf{y}$ conditional on c, and in the outer expectation averaging occurs over $c|\mathbf{y}$. The inner expectation may also appear in a conditional form:

$$\begin{aligned}
\mathbb{E}[\boldsymbol{\beta}|\mathbf{y}, \mathbf{X}, c] &= \mathbb{E}\left[\mathbb{E}(\boldsymbol{\beta}|\mathbf{y}, \mathbf{X}, \sigma^2, c)|\mathbf{y}, \mathbf{X}\right] \\
&= \mathbb{E}[\boldsymbol{\mu}^*|\mathbf{y}, \mathbf{X}] \\
&= \mathbb{E}[\frac{c}{c+1}\,\hat{\boldsymbol{\beta}}|\,\mathbf{y}, \mathbf{X}] \qquad (6.22)
\end{aligned}$$

This expectation results from integrating over the entire domain of c with respect to the posterior density of c, which leads to:

$$\mathbb{E}[\boldsymbol{\beta}|\mathbf{y}, \mathbf{X}] = \frac{\int_0^\infty \frac{c}{c+1}\, f\left(\mathbf{y}|c\right) \pi(c)\, \mathrm{d}c}{\int_0^\infty f\left(\mathbf{y}|c\right) \pi(c)\, \mathrm{d}c}\, \hat{\boldsymbol{\beta}} \qquad (6.23)$$

The denominator in the above expression denotes the posterior normalizing constant, and $\hat{\boldsymbol{\beta}}$ is the the MLE estimate of $\boldsymbol{\beta}$. Following the same steps, the Bayes estimate of the variance is:

$$\mathbb{E}[\sigma^2|\mathbf{y}, X] = \frac{\frac{1}{n-2}\, \int_0^\infty \left[\mathbf{y}'\mathbf{y} - \left(\frac{c}{c+1}\right) \mathbf{y}'\mathbf{X}\left(\mathbf{X}'\mathbf{X}\right)^{-1}\mathbf{X}'\mathbf{y}\right] f\left(\mathbf{y}|c\right) \pi(c)\, \mathrm{d}c}{\int_0^\infty f\left(\mathbf{y}|c\right) \pi(c)\, \mathrm{d}c} \qquad (6.24)$$

Equation 6.20 provides $f\left(\mathbf{y}|\, c\right)$ in the preceding expressions.

Correspondingly, the identity for the conditional variance is:

$$\mathbb{V}[\boldsymbol{\beta}|\mathbf{y},\mathbf{X}] = \mathbb{E}\left[\mathbb{V}(\boldsymbol{\beta}|\mathbf{y},\mathbf{X},c)|\mathbf{y},\mathbf{X}\right] + \mathbb{V}\left[\mathbb{E}\left(\boldsymbol{\beta}|\mathbf{y},\mathbf{X},c\right)|\mathbf{y},\mathbf{X}\right] \tag{6.25}$$

By averaging the joint posterior density over σ^2, analytical form for the marginal posterior distribution of the regression coefficients, $\pi\left(\boldsymbol{\beta}|\mathbf{X},\mathbf{y},c\right)$, admits a multivariate-t density, $\mathscr{T}_p\left(\alpha^\star,\boldsymbol{\mu}^\star,\delta^\star\mathbf{V}^\star\right)$, in which $\alpha^\star$ is the degree of freedom, $\boldsymbol{\mu}^\star$ is the location parameter, and $\delta^\star\mathbf{V}^\star$ is the $p\times p$ scale matrix. Consequently, in the right hand side of the identity 6.25, the inner variance provides the variance of the $\mathscr{T}_p$ density, and the inner expectation refers its mean. The variance of $\boldsymbol{\beta}$ is:

$$\begin{aligned}
\mathbb{V}[\boldsymbol{\beta}|\mathbf{y},\mathbf{X}] \;=\; & \left(\frac{\frac{n}{n-2}\int_0^\infty \left(\frac{c}{c+1}\right)\left[\mathbf{y}'\mathbf{y}-\left(\frac{c}{c+1}\right)\mathbf{y}'\mathbf{X}\left(\mathbf{X}'\mathbf{X}\right)^{-1}\mathbf{X}'\mathbf{y}\right] f\left(\mathbf{y}|c\right)\pi(c)\,\mathrm{d}c}{\int_0^\infty f\left(\mathbf{y}|c\right)\pi(c)\,\mathrm{d}c}\right)\left(\mathbf{X}'\mathbf{X}\right)^{-1} \\
& + \hat{\boldsymbol{\beta}}\left(\frac{\int_0^\infty \left(\frac{c}{c+1}\right)^2 f\left(\mathbf{y}|c\right)\pi(c)\,\mathrm{d}c}{\int_0^\infty f\left(\mathbf{y}|c\right)\pi(c)\,\mathrm{d}c}\right)\hat{\boldsymbol{\beta}}' \\
& - \mathbb{E}\left[\boldsymbol{\beta}|\mathbf{y},\mathbf{X}\right]'\;\mathbb{E}\left[\boldsymbol{\beta}|\mathbf{y},\mathbf{X}\right]
\end{aligned} \tag{6.26}$$

Likewise:

$$\begin{aligned}
\mathbb{V}[\sigma^2|\mathbf{y},\mathbf{X}] \;=\; & \left(\frac{\frac{1}{(n-2)(n-4)}\int_0^\infty \left[\mathbf{y}'\mathbf{y}-\left(\frac{c}{c+1}\,\mathbf{y}'\mathbf{X}(\mathbf{X}'\mathbf{X})^{-1}\mathbf{X}'\mathbf{y}\right)\right]^2 f\left(\mathbf{y}|c\right)\pi(c)\,\mathrm{d}c}{\int_0^\infty f\left(\mathbf{y}|c\right)\pi(c)\,\mathrm{d}c}\right) \\
& - \mathbb{E}\left[\sigma^2|\mathbf{y},\mathbf{X}\right]^2
\end{aligned} \tag{6.27}$$

Although the derived Bayesian point estimate and variance relations involve integrations over infinite limits, they are still easy to deal with in one dimension using ordinary numerical methods. By integrating over the parameter c, it is possible to sample directly

from the $\mathscr{NIG}$ posterior distribution independently of c.

The above development presents the application of Bayesian model selection and parameter estimation within virial family to optimally determine the truncation term given a set of isothermal data. However, the methodology is general and not limited to any specific family of equation of state. More sophisticated and more accurate EOS (such as Statistical Associated Fluid Theory (SAFT) EOS (Chapman *et al.*, 1989; Gross & Sadowski, 2001) and Multiparameter EOS (Span, 2000)) which are known to be useful for phase equilibrium calculations, can be treated in a similar fashion. It is of interest to compare credibility of different type of EOS to adapt to the behavior of fluids under specific thermodynamic conditions. However, for more complex EOS which are not mathematically linear, a closed form solution for the BF and posterior statistics no longer exist. For such problems, it is resorted to numerical techniques to tackle the high dimensional integration of equation 6.3. One limitation on the application of the BF concerns the constraint in using noninformative priors. As mentioned before, given the competing models have parameter spaces of differing dimensions, assigning noninformative improper priors to the model specific parameters yields erroneous BF estimates. Moreover, in the majority of cases, prior information available about the models is too vague or unreliable, that derivation of informative priors becomes impossible. A significant number of references can be found for determining BF statistics, but is worth noticing that this is still a research topic under development (see for example (Kass & Raftery, 1995)). Default Bayesian approaches to model selection involve approximate and asymptotic methods such as Laplace's (Tierney & Kadane, 1986; Tierney *et al.*, 1989), the Intrinsic Bayes Factor approach (IBF) (Berger & Pericchi, 1996), and numerical simulation based methods such as psuedo-prior approach (Carlin & Chib, 1995) and reversible jump MCMC algorithm (Green, 1995). Depending on the situation being analyzed, the degree of irregularity of the model, the number of competing models, sample size, availability of the computational resources, etc., distinct approaches might be employed.

6.6 Bayesian Inference for Virial Equation of State

The probabilistic model selection and point estimation approach outlined in the preceding sections is applied to a set of $P\rho T$ experimental observations describing Argon (Gilgen *et al.*, 1994*a*). Before estimating the virial coefficients, the Bayesian model selection assesses the optimum number of terms for the virial EOS. The parameters of the truncated virial EOS then fit the model into the experimental observations. The implemented comprehensive uncertainty-based approach offers a full description of the virial coefficients for each model through the joint posterior densities of the parameters (equation 6.14). The joint probability maps depicting the uncertainty of the model parameters and their degree of cross-correlation (i.e. posterior distributions) can provide a basis to assess model performance. Posterior statistics encapsulates the Bayesian point estimates, regarded as the optimal sets of model parameters, and quantifies the uncertainty associated with the estimates.

6.6.1 Data Description

The data used in this study correspond to independent experiments conducted to populate isothermal gas responses (Gilgen *et al.*, 1994*a*). During each experiment, the temperature was constant, ranging from $100K$ to $370K$. The data tables contain pressure and density measurements for each isotherm. The experimental compressibility factor is:

$$Z_{exp} = \frac{P}{\rho RT} \tag{6.28}$$

where P, ρ, R, and T denote pressure, molar density, universal gas constant, and temperature respectively. Figure 6.1 illustrates the full data series. The selected isotherms for the current study are also appear separately in figure6.1a.

6.6.2 Bayesian Model Choice for the Virial EOS

Prior to performing the model selection analysis, the explanatory variables $\left(\rho, \rho^2, \rho^3, \ldots\right)$ must be properly scaled. As the gas density approaches small values, the $\mathbf{X}'\mathbf{X}$ matrix

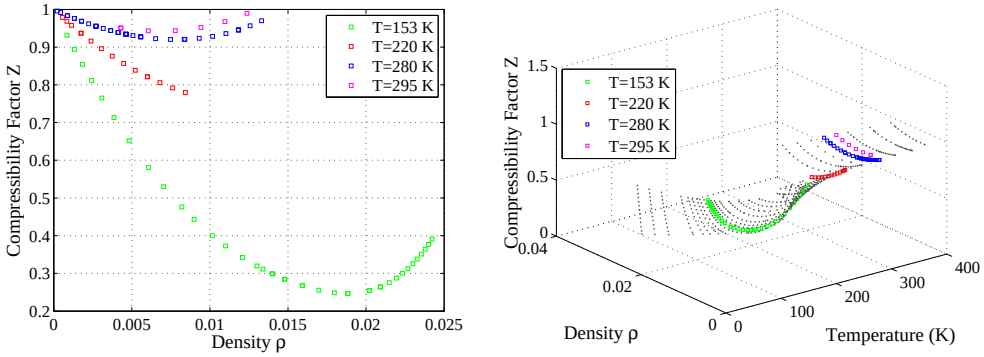

(a) (b)

Figure 6.1: Data series of isothermal experimental observations

rapidly tends to become singular, since the order of the model tends to exceed degree four for the majority of temperatures. This problem leads to model non-identifiability where no unique solution exists for maximum likelihood estimates (equation 6.16). To avoid the singularity problem, it is necessary to scale the data prior to analysis. The outputs may be rescaled later once the the posterior computations are performed.

To be in accordance with the general notations used in the definition of normal Bayesian linear regression (equation 6.6) and the derivation of the governing equations (equations 6.14 and 6.15), equation 6.1 truncated at order p, can be rewritten as $Z = 1 + \mathbf{X}\boldsymbol{\beta} + \boldsymbol{\epsilon}$ ($\mathbb{E}[Z] = 1 + \mathbf{X}\boldsymbol{\beta}$). Hence, the compressibility factor (Z) is the response parameter denoted by $\mathbf{y}$, and the design matrix $\mathbf{X}$ is of full rank p in density such that:

$$\mathbf{X} = \begin{pmatrix} \rho_1 & \rho_1^2 & \cdots & \rho_1^p \\ \rho_2 & \rho_2^2 & \cdots & \rho_2^p \\ \vdots & \vdots & \ddots & \vdots \\ \rho_n & \rho_n^2 & \cdots & \rho_n^p \end{pmatrix} \tag{6.29}$$

The probabilistic model selection approach discussed above permits searching for the most likely model for each isotherm. The proposed search strategy is to focus on BF computation for adjacent pairs of models. Table 6.2 gives the results for models selected

by the BF analysis for each isotherm. Equation 6.21 is used to define the BFs, where $\pi(c)$ is given in equation 6.11, in which $a = 3$. Each 'proposed' model is compared to a successive lower-order model, starting from a quadratic polynomial until the BF cease to show decisive evidence (BF$>$ 150) for the higher-order model. Table 6.1 contains scales to judge the evidence in favor of the 'proposed' model brought by the data. In the case of $T = 295K$, for example, $\mathrm{BF}_{3,2} = 3.39e4$ and $\mathrm{BF}_{4,3} = 2.03e3$ indicating data provide decisive support for the cubic over quadratic and quartic over cubic model respectively. On the other hand, through the 'chain rule' of BF: $\mathrm{BF}_{4,2} = \mathrm{BF}_{4,3} \times \mathrm{BF}_{3,2}$, hence, $\mathrm{BF}_{4,2} \gg 150$. Therefore the BF analysis favored the quartic model over second and third order polynomials. Notice that $\mathrm{BF}_{5,4} = 0.04$ does not provide any conclusive evidence in favor of the $p = 5$ model.

BFs relative to a base quadratic model also appear in table 6.3. The highest BF in the latter setting designates the most likely model to describe the observations. Accordingly, a quintic model is selected as the best model for $T = 153K$. Similarly, a cubic, a quartic, and a quintic model, are the best choices for $T = 220K$, $T = 280K$, and $T = 295K$ respectively.

A major benefit of using BF is that it automatically encompasses the notion of the Occam's razor principle to penalize unnecessarily complicated models. A simple comparison between the output of the Bayesian model selection with an asymptotic method such as Schwarz's criteria (BIC) (Schwarz, 1978) illustrates this notion. Although BIC is a first order approximation to the logarithm of the BFs as the sample size grows to infinity, this method is not considered a Bayesian testing scheme because the dependence on the prior assumption disappears in its formulation (Robert, 2007) and the criteria is based merely on the likelihood function and its estimate at the maximum (equation 6.30). The Schwarz criterion indicates that the model with the highest posterior probability minimizes the quantity:

$$\mathrm{BIC}\left(\mathscr{M}_k\right) = -2\log f\left(\mathbf{y}|\hat{\boldsymbol{\theta}}_k, k\right) + p\log n, \quad \boldsymbol{\theta}_k = \left(\boldsymbol{\beta}, \sigma^2\right)^T \tag{6.30}$$

in which p denotes the number of regression parameters in model $\mathscr{M}_k$, and $\hat{\boldsymbol{\theta}}_k$ is the

maximum likelihood estimate (MLE) of $\boldsymbol{\theta}_k$, assuming the model $\mathscr{M}_k$ is the true model. The second term in this identity is a type of ad hoc penalty term, combatting overfitting the data by penalizing the dimension of the model.

Equation (6.16) provides the MLE estimate of $\boldsymbol{\beta}$, ($\hat{\boldsymbol{\beta}}$), and a classical, unbiased estimator of σ^2 is:

$$\hat{\sigma^2} = \frac{1}{n-p-1}\left(\mathbf{y}-\mathbf{X}\hat{\boldsymbol{\beta}}\right)'\left(\mathbf{y}-\mathbf{X}\hat{\boldsymbol{\beta}}\right) \tag{6.31}$$

To examine the BIC to determine the appropriate order of the virial EOS, MLE models are computed using equations 6.16 and 6.31, for parameterizations that include quadratic up to tenth-order polynomials. Table 6.4 summarizes BIC factor values determined for a prescribed set of models. To illustrate this comparison, the normalized BIC factors are plotted as a function of the number of unknowns (p) in the EOS (figure 6.2). The minimum of each curve occurs at the order of the selected model. Figure 6.2 shows for $T = 153K$ the BIC method fails to select a model, because the BIC factor continues to decrease as the model order grows, without reaching a minimum. For $T = 220K$ and $T = 295K$ BIC tends to favor overly flexible models relative to those chosen by the BFs (forth order and sixth order respectively). Both BIC and BF methods choose the same model ($p_k = 5$) for $T = 280K$, which might be attributed to the relatively large sample size for this isotherm ($n = 49$). Sample sizes for $T = 153K$, $220K$, and $295K$ are 42, 17, and 10, respectively. BIC is proved asymptotically consistent, meaning that given a family of models which contains the true model, the probability that the BIC selects the correct model approaches one as the sample size grows to infinity (Hastie *et al.*, 2009).

6.6.3 Probabilistic Calibration of a Virial Equation of State

Once the most likely model parametrization is identified for each isotherm using BFs, Bayesian linear regression is performed to estimate the virial coefficients of the selected models. The inference results containing the virial coefficient estimates and their associated uncertainties are provided for each isotherm. Bayes expected estimates and covari-

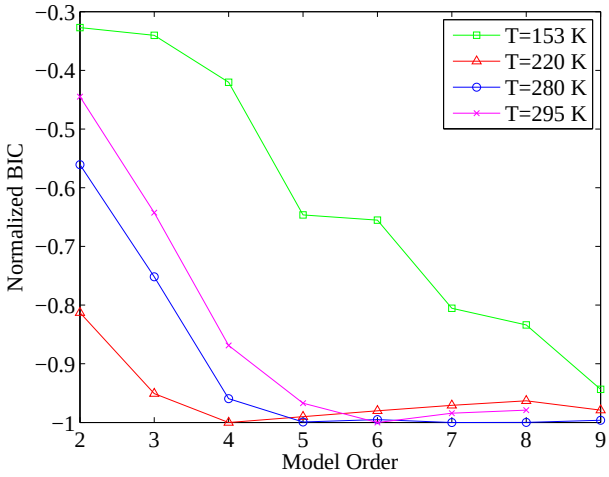

Figure 6.2: Results of the model selection study in terms of the normalized BIC as a function of the order of the virial EOS.

Table 6.2: Bayes Factors relative to a lower degree model

	T=153K	T=220K	T=280K	T=295K
BF$[\mathscr{M}_3 : \mathscr{M}_2]$	$2.45e+00$	$2.32e+04$	$1.32e+33$	$3.39e+04$
BF$[\mathscr{M}_4 : \mathscr{M}_3]$	$1.26e+10$	$6.96e-02$	$3.87e+34$	$2.03e+03$
BF$[\mathscr{M}_5 : \mathscr{M}_4]$	$1.51e+30$	$5.65e-05$	$7.13e+03$	$3.50e-02$
BF$[\mathscr{M}_6 : \mathscr{M}_5]$	$2.90e-02$	$6.63e-05$	$1.37e-04$	$4.06e-04$

ance matrix of $\boldsymbol{\beta}$ are given in tables 6.5 and 6.6 respectively. Table 6.7 gives the posterior moments of σ^2. Content of these tables are obtained by directly using closed form expressions provided in section 6.5.4 (equations 6.23, 6.24, 6.26, and 6.27). Having determined these "sufficient statistics" for the known family of posterior distribution (normal inverse-gamma), Bayesian inference for the regression coefficients $\boldsymbol{\beta}$ and hyper-parameter σ is complete.

Figures 6.3 to 6.6 introduce information about the parameter uncertainty, as well as parameter correlation structure. The information in these figures are extracted from 0.5M random realizations drawn from a multi-variate standard-t distribution with statistics (mean and covariance matrix) summarized in tables 6.5 and 6.6 (recall from section 6.5.4

Table 6.3: Bayes Factors relative to a quadratic base model

	T=153K	T=220K	T=280K	T=295K
$\mathrm{BF}[\mathscr{M}_3 : \mathscr{M}_2]$	2.44	$2.32e+04$	$1.32e+33$	$3.39e+04$
$\mathrm{BF}[\mathscr{M}_4 : \mathscr{M}_2]$	$3.07e+10$	$1.62e+03$	$5.11e+67$	$6.87e+07$
$\mathrm{BF}[\mathscr{M}_5 : \mathscr{M}_2]$	$4.65e+40$	0.09	$3.64e+71$	$2.40e+06$
$\mathrm{BF}[\mathscr{M}_6 : \mathscr{M}_2]$	$1.35e+39$	$6.04e-06$	$5.00e+67$	$9.76e+02$

Table 6.4: Results of the model selection study in terms of the BIC as a function of the order of the virial EOS.

	T=153K	T=220K	T=280K	T=295K
$p=2$	-249.36	-263.62	-509.68	-101.35
$p=3$	-259.36	-308.33	-683.30	-146.36
$p=4$	-320.44	-324.30	-872.10	-197.90
$p=5$	-492.66	-321.11	-908.25	-220.27
$p=6$	-499.36	-317.84	-904.57	-227.77
$p=7$	-613.89	-314.81	-908.97	-224.15
$p=8$	-635.49	-312.35	-908.92	-222.98
$p=9$	-719.18	-317.52	-905.47	-215.00

that the marginal posterior distribution of $\boldsymbol{\beta}|\mathbf{y}$, averaging over σ^2 and c, is a multivariate student-t with mean and variance given in equations 6.23 and 6.26 respectively, with n degrees of freedom). A major advantage of the probabilistic model calibration is that it makes it feasible to retrieve the correlation structure defining the degree of association between the regression parameters, something that cannot be achieved by typical deterministic calibrations. The histograms along the diagonal in these figures illustrate the distribution of the virial coefficients for the selected model. The off-diagonal joint probability maps are cross-plots for all combinations of the regression parameters taken two at a time. These results show a clear linear correlation among all the regression parameters. Also, it can be observed a decrease of cross correlation between coefficients when the difference between their orders increases. This effect is of great relevance for capturing multi scale correlations, since the lower terms are associated to the process trend, while the higher order terms are associated to the local effects.

It is also perceived that the degree of correlation among the successive regression parameters drastically increases for higher order terms, which is an expected phenomenon for polynomial models. This effect, also referred to as multicollinearity, may cause lack of interpretability of the regression coefficients. However, the ability to get a good predictive equation is not impaired. A similar plot shows the correlation between the variance and regression parameters β_1 and β_5 for $T = 153K$ (figure 6.7). This figure is produced by drawing 0.5M random samples directly from an inverse-gamma distribution with statistics given in table 6.7. From this plot it is observed that the variance of the error component and the regression coefficients are independent variables, even though no restricting assumption is made in definition of the priors.

Overall, these plots carry information on how interaction energy between a pair of molecules is inversely related to interaction between triples of molecules, or likewise that two-body interaction potential is positively correlated to the four-body interactions, and so on. These plot, furthermore, propose that the relation between i-body interactions for large i's is almost deterministic irrespective of degree of uncertainty in the data (measure of linear correlation between higher order virials tends to ± 1), and that little interpretation can be added in this case, for potential multi scale effects due to the smoothness of the data ensemble.

Finally, the mean posterior predictions together with the 95% credibility regions around the mean estimates are pictured in figures 6.8a and 6.9a for $T = 153K$, and $T = 295K$ respectively. These figures present a comparative analysis between the different model parameterizations (quadratic, cubic, quartic, ...) in terms of their capability to fit the Argon data. To produce the posterior mean of $Z(\rho)$, denoted by $\tilde{Z}(\rho)$, the average was computed over $20,000$ EOS posterior simulations ($\mathbb{E}[Z^{(i)}(\rho)]$), each of which produced a random sample of regression coefficients $\boldsymbol{\beta}^{(i)}$ from the posterior parametric space. Hence:

$$\tilde{Z}(\rho) \approx \frac{1}{N} \sum_{i=1}^{N} \mathbb{E}[Z^{(i)}]; \quad i = 1, \ldots, N. \tag{6.32}$$

in which $N = 20,000$ and $\mathbb{E}[Z^{(i)}] = 1 + \boldsymbol{\beta}^{(i)}\mathbf{X}$. The shaded area in these figures represents the 95% credible intervals for the posterior mean of the regression function also estimated using the generated samples. In figure 6.8a it is observed that the 4^{th} and 5^{th} order EOS follow the trend of the $T = 153K$ data comparably well, however, the width of the confidence intervals shows a substantial uncertainty reduction in prediction for $p = 5$ (which is the selected model by the BF). This enhanced model performance is also reflected by reduced standard deviation of the quintic trend model plotted over the range of the data (figure 6.8b). A similar behavior is observed in figure 6.9 for $T = 295K$ where the least model prediction uncertainty is associated with the selected model ($p = 4$).

It is worth mentioning that the considered set of isotherms represent the mean of the sampling process. A full uncertainty quantification of the thermodynamic data could not be made using the process mean, since the inherent randomness in the data is averaged out. Experimental data bear the major source of uncertainty which directly propagates to the model parameters (and hence the model prediction) variability. The provided interpretation is being made using the standard practice on the calibration of EOS, and results show that still there is significant variability on the model response, which can be now localized along the domains of interest. However, in order to fully account for the inherent sources of uncertainty in the model calibration and selection, data variability must be incorporated in the model parametrization (e.g. aleatoric uncertainty).

Table 6.5: Bayes estimate of regression coefficients

	T=153K	T=220K	T=280K	T=295K
β_1	$-8.09e+01$	$-3.85e+01$	$-1.96e+01$	$-1.64e+01$
β_2	$8.63e+02$	$1.43e+03$	$1.13e+03$	$1.15e+03$
β_3	$2.60e+05$	$4.72e+03$	$5.80e+03$	$-6.16e+03$
β_4	$-1.66e+07$		$9.23e+04$	$1.19e+06$
β_5	$3.41e+08$		$3.24e+07$	

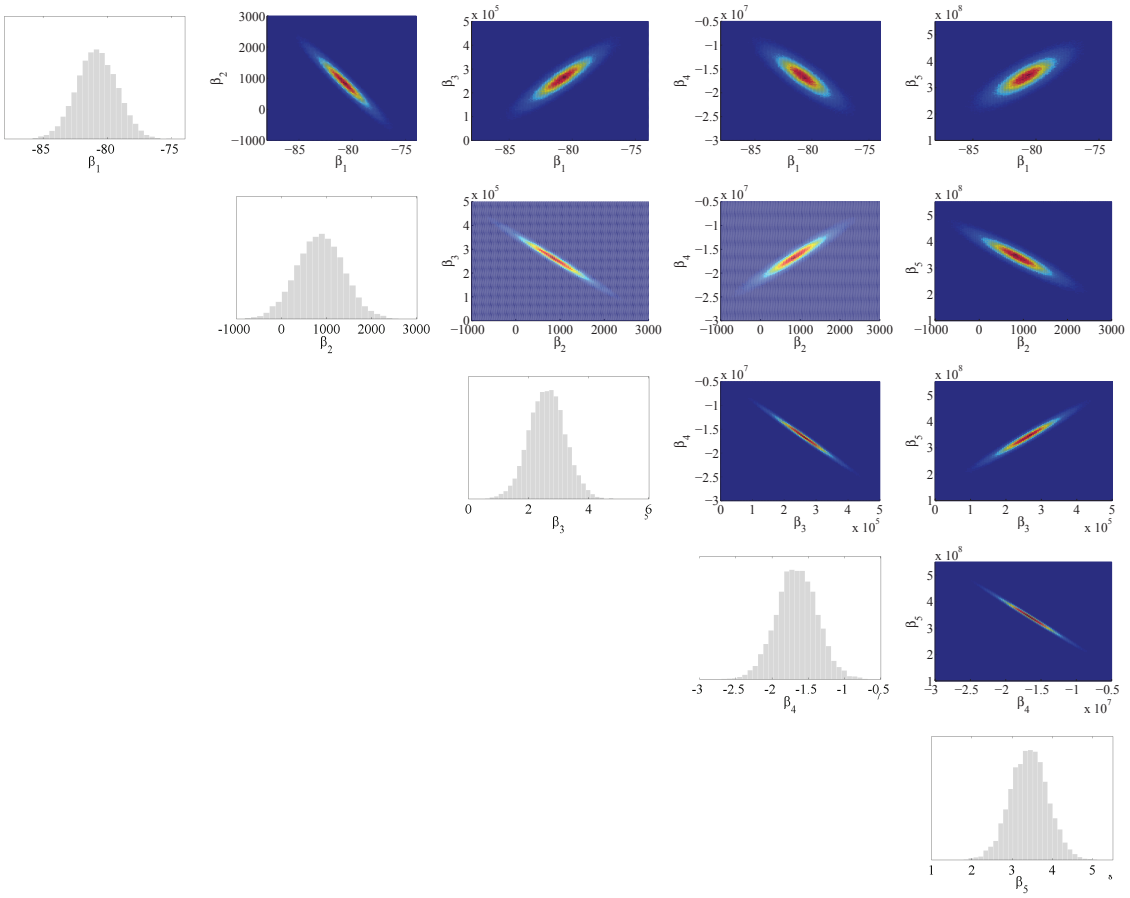

Figure 6.3: Posterior probability projections of the virial coefficients at $T = 153K$

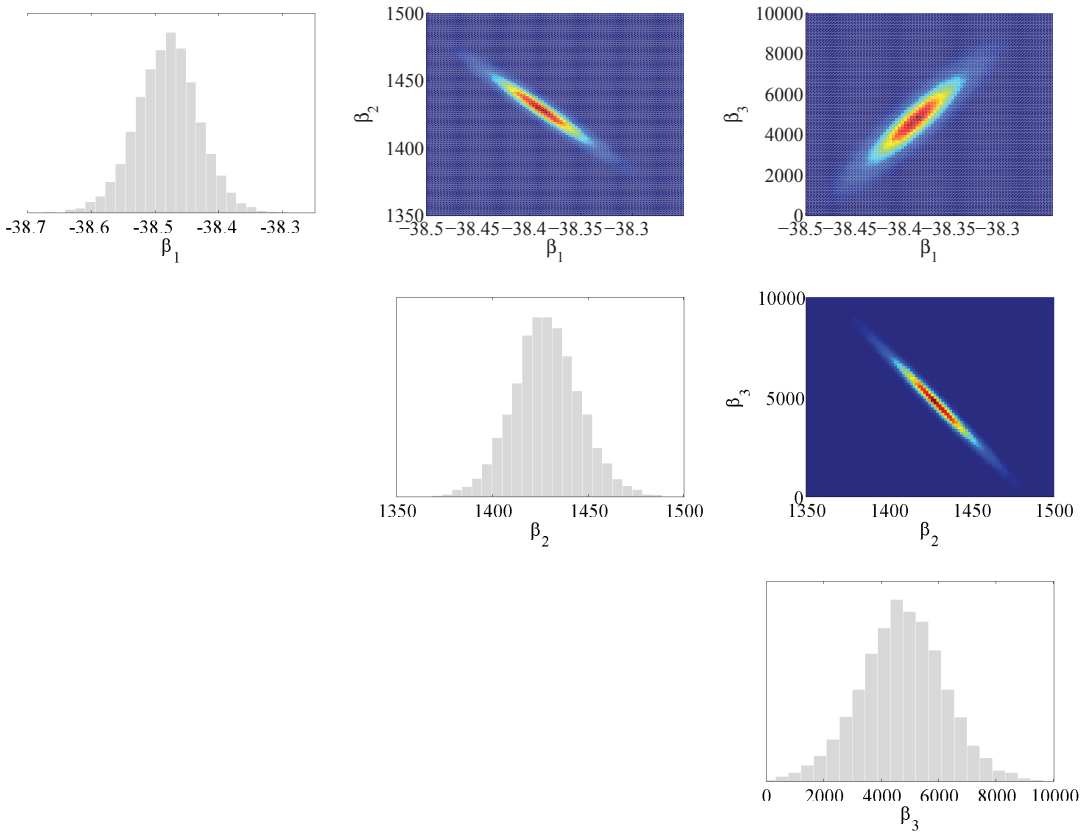

Figure 6.4: Posterior probability projections of the virial coefficients at $T = 220K$

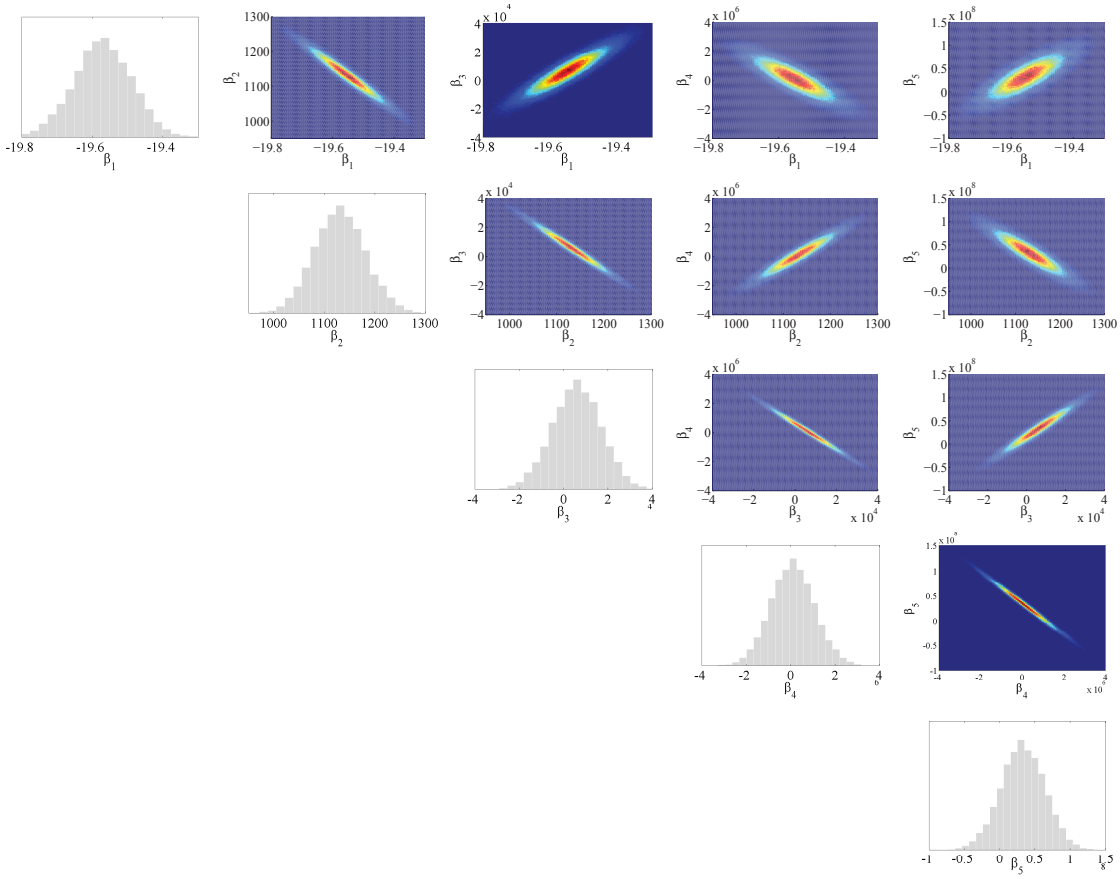

Figure 6.5: Posterior probability projections of the virial coefficients at $T = 280K$

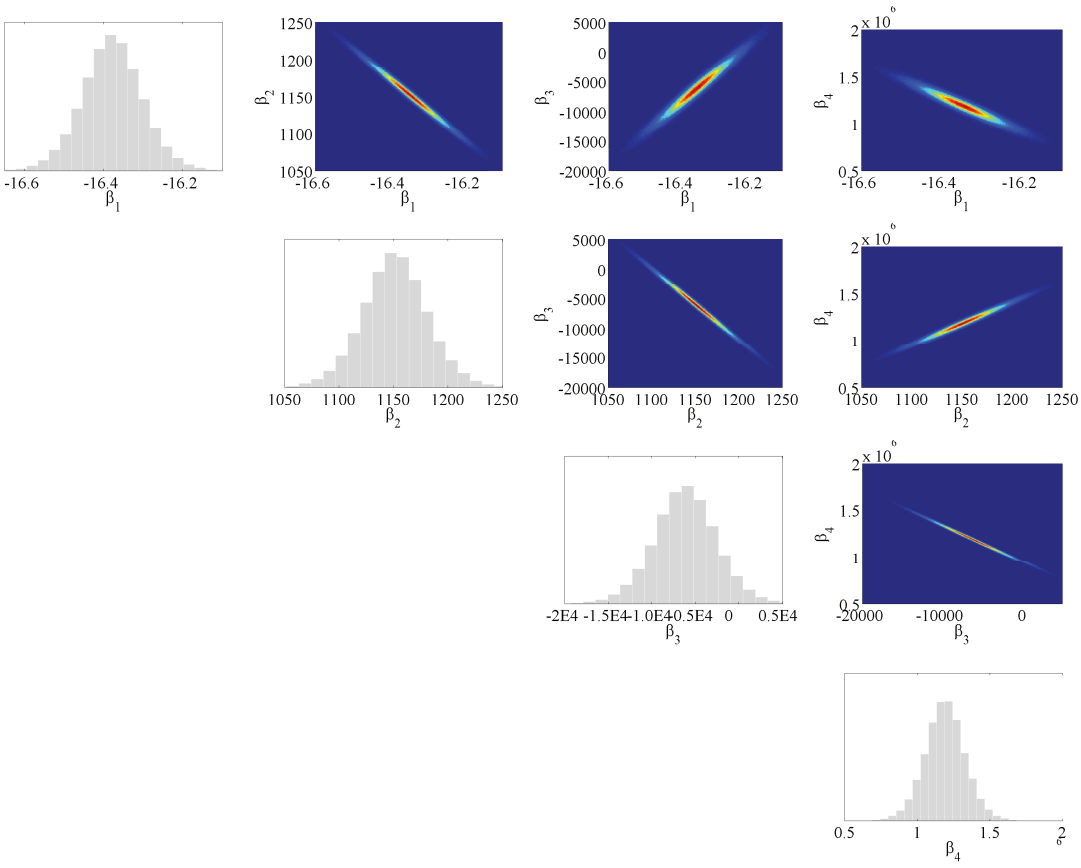

Figure 6.6: Posterior probability projections of the virial coefficients at $T = 295K$

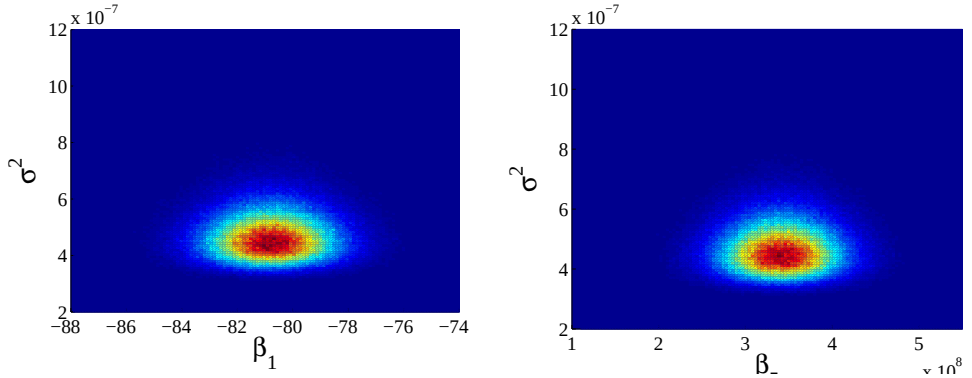

(a) β_1 Vs σ^2 (b) β_5 Vs σ^2

Figure 6.7: Posterior probability projection of regression parameters and variance of the error component at $T = 153K$

Table 6.6: Covariance matrices of regression coefficients

	$\mathbb{V}[\boldsymbol{\beta}\|\mathbf{y},\mathbf{X}]$
$T = 153K$	$\begin{pmatrix} 2.51e+00 & -7.99e+02 & 8.60e+04 & -3.82e+06 & 6.00e+07 \\ -7.99e+02 & 2.76e+05 & -3.11e+07 & 1.42e+09 & -2.29e+10 \\ 8.60e+04 & -3.11e+07 & 3.62e+09 & -1.69e+11 & 2.76e+12 \\ -3.82e+06 & 1.42e+09 & -1.69e+11 & 8.01e+12 & -1.32e+14 \\ 6.00e+07 & -2.29e+10 & 2.76e+12 & -1.32e+14 & 2.21e+15 \end{pmatrix}$
$T = 220K$	$\begin{pmatrix} 2.46e-03 & -8.45e-01 & 6.71e+01 \\ -8.45e-01 & 3.12e+02 & -2.59e+04 \\ 6.71e+01 & -2.59e+04 & 2.21e+06 \end{pmatrix}$
$T = 280K$	$\begin{pmatrix} 6.77e-03 & -4.09e+00 & 8.36e+02 & -7.00e+04 & 2.07e+06 \\ -4.09e+00 & 2.63e+03 & -5.61e+05 & 4.84e+07 & -1.46e+09 \\ 8.36e+02 & -5.61e+05 & 1.24e+08 & -1.10e+10 & 3.38e+11 \\ -7.00e+04 & 4.84e+07 & -1.10e+10 & 9.92e+11 & -3.11e+13 \\ 2.07e+06 & -1.46e+09 & 3.38e+11 & -3.11e+13 & 9.87e+14 \end{pmatrix}$
$T = 295K$	$\begin{pmatrix} 6.35e-03 & -2.45e+00 & 2.93e+02 & -1.10e+04 \\ -2.45e+00 & 9.64e+02 & -1.16e+05 & 4.39e+06 \\ 2.93e+02 & -1.16e+05 & 1.41e+07 & -5.38e+08 \\ -1.10e+04 & 4.39e+06 & -5.38e+08 & 2.06e+10 \end{pmatrix}$

Table 6.7: Bayes estimates of variances of random error component σ^2

	$\mathbb{E}[\sigma^2\|\mathbf{y},\mathbf{X}]$	$\mathbb{V}[\sigma^2\|\mathbf{y},\mathbf{X}]$
$T = 153K$	$3.70e-07$	$8.57e-15$
$T = 220K$	$7.16e-10$	$1.14e-19$
$T = 280K$	$4.17e-10$	$8.92e-21$
$T = 295K$	$1.77e-10$	$6.25e-20$

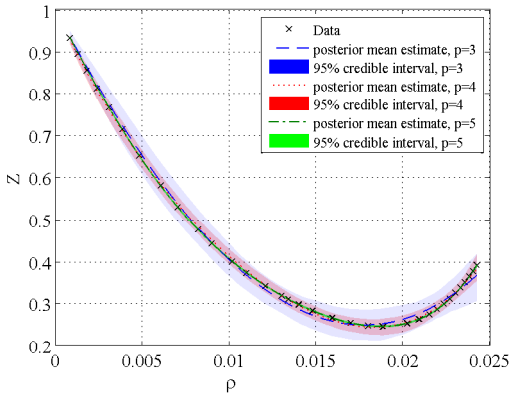

(a) Posterior mean estimates of the molar compressibility factor $\tilde{Z}(\rho)$ together with 95% credible intervals around the mean

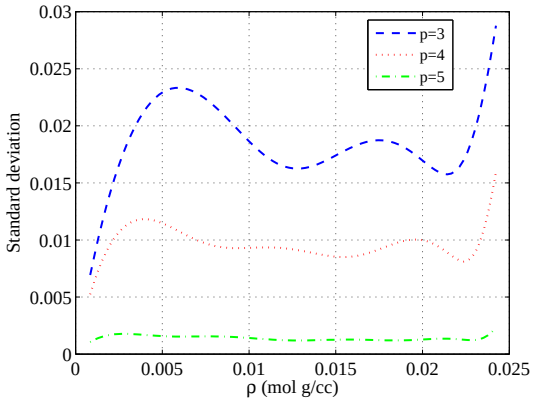

(b) Degree of variation around the mean

Figure 6.8: Posterior prediction statistics for cubic, quartic, and quintic virial EOS, $T = 153K$

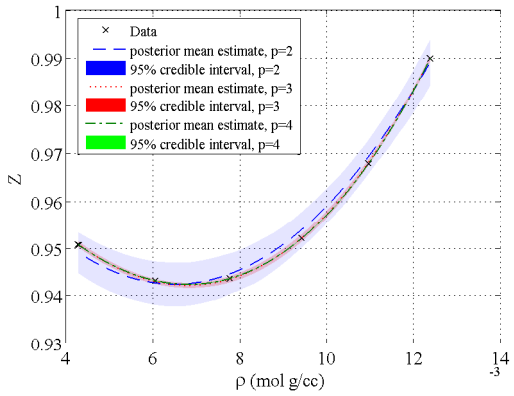

(a) Posterior mean estimates of the molar compressibility factor $\tilde{Z}(\rho)$ together with 95% credible intervals around the mean

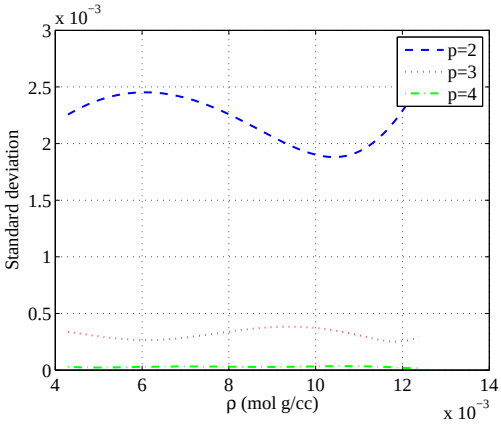

(b) Degree of variation around the mean

Figure 6.9: Posterior prediction statistics for quadratic, cubic, and quartic virial EOS, $T = 295K$

6.7 Concluding Remarks

This work introduces a probabilistic methodology to determine the best model selection for a virial EOS as applied to isothermal observations on Argon. The use of a probabilistic model selection approach allows for defining the truncation of the number of terms for a virial-type of EOS based upon the use of Bayes Factors. The virial coefficients result for the selected model using a standard Bayesian linear regression formulation. The implemented uncertainty approach offers the full description of the regression coefficients through the posterior probability density, which fully accounts for the uncertainty associated with the available data. This inherent uncertainty directly propagates to the estimates of the virial coefficients. Posterior statistics can be retrieved analytically from the proposed formulation providing posterior first and second moments.

Results on the Bayesian assessment of model performance for the virial EOS is presented to four sets of isotherms. To illustrate how the Bayes Factors automatically accommodate the notion of Occam's razor, the output of Bayesian model selection is compared to the BIC method. Even though the essence of the BIC method is to approximate the Bayes Factor asymptotically, the effect of the prior is completely overlooked in its derivation, and hence is observed as a deterministic model assessment tool. The comparison indicates that the approximate method generally favors overly-flexible models, which will perform poorly, especially in terms of prediction. The method failed to select a model for $T = 153K$, and rendered the same result as Bayes Factor for $T = 280K$, which might be attributed to the large number of data points for this isotherm.

Finally, it is worth emphasizing that a major advantage of the probabilistic approach over classical optimization methods is the possibility of retrieving the correlation structure defining the degree of association among the regression parameters, which is not feasible using typical optimization-based calibrations. This paper presents all the possible combinations of regression parameters (two at a time) in a matrix format for four isotherms. The maps provide extensive information on the state of correlation, negative or positive, extent of correlation, and the measure of uncertainty around the means. Results confirm

a clear linear regression correlation among all the regression parameters, in which the degree of correlation increases among parameters of higher-order terms, and decreases as the difference between the term's order increases.

7. CONCLUSION

7.1 Observations

The following summarizes the conclusions from this dissertation:

- A Bayesian approach was adopted to update the remolded undrained shear strength from a global dataset in the light of a new set of experimental observations from the Storegga slope region. Two variance structures have been considered in the study: homoscedastic and heteroscedastic, the former reflecting the underlying assumption in traditional deterministic regression. The probabilistic calibration has been introduced to each dataset individually to calibrate the empirical $S_{u-r} - I_L$ model. It was observed that the uncertainty of the posterior values of the parameters, conditioned on the local dataset is higher compared to that of the global dataset, which attributes to the (unusual) fact that the dispersion in the site-specific data is greater than the dispersion in the global data. Next, we applied Bayesian updating to construct a unified regression model reflecting the characteristics of the both contributing datasets. This is conducted using the "Conjunction" probability operator, which is the same practice as using the posterior from the first experiment (i.e., global data) as the prior, and updating the model information conditional on the second experiment (which forms the likelihood function). A seemingly contradictory observation of -increased posterior uncertainty as a result of Bayesian updating- was obtained. We hypothesize that the contradictory observation is due to the fact that the global and the local data belong to different populations. The hypothesis was confirmed by a two dimensional Kolmogorov-Smirnov test. The fact that the two data sets belong to different populations, questions whether the Bayesian updating is a proper choice to "joint" the two datasets. We propose the application of the "Disjunction" operator in order to arrive at a conclusive model space, particularly capable of accounting for the site dependency effect.

- We discussed a full waveform inversion approach for reconstructing the spatially varying soil elastic characteristics of one- and two-dimensional heterogeneous semi-infinite media, truncated by the Perfectly Matched Layer (PML), based on surface measurements of the medium's response to an excitation applied on the ground level. This defines an inverse medium problem in which the object of inference constructs a continuous random field. Ordinary treatment of the problem constitutes a grid-based parametrization of the unknown field where the unknown wave velocity value is explored at each discretized grid block with a Monte Carlo search. The approach proves to be computationally exhaustive, and relies on explicit regularization of the solution. We proposed a dimensionally reduction of the parameter space using Bayesian Partition Models (BPM), where the velocity random field is divided into a number of non-overlapping regions, the number of partitions, their geometry and weights (defining the intensity of the velocity field) dynamically vary during the inversion, in order to recover the subsurface image. In one dimension the partitions simply describe the soil layers, however in two dimensions all ideas of ordering are lost. In two dimensions the splits are defined via Voronoi tessellations, for which the geometry is completely defined only via the coordinates of tessellation's nuclei. We employed a hierarchical structure to strictly avoid any subjective smoothness constraint into the inversion. Since the number of unknowns is also an unknown in BPM formulation of the inverse problem, the resulting posterior density is of varying dimension. We designed a Reversible Jump Markov Chain Monte Carlo search to efficiently sample the posterior surface of varying dimension. We provided synthetic case studies for both one- and two-dimensional cases, which indicate significant functionality of the inversion scheme to retrieve the benchmark subsurface profiles.

- We developed the idea of applying the basic probability operators "Conjunction" and "Disjunction" to the probabilistic images of the subsurface material properties (constructed via Bayesian solution of an inverse medium problem) obtained from different geophysical surveys, to arrive at a more conclusive definition of subsurface geomor-

phological features. This idea relies on the ability of Bayesian method to project the information content of data (geophysical, geotechnical, hydrological, etc.) onto the probability space, in form of a posterior density function, where "Conjunction" and "Disjunction" could operate. The methodology was applied to retrieve an enhanced definition of the location of a layer interface, were synthetic electrical resistivity and seismic data were synthesized for a same site in one-dimension. The principle of conjunction of information, which applies to evidence sampled from the same population (based on same physics), results in a reduction of the uncertainty of both the material properties and the location of the geomorphological features. The use of the Disjunction operator, is an alternative when information from the parenting probability mappings are sampled from different populations (different physics), which then facilities the integration of complementary evidence for the location of geomorphological features, resulting on the enrichment of the stratigraphical description or Earth model. When the degree of complementary information between parenting probability mappings is not significant, the OR-disjunction operator simply reflects the convergence between methods to the same state of information.

- A Bayesian model selection formulation is derived for normal-linear regression models. In a Bayesian perspective, model selection is conducted through definition of Bayes factor, which offers a sound criteria to directly compare relative plausibility of a number of competing models to describe a dataset. For general non-linear models the direct calculation of BF is infeasible as this often involves performing high-dimensional integrations. In such cases either approximate methods (e.g., BIC), or numerical simulation based technicians (e.g., reversible jump MCMC) are employed. For linear (multivariate) linear models, exact analytic evaluation the BF is possible, given a specific (conjugate) family of priors is specified to the model parameters. The full formulation of the Bayes factor, first and second order statistics of parameters of a linear regression model have been derived. This framework has been introduced to a set of isothermal $P\rho T$ observations of Argon, to determine the

truncation term (number of terms) in the virial equation of state (EOS). Bayesian model selection has successfully determined the best EOS that describes the data (four sets of isotherms), where approximate (BIC) method either failed to select a model or fevered an overly-flexible (with unnecessarily high number of terms) model, which specifically perform poorly in terms of prediction.

7.2 Future Work

There are several key directions that arise as natural extensions to the present work:

- The probabilistic inversion presented in this work for one-dimensional elastic, and two-dimensional SH waves could be extended to the general three-dimensional elasticity case. The higher-dimensional formulation could be accommodated by partitioning the spatial domain through Voronoi tessellations, with mobile number and geometry, to yield the reconstruction of the unknown elasticity parameters (λ, μ). However, two major difficulty arising in this case are: the large computational cost of mixed PML formulation of wave propagation in three dimensions, which strictly limits the number of calls to the forward solver, and increased number of inverse problem unknowns.

- It is significant to improve the computational efficiency of the outlined inversion algorithm, specifically in extension to three dimensions. We propose two approaches:

  - Coupled multi-scale Markov chain Monte Carlo sampling: This is based on running two or more Markov chain in parallel on different scales (mesh resolutions). A coarsened version of the inverse problem yields a more tractable posterior distribution which "guides" the posterior simulation on the fine-scale specification. This approach is particularly favored, since it is embarrassingly parallel.
  - Two-stage Markov chain Monte Carlo sampling: This approach is aiming to increase the acceptance rate of the reversible jump MCMC by using a coarse-scale model to screen the proposed values of the Markov cahin, in order to decide whether to run the expensive fine-scale simulation.

- In the present work we assumed the soil density be a known constant and the attenuation is disregarded. Characterizing the soil's attenuation properties and density should be considered in the future efforts.

- Integrating different geo-survey data using the conjunction and disjunction probability operators was presented in a one-dimensional study. Extension to higher dimensions, where delineating the subsurface geomorphological features requires the use of a classifier, is subject of a future study.

- One of the difficulties we encountered in the two-dimensional waveform inversion was relatively high computational cost of forward model runs. This limits the number of forward model calls required to infer the estimators in MCMC algorithm, and restricts high resolution forward model discretizations. The use of surrogate models such as Gaussian process emulators as a proxy to the forward simulator could significantly reduce the computational cost of a statistical inverse problem.

REFERENCES

Agostinetti, N. Piana & Malinverno, A. 2010 Receiver function inversion by trans-dimensional monte carlo sampling. *Geophysical Journal International* **181** (2), 858–872.

Akaike, H. 1974 A new look at the statistical model identification. *Automatic Control, IEEE Transactions on* **19** (6), 716–723.

Arson, Chloe & Medina-Cetina, Zenon 2014 Bayesian paradigm to assess rock compression damage models. *Environmental Geotechnics* DOI: 10.1680/envgeo.13.00039.

Bamberger, A., Chavent, G. & Lailly, P. 1977 Une application de la théorie du contrôle à un problème inverse sismique. *Annales de Géophysique* **33**, 183–200.

Bang, S., Preber, T., Cho, Y., Thomason, J., Karnoski, S.R. & Taylor, R.J. 2000 Suction piles for mooring of mobile offshore bases. *Marine Structures* **13** (4-5), 367–382.

Basu, Ushnish & Chopra, Anil K. 2003 Perfectly matched layers for time-harmonic elastodynamics of unbounded domains: theory and finite-element implementation. *Computer Methods in Applied Mechanics and Engineering* **192** (11-12), 1337–1375.

Basu, Ushnish & Chopra, Anil K. 2004 Perfectly matched layers for transient elastodynamics of unbounded domains. *International Journal for Numerical Methods in Engineering* **59** (8), 1039–1074.

Berger, James O. & Pericchi, Luis R. 1996 The intrinsic bayes factor for model selection and prediction. *Journal of the American Statistical Association* **91** (433), 109–122.

Berger, J. O. & Pericchi, L. R. 1998 Accurate and stable bayesian model selection: The median intrinsic bayes factor. *Sankhya: The Indian Journal of Statistics, Series B (1960-2002)* **60** (1), 1–18.

Bernardo, J.M. & Smith, A.F.M. 2009 *Bayesian theory. Wiley Series in Probability and Statistics* . Chichester, New York: Wiley.

Besag, Julian, York, Jeremy & Mollie, Annie 1991 Bayesian image restoration, with two applications in spatial statistics. *Annals of the Institute of Statistical Mathematics* **43** (1), 1–20.

Bilancia, Massimo, Graziano, Giusi & Demarinis, Giacomo 2013 Geographical disparities in mortality rates: Spatial data mining and bayesian hierarchical modeling. In *Statistical methods for spatial planning and monitoring* (ed. Silvestro Montrone & Paola Perchinunno), chap. 1, pp. 1–30. Milan, Italy: Springer.

Biondi, Biondo 2006 *3D seismic imaging*. Tulsa, OK: Society of Exploration Geophysicists.

Bodin, Thomas & Sambridge, Malcolm 2009 Seismic tomography with the reversible jump algorithm. *Geophysical Journal International* **178** (3), 1411–1436.

Bodin, Thomas, Sambridge, Malcolm, Rawlinson, Nick & Arroucau, Pierre 2012 Transdimensional tomography with unknown data noise. *Geophysical Journal International* **189** (3), 1536–1556.

Box, George E.P. & Tiao, George C. 1992 *Bayesian inference in statistical analysis*. Reading, MA: John Wiley & Sons, Inc.

Brooks, Stephen & Giudici, Paolo 1999 In *Convergence assessment for reversible jump MCMC simulations* (ed. J.M. Bernardo). Clarendon Press.

Brooks, Stephen P. & Roberts, Gareth O. 1998 Convergence assessment techniques for markov chain monte carlo. *Statistics and Computing* **8** (4), 319–335.

Cao, Z. & Wang, Y. 2013 Bayesian approach for probabilistic site characterization using cone penetration tests. *Journal of Geotechnical and Geoenvironmental Engineering* **139** (2), 267–276.

Cardiff, M. & Kitanidis, P. K. 2009 Bayesian inversion for facies detection: An extensible level set framework. *Water Resources Research* **45** (10).

Carlin, Bradley P. & Chib, Siddhartha 1995 Bayesian model choice via markov chain monte carlo methods. *Journal of the Royal Statistical Society. Series B (Methodological)* **57** (3), 473–484.

Carrier, W. D. & Beckman, J. F. 1984 Correlations between index tests and the properties of remoulded clays. *Geotechnique* **34** (2), 211–228.

Cary, P. W. & Chapman, C. H. 1988 Automatic 1-d waveform inversion of marine seismic refraction data. *Geophysical Journal* **93** (3), 527–546.

Casella, G. & Berger, R.L. 2002 *Statistical inference*, 2nd edn. Australia: Thomson Learning.

Chapman, W.G., Gubbins, K.E., Jackson, G. & Radosz, M. 1989 Saft: Equation-of-state solution model for associating fluids. *Fluid Phase Equilibria* **52**, 31–38.

Chavent, Guy & Jacewitz, Chester A. 1995 Determination of background velocities by multiple migration fitting. *Geophysics* **60** (2), 476–490.

Chib, Siddhartha & Jeliazkov, Ivan 2001 Marginal likelihood from the metropolis-hastings output. *Journal of the American Statistical Association* **96** (453), 270–281.

Cowles, Mary Kathryn & Carlin, Bradley P. 1996 Markov chain monte carlo convergence diagnostics: A comparative review. *Journal of the American Statistical Association* **91** (434), 883–904.

Cressie, Noel & Chan, Ngai H. 1989 Spatial modeling of regional variables. *Journal of the American Statistical Association* **84** (406), 393–401.

Demars, KR 1978 Design of marine pipelines for areas of unstable sediment. *Transport J.* **104** (1), 109–112.

Denison, D.G.T., Adams, N.M., Holmes, C.C. & Hand, D.J. 2002*a* Bayesian partition modelling. *Computational Statistics & Data Analysis* **38** (4), 475–485.

Denison, D. G. T. & Holmes, C. C. 2001 Bayesian partitioning for estimating disease risk. *Biometrics* **57** (1), 143–149.

Denison, David G. T., Holmes, Christopher C., Mallick, Bani K. & Smith, Adrian F. M. 2002*b* *Bayesian methods for nonlinear classification and regression*. Chichester, UK: John Wiley & Sons.

Denison, D. G. T., Mallick, B. K. & Smith, A. F. M. 1998 Automatic bayesian curve fitting. *Journal of the Royal Statistical Society. Series B (Statistical Methodology)*

60 (2), 333–350.

Dettmer, Jan, Dosso, Stan E. & Holland, Charles W. 2009 Model selection and bayesian inference for high-resolution seabed reflection inversion. *The Journal of the Acoustical Society of America* **125** (2), 706–716.

Dettmer, Jan, Dosso, Stan E. & Holland, Charles W. 2010 Trans-dimensional geoacoustic inversion. *The Journal of the Acoustical Society of America* **128** (6), 3393–3405.

Dosso, Stan E. 2002 Quantifying uncertainty in geoacoustic inversion. i. a fast gibbs sampler approach. *The Journal of the Acoustical Society of America* **111** (1), 129–142.

Dosso, Stan E & Dettmer, Jan 2011 Bayesian matched-field geoacoustic inversion. *Inverse Problems* **27** (5).

Duda, R.O., Hart, P.E. & Stork, D.G. 2001 *Pattern classification*, 2nd edn. New York: John Wiley & Sons.

Duijndam, A. J. W. 1988*a* Bayesian estimation in seismic inversion. part i: Principles. *Geophysical Prospecting* **36** (8), 878–898.

Duijndam, A. J. W. 1988*b* Bayesian estimation in seismic inversion. part ii: Uncertainty analysis. *Geophysical Prospecting* **36** (8), 899–918.

Dymond, J. H. & Alder, B. J. 1971 Triplet potential for argon. *The Journal of Chemical Physics* **54** (8), 3472–3478.

Earl, DJ & Deem, MW 2005 Parallel tempering: Theory, application, and new perspectives. *Phys Chem Chem Phys* **7**, 3910–3916.

Edgar, T. F. & Himmelblau, D. M. 1988 *Optimization of chemical processes*. New York, NY.: McGraw-Hill.

Efendiev, Y., Datta-Gupta, A., Hwang, K., Ma, X. & Mallick, B. 2011 *Bayesian partition models for subsurface characterization*, pp. 107–122. Hoboken, NJ: John Wiley & Sons, Ltd.

Efendiev, Y., Hou, T. & Luo, W. 2006 Preconditioning markov chain monte carlo simulations using coarse-scale models. *SIAM Journal on Scientific Computing* **28** (2),

776–803.

Engl, H W, Hanke, M & Neubauer, A 1996 *Regularization of inverse problems*. Dordrecht, Boston: Springer.

Epanomeritakis, I, Akçelik, V, Ghattas, O & Bielak, J 2008 A newton-cg method for large-scale three-dimensional elastic full-waveform seismic inversion. *Inverse Problems* **24** (3).

Esmailzadeh, Saba, Medina-Cetina, Zenon, Yang, S. L. & Nadim, Farrokh 2011 Joint states of information from different probabilistic calibrations of undrained shear strength of submarine clays. In *Geo-Frontiers 2011: Advances in Geotechnical Engineering* (ed. Jie Han & Daniel E. Alzamora), pp. 2669–2678. American Society of Civil Engineers.

Everett, Mark E 2013 *Near-surface applied geophysics*. Cambridge, UK: Cambridge University Press.

Ewing, M.B. & Marsh, K.N. 1979 A differential burnett apparatus: virial coefficients for argon and neopentane at various temperatures. *The Journal of Chemical Thermodynamics* **11** (8), 793–810.

Fadale, Tushar D., Nenarokomov, Aleksey V. & Emery, Ashley F. 1995 Uncertainties in parameter estimation: the inverse problem. *International Journal of Heat and Mass Transfer* **38** (3), 511–518.

Feldman, RM & Valdez-Flores, C 2010 *Applied probability and stochastic processes*, 2nd edn. Berlin Heidelberg: Springer.

Ferreira, Marco A.R. & Lee, Herbert K.H. 2007 *Multiscale modeling- A Bayesian perspective*. New York: Springer Series in Statistics.

Ferreira, Marco A.R. & Oliveira, Victor De 2007 Bayesian reference analysis for gaussian markov random fields. *Journal of Multivariate Analysis* **98** (4), 789–812.

Fichtner, Andreas 2010 *Full seismic waveform modelling and inversion*. Berlin, Heidelberg: Springer.

Foster, Dean P. & George, Edward I. 1994 The risk inflation criterion for multiple

regression. *The Annals of Statistics* **22** (4), 1947–1975.

Frangos, M., Marzouk, Y., Willcox, K. & van Bloemen Waanders, B. 2010 *Surrogate and reduced-Order modeling: A comparison of approaches for large-scale statistical inverse problems*, pp. 123–149. Hoboken, NJ: John Wiley & Sons, Ltd.

Gauer, Peter, Medina-Cetina, Zenon, Lied, Karstein & Kristensen, Krister 2009 Optimization and probabilistic calibration of avalanche block models. *Cold Regions Science and Technology* **59** (2–3), 251–258.

Gelman, A., Carlin, J.B., Stern, H.S. & Rubin, D.B. 2003 *Bayesian data analysis*, 2nd edn. Boca Raton, FL: Taylor & Francis.

Gentle, J.E., Härdle, W. & Mori, Y. 2004 *Handbook of computational statistics: Concepts and methods*. Heidelberg, New York: Springer.

Geyer, CJ & Thompson, EA 1995 Annealing markov chain monte carlo with applications to ancestral inference. *J Am Stat Assoc.* **90** (431), 909–920.

Ghanem, R.G. & Spanos, P.D. 2003 *Stochastic finite elements: A spectral approach*. New York: Dover Publications.

Ghosh, D. P. 1971*a* The application of linear filter theory to the direct interpretation of geoelectrical resistivity sounding measurements. *Geophysical Prospecting* **19** (2), 192–217.

Ghosh, D. P. 1971*b* Inverse filter coefficients for the computation of apparent resistivity standard curves for a horizontally stratified earth. *Geophysical Prospecting* **19** (4), 769–775.

Gilgen, R., Kleinrahm, R. & Wagner, W. 1994*a* Measurement and correlation of the (pressure, density, temperature) relation of argon i. the homogeneous gas and liquid regions in the temperature range from 90 k to 340 k at pressures up to 12 {MPa}. *The Journal of Chemical Thermodynamics* **26** (4), 383–398.

Gilgen, R., Kleinrahm, R. & Wagner, W. 1994*b* Measurement and correlation of the (pressure, density, temperature) relation of argon ii. saturated-liquid and saturated-vapour densities and vapour pressures along the entire coexistence curve. *The Journal*

of Chemical Thermodynamics **26** (4), 399–413.

Gilks, W. R., Richardson, S. & Spiegelhalter, David, ed. 1996 *Markov Chain Monte Carlo in practice*, 1st edn. London: Chapman and Hall/CRC.

Gouveia, Wences P. & Scales, John A. 1998 Bayesian seismic waveform inversion: Parameter estimation and uncertainty analysis. *Journal of Geophysical Research: Solid Earth* **103** (B2), 2759–2779.

Green, Peter J. 1995 Reversible jump markov chain monte carlo computation and bayesian model determination. *Biometrika* **82** (4), 711–732.

Gross, Joachim & Sadowski, Gabriele 2001 Perturbed-chain saft: An equation of state based on a perturbation theory for chain molecules. *Industrial & Engineering Chemistry Research* **40** (4), 1244–1260.

Guptasarma, D. & Singh, B. 1997 New digital linear filters for hankel j_0 and j_1 transforms. *Geophysical Prospecting* **45** (5), 745–762.

Haflidason, Haflidi, Lien, Reidar, Sejrup, Hans Petter, Forsberg, Carl Fredrik & Bryn, Petter 2005 The dating and morphometry of the storegga slide. *Marine and Petroleum Geology* **22** (1-2), 123–136.

Hastie, T., Tibshirani, R. & Friedman, J. 2009 *The elements of statistical learning: Data mining, inference, and prediction*, 2nd edn. New York, NY: Springer.

Hering, A., Misiek, R., Gyulai, A., Ormos, T., Dobroka, M. & Dresen, L. 1995 A joint inversion algorithm to process geoelectric and sutface wave seismic data. part i: basic ideas1. *Geophysical Prospecting* **43** (2), 135–156.

Hey, T. 2009 *The fourth paradigm: Data-intensive scientific discovery*. Microsoft Research.

Higdon, Dave 2002 Space and space-time modeling using process convolutions. In *Quantitative methods for current environmental issues* (ed. CliveW. Anderson, Vic Barnett, PhilipC. Chatwin & AbdelH. El-Shaarawi), pp. 37–56. Springer London.

Hirata, S, Yao, S & Nishida, K 1990 Multiple regression analysis between the mechanical and physical properties of cohesive soils. *Soils Found.* **30** (3), 91–108.

Holmes, C. C., Denison, D. G. T., Ray, S. & Mallick, B. K. 2005 Bayesian prediction via partitioning. *Journal of Computational and Graphical Statistics* **14** (4), 811–830.

Hopcroft, Peter O., Gallagher, Kerry & Pain, Chris C. 2007 Inference of past climate from borehole temperature data using bayesian reversible jump markov chain monte carlo. *Geophysical Journal International* **171** (3), 1430–1439.

Hopcroft, Peter O., Gallagher, Kerry & Pain, Christopher C. 2009 A bayesian partition modelling approach to resolve spatial variability in climate records from borehole temperature inversion. *Geophysical Journal International* **178** (2), 651–666.

Huang, Chen-Fen, Gerstoft, Peter & Hodgkiss, William S. 2006 Uncertainty analysis in matched-field geoacoustic inversions. *The Journal of the Acoustical Society of America* **119** (1), 197–207.

Jaynes, E.T. & Bretthorst, G.L. 2003 *Probability theory: The logic of science*. Cambridge, UK: Cambridge University Press.

Jefferys, William H. & Berger, James O. 1992 Ockham's razor and bayesian analysis. *American Scientist* **80** (1), 64–72.

Jeffreys, Harold 1935 Some tests of significance, treated by the theory of probability. In *Proceedings of the Cambridge Philosophical Society*, , vol. 31, pp. 203–222. Cambridge University Press.

Jeffreys, Harold 1946 An invariant form for the prior probability in estimation problems. *Proceedings of the Royal Society of London. Series A. Mathematical and Physical Sciences* **186** (1007), 453–461.

Jeffreys, H. 1998 *The theory of probability*, 3rd edn. Oxford University Press.

Kaipio, Jari P & Somersalo, Erkki 2005 *Statistical and computational inverse problems*, , vol. 160. New York: Springer.

Kang, Jun Won & Kallivokas, Loukas F. 2010*a* The inverse medium problem in 1d pml-truncated heterogeneous semi-infinite domains. *Inverse Problems in Science and Engineering* **18** (6), 759–786.

Kang, J. W. & Kallivokas, L. F. 2010*b* Mixed unsplit field perfectly matched lay-

ers for transient simulations of scalar waves in heterogenous domains. *Computational Geosciences* **14**, 623–648.

Kass, Robert E. & Raftery, Adrian E. 1995 Bayes factors. *Journal of the American Statistical Association* **90** (430), 773–795.

Kass, Robert E. & Steffey, Duane 1989 Approximate bayesian inference in conditionally independent hierarchical models (parametric empirical bayes models). *Journal of the American Statistical Association* **84** (407), 717–726.

Kass, Robert E. & Wasserman, Larry 1995 A reference bayesian test for nested hypotheses and its relationship to the schwarz criterion. *Journal of the American Statistical Association* **90** (431), 928–934.

Kass, Robert E. & Wasserman, Larry 1996 The selection of prior distributions by formal rules. *Journal of the American Statistical Association* **91** (435), 1343–1370.

Kaynia, A.M., Papathoma-Kohle, M., Neuhauser, B., Ratzinger, K., Wenzel, H. & Medina-Cetina, Z. 2008 Probabilistic assessment of vulnerability to landslide: Application to the village of lichtenstein, baden-wurttemberg, germany. *Engineering Geology* **101** (1–2), 33–48.

Keilis-Borok, V. I. & Yanovskaya, T. B. 1967 Inverse problems in seismology. *Geophysical Journal of the Royal Astronomical Society* **13**, 223–234.

Kennedy, Marc C. & O'Hagan, Anthony 2001 Bayesian calibration of computer models. *Journal of the Royal Statistical Society: Series B (Statistical Methodology)* **63** (3), 425–464.

Key, J. T., Pericchi, L. R. & Smith, A. F. M. 1999 Bayesian model choice: what and why. Oxford University Press.

Kleinrahm, R. & Wagner, W. 1986 Measurement and correlation of the equilibrium liquid and vapour densities and the vapour pressure along the coexistence curve of methane. *The Journal of Chemical Thermodynamics* **18** (8), 739–760.

Koefoed, O. 1979 *Geosounding principles: Resistivity sounding measurements. 1*. Amsterdam, Netherlands: Elsevier Scientific Publishing Company.

Koutsourelakis, P.S. 2009 A multi-resolution, non-parametric, bayesian framework for identification of spatially-varying model parameters. *Journal of Computational Physics* **228** (17), 6184–6211.

Kvalstada, TJ, Nadim, F, Kayniaa, AM, Mokkelbosta, KH & Brynb, P 2005 Soil conditions and slope stability in the ormen lange area. *Mar Petrol Geol.* **22** (1-2), 299–310.

Lee, C. Y., Poulos, Harry George & Hull, Timothy Stephen 1991 Effect of seafloor instability on offshore pile foundations. *Canadian Geotechnical Journal* **28** (5), 729–737.

Lee, Herbert K H, Higdon, Dave M, Bi, Zhuoxin, Ferreira, Marco A R & West, Mike 2002 Markov random field models for high-dimensional parameters in simulations of fluid flow in porous media. *Technometrics* **44** (3), 230–241.

Lehmann, E.L. & Casella, G. 1998 *Theory of point estimation*. New York: Springer.

Lelièvre, Peter G., Farquharson, Colin G. & Hurich, Charles A. 2012 Joint inversion of seismic traveltimes and gravity data on unstructured grids with application to mineral exploration. *Geophysics* **77** (1), K1–K15.

Li, Wei & Cirpka, Olaf A. 2006 Efficient geostatistical inverse methods for structured and unstructured grids. *Water Resources Research* **42** (6).

Liang, Feng, Paulo, Rui, Molina, German, Clyde, Merlise A & Berger, Jim O 2008 Mixtures of g priors for bayesian variable selection. *Journal of the American Statistical Association* **103** (481), 410–423.

Lindley, D. V. 1957 A statistical paradox. *Biometrika* **44** (1/2), 187–192.

Liszkowski, J, Tschuschke, M, Mlynarek, Z & Tschuschke, W 2004 Statistical evaluation of the dependence of the liquidity index and undrained shear strength of cptu parameters in cohesive soils. In *Proceedings ISC-2 on Geotechnical and Geophysical Site Characterization, Millpress, Rotterdam*, pp. 979–985. Millpress, Rotterdam.

Liu, J.S. 2001 *Monte Carlo strategies in scientific computing*. New York: Springer.

Locat, J & Demers, D 1988 Viscosity, yield stress, remolded strength, and liquidity

index relationships for sensitive clays. *Can Geotech J.* **25**, 799–806.

Lucas, K. 1991 *Applied statistical thermodynamics*. New York, NY.: Springer-Verlag.

MacKay, David JC 1995 Probable networks and plausible predictions-a review of practical bayesian methods for supervised neural networks. *Network: Computation in Neural Systems* **6** (3), 469–505.

Malinverno, Alberto 2002 Parsimonious bayesian markov chain monte carlo inversion in a nonlinear geophysical problem. *Geophysical Journal International* **151** (3), 675–688.

Manglik, A. & Verma, Saurabh K. 1998 Delineation of sediments below flood basalts by joint inversion of seismic and magnetotelluric data. *Geophysical Research Letters* **25** (21), 4015–4018.

Martinez, W. L. & Martinez, A. R. 2001 *Computational statistics handbook with MATLAB*. Boca Raton, FL: Taylor & Francis.

Marzouk, Youssef M. & Najm, Habib N. 2009 Dimensionality reduction and polynomial chaos acceleration of bayesian inference in inverse problems. *Journal of Computational Physics* **228** (6), 1862–1902.

Marzouk, Youssef M., Najm, Habib N. & Rahn, Larry A. 2007 Stochastic spectral methods for efficient bayesian solution of inverse problems. *Journal of Computational Physics* **224** (2), 560 – 586.

Masters, A J 2008 Virial expansions. *Journal of Physics: Condensed Matter* **20** (28).

McElroy, P.J., Battino, R. & Dowd, M.K. 1989 Compression-factor measurements on methane, carbon dioxide, and (methane + carbon dioxide) using a weighing method. *The Journal of Chemical Thermodynamics* **21** (12), 1287–1300.

Medina-Cetina, Z. 2006 Probabilistic calibration of a soil model. Published doctoral dissertation, The Johns Hopkins University.

Medina-Cetina, Zenon & Arson, Chloe 2014 Probabilistic calibration of a damage rock mechanics model. *Geotechnique Letters* **4**, 17–21(4).

Medina-Cetina, Zenon, Esmailzadeh, Saba, Kang, Jun Wong & Kallivokas, Loukas 2013 Bayesian inversion of heterogeneous media: Introducing the next genera-

tion of integrated studies for offshore site investigations. In *Offshore Technology Conference*. Offshore Technology Conference.

Medina-Cetina, Zenon & Rechenmacher, Amy 2010 Influence of boundary conditions, specimen geometry and material heterogeneity on model calibration from triaxial tests. *International Journal for Numerical and Analytical Methods in Geomechanics* **34** (6), 627–643.

Mienert, Juergen 2004 Costa-continental slope stability: major aims and topics. *Marine Geology* **213** (1), 1–7.

Minsley, Burke J. 2011 A trans-dimensional bayesian markov chain monte carlo algorithm for model assessment using frequency-domain electromagnetic data. *Geophysical Journal International* **187** (1), 252–272.

Mondal, A., Efendiev, Y., Mallick, B. & Datta-Gupta, A. 2010 Bayesian uncertainty quantification for flows in heterogeneous porous media using reversible jump markov chain monte carlo methods. *Advances in Water Resources* **33** (3), 241–256.

Montgomery, Douglas C. & Runger, George C. 2010 *Applied statistics and probability for engineers*, 5th edn. Hoboken, NJ: Wiley, John & Sons, Inc.

Mosegaard, Klaus & Tarantola, Albert 1995 Monte carlo sampling of solutions to inverse problems. *Journal of Geophysical Research: Solid Earth* **100** (B7), 12431–12447.

Na, S. W. & Kallivokas, L. F. 2008 Continuation schemes for shape detection in inverse acoustic scattering problems. *Computer Modeling in Engineering & Sciences* **35** (1), 73–90.

NGI 2002 Early soil investigations for "fast trac projects". *Tech. Rep.* 521553. Norwegian Geotechnical Institute, NGI, Oslo, Norway.

Parasnis, D.S. 1997 *Principles of applied geophysics*, 5th edn. London: Springer.

Patil, Prashant, Ejaz, Saquib, Atilhan, Mert, Cristancho, Diego, Holste, James C. & Hall, Kenneth R. 2007 Accurate density measurements for a 91% methane natural gas-like mixture. *The Journal of Chemical Thermodynamics* **39** (8), 1157 – 1163.

Peacock, JA 1983 Two-dimensional goodness-of-fit testing in astronomy. *Mon Not R astr Soc* **202**, 615–627.

Plessix, R., De Roeck, Y. & Chavent, G. 1998 Waveform inversion of reflection seismic data for kinematic parameters by local optimization. *SIAM Journal on Scientific Computing* **20** (3), 1033–1052.

Plessix, Rene-Edouard 2008 Introduction: Towards a full waveform inversion. *Geophysical Prospecting* **56** (6), 761–763.

Press, Frank 1968 Earth models obtained by monte carlo inversion. *Journal of Geophysical Research* **73** (16), 5223–5234.

Privat, Romain, Privat, Yannick & Jaubert, Jean-Nol 2009 Can cubic equations of state be recast in the virial form? *Fluid Phase Equilibria* **282** (1), 38–50.

Radford, NM 1996 Sampling from multimodal distributions using tempered transitions. *Stat Comput.* **6** (4), 353–366.

Rechenmacher, A. & Medina-Cetina, Z. 2007 Calibration of soil constitutive models with spatially varying parameters. *Journal of Geotechnical and Geoenvironmental Engineering* **133** (12), 1567–1576.

Robert, Christian 2007 *The Bayesian choice: from decision-theoretic foundations to computational implementation*, 2nd edn. New York: Springer.

Robert, Christian P & Casella, George 2004 *Monte Carlo statistical methods*, 2nd edn., *Springer series in statistics*, vol. 319. New York: Springer.

Sambridge, M., Bodin, T., Gallagher, K. & Tkalcic, H. 2013 Transdimensional inference in the geosciences. *Philosophical Transactions of the Royal Society A: Mathematical, Physical and Engineering Sciences* **371** (1984).

Sambridge, M., Gallagher, K., Jackson, A. & Rickwood, P. 2006 Transdimensional inverse problems, model comparison and the evidence. *Geophysical Journal International* **167** (2), 528–542.

Scales, J. & Tenorio, L. 2001 Tutorial: Prior information and uncertainty in inverse problems. *Geophysics* **66** (2), 389–397.

Schwarz, Gideon 1978 Estimating the dimension of a model. *The Annals of Statistics* **6** (2), 461–464.

Sheskin, DJ 2004 *Handbook of parametrik and nonparametric statistical procedures*, 3rd edn. Boca Raton, FL.: Chapman & Hall/CRC,.

Sivia, Devinder S 1996 *Data analysis: A Bayesian tutorial*. Oxford, UK: Oxford University Press.

Solheim, A., Berg, K., Forsberg, C.F & Bryn, P. 2005 The storegga slide complex: repetitive large scale sliding with similar cause and development. *Marine and Petroleum Geology* **22** (1-2), 97–107.

Span, R. 2000 *Multiparameter equations of state: An accurate source of thermodynamic property data*. Berlin: Springer.

Stefanesco, S., Schlumberger, C. & Schlumberger, M. 1930 Sur la distribution électrique potentielle autour d'une prise de terre ponctuelle dans un terrain à couches horizontales, homogènes et isotropes. *J. Phys. Radium* **1** (4), 132–140.

Stephenson, John, Gallagher, K. & Holmes, C.C. 2004 Beyond kriging: Dealing with discontinuous spatial data fields using adaptive prior information and bayesian partition modelling. *Geological Society Special Publication* **239** (1), 195–209.

Stephenson, John, Gallagher, K. & Holmes, C.C. 2006 Low temperature thermochronology and strategies for multiple samples: 2: Partition modelling for 2d/3d distributions with discontinuities. *Earth and Planetary Science Letters* **241** (3-4), 557–570.

Stewart, Richard B. & Jacobsen, Richard T. 1989 Thermodynamic properties of argon from the triple point to 1200 k with pressures to 1000 mpa. *Journal of Physical and Chemical Reference Data* **18** (2), 639–798.

Sun, Ne-Zheng & Yeh, William W-G. 1992 A stochastic inverse solution for transient groundwater flow: Parameter identification and reliability analysis. *Water Resources Research* **28** (12), 3269–3280.

Symes, William W. 2008 Migration velocity analysis and waveform inversion. *Geophysical*

Prospecting **56** (6), 765–790.

Tahvildari, Navid & Kaihatu, James M. 2011 Optimized determination of viscous mud properties using a nonlinear wave-mud interaction model. *Journal of Atmospheric and Oceanic Technology* **28**, 1486–1503.

Tarantola, A 1987 *Inverse problem theory*. New York, NY.: Elsevier.

Tarantola, Albert 2005 *Inverse problem theory and methods for model parameter estimation*. Philadelphia, PA: Society for Industrial and Applied Mathematics.

Tarantola, Albert & Valette, Bernard 1982 Inverse problems= quest for information. *J. geophys* **50** (3), 150–170.

Terzaghi, K, Peck, RB & Mesri, G 1996 *Soil mechanics in engineering practice*, 3rd edn. New York, NY.: Wiley.

Tierney, Luke & Kadane, Joseph B. 1986 Accurate approximations for posterior moments and marginal densities. *Journal of the American Statistical Association* **81** (393), 82–86.

Tierney, Luke, Kass, Robert E. & Kadane, Joseph B. 1989 Fully exponential laplace approximations to expectations and variances of nonpositive functions. *Journal of the American Statistical Association* **84** (407), 710–716.

Tikhonov, A. N. 1963 Solution of incorrectly formulated problems and the regularization method. *Soviet Math. Doklady* **4**, 1035–1038.

Ulrych, Tadeusz J., Sacchi, Mauricio D. & Woodbury, Alan 2001 A bayes tour of inversion: A tutorial. *Geophysics* **66** (1), 55–69.

Virieux, J. & Operto, S. 2009 An overview of full-waveform inversion in exploration geophysics. *Geophysics* **74** (6), WCC1–WCC26.

Vuong, Quang H. 1989 Likelihood ratio tests for model selection and non-nested hypotheses. *Econometrica* **57** (2), 307–333.

Wang, Yu, Huang, Kai & Cao, Zijun 2013 Probabilistic identification of underground soil stratification using cone penetration tests. *Canadian Geotechnical Journal* **50** (7), 766–776.

Wohlberg, Brendt & Tartakovsky, Daniel M. 2009 Delineation of geological facies from poorly differentiated data. *Advances in Water Resources* **32** (2), 225–230.

Wroth, C. P. & Wood, D. M. 1978 The correlation of index properties with some basic engineering properties of soils. *Canadian Geotechnical Journal* **15** (2), 137–145.

Yan, Liang, Yang, Fenglian & Fu, Chuli 2009 A bayesian inference approach to identify a robin coefficient in one-dimensional parabolic problems. *Journal of Computational and Applied Mathematics* **231** (2), 840–850.

Yang, SL, Medina-Cetina, Z & Nadim, F 2010 Uncertainty analysis on remolded undrained shear strength of marine clay. *Georisk.* **4** (1), 43–50.

Zellner, A. 1986 On assessing prior distributions and bayesian regression analysis with g-prior distributions. In *Bayesian inference and decision techniques: Essays in honor of Bruno de Fenetti*, pp. 233–243.

APPENDIX A

POSTERIOR INTEGRATION USING THE MCMC-METROPOLIS HASTINGS ALGORITHM

Markov Chain Monte Carlo (MCMC) method is a numerical procedure that allows for the direct sampling of a posterior. An important property of the MCMC method is that it converges to the target joint density as the sample grows. The decision rule that selects the samples is the Metropolis-Hastings (MH), which is a generalized form of the Metropolis and Gibbs methods (Robert & Casella, 2004).

Suppose we want to generate from a target distribution $p\left(\mathbf{m}|\mathbf{d}_{obs}\right)$. That is to construct a Markov chain $\{(\mathbf{m})_n\}$ which has stationary distribution $p\left(\mathbf{m}|\mathbf{d}_{obs}\right)$. At the sth iteration the chain state is $\mathbf{m}^{(s)}$. A new model is proposed by sampling a candidate model $\mathbf{m}^*$ from a proposal distribution $q\left(.|\mathbf{m}^{(s)}\right)$. The latter is conditioned only on the previous state of the chain $\left(\mathbf{m}^{(s)}\right)$.

The candidate point $\mathbf{m}^*$ is accepted or rejected as the next state of the chain with a probability given by:

$$\alpha(\mathbf{m}^{(s)}, \mathbf{m}^*) = \min\left\{1,\ \frac{p\left(\mathbf{m}^*|\mathbf{d}_{obs}\right) q\left(\mathbf{m}^{(s)}|\mathbf{m}^*\right)}{p\left(\mathbf{m}^{(s)}|\mathbf{d}_{obs}\right) q\left(\mathbf{m}^*|\mathbf{m}^{(s)}\right)}\right\} \tag{A.1}$$

Notice that $p\left(\mathbf{m}|\mathbf{d}_{obs}\right)$ in the above equation is the posterior kernel (unnormalized posterior) which is the multiplicity of the prior density and the likelihood function. As the above decision rule appears as a ratio, the constant of the proportionality (the denominator in equation 5.3) cancels out. There for the direct sampling of the posterior is feasible without the need to perform the integration.

The Metropolis-Hastings algorithm is as follows

1. Set initial guess of the model parameters vector $\mathbf{m}^{(1)}$ at $s = 1$

2. Generate a candidate point $\mathbf{m}^*$ from $q\left(.|\mathbf{m}^{(s)}\right)$

3. Draw U from a uniform $[0, 1]$ distribution

4.

$$\mathbf{m}^{(s+1)} = \begin{cases} \mathbf{m}^* & \text{if } U \leq \alpha(\mathbf{m}^{(s)}, \mathbf{m}^*) \\ \mathbf{m}^{(s)} & \text{if } U > \alpha(\mathbf{m}^{(s)}, \mathbf{m}^*) \end{cases}$$

5. Set $s = s + 1$ and repeat steps 2 through 5.

APPENDIX B

PARALLEL TEMPERING MARKOV CHAIN MONTE CARLO

Markov Chain Monte Carlo methods has been extensively employed to treat a variety of statistical applications, wherever an intractable integration is involved in the analysis. Although the method works well often times, slow chain mixing and lack of convergence arise in more complex, high dimensional, highly correlated, multi-modal target density configurations. Parallel tempering, also known as replica exchange MCMC sampling (Geyer & Thompson, 1995; Earl & Deem, 2005; Radford, 1996), offers a simulation scheme which speeds up mixing and alleviates convergence concerns by improving the dynamic behavior of Monte Carlo sampling methods. The essence of the method is to draw the realizations from a sequence of distributions each at a different "temperature" level, allowing the distributions trade configurations randomly as the chain proceeds. Even though often times one specific configuration (with a specific temperature) is of interest, the simulation results are robust ensembles for all the distributions.

Contrary to the classical Monte Carlo update schemes which consist of a single stochastic process, parallel tempering MCMC method simulates N replica of a distribution of interest which is generally the kernel of the target density $h_i(x),\ i = T_1, \cdots, T_N$, each replica being indexed by a parameter called "temperature" (T_i). Generally, $T_1 < T_2 < \cdots < T_N$, and for majority of cases T_1 corresponds to the target distribution. Accordingly, $h_{T_1}(x)$ is called "cold" distribution (configuration), and $h_{T_N}(x)$ is the "hot" distribution, which is the easiest density to simulate. Normally, sampling from the cold distribution is of interest, and the high temperature systems contribute to expedite the mixing process. The main un-normalized density $h(x)$ is "powered up" to a sequence of unnormalized densities $h(x)^{1/\beta_i}$, where $\beta_i > 1$. $\beta_i = \frac{1}{k_B T_i}$ is proportional to the reciprocal temperature, and k_B is the Boltzmann constant. The terminology is borrowed from statistical physics, where the distribution of a thermodynamic equilibrium has a kernel of the form $e^{\frac{-U(x)}{k_B T}}$, where $U(x)$

is potential energy function of the system.

It is primarily supposed that within each configuration at temperature T_i a sampling scheme, Gibbs or Metropolis Hastings, is available to update state x that has a stationary distribution $e^{-U(x)/k_B T_i}$. Transition between distributions are also allowed. The adjacent configurations i, j are exchanged through a Monte Carlo process, typically with Metropolis-Hastings acceptance criteria. The swapping attempts are made with the probability of $q_{i,j} = 1/2$. The states at which the chains are swapped, i, is randomly chosen, and the attempt is accepted with the following probability

$$r = \min\left(1, e^{(U_i - U_j)(\beta_i - \beta_j)}\right) \tag{B.1}$$

Obviously the probability to accept a proposed swamp grows as the two adjacent systems are less different in temperature, and as the systems become smaller. Here is the strategy; The high temperature replicas are generally able to sample a large volume of the domain of interest, whereas the low temperature systems are more likely to be trapped in the local "energy" minima, whilst they certify to achieve precise sampling in a local domains of the parameter space. The contribution of the parallel tempering is to allow within configuration transitions. As a result, a "cold" simulation is given a fresh configuration for sampling at a point in space, which is presumably distant enough from the point from which it is swapped. Moreover, the low temperature configuration is exchanged with a higher temperature, at which it has a higher chance of being released from the local energy minima, and access to a new region of space before being swapped back into a low temperature simulation. In fact high temperature systems carry the low temperature samplers to a set of local regions of the space to draw samples.

Here, eleven levels of temperature are considered, where the eleven replicas are running in parallel. The median temperature value is one which retrieves the desired target density. The swapping probability is 1/2, and the within chain and between chain transitions are carried out according to Metropolis Hastings criteria. A thinning algorithm is applied to

to store every $M = 5$ samples to save memory usage.

APPENDIX C

ALTERNATIVE APPROACHES TO INFER PARAMETERS OF A DISTRIBUTION FROM TWO SETS OF DATA

Suppose two data vector $\mathbf{y}_1$ and $\mathbf{y}_2$ are populated from a probability distribution with parameter θ, and $p(\theta)$ expresses the prior before the first data set $\mathbf{y}_1$ is observed. Two alternative approaches might be followed to infer θ, having observed both $\mathbf{y}_1$ and $\mathbf{y}_2$: 1. Using the posterior from the first experiment as the prior leading into experiment two, where $\mathbf{y}_2$ is observed. Hence the posterior after the second experiment is

$$\begin{aligned} p_2(\theta|\mathbf{y}_2) &\propto p_2(\theta|\mathbf{y}_1) f_2(\mathbf{y}_2|\theta) \\ &\propto f_1(\mathbf{y}_1|\theta) f_2(\mathbf{y}_2|\theta) p(\theta) \end{aligned} \tag{C.1}$$

where $f(.)$ denotes the likelihood function.

2. The second possibility is to treat $(\mathbf{y}_1, \mathbf{y}_2)$ as a single data set, hence, $p(\theta|\mathbf{y}_1, \mathbf{y}_2) \propto f(\mathbf{y}_1, \mathbf{y}_2|\theta) p(\theta)$. Comparing this proportionality with proportionality C.1 shows in general the two approach give rise to the same inference about the parameter θ if and only if

$$p(\theta|\mathbf{y}_1, \mathbf{y}_2) \propto f_1(\mathbf{y}_1|\theta) f_2(\mathbf{y}_2|\theta) \quad \forall\, \theta \tag{C.2}$$

which requires $\mathbf{y}_1$ and $\mathbf{y}_2$ be statistically independent.

APPENDIX D

BAYESIAN OCCAM'S RAZOR

A simple explanation of why the Bayesian model selection adheres to the concept of parsimony is presented in figure D.1. This figure illustrates the Bayesian embodiment to the later concept (Jefferys & Berger, 1992; MacKay, 1995; Denison *et al.*, 2002*b*). The horizontal axes presents the data space, and the vertical axes shows the measure of the marginal likelihood. $\mathcal{M}_1$ and $\mathcal{M}_2$ are two competing explanations of a same process. Model $\mathcal{M}_1$ is the simpler theory, and $\mathcal{M}_2$ is the more complex one. The simple model is only capable of reaching a limited subdomain in the data space $\mathcal{D}_1$, whereas the more complex model is able to embrace a wider space due to it's flexibility. As both $p(\mathbf{d}|\mathcal{M}_1)$ and $p(\mathbf{d}|\mathcal{M}_2)$ are integrated to one over the data space, if the observed data lies in $\mathcal{D}_1$ which is accessible by the both models, then $\mathcal{M}_1$ is favored over $\mathcal{M}_2$, as it assumes higher probability in this region.

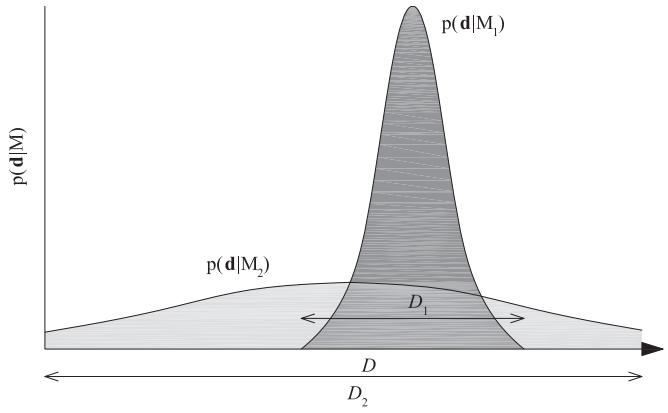

Figure D.1: Schematic presentation of Bayesian Occam's razor

APPENDIX E

BAYESIAN MODEL SELECTION AND UNIDENTIFIABLE BAYES FACTORS

Improper priors can not be assigned to model specific parameters in Bayesian model determination, as the choice of the arbitrary normalizing constant will influence the Bayes factor. The Bayes factor is a multiple of the prior normalizing constant.

Inherent to a Bayesian model selection is to compare the relative merits of a number of competing models via the definition of the Bayes factor. Consider a set of K plausible models (here these K models correspond to K different discretization scenarios of the unknown random field with k tessellations, where $k \in \{1, \ldots, K\}$). Denoting model k with $\mathcal{M}_k$ (here $\mathcal{M}_k$ refers to the model with k tessellations), Bayes factor offers a thorough criteria to pairwise comparison of members in $\{\mathcal{M}_k\}$. The relative plausibility of model i versus model j having observed data $\mathbf{d}_{\text{obs}}$ is determined by the Bayes factor given by

$$BF\left[\mathcal{M}_i : \mathcal{M}_j\right] = \frac{p\left(\mathcal{M}_i|\mathbf{d}_{\text{obs}}\right)/p(\mathcal{M}_i)}{p\left(\mathcal{M}_j|\mathbf{d}_{\text{obs}}\right)/p(\mathcal{M}_j)} \tag{E.1}$$

which by definition is the posterior to prior odds ratio. Here $p\left(\mathcal{M}_i\right)$ and $p\left(\mathcal{M}_i|\mathbf{d}_{\text{obs}}\right)$ are the prior and the posterior probability of $\mathcal{M}_i$ being the true model respectively. It can be shown that the above expression is equivalent to

$$BF\left[\mathcal{M}_i : \mathcal{M}_j\right] = \frac{p\left(\mathbf{d}_{\text{obs}}|\mathcal{M}_i\right)}{p\left(\mathbf{d}_{\text{obs}}|\mathcal{M}_j\right)} \tag{E.2}$$

where $p\left(\mathbf{d}_{\text{obs}}|\mathcal{M}_i\right)$ is the marginal likelihood of data given model $\mathcal{M}_i$ is the true model

$$p\left(\mathbf{d}_{\text{obs}}|\mathcal{M}_i\right) = \int_{\boldsymbol{\Theta}_i} p\left(\mathbf{d}_{\text{obs}}|\mathcal{M}_i, \boldsymbol{\theta}_i\right) p\left(\boldsymbol{\theta}_i|\mathcal{M}_i\right) \mathrm{d}\boldsymbol{\theta}_i \tag{E.3}$$

$\boldsymbol{\theta}_i$ is a set of parameters specific to model $\mathcal{M}_i$, and $p\left(\mathbf{d}_{\text{obs}}|\mathcal{M}_i, \boldsymbol{\theta}_i\right)$ and $p\left(\boldsymbol{\theta}_i|\mathcal{M}_i\right)$ are the

likelihood function and the prior density of the model specific parameters $\boldsymbol{\theta}_i$, respectively, given $\mathcal{M}_i$ is the true model.

One could rewrite $BF\left[\mathcal{M}_i : \mathcal{M}_j\right]$ of equation E.2 in the following form

$$BF\left[\mathcal{M}_i : \mathcal{M}_j\right] = \frac{p_i/c_i}{p_j/c_j} \tag{E.4}$$

where $h_i\left(\boldsymbol{\theta}_i\right) \propto p\left(\boldsymbol{\theta}_i|\mathcal{M}_i\right)$, and $c_i = \int h_i\left(\boldsymbol{\theta}_i\right) \mathrm{d}\boldsymbol{\theta}_i$ is the normalizing constant. p_i is the unnormalized marginal likelihood $p_i = \int p\left(\mathbf{d}_{\text{obs}}|\mathcal{M}_i, \boldsymbol{\theta}_i\right) h_i\left(\boldsymbol{\theta}_i\right) \mathrm{d}\boldsymbol{\theta}_i$ (see equation E.3), and p_j and c_j have identical definitions as p_i and c_i, respectively. The Bayes factor is a multiple of the prior normalizing constant.

By the virtue of equation E.4 it is necessary for the prior density being proper (c_i and c_j being finite) for the ratio c_j/c_i being well defined. In case improper priors (c_i and c_j infinite) are assigned to model specific parameters, the Bayes factor becomes "unidentifiable" and results in erroneous model comparison output.

APPENDIX F

THE JACOBIAN OF THE DIMENSION MATCHING TRANSFORMATION

When moving between dimensions (Birth and Death) the acceptance probability includes a Jacobian term. Let a Birth move is proposed: $k^* = k^{(s)} + 1$. The Jacobian term accounts for the following change in variables:

$$\boldsymbol{\theta}^{(s)} := \left(\{x_c^{(s)}\}_{i=1}^{k^{(s)}}, \{c_s^{(s)}\}_{i=1}^{k^{(s)}}, u_x, u_c \right) \overset{\mathcal{T}}{\leftrightarrow} \boldsymbol{\theta}^* := \left(\{x_c^*\}_{i=1}^{k^*}, \{c_s^*\}_{i=1}^{k^*} \right) \tag{F.1}$$

The above transformation $\mathcal{T}$ must be bijective for its Jacobian to exist. The random variable u_x is populated from a discrete uniform distribution $u_x \sim \mathcal{U}(1, T)$ to add a new nucleus from a set of available grid locations $\mathscr{T}$, where $T = |\mathscr{T}|$. Another random number is drawn from a Gaussian density $u_c \sim \mathcal{N}(0, 1)$ to determine the velocity of the newly generated cell by perturbing the current velocity value where the Birth takes place, as follows:

$$\mathcal{T}\left(\mathbf{c}_s^{(s)}, u_c\right) = \begin{cases} c_{s_1}^* & = c_{s_1}^{(s)} \\ & \vdots \\ c_{s_i}^* & = c_{s_i}^{(s)} \\ & \vdots \\ c_{s_{k^{(s)}+1}}^* & = c_{s_i}^{(s)} + u_c \end{cases} \tag{F.2}$$

The Jacobian for the above dimension matching transformation is given by

$$|\mathbf{J}|_{\text{Birth}} = \left| \frac{\partial \mathcal{T}(\mathbf{c}_s^{(s)}, u_c)}{\partial \mathbf{c}_s^{(s)} \partial u_c} \right| = \left| \frac{\partial (c_{s_i}^*, c_{s_{k^{(s)}+1}}^*)}{\partial c_{s_i}^{(s)} \partial u_c} \right| = \begin{vmatrix} 1 & 0 \\ 1 & 1 \end{vmatrix} = 1 \tag{F.3}$$

The Jacobian for the death move is $|\mathbf{J}|_{\text{Death}} = |\mathbf{J}|^{-1}_{\text{Birth}} = 1$. Notice that the parameter space for the nuclei positions is discrete (whereas its continuous for the velocity space), and the random variable u_x we drew to propose the position of the new nucleus is also discrete. Denison etal Denison *et al.* (2002*a*) shows that the Jacobian term is always unity for discrete transformations. Therefore only where continuous model spaces change in dimensions, determining the Jacobian is required.